MODELING, DYNAMIC IDENTIFICATION, AND NONLINEAR ASSESSMENT OF CIVIL STRUCTURES FROM RECORDED EARTHQUAKES AND AMBIENT VIBRATIONS

by

Ángel J. Alicea-Rodríguez

Dissertation submitted in partial fulfillment
of the requirements for the degree of

DOCTOR OF PHILOSOPHY
in
CIVIL ENGINEERING

UNIVERSITY OF PUERTO RICO
MAYAGÜEZ CAMPUS
2018

Approved by:

_____	_____
Ricardo R. López-Rodríguez, Ph.D. President, Graduate Committee	Date
_____	_____
Luis E. Suárez-Colche, Ph.D. Member, Graduate Committee	Date
_____	_____
José A. Martínez-Cruzado, Ph.D. Member, Graduate Committee	Date
_____	_____
Carlos I. Huerta-López, Ph.D. Member, Graduate Committee	Date
_____	_____
Ismael Pagán-Trinidad, M.S.C.E. Chairperson of the Department	Date
_____	_____
Aidcer L. Vidot-Vega, Ph.D. Representative of Graduate School	Date

ABSTRACT

America's infrastructure was constructed mainly during the mid-20th century. Its aging effects are increasing every year, creating a dilemma in which the United States is not alone. Moreover, the great majority of buildings and bridges are seismically non-compliant with current building codes and many have been in place far beyond their design lives. This issues acquire special relevance in countries that are located in seismically prone regions and that historically have suffered the onslaught of strong seismic events. In large urban areas the problem is particularly acute because space is scarce and growing populations stress city support systems. Puerto Rico, as many other countries and cities in the United States, is geographically located in a highly active seismic region. The island has suffered and documented the onslaught of four destructive events of 7.5M and greater. Moreover, since 2014 more than 3,000 tremors are registered per year by the Puerto Rico Seismic Network. This study aims to assess two aged structural systems which are representative of two of the main infrastructure systems in the island.

A 2-span reinforced concrete highway bridge located in Ponce, PR and a high-rise reinforced concrete residential building in San Juan, PR are evaluated by implementing state-of-the-art practices on dynamic identification to recorded earthquakes and ambient vibrations. Analytical and computational models are generated for each structure and updated from time and frequency domain methods. Analytical and experimental Frequency Response Functions are generated to better understand the expected behavior of both structural systems in the linear-elastic regime when subjected to minor intensity seismic events. Furthermore, unrecorded seismic events were successfully identified by output-only recorded data and updated Frequency Response Functions. A proposed method is implemented to identify structural dynamic properties with increased fidelity where there is no input excitation recording.

In addition, a simplified approach for modeling complex structural systems is presented and effectively implemented in computational nonlinear analyses. A set of seven probable earthquakes for each city are modified to meet current building code requirements and are used in nonlinear analyses of both structures as input ground motions. It was found that the bridge behaved predominantly linear-elastic with spontaneous events of minor nonlinearities. A pushover capacity curve was generated to confirm if the bridge behaved beyond its elastic range when subjected to

the probable earthquakes in the nonlinear analyses. The results for the building shows that it suffered excessive permanent deformations for two of the probable earthquakes and collapsed for the other five probable earthquakes used as input ground motions.

RESUMEN

La infraestructura de América fue construida principalmente durante mediados del siglo XX. Sus efectos de envejecimiento aumentan cada año, creando un dilema en el que los Estados Unidos no están solos. Además, la gran mayoría de los edificios y puentes no están conforme a las provisiones sísmicas de los códigos de edificación vigentes y muchos han excedido su vida de diseño. Este asunto adquiere especial relevancia en países que están ubicados en regiones propensas a terremotos y que históricamente han sufrido el embate de eventos sísmicos fuertes. En las grandes áreas urbanas, el problema es particularmente grave porque el espacio es escaso y la creciente población suprime los sistemas de apoyo a la ciudad. Puerto Rico, como muchos otros países y ciudades en los Estados Unidos, esta geográficamente localizado en una región sísmica altamente activa. La Isla ha sufrido y documentado el embate de cuatro eventos destructivos de magnitud igual y mayor a 7.5M. Además, desde el año 2014 mas de 3,000 temblores son registrados anualmente por la Red Sísmica de Puerto Rico. Este estudio tiene como objetivo evaluar dos sistemas estructurales envejecientes, los cuales son representativos de dos de los sistemas de infraestructura principales en la Isla.

Un puente de autopista de dos tramos de hormigón reforzado localizado en Ponce, PR y un edificio residencial de gran altura de hormigón reforzado localizado en San Juan, PR son evaluados implementando prácticas del estado-del-arte sobre identificación dinámica a terremotos registrados y vibraciones ambientales. Modelos analíticos y computacionales son generados para cada estructura y calibrados mediante métodos en los dominios del tiempo y la frecuencia. Funciones de Respuesta en Frecuencia analíticas y experimentales son generadas para entender mejor el comportamiento esperado de ambos sistemas en el rango elástico-lineal cuando sea sometido a eventos sísmicos de baja intensidad. Además, se logró identificar exitosamente eventos sísmicos que no fueron registrados, mediante datos registrados de respuesta y Funciones de Respuesta en Frecuencia calibradas. Se implementa un método propuesto para identificar con mayor fidelidad las propiedades dinámicas de la estructura cuando no se hayan registrado excitaciones de entrada.

En adición, un enfoque simplificado para modelar sistemas estructurales complejos es presentado e implementado efectivamente en los análisis computacionales no lineales. Un

conjunto de siete terremotos probables para cada ciudad es modificado para cumplir los requerimientos actuales del código de edificación y son utilizados en los análisis no lineales como excitación de entrada en el suelo. Se obtuvo que el puente se comportó predominantemente en el rango elástico-lineal con eventos espontáneos de inelasticidades leves. Una curva de capacidad de empuje lateral se generó para confirmar si el puente se comportó más allá de su rango elástico al ser sometido a los terremotos probables en los análisis no lineales. Los resultados para el edificio mostraron que éste sufrió de excesivas deformaciones permanentes para dos de los terremotos probables y colapsó para los otros cinco terremotos que se utilizaron como excitaciones de entrada en el suelo.

© Ángel J. Alicea-Rodríguez, 2018

This dissertation is dedicated to my parents, Mr. Ángel G. Alicea González and Mrs. Lourdes M. Rodríguez Muñíz, and to my beloved Andrea E. Cruz Chamorro for their patience and unconditional support during my academic career.

ACKNOWLEDGEMENTS

I would like to sincerely thank my research advisor, Dr. Ricardo R. López Rodríguez, for his continued guidance and support throughout the development of this study. His willingness to discus ideas and findings as well as to clarify questions that came up win the research process has been key aspects for the successful completion of this research project. Moreover, for always encouraging me to pursue multiple and diverse opportunities throughout my years as a graduate student, always believing these experiences were an important part of my academic and professional development.

I would also like to thank my graduate committee members for their valuable suggestions and advise when needed. Special thanks to Dr. Luis E. Suárez Colche for his valuable advice and suggestions during the development of this study; for his willingness to always discuss ideas and to encourage the development of new ones. To Dr. José A. Martínez Cruzado for allowing me to work in this research initiative and for his support and trust throughout the whole process. To Dr. Carlos I. Huerta López for his valuable suggestions and availability to discuss methods and ideas.

It is important to recognize the influence and continued support of other professors that always believed in me and encouraged my continued development throughout these past years. To Dr. Ingrid Y. Padilla Cestero, for always encouraging my academic development and believe in my potential to fulfill this and other goals since the beginning of my graduate studies. Her continued support and provided opportunities were key to my professional development and for the development of this study. Similarly, to Dr. Felipe J. Acosta Costa, for first encouraging me to pursue doctoral studies and for providing me access to high performance computers when needed without hesitation. To Dr. Benjamin Colucci Ríos, for his continued support and trust throughout my doctoral studies and for his teachings in and outside of the academic environment, which has been important in my professional development. And to Prof. Ismael Pagán Trinidad for his enthusiastic support throughout my academic career and for providing opportunities for my professional development.

In addition, I would like to thank the Puerto Rico Strong Motion Program for providing me the experimental data needed for this study and other related information. Special thanks to Eng.

Jaffet Martínez and Mr. Erick Santana, for their availability and responsiveness in the acquisition of experimental data for this study and their continued help when needed.

Special thanks are given to my family, for their understanding and continued support throughout my entire academic career. To my parents, Mr. Ángel G. Alicea González and Mrs. Lourdes M. Rodríguez Muñíz, for always encouraging me to pursue my goals and always believe in me and in my potential to fulfill this milestone in my life.

To my beloved Andrea E. Cruz Chamorro, for her constant support, patience, and continued comprehension throughout this tedious research process. For always believing in me and providing me the right words and the animosity to improve my pace and maintain my focus, helping me to overcome all the difficult moments that this process implies.

This research work was partially supported by Intelligent Diagnostics for Aging Civil Infrastructure, under the IGERT Fellowship Program of the National Science Foundation (Award Number: DGE-0654176). In addition, partial support was provided by the Dwight Eisenhower Fellowship Program on Transportation for Hispanic Serving Institutions.

TABLE OF CONTENTS

CHAPTER 1. INTRODUCTION 1
1.1 Research Significance and Motivation 1
1.2 Research Objectives and Scope 5
1.2.1 Reinforced Concrete Highway Bridge 6
1.2.2 Reinforced Concrete Multi-Story Residential Building 7
1.3 Methodology 7
1.4 Dissertation Overview 8
CHAPTER 2. LITERATURE REVIEW 11
2.1 Instrumentation 11
2.2 System's Dynamic Identification 15
2.3 Damage Identification in Civil Structures 18
2.4 Mathematical Tools in Experimental Dynamic Identification 22
2.4.1 Random Decrement Technique 22
2.4.2 Fourier Transform 26
2.4.3 Hilbert Transform 30
2.4.4 Hilbert-Huang Transform 32
2.4.5 Wavelet Transform 34
2.5 Performance and Nonlinear Behavior of Structures 40
2.5.1 Inelastic Models for Structural Components 43
2.5.2 Hysteretic Nonlinear Models 44
CHAPTER 3. STRUCTURAL SYSTEMS STUDIED 51
3.1 Ponce Highway Bridge Structure 51
3.1.1 Bridge Description 52
3.1.2 Bridge Instrumentation 53
3.2 High-Rise Residential Building 54
3.2.1 PRILA Condominium Description 54
3.2.2 Building Instrumentation 55

CHAPTER 4. ANALYTICAL STRUCTURAL MODELS 57
4.1 Mathematical model for the Ponce Highway Bridge 57
4.2 Computational Model for the PRILA Condominium 62
CHAPTER 5. EXPERIMENTAL DYNAMIC ANALYSES 67
5.1 Ponce Highway Bridge [ID: 2348] 69
5.1.1 Dynamic Assessment from Ambient Vibration Records 69
5.1.2 Model Updating from Ambient Vibration Analyses 80
5.1.3 Dynamic Assessment from Earthquake Records 82
5.2 PRILA Condominium 98
5.2.1 Dynamic Assessment from Ambient Vibration Records 98
5.2.2 Updated Linear-Elastic Models for PRILA Condominium 106
CHAPTER 6. FREQUENCY RESPONSE FUNCTIONS 111
6.1 FRF Dynamic Analyses for the Ponce Highway Bridge [ID: 2348] 113
6.1.1 FRFs from updated mathematical model of the bridge 113
6.1.2 Experimental FRFs from recorded ambient vibrations in the bridge 115
6.2 FRF Dynamic Analyses of the PRILA Condominium 124
6.2.1 FRFs from updated mathematical model of the building 124
6.2.2 Experimental FRFs from recorded ambient vibrations 132
CHAPTER 7. EARTHQUAKES AND NONLINEAR ASSESSMENT 140
7.1 Seismicity in the Puerto Rico Region and Probable Earthquakes 140
7.1.1 Probable earthquakes generation for Ponce, PR 146
7.1.2 Probable earthquakes generation for San Juan, PR 153
7.2 Nonlinear Assessment of the Ponce Highway Bridge [ID: 2348] 158
7.2.1 Moment-curvature relation for bridge's lateral force resisting system 159
7.2.2 Nonlinear time-history analysis of the bridge structure 161
7.2.3 Static pushover analysis of the bridge structure 162
7.3 Nonlinear Assessment of the PRILA Condominium 163
7.3.1 Moment-curvature relation for PRILA's lateral force resisting system 164
7.3.2 Nonlinear time-history analysis of PRILA 165
7.3.3 Static pushover analysis for PRILA 166

CHAPTER 8. CONCLUSIONS AND RECOMMENDATIONS 168
8.1 Implemented mathematical identification tools 169
8.1.1 Fast Fourier Transform 169
8.1.2 Random Decrement Technique 170
8.1.3 Wavelet Transform 171
8.2 Frequency Response Functions 173
8.3 Nonlinear Procedures and Analyses for Structural Assessment……..……176
CHAPTER 9. REFERENCES 179

LIST OF FIGURES

Figure 1-1: United States' bridge distribution by age. Extracted from the 2017 ASCE's US Infrastructure Report Card. 2

Figure 2-1: Six models for the instrumentation of a building. 13

Figure 2-2: A one-station random response and its corresponding RDS (Ibrahim, 1977) 24

Figure 2-3: Two-station random responses with $y_1(t)$ used as the leading sensor (Ibrahim, 1977) 24

Figure 2-4: Example of an aperiodic and continuous signal (Smith, 2003) 27

Figure 2-5: Example of a periodic and continuous signal (Smith, 2003) 28

Figure 2-6: Example of an aperiodic and discrete signal (Smith, 2003) 28

Figure 2-7: Example of a periodic and discrete signal (Smith, 2003) 29

Figure 2-8: Graphical explanation of the DFT and the IDFT in time and frequency domains (Smith, 2003) 29

Figure 2-9: Comparison of STFT resolution. a) Frequency resolution reduced with increased time resolution. b) Time resolution reduced with increased frequency resolution. 35

Figure 2-10: Comparison of time resolution between the (a) STFT and the (b) Wavelet Transform 37

Figure 2-11: Pushover curves. a) Static Pushover curve with backbone (FEMA,2005). b) Idealized pushover curve 42

Figure 2-12: Idealized models of beam-column elements (Deierlein et al., 2010) 43

Figure 2-13: Nonlinear hysteresis loop curve with backbone 45

Figure 2-14: Hysteresis stages. a) Hysteresis loop without degradation. b) Hysteresis loop with degradation. c) Pinching effect 45

Figure 2-15: Elastic Hysteresis Model. 46

Figure 2-16: Kinematic Hysteresis Model 46

Figure 2-17: Degrading Hysteresis Model 47

Figure 2-18: Takeda Hysteresis Model 47

Figure 2-19: Pivot Hysteresis Model 48

Figure 2-20: Concrete Hysteresis Model 49

Figure 2-21: BRB Hardening Hysteresis Model 49

Figure 2-22: Isotropic Hysteresis Model 50

Figure 3-1: Ponce Highway Bridge [ID: 2348] (Photo by the author) 51

Figure 3-2: Aerial view of Ponce Highway Bridge [ID: 2348] (Image from Google Earth Pro) 51

Figure 3-3: Schematic plan view of the eight columns supporting the bridge 52

Figure 3-4: Schematic elevation view of the eight columns supporting the bridge 52

Figure 3-5: Schematic drawing with sensors layout 53

Figure 3-6: Kinemetrics EpiSensor accelerometers. a.) EpiSensor ES-T model; b.) EpiSensor ES-U2 model 53

Figure 3-7: PRILA Condominium. a.) South view. b.) Side (west) view. c.) North view. 54

Figure 3-8: Shear walls layout in PRILA's typical stories 54

Figure 3-9: Footings location 55

Figure 3-10: Schematic drawing of PRILA Condominium's south and east views with the installed sensors' location 56

Figure 4-1: a.) Simplified drawing of the bridge structure. b.) Schematic description of the bridge's equivalent analytical model 57

Figure 4-2: Sequence for analytical model development. a.) Simplified drawing of bridge's lateral system. b.) Damped simple oscillator assumption. c.) Free-body diagram of analytical model 58

Figure 4-3: 3D model and real structure. a.) PRILA front view. b.) PRILA rear view 62

Figure 4-4: First translational mode shape for PRILA Condominium 63

Figure 4-5: Second translational mode shape for PRILA Condominium..... 64

Figure 4-6: Third translational mode shape for PRILA Condominium..... 64

Figure 4-7: Fourth translational mode shape for PRILA Condominium..... 64

Figure 4-8: Sensor accelerometers' location per selected story 66

Figure 5-1: Eighteen hours of ambient vibrations recording in sensor #5 at Ponce Highway Bridge [ID: 2348]..... 69

Figure 5-2: Frequency spectrum for eighteen hours of recorded ambient vibrations in sensor #5 at Ponce Highway Bridge 70

Figure 5-3: Random decrement signature for ambient vibration response at sensor #5..... 71

Figure 5-4: Idealized free vibration response of a SDOF system..... 71

Figure 5-5: Random decrement signature with the 1st pair of selected peaks to implement the logarithmic decrement method. 73

Figure 5-6: Random decrement signature with the 2nd pair of selected peaks to implement the logarithmic decrement method. 73

Figure 5-7: Graph of the Complex Morlet Wavelet basis function 76

Figure 5-8: Spectrogram for wavelet transform computed to random decrement signature of ambient response at sensor #5..... 77

Figure 5-9: Skeleton curve from 3 Hz to 4 Hz corresponding to the computed wavelet map..... 77

Figure 5-10: 3D spectrograms for ambient vibration records from sensor #5 at Ponce Highway Bridge 79

Figure 5-11: Skeleton curve from 2.5 Hz to 4 Hz corresponding to the computed ambient recording's wavelet map..... 80

Figure 5-12: Acceleration response EQ-1 recorded at sensor #5 on May 16, 2010 84

Figure 5-13: Acceleration response EQ-2 recorded at sensor #5 on December 24, 2010..... 85

Figure 5-14: Acceleration response EQ-3 recorded at sensor #5 on January 13, 2014..... 85

Figure 5-15: Acceleration response EQ-4 recorded at sensor #5 on May 28, 2014..... 85

Figure 5-16: Frequency spectrum for earthquake response EQ-1 recorded at sensor #5 on May 16, 2010 87

Figure 5-17: Frequency spectrum for earthquake response EQ-2 recorded at sensor #5 on December 24, 2010 87

Figure 5-18: Frequency spectrum for earthquake response EQ-3 recorded at sensor #5 on January 13, 2014 87

Figure 5-19: Frequency spectrum for earthquake response EQ-4 recorded at sensor #5 on May 28, 2014 88

Figure 5-20: 3D wavelet map for earthquake response EQ-1 recorded in sensor #5 on May 16, 2010 89

Figure 5-21: Dominant frequencies for earthquake response EQ-1 recorded in sensor #5 on May 16, 2010 89

Figure 5-22: 3D wavelet map for earthquake response EQ-2 recorded in sensor #5 on December 24, 2010 89

Figure 5-23: Dominant frequencies for earthquake response EQ-2 recorded in sensor #5 on December 24, 2010 90

Figure 5-24: 3D wavelet map for earthquake response EQ-3 recorded in sensor #5 on January 13, 2014 90

Figure 5-25: Dominant frequencies for earthquake response EQ-3 recorded in sensor #5 on January 13, 2014 90

Figure 5-26: 3D wavelet map for earthquake response EQ-4 recorded in sensor #5 on May 28, 2014 91

Figure 5-27: Dominant frequencies for earthquake response EQ-4 recorded in sensor #5 on May 28, 2014 91

Figure 5-28: Arias intensity delimiting the interval where 90% of the imparted energy was dissipated by the bridge in EQ-1 93

Figure 5-29: Arias intensity delimiting the interval where 90% of the imparted energy was dissipated by the bridge in EQ-2 94

Figure 5-30: Arias intensity delimiting the interval where 90% of the imparted energy was dissipated by the bridge in EQ-3 94

Figure 5-31: Arias intensity delimiting the interval where 90% of the imparted energy was dissipated by the bridge in EQ-4 94

Figure 5-32: Significant duration of 20.9 seconds in earthquake response EQ-1 and its corresponding frequency spectrum 95

Figure 5-33: Significant duration of 23.305 seconds in earthquake response EQ-2 and its corresponding frequency spectrum 96

Figure 5-34: Significant duration of 27.975 seconds in earthquake response EQ-3 and its corresponding frequency spectrum 96

Figure 5-35: Significant duration of 36.505 seconds in earthquake response EQ-4 and its corresponding frequency spectrum 97

Figure 5-36: Twenty-four hours of ambient vibrations recording in sensor #33 at PRILA Condominium 98

Figure 5-37: PSD for twenty-four hours of recorded ambient vibrations in sensor #33 at PRILA Condominium 99

Figure 5-38: Random decrement signature for ambient vibration response at sensor #33 102

Figure 5-39: Spectrogram for wavelet transform computed to random decrement signature of ambient response at sensor #33 102

Figure 5-40: Skeleton curve from 0.5 Hz to 1.5 Hz corresponding to the computed wavelet map 102

Figure 5-41: Experimental Damping Ratio Identified for PRILA's 1st, 2nd, 3rd, and 4th modes of vibration 105

Figure 5-42: a.) PRILA Condominium 3D model in ETABS; b.) PRILA 2D model in SAP2000 108

Figure 6-1: Block diagram for an input-output system (adapted from Agilent Technologies, 2000) 111

Figure 6-2: 3D Laplace Representation. The surface represents the Transfer Function and the dashed line represents the FRF. a.) Representation by real and imaginary parts; b.) Representation by magnitude and phase (Agilent Technologies, 2000) 112

Figure 6-3: Accelerance function for updated mathematical model of the bridge 114

Figure 6-4: Artificial close-to-ideal white noise signal. a.) Signal and its frequency spectrum; b.) PDF and its statistical moments 116

Figure 6-5: Signal recorded at sensor #2. a.) Recorded signal and its frequency spectrum; b.) PDF and its statistical moments 116

Figure 6-6: Experimental FRF for Ponce Highway Bridge [ID: 2348] with sensor #2 as input and sensor #5 as output. a.) Absolute value of real part of FRF; b.) Imaginary part of FRF 118

Figure 6-7: Experimental FRF for Ponce Highway Bridge [ID: 2348] with simulated white noise used as input and sensor #5 as output. a.) Absolute value of real part of FRF; b.) Imaginary part of FRF 119

Figure 6-8: Absolute accelerance function for updated mathematical model of the bridge 121

Figure 6-9: Equivalent earthquake EQ-1 and its frequency spectrum 122

Figure 6-10: Equivalent earthquake EQ-2 and its frequency spectrum 122

Figure 6-11: Equivalent earthquake EQ-3 and its frequency spectrum 123

Figure 6-12: Equivalent earthquake EQ-4 and its frequency spectrum 123

Figure 6-13: Absolute accelerance FRF for PRILA; a.) FRF defined over all frequencies range; b.) FRF in the range of the first four natural frequencies 131

Figure 6-14: Example of experimental FRF computed for output sensor #33 133

Figure 6-15: Imaginary part of experimental FRF computed for output sensor #33 134

Figure 6-16: Experimental deformed shape for PRILA's 1st mode of vibration recorded at its east side 136

Figure 6-17: Experimental deformed shape for PRILA's 2nd mode of vibration recorded at its east side 136

Figure 6-18: Experimental deformed shape for PRILA's 3rd mode of vibration recorded at its east side 137

Figure 6-19: Experimental deformed shape for PRILA's 4th mode of vibration recorded at its east side 137

Figure 6-20: Experimental deformed shape for PRILA's 1st mode of vibration recorded at its west side 138

Figure 6-21: Experimental deformed shape for PRILA's 2nd mode of vibration recorded at its west side 138

Figure 6-22: Experimental deformed shape for PRILA's 3rd mode of vibration recorded at its west side 139

Figure 6-23: Experimental deformed shape for PRILA's 4th mode of vibration recorded at its west side..... 139

Figure 7-1: Seismicity in the Caribbean. a.) The Caribbean tectonic plate's relative movements and its faults. (Caribbean Studies Course) b.) The most active seismic zone on the Caribbean plate is at its borders. (E. Calais, Caribbean Active Tectonics)..... 140

Figure 7-2: The archipelago of Puerto Rico and most of its active known seismic faults..... 141

Figure 7-3: Registered seismic activity in the Puerto Rico region (data from PRSN) 142

Figure 7-4: Elastic Design Response Spectra for Puerto Rico Building Codes for Soil Type D in Ponce, PR..... 145

Figure 7-5: Elastic Design Response Spectra for Puerto Rico Building Codes for Soil Type D in San Juan, PR..... 145

Figure 7-6: Artificial Strong Motion Record Recommended for Ponce, PR and Mayagüez, PR (Irizarry, 1999) 146

Figure 7-7: Elastic design response spectrum for soil type D in Ponce, PR as per ASCE7-16..... 148

Figure 7-8: Probable Earthquake CIG.EW for Ponce, PR for soil type D as per ASCE7-16 and its frequency spectrum..... 149

Figure 7-9: Probable Earthquake HSH.EW for Ponce, PR for soil type D as per ASCE7-16 and its frequency spectrum..... 150

Figure 7-10: Probable Earthquake IGN.EW for Ponce, PR for soil type D as per ASCE7-16 and its frequency spectrum..... 150

Figure 7-11: Probable Earthquake IVU.EW for Ponce, PR for soil type D as per ASCE7-16 and its frequency spectrum..... 151

Figure 7-12: Probable Earthquake UCA.EW for Ponce, PR for soil type D as per ASCE7-16 and its frequency spectrum 151

Figure 7-13: Probable Earthquake USACA18.033 for Ponce, PR for soil type D as per ASCE7-16 and its frequency spectrum 152

Figure 7-14: Probable Earthquake USACA36.011 for Ponce, PR for soil type D as per ASCE7-16 and its frequency spectrum 152

Figure 7-15: Artificial Strong Motion Record Recommended for San Juan, PR (Irizarry, 1999) 153

Figure 7-16: Elastic design response spectrum for soil type D in San Juan, PR as per ASCE7-16 154

Figure 7-17: Probable Earthquake JAP03.104 for San Juan, PR for soil type D as per ASCE7-16 and its frequency spectrum 155

Figure 7-18: Probable Earthquake JAP03.173 for San Juan, PR for soil type D as per ASCE7-16 and its frequency spectrum 155

Figure 7-19: Probable Earthquake MEX03.112 for San Juan, PR for soil type D as per ASCE7-16 and its frequency spectrum 156

Figure 7-20: Probable Earthquake pacoimaw.v2 for San Juan, PR for soil type D as per ASCE7-16 and its frequency spectrum 156

Figure 7-21: Probable Earthquake rollhill.v2 for San Juan, PR for soil type D as per ASCE7-16 and its frequency spectrum 157

Figure 7-22: Probable Earthquake USAAK02.067 for San Juan, PR for soil type D as per ASCE7-16 and its frequency spectrum 157

Figure 7-23: Probable Earthquake USACA66.001 for San Juan, PR for soil type D as per ASCE7-16 and its frequency spectrum 158

Figure 7-24: SDOF model for Ponce Highway Bridge [ID: 2348]; a.) Simplified schematic representation; b.) SAP2000 2D model 159

Figure 7-25: Equivalent moment-curvature bilinear approximation for SDOF model of Ponce Highway Bridge [ID: 2348] 160

Figure 7-26: Pushover capacity curve for Ponce Highway Bridge [ID: 2348] and maximum base shear and displacement from nonlinear dynamic analyses (red dot). 163

Figure 7-27: Pushover capacity curve for PRILA Condominium 167

LIST OF TABLES

Table 3-1: Traffic requirements for Ponce Highway Bridge [ID: 2348] design 52

Table 4-1: Physical properties for Type IV AASHTO concrete beams 58

Table 4-2: Physical properties of the highway bridge piers 59

Table 4-3: Physical properties of the highway bridge concrete deck 59

Table 4-4: Physical properties of the highway bridge concrete parapets 59

Table 4-5: Physical properties of the highway bridge concrete median barriers 59

Table 4-6: Physical properties of the bridge's cap bean located at joint B in figure 4-1b 59

Table 4-7: Assumed boundary conditions for bridge's analytical model 60

Table 4-8: Natural periods and frequencies of vibration for 65

Table 5-1: Mathematical relations between damped and undamped dynamic parameters 71

Table 5-2: Dynamic parameters results implementing the logarithmic decrement method 74

Table 5-3: Summary of results for bridge's identified dynamic parameters 81

Table 5-4: Information on the ground motions received by Ponce Highway Bridge [ID: 2348] 82

Table 5-5: Acceleration, velocity, and displacement responses' peak values for EQ-1 recorded in sensors #2, #5, #6, #8, and #10 83

Table 5-6: Acceleration, velocity, and displacement responses' peak values for EQ-2 recorded in sensors #2, #5, #6, #8, and #10 83

Table 5-7: Acceleration, velocity, and displacement responses' peak values for EQ-3 recorded in sensors #2, #5, #6, #8, and #10 83

Table 5-8: Acceleration, velocity, and displacement responses' peak values for EQ-4 recorded in sensors #2, #5, #6, #8, and #10 84

Table 5-9: Computed Signal-to-Noise ratios for each of the recorded earthquake responses 86

Table 5-10: Significant duration for each of the recorded earthquake responses in sensor #5 95

Table 5-11: Identified natural frequencies from east-side sensors in PRILA 100

Table 5-12: Identified natural frequencies from west-side sensors in PRILA 100

Table 5-13: Summary of first four identified natural frequencies and periods by PSD 101

Table 5-14: PRILA's fundamental frequency identified by wavelet transform on RDS 103

Table 5-15: Frequency bands for each mode 103

Table 5-16: PRILA's 1st natural frequency identified by wavelet transform on RDS of filtered signal 104

Table 5-17: PRILA's 2nd natural frequency identified by wavelet transform on RDS of filtered signal 104

Table 5-18: PRILA's 3rd natural frequency identified by wavelet transform on RDS of filtered signal 104

Table 5-19: PRILA's 4th natural frequency identified by wavelet transform on RDS of filtered signal 105

Table 5-20: Summary of results for PRILA Condominium's identified dynamic parameters 106

Table 5-21: Tributary mass and weight for each story 107

Table 5-22: Comparison between natural frequencies from experiments and from updated model 107

Table 5-23: PRILA Condominium stiffness matrix, $\boldsymbol{K}$, [kip/in] 110

Table 5-24: PRILA Condominium mass matrix, $\boldsymbol{M}$, [slugs] 110

Table 6-1: Variations in frequency responses 112

Table 6-2: Peak acceleration, velocity, and displacement values for equivalent earthquakes 124

Table 6-3: Experimental natural frequencies and modal deformed shapes extracted from FRFs on east side of PRILA 135

Table 6-4: Experimental natural frequencies and modal deformed shapes extracted from FRFs on west side of PRILA 135

Table 7-1: Historic destructive earthquakes in the Puerto Rico region 142

Table 7-2: Earthquake records selected for Ponce, PR 143

Table 7-3: Earthquake records selected for San Juan, PR 144

Table 7-4: Seismic design details for the structure's analysis in Ponce, PR as per ASCE7-16 147

Table 7-5: Seismic design details for the structure's analysis in San Juan, PR as per ASCE7-16 154

Table 7-6: Equivalent Moment-Curvature Bilinear Approximation for Ponce Highway Bridge [ID: 2348] 160

Table 7-7: Peak values of demand parameters and final condition for Ponce Highway Bridge [ID: 2348] 161

Table 7-8: Maximum inelastic curvatures for Ponce Highway Bridge [ID: 2348] due to probable earthquakes 162

Table 7-9: Ponce Highway Bridge [ID: 2348]'s state capacities 163

Table 7-10: Hinge capacities defining the moment-curvature relationship per story for PRILA Condominium 165

Table 7-11: Peak values of demand parameters and final condition for PRILA Condominium 166

Table 7-12: PRILA Condominium's state capacities 166

CHAPTER 1. INTRODUCTION

1.1 Research Significance and Motivation

America's infrastructure was constructed mainly during the 1950's and 1960's. Today it is commonly noticed that it is aging, creating a dilemma in which the United States is not alone. The great majority of buildings and bridges are seismically non-compliant with current building codes and many have been in place far beyond their design lives. This conforms a major problem because many countries throughout the entire American continent are located in seismically prone regions, and historically have suffered the onslaught of strong seismic events. The seismic hazard is the probability that in a given location and for a reference period of time occurs an earthquake with ground motion intensity exceeding a given threshold. Because constructions in many of those countries are old and deficient, many deaths have occurred due to extreme events such as earthquakes, hurricanes, and floods, among others. In large urban areas the problem is particularly acute because space is scarce and growing populations stress city support systems. This causes the imposition of new safety requirements due to the threat of accidents, natural disasters, and terrorism.

In 2017, the American Society of Civil Engineers (ASCE) released its latest report card for America's infrastructure, which depicts the condition and performance of the nation's infrastructure in the familiar form of a school report. The overall grade point average was a D^+, with an estimated investment of $3.6 trillion needed by 2020 in order to move our infrastructure's health conditions to acceptable levels. It is estimated that from 2016 to 2025, each household will lose $3,400 each year in disposable income due to infrastructure deficiencies. In this report card, our bridge infrastructure obtained a C^+, representing a safety issue to all the citizens that make daily use of them. According to the report, one in eleven of the nation's bridges are rated as structurally deficient, while the average age of the nation's 614,387 bridges is currently 43 years. This represents 6.3% of the total bridge decking area in the United States. Furthermore, 40% of the total of bridges are 50 years or older. This is of special importance after considering that most of the bridges in the United States were designed for a lifespan of 50 years. In Figure 1-1, the percentage distribution of the United States' bridges (excluding Puerto Rico) by age is illustrated.

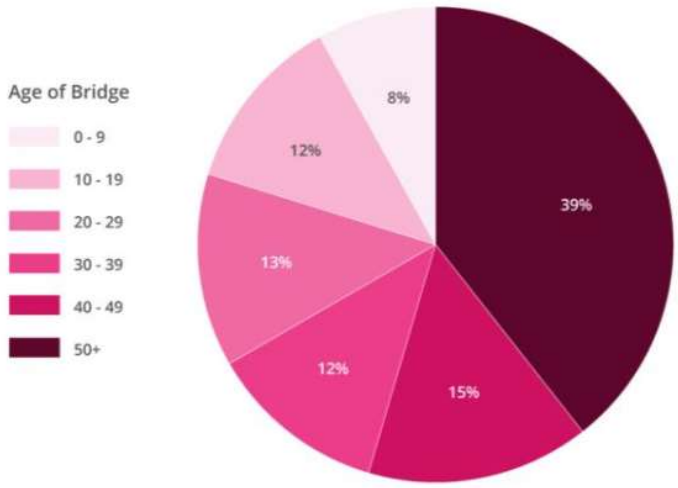


Figure 1-1: United States' bridge distribution by age. Extracted from the 2017 ASCE's US Infrastructure Report Card.

Encouragingly, bridges with higher traffic volume are less likely to be structurally deficient. However, on average, there were 188 million trips across a structurally deficient bridge each day in 2016. In particular, the study revealed that in some states, such as Rhode Island, up to 24.9% of the nation's bridges are deficient. Consequently, the ASCE's most recent published estimate puts the nation's backlog of bridge's rehabilitation needs at $123 billion. Analogous to the ASCE report, the U.S. Government Accountability Office (GAO) reported in its 2015 report on "Transportation Infrastructure: Information on Bridge Conditions" that 10% of all bridges that are deficient are categorized as structurally deficient and 14% as functionally obsolete. In the same way, GAO's study revealed that between 2005 and 2014, the number of structurally deficient bridges decreased in 43 states and the District of Columbia (D.C.), but increased in 7 states and Puerto Rico. Likewise, the number of functionally obsolete bridges decreased in 33 states and D.C. but increased in 17 states and Puerto Rico.

On the other hand, the buildings infrastructure is not included in the ASCE's Infrastructure Report Card. However, a large number of public and private buildings throughout the United States are considered structurally and/or seismically deficient. According to the Meriam-Webster dictionary, the term deficiency is defined as the lack of something that is needed or the state of not having enough of something necessary. In this respect, it is easily inferred that a great number of existing buildings fail to meet specific design conditions or characteristics required by current building codes. This makes them non-compliant with state-of-the-practice requirements which may consequently lead to unacceptable damage in the occurrence of a natural event. Furthermore,

a recently designed and built building in compliance with current design practices may be classified as seismically deficient if new seismicity findings in the region are incorporated in the building codes resulting in increased design forces for which the recently constructed building was not designed.

The United States started to develop seismic codes in the 1920's and their use was voluntary. Eventually on 1933, a mandatory code was enforced in California. It was not until the 1950's and 1960's that the first "modern" seismic codes were hence applied only in regions of known high seismicity. Since then, new knowledge has been developed providing a better understanding on ground motions and the expected behavior of seismic-resistant structures. As a result, increases on design forces and more rigorous detailing requirements have been incorporated into the building codes throughout the last decades. Despite these technical advancements, non-ductile concrete construction prevailed in the United States until 1980, when that practice started to decrease as the state governments began to enforce the new and improved detailing requirements to account for ductility demands in the structures. However, the west coast of the United States began to gradually eliminate non-ductile concrete construction since the 1950s.

At present day, it is expected that all new infrastructure developments comply with the latest requirements mandated by the codes approved by the authority having jurisdiction. However, it is not the case on aged structures, regardless of whether they were retrofitted in the past, because many of them could still represent a hazard to its inhabitants. For instance, most of the older reinforced concrete buildings had not been inspected for seismic safety. In urban regions with higher population density, the matter could get worse depending on the time of the day when a natural event occurs. During daily peak labor hours, casualties due to buildings' extreme damage or collapse could be on the order of thousands. For this reason, some states such as California have been creating an inventory of older concrete buildings and its current health condition in order to develop and implement a retrofit program.

The case of Puerto Rico's infrastructure is of particular interest due to the fact that for its nature of being an island, it is completely subjected to harsh marine and environmental conditions. Furthermore, some of the island oldest bridges were built by the end of the 19th century and are still in use. This increases the probability of damage occurrence of any bridge at any location within the island. Not only the aging conditions but the geographic location of the island represents a threat to its deficient infrastructure. Puerto Rico is located at a seismic prone region at the border

of the Caribbean plate and contains more than 10 known active faults in its surroundings making it highly vulnerable to the occurrence of a catastrophic natural event. Currently, the island possesses 2,270 bridges in the U.S. National Bridge Inventory of which, by 2013, 31 were considered fracture critical, meaning that there is no redundancy protection in its structural system, and it may collapse if just one vital component fails. Likewise, the island's building infrastructure is old, and a vast number of buildings do not comply with the latest design codes. Furthermore, the island is subjected to tropical storms and hurricanes in a yearly basis, which accelerates the detriment of the infrastructure systems. This, in combination with the lack of building maintenance, increases their vulnerability to subsequent natural events. Structural inspections, retrofitting, and rehabilitation to vulnerable and deficient buildings is very limited, creating a safety issue to its users. For these reasons, it is of extreme importance to establish the best health monitoring practices to our decaying infrastructure to better provide better solution to its deficiencies.

In recent years, an increased interest in the field of Structural Health Monitoring (SHM) has started to develop. This may be the effect of catastrophic disasters that have occurred in the past due to the limited information available concerning the current state of different mechanical systems and infrastructure in general. SHM aims to provide the necessary tools and methodologies for scientists and engineers to use in order to have the ability to monitor a specific system and to detect any damage at the earliest possible stage, increasing the infrastructure safety and reliability while at the same time reducing its maintenance and repairing costs.

In this proposed research, it is intended to evaluate the current structural health of a 2-span reinforced concrete highway bridge located in PR #52 in Ponce, PR and of a 20-story residential building located in the urban area of San Juan, PR by implementing SHM state-of-the-art practices on system identification. This growing field is a branch of SHM that can be defined as the science that leads to the process of building mathematical models for obtaining descriptions of dynamic systems based on experimental analysis observations of input-output data. System Identification plays a central role in the design of algorithms used to identify and characterize undesirable changes (i.e. faults or damages) that may appear during the service life of a structure or mechanism and its major benefit is the improvement of the analytical model of a structure.

Modal parameter identification means the process of measuring signals produced by a structure and identifying modal parameters (natural frequencies, mode shapes, and damping). In this

research the identification of the modal properties of both structures will be executed by performing time-frequency analyses and frequency response functions. In signal processing, time-frequency analysis comprises those techniques that study a signal in both the time and frequency domains simultaneously. On the other hand, modal analysis using Frequency Response Functions loses all time information of the occurrence of frequency changes. However, this method is very popular among dynamic analysts.

In addition, probable earthquakes will be artificially generated for the municipalities of Ponce, PR and San Juan, PR. These earthquakes will be made compatible with the elastic demand spectrum established in the ASCE7-16 and properly scaled to the required peak ground acceleration (PGA). Nonlinear static and dynamic analyses will be performed to both structures to investigate their respective behavior under expected strong excitations against its designed lateral capacities. These results will provide valuable insight on the expected behavior of two different types of structures commonly found throughout the island and which accurately represent their design deficiencies due to their contemporary design requirements.

The proposed study will advance in understanding the performance of aged and/or deficient infrastructure located in seismic prone regions and subjected to seismic activity as well as to different vibration scenarios. America's infrastructure is aging, and a vast number of bridges and buildings are not compliant with current design codes or possess construction flaws representing a threat to its users, the surroundings, and the economy in general. In a more general aspect, if successful, this study intends to mitigate the hazard of these structures due to natural events by setting a precedent on procedures of rapid dynamic analysis and nonlinear modeling in order to obtain the best estimate of the health of bridge and building structures to better address the prioritization of retrofit efforts.

1.2 Research Objectives and Scope

In this proposed research, it is intended to evaluate the current structural health of a 2-span reinforced concrete highway bridge located in PR #52 in Ponce, PR and of a multi-story residential building located in the urban area of San Juan, PR by implementing SHM state of the art practices on system identification and nonlinear static and dynamic analyses. Both structures are part of the network of instrumented structures administered by the Puerto Rico Strong Motion Program (PRSMP). The highway bridge and the condominium were instrumented with 12 and 36

Kinemetrics® uniaxial and triaxial Episensor accelerometers, respectively. This allows the recording of small amplitude random and environmental vibrations as well as any seismic activity that may be perceived by the structures.

The scope of this research is to study the dynamic behavior of these two structures currently in use while being subjected to real and expected vibration scenarios such as ambient and strong motions, respectively. Through this study, it is intended to establish predictable behavior and damage patterns to make a better assessment of those types of structures. This will serve as an effective tool for the rehabilitation and retrofit prioritization of these and similar structures by accounting empirical and analytical data jointly with life safety engineering criteria. The objectives for the study of each structure is presented below.

1.2.1 Reinforced Concrete Highway Bridge

The assessment study for the highway bridge can be divided into seven main objectives stated as follow:

1. Develop a mathematical model of the bridge as-designed as second order differential equation of motion for a single degree of freedom structure.
2. Implement validated sensor-based methodologies to determine the actual dynamic properties of the bridge.
3. Update the previously developed mathematical model with the identification results obtained from the collected experimental data.
4. Develop the bridge's Frequency Response Functions for input-output signal identification, in particular of unrecorded strong motions.
5. Create a simplified 2D model from the initial predictive mathematical model to facilitate further dynamic analyses and alleviate the need of computational power.
6. Generate probable artificial earthquakes for the municipality of Ponce, PR based on previous seismological studies. These artificial earthquakes are made compatible with the elastic design spectrum specified in ASCE7-16 and scaled to the required PGA in accordance with the soil type.
7. Use the previously generated probable earthquakes to assess the bridge's expected dynamic behavior under these ground motions by performing nonlinear static and dynamic analyses to the updated simplified 2D model of the bridge.

1.2.2 Reinforced Concrete Multi-Story Residential Building

The assessment study for the multi-story residential building can be divided into six main objectives stated as follow:

1. Develop a 3D computational model of the structure as-designed and perform a modal analysis to establish optimal sensor quantity and placement.
2. Implement sensor-based methodologies to determine the actual dynamic properties of the aged multi-story building. These methodologies are validated using the predictive linear 3D model under simulated ambient vibrations.
3. Create a simplified 2D model from the initial predictive model to alleviate the need of computational power and update the new model with the collected experimental data results.
4. Establish a linear updated analytical model of the real structure and develop its Frequency Response Functions for future input-output dynamic identification needs.
5. Generate probable artificial earthquakes for the municipality of San Juan, PR based on previous seismological studies. These artificial earthquakes are made compatible with the elastic design spectrum specified in ASCE7-16 and scaled to the required PGA in accordance with the soil type.
6. Use the previously generated probable earthquakes to assess the building expected dynamic behavior under these ground motions by performing nonlinear static and dynamic analyses to the updated simplified 2D model of the building.

1.3 Methodology

The plan established for this research is divided into five milestones. The first consists in a literature review encompassing: (1) seismic instrumentation aspects and its current state-of-the-practice, (2) the applicable analysis methodologies for structural systems and its dynamic identification, (3) analytical modeling techniques, (4) model updating aspects, (5) seismology in the Caribbean region, (6) and nonlinear analysis of structural systems. The second milestone consists in the analytical model development, modal analysis, and the assessment of the structures' instrumentation. The third milestone will be to apply system identification techniques to collected experimental data to describe the actual dynamic properties of each structure and characterize its

current structural health. The fourth milestone includes the generation of artificial probable earthquakes for Ponce, PR and San Juan, PR and the realization of nonlinear analyses to both structures. The fifth consists in driving conclusions and recommendations based on analysis results for each structure. A more detailed description for the established tasks for this research is presented below.

Task 1. Perform a literature review on seismic instrumentation of bridges and buildings, system identification, filtering techniques, model updating methodologies, and computational nonlinear analyses. Select the analytical methodologies and tools for its application in linear and barely nonlinear structural analysis and identification.

Task 2. Develop an analytical model of each structure using as-built structural plans and identify its theoretical modal properties for behavior prediction.

Task 3. System identification techniques will be applied to measured experimental data consisting of ambient vibrations. This will serve to perform the model updating or calibration process in the mathematical and computational models.

Task 4. Compare the results obtained by the system identification procedures and the linear theoretical model. Update the theoretical models by adjusting its dynamic parameters.

Task 5. Compute Frequency Response Functions from experimentally recorded ambient vibration data. In addition, mathematically obtain the updated model's Frequency Response Function to identify input unrecorded earthquakes in the bridge structure.

Task 6. Generate probable artificial earthquakes compatible with the elastic design spectrum in ASCE7-16 for the municipalities of Ponce, PR and San Juan, PR. This will be based on previous seismological studies on the fault system in the region of Puerto Rico.

Task 7. Define equivalent moment-curvature relations for each structure. Perform a static nonlinear pushover analysis to both structures and several nonlinear dynamic analyses using as input the previously generated artificial earthquakes.

Task 8. Develop conclusions and recommendations.

1.4 Dissertation Overview

This dissertation can be divided into five major sections, each containing one or two chapters that address related topics. The first section includes Chapters 1 and 2, which are introductory and

provide deep insight on the problem, the study scope and significance, and a review of related research. The second section contains Chapters 3 and 4, presenting the studied physical systems and their representation as analytical models. The third section, described in Chapters 5 and 6, deals with the experimental dynamic identification of the previously presented structural systems by implementing different methodologies. A fourth section, with Chapter 7, focuses on seismicity and nonlinear structural assessment by applying computational analysis procedures. Conclusions and recommendations can be found in a fifth section, contained in Chapter 8. A more detailed summary of each chapter in this manuscript is presented below.

Chapter 1. The cause and motivation for the present study is described with supporting data. In addition, the scope and significance of the study is presented, followed by the proposed research methodology.

Chapter 2. A review of related research, theory, history, instrumentation, tools, and procedures is thoroughly presented and described. A major emphasis is displayed in topics of experimental dynamics and nonlinear analysis concepts and methods.

Chapter 3. A detailed description of both structural systems studied is provided and complemented with photos and drawings of the physical systems. In addition, information on the instrumentation and its current location in the structures is provided and referenced with drawings.

Chapter 4. A description of the analytical models for both structures is presented. In addition, instrumentation criteria for optimal sensor placement in PRILA Condominium is illustratively described and explained.

Chapter 5. Procedures on experimental dynamic analyses with different mathematical tools is presented for both structures. Identification analyses are performed to ambient vibration records from sensors distributed throughout the entire structures. In addition, the analytical models developed in Chapter 4 for each structure are updated with experimental dynamic parameters for further analyses.

Chapter 6. Mathematical formulation of Frequency Response Functions for both structures are developed and used to identify input excitations in Ponce Highway Bridge [ID: 2348]. In addition, Frequency Response Functions are computed for both structures

from recorded ambient vibration measurements to identify their current state dynamic parameters.

Chapter 7. An overview on the seismicity in the Puerto Rico region is presented. Accordingly, probable earthquakes are generated for the municipalities of Ponce, PR and San Juan, PR in accordance with ASCE7-16. A nonlinear analysis is then performed to each of the structures to assess their dynamic behavior under expected seismic events.

Chapter 8. Conclusion are presented for each of the analysis methods implemented in this study. Recommendations are provided to improve future analyses and future research initiatives.

CHAPTER 2. LITERATURE REVIEW

2.1 Instrumentation

The use of instrumentation in civil structures to measure its dynamic response during seismic events results in the gathering of valuable information that provides a better insight of the forces exerted in the structure and its post-event damage and structural health. The first large set of strong motion records were obtained during the 1971 San Fernando earthquake and the measurements were recorded on film (Shakal and Huang, 2008). The processing of those records required an enormous effort in the digitizing of the data due to the nature of the data collection system and its lack of sensitivity for obtaining displacement and spectral values. Nowadays accelerometer readings are recorded in already digitized solid-state memories taking a big step in the recovering and processing of the data right after the occurrence of a seismic event. In addition, modern instruments guarantee quality data by activating within milliseconds after initiating an event, even after years at standby.

In order to achieve an effective instrumentation, the installation of accelerometers at key locations of any structure is a must. This is because the number and location of sensors determines the amount of information that may be recovered about its response after an earthquake. The relevance for an adequate arrangement of sensors throughout the structure is because when installed at key locations (key structural elements), the important modes of vibration can be recorded, and with them specific measurement objectives can be achieved. By studying lateral force resisting systems engineers can ensure an optimal layout of a limited number of sensors. The main purpose of this stage is to allow the collection of as much information as possible about the global motion of the structure as well as the motion in the first few directional modes.

For buildings, there are multiple instrumentation models used as guidelines for response monitoring and system identification purposes. The California Strong Motion Instrumentation Program (CSMIP) in the California Geological Survey has implemented and published complete instrumentation layouts consisting in installing accelerometers in eight or more locations throughout the height of a building. The sensor layout depends on the geometry of the building, its size, and the specific interests of the research engineer. Typically, 12 to 20 sensors are installed

in a building. According to Huang and Shakal (2001), a good instrumentation plan for a building always should include sensors at the base of the building and at the roof. In addition, sensors should be included on as many intermediate levels as appropriate for each specific building and in accordance with the study interests. It is recommended to install a free-field station nearby to provide a record of the ground motion. Therefore, the number of sensors that should be installed in intermediate levels are a function of the building configuration and height. For buildings up to three stories in height, each level is often instrumented to allow calculation of inter-story drift at each story. For buildings of four to seven stories (mid-rise buildings), two intermediate levels are usually instrumented. For buildings of eight stories or more (high-rise buildings), at least two intermediate levels are instrumented, and additional instruments may be added at levels where there is a discontinuity in stiffness. Additional levels should be instrumented for tall buildings of 15 stories and up. Building instrumentation objectives generally include measurements of the following parameters:

- input ground motion
- building base motion
- lateral floor motion
- torsional floor motion
- floor or wall diaphragm motions
- shear wall rocking motion

Valuable information concerning the dynamic response of the structure can generally be computed from the following measurements:

- building period
- damping ratios
- base shears
- interstory drifts
- peak floor accelerations

General approaches to the instrumentation of a building fall into one of the six models shown in Figure 2-1, depending on the budget and structural system (Huang and Shakal, 2001).

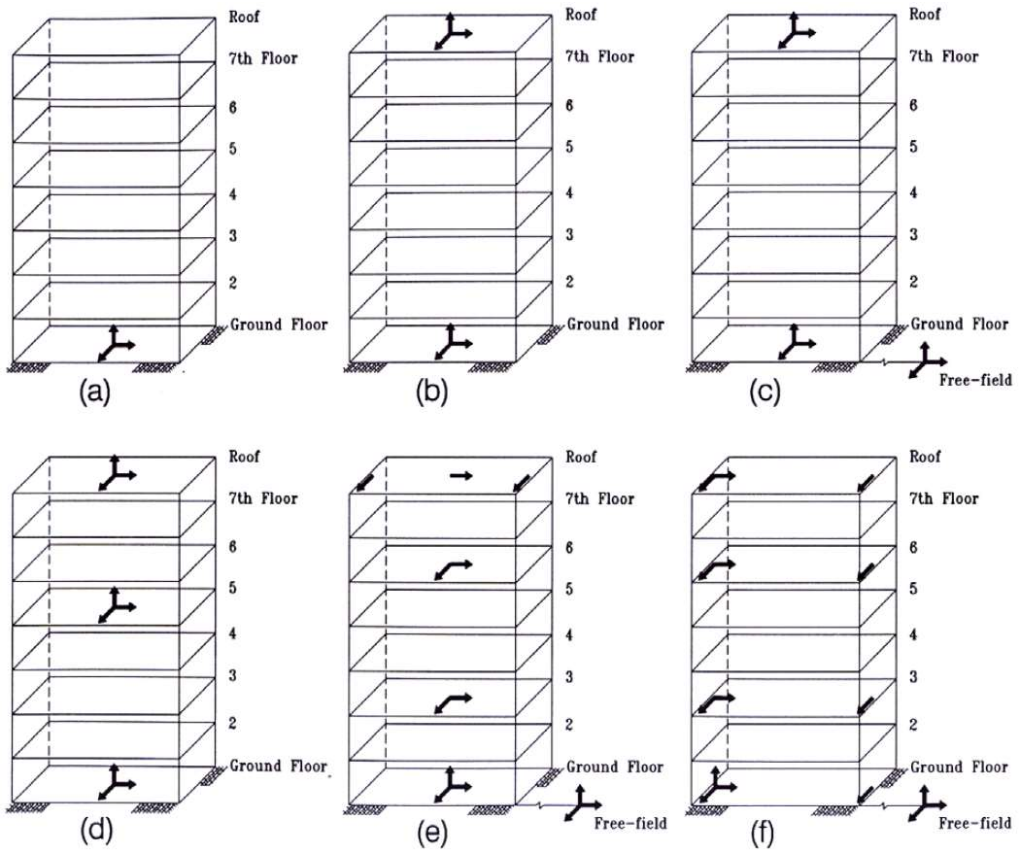


Figure 2-1: Six models for the instrumentation of a building

They are listed next:

a, Base or Reference Free-Field Only

b, Base and Roof

c, Reference/Free-Field, Base and Roof

d, Base, Mid-height, and Roof

e, Free-Field Multi-Level Lateral Motion, Roof-Only Torsion

f, Free-Field Multi-Level Lateral and Torsional Motion

In the case of bridge structures, there are less available guidelines for optimal instrument placement and the analyst must rely in his experience and engineering judgement, which is typically controlled by certain requirements and limitations such as the measurements' final purpose and the number of sensors available. For any structure the optimal sensor location can be obtained by a computational modal analysis of a 3D as-built model. However, in most occasions a 3D model is not available, and the analyst needs to follow different criteria based on the geometry of the bridge, its size, and the specific research interests.

The typical sensor layout should include, as a minimum requirement, bi-axial accelerometers in the longitudinal and transverse directions in both abutments and in the cap beams of each piers' frame system. This arrangement accounts for lateral loads that may be imparted by any seismic activity, crash accident at any pier, or any other meteorological event that may or may not represent a hazard to the structural integrity of the bridge's main lateral force resisting systems. In addition, vertical uniaxial accelerometers should be installed in the mid-span between each pair of piers' frame system to measure the vertical vibration due to traffic and similar excitations. With these vertical set of measurements, it can be possible to detect structural abnormalities caused by deck deterioration and changes in the boundary conditions and supports.

It is highly recommended to select digital accelerometers that have a wide frequency band to capture small and large amplitude shaking. In addition, a free-field station with a tri-axial accelerometer should be placed sufficiently away from the influence of any surrounding structure to minimize, as best as possible, any contaminating effect in its recording. This station is intended for recording any input ground motion of the structure and is recommended to be installed over very stiff soils or preferably on a rock outcrop, if available. The data collected can also be used to create strong ground shaking intensity maps.

With regards to the sensor system, it should be adequately shielded and grounded to avoid problems with electrical noise sources due to the low voltages generated by the sensors. Modern strong motion systems typically have a noise level of a fraction of a gal (i.e., 0.1% of the acceleration due to gravity) and a maximum recording capacity of 2 g or more (Shakal and Huang, 2008). By eliminating or limiting the noise levels, the post-processing results of displacement and long period spectral values will be more accurate due to a direct effect in controlling the noise of the numerical integration.

The processing of strong motion records began in the 1970's as a developmental effort in Caltech and throughout the decades has become more and more advanced and standardized. For moderate and larger motions, current processing will yield accurate results of accelerations and displacements over a broad range of frequencies (e.g., from DC to 40 Hz or higher). When analyzing residual displacement in structures (e.g., permanent drift) more advanced processing techniques are needed, in addition to adequate instrumentation such as GPS. Valuable information concerning the dynamic response of the structure can generally be computed from the following measurements:

- natural periods of vibration
- modal damping ratios
- base shears
- drifts

In conclusion, some of the most important applications of structural instrumentation are:

1. Measuring the actual structural response due to seismic events for evaluation of its performance during an earthquake compared to design targets.
2. Make informed decisions about occupancy modification and post-event business resumption based on previously developed threshold levels.

However, the main goal of instrumenting a structure is to improve general predictive models. This is because they are the focus on earthquake engineering from post-earthquake investigations, evaluating and retrofitting structures, structure design, and performance-based design. According to Stepp (2002), the guiding objective of building instrumentation should be to gain understanding of the behavior of representative building types in order to improve general predictive models by:

- challenging, verifying, or calibrating models
- calibrating design and retrofit rules (codes); and
- calibrating post-earthquake evaluation rules

2.2 System's Dynamic Identification

In the field of structural dynamics, analysts are interested in the study of the behavior of structural systems in response to dynamic inputs (forces or displacements). The energy of the acting inputs is imparted to the structure and manifested in it in the form of small or large amplitude vibrations, depending on the size of the input energy. In civil engineering, the most relevant and damaging forms of natural excitation energy are earthquakes and for that reason their effects on civil structures has been extensively studied for decades. For the engineer, it is very important to identify a structure's dynamic properties (i.e., natural frequencies, damping, and mode shapes) to evaluate its vulnerability to a potential seismic event before its occurrence. This allows for adequate retrofitting measures that will extend the life cycle of the structure while at the same time guaranteeing the safety of its occupants.

The process for dynamic identification is carried out by installing accelerometers throughout the entire structure and recording its response to experimental input excitations. Those inputs may

be imparted as an induced initial displacement (zero initial velocity) of the structure or an induced impulse (initial velocity with zero initial displacement). These two initial conditions are effective in identifying the fundamental dynamic properties in the form of a free vibration response analysis. Nevertheless, they are not effective in identifying higher modal features although the structure's physical characteristics imply their existence or if there are not enough sensors to capture them. Moreover, for large scale structures the logistic of imparting these excitations is complicated and expensive. An alternate approach to excite a structure for dynamic identification purposes and to overcome the aforementioned issues is to install a synchronized shaker at one point in the structure to induce controlled mechanical vibrations. With this instrument, it is possible to generate multiple excitations with a specific frequency content or even a Compressed High Intensity Radar Pulse (CHIRP) signal, which changes its frequency content with time. This is useful to study the structure's behavior to different frequencies and consequently to identify its dynamic parameters. However, just as the first mentioned excitation alternatives, some drawbacks of this alternative are its equipment costs, the execution logistic in operational civil structures, and its risk of malfunctioning due to any accidental incident. For these reasons, scientists have popularly adopted the study of small amplitude vibrations induced by ambient excitations to identify the dynamic properties of any structure.

Ambient vibrations can be described as a random signal with similar properties to a white noise. Accelerometers throughout the entire structure record small amplitude response vibrations in which all the dynamic characteristics of the studied structure are embedded. There are numerous mathematical methodologies to extract the structure's information from these signals and dynamic analysts implement them to create accurate mathematical descriptions of any physical system. Furthermore, when there are available previously created models of a system, they can be improved to reduce errors between their actual prediction and the real response due to a physical excitation.

Models are low-order representations of a high-order system which can be utilized to make predictions and conclusions about that system. Although most models are developed only from physical laws, rules, and insight on a system, they can also be developed entirely or partially based on actual measurements or responses from it. This second type of model development is called System Identification.

System Identification plays a central role in the design of algorithms used to identify and characterize undesirable changes (i.e. faults or damages) that may appear during the service life of a structure or mechanism. According to Juang (2000), identification is the process of developing or improving a mathematical representation of a system using experimental data.

The major benefit of system identification is the improvement of the analytical model of a structure. In the best cases, the initial numerical model of a simple metallic structure can be found to be incorrect by as much as 10% in the lowest frequencies. In the case of reinforced concrete structures, and as a function of their size, foundation type, and geometry, the models may incur in errors of as much as 50% from the experimental lowest frequencies. These inaccuracies are due to a combination of factors, including but not restricted to: approximations in the finite element derivations; mismodeling of structural elements; differences in actual material properties and dimensions from those assumed in the model; and lack of convergence of the numerical model.

The identification task is to identify a model which will adequately describe the input and output map. On the other hand, the primary interest in modal testing is to analyze the properties of a dynamic system, such as stiffness, damping, and frequency among others. If in theory, active control hardware can be used for modal testing, the data may not be refined enough due to the lack of enough response channels and possibly the inability to excite all the modes of interest. Hence, additional instrumentation may be required (Juang, 2000). The key steps in the system identification task for a complex flexible structure are outlined below.

1. Develop an analytical model of the structure.
2. Establish the levels of structural dynamic response which are likely to occur, using the analytical model and characteristics of the anticipated excitation sources.
3. Set the instrumentation requirements from this information for a measurement system needed to sense the motion with prescribed accuracy and spatial resolution.
4. Perform experiments and record experimental data.
5. Apply system identification techniques to identify the characteristics of the structure such as the flexible body modes that are excited and, to the extent possible, determine other significant quantities of interest, such as the characteristics of input/output noise, the degree of nonlinearity, and the strength of various excitation sources.
6. Refine the analytical model if necessary, for example, for structure redesign.

According to Juang (2000), modal parameter identification, which is generally referred to as modal testing in the field of structures, is the process of measuring signals produced by a structure and identifying modal parameters (damping, frequencies, mode shapes and modal participation factors). System Identification in the field of controls means the process of measuring signals produced by a system to build a model which represents that system for control design. If the identified model is a linear model in state-space representation, the eigensolution of the model provides eigenvalues and eigenvectors which in turn determine modal parameters for structures.

In this research the identification of the dynamic properties of the structure will be executed by performing time domain, frequency domain, and time-frequency domain analyses. The time domain methodologies consist in analyzing physical data represented by experimental and simulated time series of signals or by mathematical functions with values known for all domain of real numbers. Some approaches within this signal processing methodology include auto and cross-correlation analysis, state-space representation and analysis, impulse response functions and convolution analysis, among others. On the other side, the frequency domain methodologies consist in analyzing time series of signals that represent physical phenomena by its description as a complex function in the frequency domain. Instead of showing signal changes through time, this approach shows the frequency content of each sinusoid contained in the studied signal. Some approaches within this signal processing methodology include Fourier analyzers (series and transforms) and spectral density analysis, cross-spectrum analysis, coherence functions, and transfer functions, among others. Finally, time-frequency analysis comprises those techniques that study and describe a signal in both the time and frequency domains simultaneously using various time-frequency representations often called “Time-Frequency Distributions”. Each representation is a view of both time and frequency in which the distribution shows the energy of a signal in both domains simultaneously. This is accomplished by extracting the frequency content of a signal at each instant of time. Some approaches within this signal processing methodology include the Short Time Fourier Transform, the Hilbert Transform, and Wavelet Transforms among others.

2.3 Damage Identification in Civil Structures

Currently there are extensive techniques and methodologies for damage identification in structural members. Vibration-based techniques are the most widely used for damage detection and localization on civil infrastructure. The localization of damage is a part of a wider spectrum

of techniques that have been developed to detect, identify, quantify, and predict damage. According to Gandomi et. al (2008), damage identification can be divided into five levels:

- Level 1: detection of fault existence in a structure (existence)
- Level 2: localization of fault (location)
- Level 3: identification of the fault type (type)
- Level 4: quantification of fault severity (extent)
- Level 5: prediction of the remaining life (prognosis)

The challenge in the damage identification techniques for structural systems lies in the methods used to obtain information of emergence, location, and severity of the damage by measuring the system dynamic responses. The principal methodologies used in the vibration-based damage identification field are: frequency changes, mode shape changes, mode shape curvature changes, and measured flexibility changes. Different mathematical algorithms are then applied in some of those methodologies in order to provide not just the identification of the damage (Level 1) but also the location, type, and extent (Level 2 – Level 4). For the interested reader, more detailed information on vibration-based identification techniques and its alternative approaches can be found in Herrera (2005) and Doebling et al. (1998).

Typical damage identification studies are performed under ideal or controlled conditions and often to isolated structural members and/or assemblies. In these cases, the identification analysis approach is more structured and simpler. Furthermore, due to the nature of the experimental conditions, the results possess less uncertainties and sometimes minimum variation from what is expected. In this research, vibration-based damage identification methodologies are going to be applied to a full-scale bridge structure under uncontrolled conditions subjected to all kinds of excitations encountered in its location. This creates a challenge in the identification analysis techniques and its implementation because the level of uncertainty is greatly increased. Variability due to environmental conditions, multiple simultaneous excitations of different nature, soil-structure interaction, the type of instrumentation used and its location throughout the structure, the types of structural and non-structural elements that encompasses the structure, the aged condition of the structure, and the fact that it is completely made of reinforced concrete, which is a highly nonlinear permeable material, makes imperative a holistic focus of analysis and assessment. This modified approach should address these issues and still deliver confident results whose

interpretation provides a reliable and complete assessment. It should focus not only in monitoring the changes in the dynamic properties of the structure but also on the structure overall performance.

Engineering Demand Parameters (EDP) are structural response quantities that can be used to predict damage to structural and nonstructural components and systems (ATC-58, 2004). Existing design codes implement EDPs developed from a performance-based seismic design perspective in order to predict the earthquake performance of a structure. With this approach it is expected to mitigate the potential losses due to earthquakes. Some of these EDPs of interest include local deformations, curvature ductility, story shears, overturning moments, floor accelerations and velocities, and roof and story drifts among others. The possibility of monitoring those parameters' measurements under seismic and ambient excitations on full-scale non-ideal conditions would greatly contribute in the advancement of the Performance-Based Earthquake Engineering (PBEE) field as well as the structural engineering knowledge in general. The concept of PBEE implies design, evaluation, and construction of engineered facilities whose performance under common and extreme loads responds to diverse needs and objectives of owners-users and society (Krawinkler, 1999). It seeks to improve seismic risk decision-making through assessment and design methods that have a strong scientific basis and that express options in terms that enable stakeholders to make informed decisions (Moehle and Deierlein, 2004). Therefore, the combined application of SHM and PBEE opens a range of opportunities for improving the damage identification and assessment in any type of structure at any time. SHM end purpose is to guarantee an acceptable performance of a structure under service loads, at least for its design life, with the possibility of extending it by avoiding that the structure reaches a critical state. In the case of a natural disaster, SHM information should allow for rapid post event damage assessment while improving the resilience capacity of the structure. The difference between the classical SHM approach and the performance-based SHM approach is that on the first one, changes in modal and/or model parameters are tracked in order to find any anomalies that may indicate a possible damage state but on the second one key EDP are tracked, while addressing uncertainties such as nonlinear responses, and then these changes in EDPs are mapped to damage measures in order to quantify the uncertainty associated with the response damage relationships. Damage measures are empirical parameters describing the level of damage in structural and nonstructural components such as concrete cracking and spalling (Skolnik and Wallace, 2010).

Among all the EDPs that can be monitored in a structure, the inter-story drift ratio has been shown to correlate best with observed damage of structural and some nonstructural components (Algan, 1982; Sozen, 1983). Inter-story drift ratio is defined as the relative horizontal displacement between two consecutive floors normalized by the story height. It is an important indicator of structural performance, especially in structures that undergo inelastic deformations. Because these deformations are directly related to this EDP, building codes such as the IBC and ASCE establish limit values for it in order to limit *p-delta* effects in structures and consequently ensure acceptable structural performance with limited or no damage.

In this research, both classical SHM and performance-based SHM approaches will be implemented to recorded data for obtaining a reliable damage assessment in the structure. Low and high frequency analysis together with verification of changes in dynamic properties are the classical techniques that will be implemented. For the performance-based approach SHM, the evaluation of EDPs will be performed giving emphasis to peak floor acceleration and inter-story drift ratios. According to Worden (1990), there are a series of issues when applying the double integration method to recorded acceleration time histories. Some of them are missing data due to sparse building instrumentation and excessive long period drifts in the computed displacement histories due to baseline shifts in acceleration. Also, there are some uncontrollable circumstances (e.g., temperature fluctuations) that inevitable add noise to the raw recorded data, often having some nominally constant offset. The double integration method produces acceptable errors of less than 5% in peak value for linear responses but yields unreliable results with errors of more than 12% when analyzing nonlinear responses (Skolnik and Wallace, 2010). For that reason, the structural analyst should be aware of these issues and follow specific delicate signal processing steps such as baseline correction, zero-padding signal ends, and band-pass filtering. However, despite these drawbacks it is the most common method for obtaining displacements for calculating inter-story drift ratios. This is thanks to the large strong motion instrumentation programs around the world and the standardized way of how data is collected. Skolnik (2008) shows that contact methods, such as using displacement sensors (e.g., LVDT) to directly measure the absolute displacement, work reasonably well in laboratory setups but they are impractical for real buildings. Other contact methods implementing strain-sensitive fibers usually embedded in concrete members to measure structural displacement (Ansari, 2007; Casas and Cruz, 2003) and time domain reflectometry using coaxial cables (Su, 1998) were proposed and studied by the scientific

community. Unfortunately, more development on the application of these methodologies is needed to successfully implement it in buildings to measure inter-story drifts. Noncontact methods are another rising alternative analysis tools for measuring interstory drifts. They include, but are not limited to, the use of GPS sensors (Celebi and Sanli, 2002; Tamura et al., 2002; Nakamura, 2000; Hudnut and Behr, 1998), video Amaras for motion-tracking in bridges (Wahbeh et al., 2003), and laser and position sensitive photodiodes (Bennett and Batroney, 1997; Chen et al. 1998). Among other techniques, some of those tools offer road projections for future implementation in measuring interstory drifts both in the elastic and inelastic ranges. However, more research is needed to address some issues regarding resolution, susceptibility to rotation, and measurement range (Skolnik and Wallace, 2010).

2.4 Mathematical Tools in Experimental Dynamic Identification

The following sections present a summary of commonly used methodologies for the identification of structural dynamic parameters. This research will be mainly focused on the implementation of the Random Decrement Technique from a time domain approach, the Fourier transform, from a frequency domain approach, and wavelet transforms from a time-frequency domain approach. However, several other commonly used techniques are presented because they precede some of the proposed methodologies for this research and their familiarity will facilitate the understanding of the ones implemented in this study.

2.4.1 Random Decrement Technique

The Random Decrement Technique (RDT) is a time domain algorithm proposed and developed by Henry A. Cole (1973) as a method to detect flaws (e.g., crack emergence and growth) on in-service aerospace structures by estimating changes in its dynamic properties. Cole's motivation arose from the need to have a real time reliable approach to estimate its damping from a system's response to operational loads. With this he intended to overcome the difficulties being encountered using frequency domain analyses while enhancing the accuracy of the results. Since then, the implementation of this algorithm has been extensively studied in different engineering fields. Chang (1975) applied the technique to characterize aero-elastic systems. Ibrahim (1977) proposed a modification to the RDT for modal identification of multi-degrees of freedom (MDOF) structures. Assmussen et al. (1997) introduced the concepts for quality assessment of random

decrement signatures. Spanos and Zelding (1996) studied the fidelity of the random decrement signatures under the assumption of white noise excitation. In addition, Aggour et al. (1982) and Yang et al. (1989) applied the RDT to estimate in-situ soil properties. More recently, Huerta (2002) used the technique to determine soil properties from earthquake data.

This technique is based on linear systems theory and consists in selecting N number of segments of length T from a random time history $y(t)$ and which starts at a specified triggering condition y_s. Once selected, these segments are averaged to form a new curve, known as the "Random Decrement Signature" (RDS). This new signature is proportional to the correlation functions of a structure's random responses to its random input excitations (e.g., loads). The RDS is characterized by its similitude to a free vibration response signal of a single degree of freedom (SDOF) system although they do not represent the same. This similitude can be explained from the premise that the random response of a structure or system to random input excitations is made up of a deterministic part and a random part. The deterministic part of the response corresponds to any of the following two input excitations: an initial displacement (with zero velocity) or an initial velocity (impulse). The random part of the response is assumed to have a zero-mean distribution (similar to a white noise). Hence, by averaging a large number of N selected segments of the response signal its random part gradually vanishes, leaving only the deterministic part of the signal. Consequently, the generated RDS decays in an exponential-like manner in accordance to its input-output mathematical correlation.

The original development of the RDT was based on the auto-correlation function, $R_{yy}(\tau)$, of a unique response, $y(t)$, defined by equation (2.1) and as shown in Figure 2-2. This approach allows the experimental identification of natural frequencies and damping ratios of SDOF and MDOF systems while conversely limiting their mode shapes calculation.

$$R_{yy}(\tau) = \frac{1}{N}\sum_{i=1}^{N} y(t_i + \tau)\,|y_s \qquad (2.1)$$

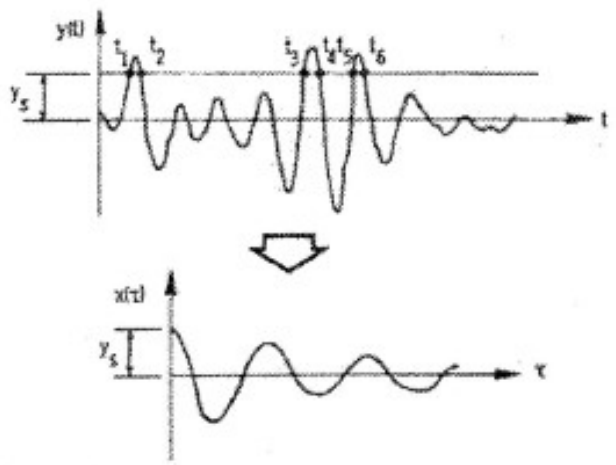


Figure 2-2: A one-station random response and its corresponding RDS (Ibrahim, 1977)

Later, Ibrahim (1977) proposed a modification of the method in which the time correlation between two or more measured signals does not change. Supposing there are two measured response signals $y(t)$ and $x(t)$, the cross-correlation function can be defined by equation (2.2).

$$R_{xy}(\tau) = \frac{1}{N}\sum_{i=1}^{N} x(t_i + \tau)\,|y_s \qquad (2.2)$$

This modification ensures time correlation between RDSs generated from multiple sensors throughout the structure as shown in Figure 2-3. It allows the computation of mode shapes to complete the identification process in both SDOF and MDOF systems.

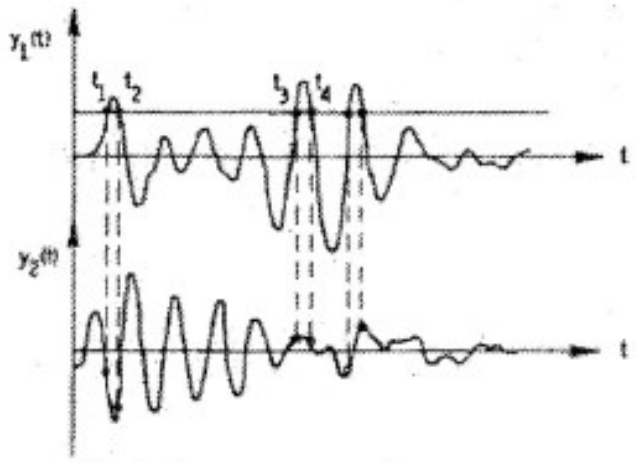


Figure 2-3: Two-station random responses with $y_1(t)$ used as the leading sensor (Ibrahim, 1977)

It is important to note that to successfully complete the identification process, all responses should be recorded simultaneously to dynamically couple them.

In addition, the selection of the triggering condition is of particular importance because this will greatly enhance the fidelity of the generated RDSs and will help to avoid averaging out the deterministic part of the system's response. Some of the most commonly used triggering conditions for the application of the RDT are stated below.

1. Level crossing

$$y_s = \{y(t_i) = a\} \tag{2.3}$$

2. Positive points

$$y_s = \{a \leq y(t_i) \leq b\} \tag{2.4}$$

3. Positive slope and zero level crossing

$$y_s = \{y(t_i) = 0 \ \& \ \dot{y}(t_i) > 0\} \tag{2.5}$$

4. Negative slope and zero level crossing

$$y_s = \{y(t_i) = 0 \ \& \ \dot{y}(t_i) < 0\} \tag{2.6}$$

5. Local extremum

$$y_s = \{a \leq y(t_i) < b \ \& \dot{y}(t_i) = 0\} \tag{2.7}$$

It is useful to note that the "positive points condition" in expression equation (2.4) can also be applied in the negative part of the signal for the selection of response signal segments. In this case, it is necessary a change in the sign of these selected signal segments in order to be averaged with the positive ones extracted from the original triggering condition. This will improve the quality of the generated RDS due to the increase in averaged signal segments. Chang (1975) investigated

the amount of response signal segments and the length needed to produce a reliable RDS. Based on results from simulations of one and two degrees of freedom systems he recommended about 2,000 ensemble averages for accurate estimation of natural frequencies and damping ratios, and a length ranging from about 50% to 125% of the beat period of the two eigenfrequencies. However, this may not be completely reliable for identification of higher order modal parameters from experimental response measurements of complex MDOF systems. In those cases, it is recommended to generate a RDS which completely decays to zero and does not shows signs of beating. With respect to the selection of the triggering levels a and b from equations (2.3), (2.4), and (2.7), it is important to consider that, although the more points the better estimation, the lowest points tend to be more noise contaminated. For that reason, an equilibrium must be made at the time of levels selection. According to Rodrigues and Brincker (2005), a good alternative may be to select the positive points triggering condition considering the levels $a = \sigma_x$ and $b = \infty$, where σ_x refers to the standard deviation of the entire response signal being analyzed. In this respect, Assmussen (1997) states the possibility to define optimum triggering level minimizing the variance of the estimate of the RDSs. Accordingly, in the case of the level crossing triggering condition, this optimum level is found to be $a = \sqrt{2}\,\sigma_x$.

2.4.2 Fourier Transform

The Fourier transform is a mathematical technique based on decomposing signals into sinusoids. In simple words, it is the mathematical transformation of a signal between the time domain and the frequency domain. It is a reversible technique because it is possible to transform from either domain to the other. It was named after Jean Baptiste Joseph Fourier and his theory was first presented to the *Institut de France* on December 21, 1807 on his paper "*Mémoire sur la Propagation de la Chaleur dans les Corps Solides*" (Treatsie on the Propagation of Heat in Solid Bodies). In it he proposed the use of sinusoids to represent temperature distributions and a committee consisting of Joseph-Louis Lagrange, Pierre-Simon Laplace, Gaspard Monge, and Silvestre François Lacroix reviewed on the work. While Laplace and other reviewers voted to publish the paper, Lagrange adamantly protested because he stated that a signal with corners cannot be represented by a summation of sinusoids. However, it was later demonstrated that one can get so close that the difference between the two has zero energy, which proves Fourier was

also right. A continuous signal, $x(t)$, or discrete signal, $x[n]$, respectively has zero energy, E, when:

$$E_\infty = \lim_{T\to\infty} \int_{-T}^{T} |x(t)|^2\, dt = \int_{-\infty}^{\infty} |x(t)|^2\, dt = 0 \tag{2.8}$$

$$E_\infty = \lim_{N\to\infty} \sum_{n=-N}^{N} |x[n]|^2 = \sum_{m=-\infty}^{\infty} |x[n]|^2 = 0 \tag{2.9}$$

Today this phenomenon is called the *Gibbs effect*. Lagrange's objection to Fourier's proposition apply only to continuous signals while for discrete signals the decomposition is mathematically exact.

When applying the Fourier decomposition to a signal it results in a group of cosine and sine waves of the same size. Each resultant signal has a different frequency and amplitude. The advantage of decomposing a signal into cosines and sines is that they have *sinusoidal fidelity*. In simple words, when a sinusoidal signal is input to a system it is guaranteed to produce a sinusoidal output. While the amplitude and phase of the response can change, the frequency and the wave shape remain the same.

The Fourier transform have four variations corresponding to the four basic types of signals that can be encountered. There exist aperiodic or periodic signals and continuous or discrete signals. All these types of signals extend to positive and negative infinity. Below is a brief description of the four types of Fourier transform variations and its respective combination of signals.

a. <u>*Continuous Fourier Transform*</u>: This type of Fourier transform is employed in the decomposition of aperiodic and continuous signals. These signals extend from negative to positive infinity without repeating itself in a periodic pattern. Figure 2-4 shows an example of this signal and equation (2.10) shows the equation representing the Fourier Transform, where ω_0 is the natural frequency.



Figure 2-4: Example of an aperiodic and continuous signal (Smith, 2003)

$$X[\omega] = \int_{-\infty}^{\infty} x(t)\, e^{-j\omega_0 t} dt \tag{2.10}$$

b. *Fourier Series*: This type of Fourier transform is applied to decompose periodic and continuous signals. These signals include any waveform extended from negative to positive infinity and repeating itself in a regular pattern. Figure 2-5 shows an example of this signal and equation (2.11) shows the equation representing the Fourier Transform.



Figure 2-5: Example of a periodic and continuous signal (Smith, 2003)

$$X(\omega) = a_k = \frac{1}{T}\int_{t_0}^{t_0+T} x(t)\, e^{-jk\omega_0 t}\, dt \tag{2.11}$$

c. *Discrete Time Fourier Transform (DTFT)*: This type of Fourier transform is applied to decompose discrete and aperiodic signals. These signals are defined at single points ranging from negative to positive infinity and do not repeat themselves in a regular fashion. Figure 2-6 shows a representative signal and equation (2.12) shows the DTFT.



Figure 2-6: Example of an aperiodic and discrete signal (Smith, 2003)

$$X[\omega] = \sum_{n=-\infty}^{\infty} x[n] e^{-i\omega n} \tag{2.12}$$

d. *Discrete Fourier Transform (DFT)*: This type of Fourier transform is also called the *Discrete Fourier Series*. It is applied to decompose discrete and periodic signals. These signals are defined at single points and repeat themselves from negative to positive infinity in a periodic pattern. Figure 2-7 shows a representative signal and equation (2.13) shows the DFT.



Figure 2-7: Example of a periodic and discrete signal (Smith, 2003)

$$X[k] = a_k = \sum_{n=0}^{N-1} x[n]\, e^{-i\,\omega_k n} \tag{2.13}$$

The DFT decomposes an N point input signal into two $^{N}/_{2} + 1$ point output signals. The resultant two signals contain the amplitudes of the component sine and cosine waves. The description of those amplitudes is called the *frequency domain*.

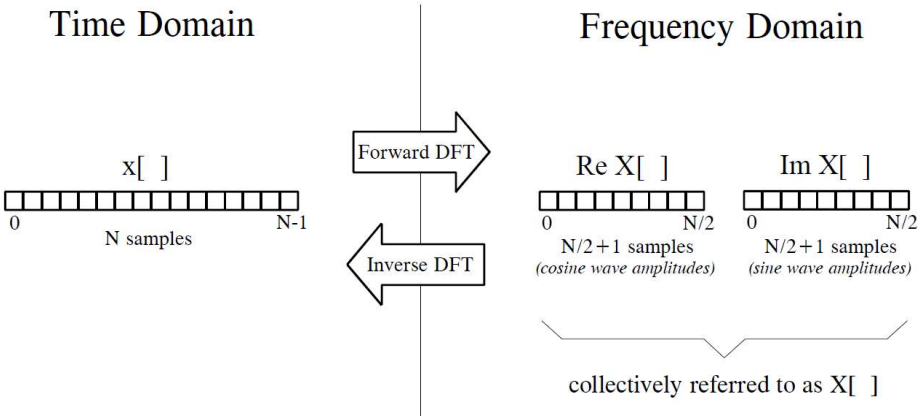


Figure 2-8: Graphical explanation of the DFT and the IDFT in time and frequency domains (Smith, 2003)

In order to retrieve the original signal, it is needed to apply the Inverse Discrete Fourier Transform (IDFT), which is shown in equation (2.14) and is also known as the synthesis equation.

$$x_k[n] = \sum_{k=0}^{N-1} X[j\omega]\, e^{jk\ \ {}_0 n} \tag{2.14}$$

Any N-point signal, $x[i]$, can be created by adding each $^{N}/_{2} + 1$ sine and cosine waves. The arrays $Im\,X[k]$ and $Re\,X[k]$ shown in Figure 2-8 contain the amplitudes of the sine and cosine waves respectively. Scaled, those amplitudes are multiplied by the basis functions shown in equations (2.15) and (2.16). Then they are added to produce the time-domain signal, $x[i]$.

$$c_k[i] = \cos(k\omega_0 i) \tag{2.15}$$

$$s_k[i] = \sin(k\omega_0 i) \tag{2.16}$$

2.4.3 Hilbert Transform

The use of the Hilbert Transform in signal processing operations of continuous and discrete systems has been widely use in the past decades. Some authors state that it is, without question, the most important linear operator in analysis. It is the inspiration for higher-dimensional singular integrals, which are about 60 years old. The name "Hilbert Transform" was given by British mathematician G.H. Hardy in honor of Hilbert's pioneering work on integral equations (King, 2009a). Hardy's early work, and not David Hilbert's, established the actual definition with the mathematical rigor of the Hilbert transform.

The idea behind of the Hilbert transform is to find a companion function $y(t)$ for a real function $x(t)$ such that an analytical signal $z(t)$ can be constructed. That analytical signal is also known as the Gabor signal (Gabor, 1946) and is shown in equation (2.17).

$$z(t) = x(t) + jy(t) = x(t) + jH[x(t)] \tag{2.17}$$

The Hilbert transform can be computed in three simple steps:

1. Compute the Fourier transform of the input signal $x(t)$.
2. Reject the negative frequencies
3. Compute the Inverse Fourier Transform (IFT)

The IFT generates complex-valued signals whose real and imaginary parts are a Hilbert transform pair.

As noted before, the analytical signal is complex and its frequency spectrum is zero for negative frequencies. Its real part is equal to the original signal $x(t)$. Equation (2.17) can be alternatively written as

$$z(t) = a(t)e^{j\theta(t)} \tag{2.18}$$

The analytical signal allows to segregate the amplitude, $a(t)$, and instantaneous phase, $\theta(t)$, components of a determined input signal. By definition, $a(t)$ and $\theta(t)$ are expressed as follows:

$$a(t) = \sqrt{x^2 + y^2} \tag{2.19}$$

$$\theta(t) = \tan^{-1}\left[\frac{y(t)}{x(t)}\right] \tag{2.20}$$

According to Ville (1948), in order to obtain the instantaneous frequency (IF) of a signal the time derivative of $\theta(t)$ has to be computed as expressed in equation (2.21).

$$IF(t) = \frac{1}{2\pi}\frac{d}{dt}\theta(t) \tag{2.21}$$

The instantaneous amplitude (IA) is obtained with the envelopes of the time signal. After computing the instantaneous phase of the signal, it can be noted that the result possesses discontinuities between $-\pi$ and π. When the IF is computed by numerically differentiating the instantaneous phase, the results will exhibit discontinuities in the same time instants where the instantaneous phase shows discontinuities. One commonly used technique to solve this problem is to *unwrap* the computed instantaneous phase. This is done by adding 2π to the phase after a complete cycle in order to smoothen the discontinuities before taking the derivative.

It is important to note that a limitation of the Hilbert transform in the determination of the IF is that it will provide satisfactory results only if the signal is mono-component. A monocomponent signal is multicomponent the IF results will be just the average value per time instant (Ramírez-Castro and Montejo, 2011). In order to successfully apply the Hilbert transform to a multi-

component signal, it has to be decomposed in its mono-components through the *Empirical Mode Decomposition* (Huang, 1998), the *Hilbert Vibration Decomposition* (Feldman, 2006), or the *Synchrosqueezed Wavelet Transform* (Daubechies et al., 2011).

Today's application of the Hilbert transform includes latency analysis (Recio-Spinoso et al., 2011; van Drongelen, 2007), design of bizarre stimuli for psychoacoustic experiments (Potamianos and Maragos, 1994), regularization of convergence problems in multi-channel acoustic echo cancellation (Liu and Smith, 2002), and signal processing for auditory prostheses (Nie et al., 2006). In the field of SHM the Hilbert transform was used for the determination of the natural frequencies and damping in free vibration.

2.4.4 Hilbert-Huang Transform

Real world phenomena can be described by analyzing the data collected from natural events or empirical processes. In the past, the collected data was processed by routinely putting it through certain well-established algorithms and extracting some standard parameters. This was mainly done to strictly follow the mathematical rigor characteristic of a specific algorithm that can work in the parameter extraction process of the collected data. The dilemma associated with this approach is that in order not to deviate from that mathematical rigor, typical assumptions of linearity and stationarity in the studied systems had to be made. That presented restrictions for further types of analysis in more complex systems with more realistic conditions. The truth is that the real world is neither linear nor stationary. This creates inadequacy when applying linear and stationary data analysis methods to real world data possessing a nonlinear and/or nonstationary mature just for the desire of adherence to a specific and strong mathematical basis.

The end goal of data analysis is to better understand the behavior of studied systems by providing interpretations of analysis results that reveals the hidden mechanisms that explain a real-world phenomenon. So, it is better to apply analysis methods that adapt to the nature of the data instead of letting the method impose rigorous mathematical rules that are irrelevant to the data. By applying these adaptive methods, the obtainment of inaccurate or irrelevant results can be avoided. An adaptive behavior is one that is used to adjust another type of behavior. In the sense of signal processing, these adaptive methods take an input signal and produce an output in a manner which changes depending on the characteristics of the inputs and the previous outputs. Some available methods used for signal analysis of stationary processes rely mostly on feedback

loops. Even though they are called adaptive, they are not. After considering this definition, it can be concluded that adaptively is unnecessary for nonstationary and nonlinear data. Unfortunately, there are not many adaptive methods that can be effectively employed in the processing of these types of signals.

The Hilbert-Huang Transform (HHT) is a methodology, named by National Aeronautics and Space Administration (NASA), for decomposing signals into Intrinsic Mode Functions (IMF). An IMF is defined as any function having the same numbers of zero-crossing and extrema or at least differing at most by one. Also, IMFs have symmetric envelopes defined by the local maxima and minima, respectively. These characteristics of IMFs guarantee a well-behaved application of the Hilbert transform. It is the combination of the Hilbert Spectral Analysis (HAS) and the Empirical Mode Decomposition (EMD) (Huang et al., 1996, 1998, 1999). HAS is the use of the Hilbert transform to compare the IF of signals by taking the derivative of the instantaneous phase. The HHT, with its empirical approach, is more like an algorithm especially designed for analyzing data sets that are nonlinear and nonstationary.

The most essential feature of the HHT is the employment of the EMD for decomposing complicated data sets into a finite and often small number of IMFs. This implicitly assumes that at any specific time the input signal is multicomponent. EMD was developed by Huang et al. (1998) in the late 1990's to analyze nonlinear and nonstationary systems by obtaining IMF's through a sifting process. The proposed iterative sifting process consist in:

a. Identify the local extremes (maxima and minima) of $x(t)$.
b. Apply a cubic spline to interpolate between the maximum points in to obtain an envelope, e_{max}, over the entire signal. Do the same with the minimum points to obtain e_{min}.
c. Compute the envelope's mean, m, with:

$$m = \frac{e_{max} + e_{min}}{2} \tag{2.22}$$

d. Detrend the data by computing:

$$h(t) = x(t) - m \tag{2.23}$$

Here $h(t)$ is an IMF candidate. Steps (a) through (d) should be repeated changing $h(t)$ as a new function until it meets the two conditions specified earlier that characterizes IMF's and any other special condition.

e. When conditions are met, $h(t)$ is taken as the first IMF.

f. Compute a remainder, $r(t)$, as

$$r(t) = x(t) - \sum IMF \tag{2.24}$$

Now $r(t)$ becomes the new function and steps (a) through (f) are repeated to find the next IMF.

g. Iterate the entire procedure until it meets a specified stopping criterion or when it can be considered a monotonic function.

It is possible to reconstruct the decomposed signal by adding all the computed IMF's and the remainder as shown in equation (2.25).

$$x(t) = \sum IMF + r(t) \tag{2.25}$$

Due to the nature of the sifting process the IMF's will appear in decreasing order of frequencies. A drawback of the EMD is that it lacks mathematical rigor. Being an algorithm, the results may vary by tweaking the variables involved in the analysis. Two examples of this are how to define the boundary conditions to construct the envelopes and which would be the stopping criterion to finish the sifting process.

2.4.5 Wavelet Transform

The implementation of the Fourier transform and the Hilbert transform in system identification procedures, although useful in many instances, possess certain limitations. The most significant one is that after the transformation is executed, the time or space information is lost. This creates a problem because it becomes impossible to determine when or where a particular event took place (Ovanesova and Suárez, 2004). It is a fact that life phenomena can be described by recorded signals possessing in its clear majority nonstationary and nonlinear behavior. Some signals of interest may be reflecting trends, drift behavior, transient conditions, or the beginning and end of an event (e.g., earthquakes, vibrating machinery, etc.). In order to track the changes in the dynamic properties of a structure a joint time-frequency analysis is required. This type of analysis identifies the specific time at which one or more frequencies are embedded in a signal. That is typically

obtained by calculating a frequency spectrum at regular intervals of time. There are several popular methodologies to achieve this, but the most widely used are Short Time Fourier Transform (STFT) and the Wavelet Transform. The STFT is the application of the Fourier transform to a segmented signal using a sliding or time-localized window to each segment in order to obtain a spectrogram. It produces a visual representation of the frequency spectrum contained in a signal as a function of time or space. However, the use of the STFT presents an issue with respect to the window used for the analysis. The length of the window limits the resolution in frequency. The STFT is capable to analyze either high frequency components using narrow windows (or wide-band frequency analysis) or low frequency components using wide windows (or narrow-band frequency analysis). A drawback of the STFT is that it has a fixed resolution. This is shown in Figure 2-9.

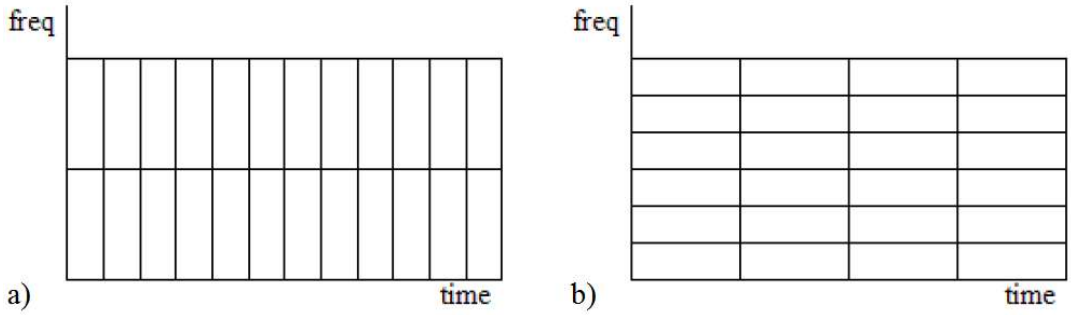


Figure 2-9: Comparison of STFT resolution. a) Frequency solution reduced with increased time resolution. b) Time resolution reduced with increased frequency resolution.

As mentioned before, wide window gives better frequency resolution but poor time resolution and a narrower window gives good time resolution but poor frequency resolution. This problem of the STFT can be solved by implementing the Wavelet transform.

A *wavelet* is a special function on which the Wavelet transform is based. It is an irregular and often asymmetrical little waveform of limited duration having and average value of zero (Misiti et al., 2000). Each wavelet has a pseudo-frequency because its frequency varies slightly over its length. They are great at describing anomalies, pulses, and any other events that are contained within the duration of a signal. Because they can stretch or shrink in time, they can replicate any frequency change present in a signal due to any of the reasons previously mentioned. In addition, they can be shifted in time to best correlate (or line-up) with the event. These two properties of the wavelet provide the time-frequency information of the event of interest.

The history of the Wavelet transform dates back to 1909 when the mathematician Alfred Haar published the Haar wavelet, although the concept of a wavelet did not exist at that time (Chun-Lin, 2010). That concept was proposed in 1981 by the geophysicist Jean Morlet and the term "wavelet" was invented by himself and the physicist Alex Grossman in 1984. The Haar wavelet was the first orthogonal wavelet and was followed by the Meyer wavelet in 1985, which was developed by the mathematician Yves Meyer. The first international conference on wavelets was held in France in 1987 and it gathered most the scholars that were immersed in this emerging field. Later in 1986, the idea of Multi-Resolution Analysis (MRA) was developed by Stephanie Mallat and Meyer. This became Mallat's Ph.D. dissertation in 1988. Mallat and Ingrid Daubechies developed the transition from continuous to discrete signal analysis. Also in 1988, Daubechies developed a systematical method to construct compact support orthogonal wavelets. This development laid the foundations of the modern wavelet theory. Mallat proposed in 1989 the Fast Wavelet Transform (FWT) and with it the signal processing applications for the Wavelet transform vastly increased. More information on the history of the Wavelet transform can be found in Daubechies (1996) and Polikar (1999).

A Wavelet transform consists in breaking up a signal into shifted and scaled versions of a basis wavelet. This mother wavelet is a basis function that characterizes a basic wavelet shape and covers the entire domain of interest. In simple terms, it is a representation of a function in real space as a linear combination of wavelet basis functions. Nowadays, it is highly preferred over other joint time-frequency transformations in civil engineering applications. Its main advantage lies in its capability of revealing data aspects that may be missed by other analysis techniques (e.g., trends, breakdown points, and discontinuities). This is possible by selecting a suitable basis function to execute the analysis. Consequently, it allows the transformation to only change in time extension but not in shape. Those changes in time extension should conform to the corresponding analysis frequency of the basis function.

There are two types of Wavelet transforms: the continuous and discrete versions. The *Continuous Wavelet Transform* (CWT) of a function $x(t)$ of a real variable is defined as a function of two variables, $X_w(a,b)$. It is the convolution of $x(t)$ and a scaled and shifted version of a mother wavelet, $\psi(x)$. The wavelet coefficients, $X_w(a,b)$, are a measure of the similarity between the shifted mother wavelet and the signal at the time position b and scale a, which can be related

with frequency (Kijewski and Kareem, 2003). Mathematically, the CWT is given by equation (2.26)

$$X_w(a,b) = \frac{1}{\sqrt{a}} \int_{-\infty}^{\infty} x(t)\, \psi^* \left(\frac{t-b}{a} \right) dt \quad \begin{cases} a \in [0, \infty) \\ b \in (-\infty, \infty) \end{cases} \tag{2.26}$$

where b is the time translation and a is the dilation of the wavelet. The function ψ^* denotes the complex conjugate of ψ. It can be shown that the Wavelet transform provides information similar to the STFT but with the additional special properties of wavelets. These improved features show up at the resolution in time at higher analysis frequencies of the basis functions. According to the Heisenberg's Uncertainty Principle of signal processing, defined by equation (2.27), the higher the required resolution in time, the lower the resolution in frequency results.

$$\Delta t\, \Delta \omega \geq \frac{1}{2} \tag{2.27}$$

Heisenberg's Uncertainty Principle states that a function cannot be arbitrarily well localized both in time and frequency. In simple terms, increasing the localization in time can be achieved only at the expense of decreasing localization in frequency. Depending on the extension of the selected analysis window, the resolution in time and frequency will vary. Thus, when Δt is large, a bad time resolution but good frequency resolution is obtained. Also, a large scaling factor is required for representing low frequencies. Exactly the opposite happens when Δt is chosen small. Figure 2.10 shows differences in time resolution at ascending frequencies for the STFT and the Wavelet transform.

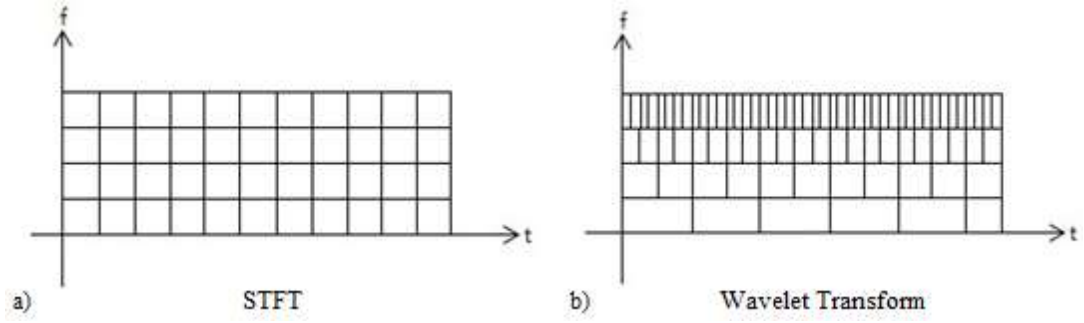


Figure 2-10: Comparison of time resolution between the (a) STFT and the (b) Wavelet Transform

Because of the variation in time resolution, edge effects in wavelet analysis become a critical point because they can significantly affect the quality of the wavelet coefficients. Those wavelet

coefficients can be illustrated on a wavelet map where the response function $x(t)$ can be represented in the time-frequency domain. In order to estimate IFs embedded in the signal, a ridge in the time-frequency plane should be identified. This can be done by locating the local maxima in $X_w(a, b)$ at each instant (Montejo, 2011). Also, analogously to other transforms, the CWT has an inverse version to reconstruct the signal $x(t)$ from its coefficients $X_w(a, b)$. The inverse CWT is defined as the equation (2.28):

$$x(t) = \frac{1}{C_\psi} \int_0^\infty \int_{-\infty}^\infty \frac{1}{\sqrt[5]{a}} X_w(a, b) \psi\left(\frac{t-b}{a}\right) db\, da \tag{2.28}$$

where C_ψ is the wavelet admissible constant satisfying $0 < C_\psi < \infty$. The admissibility criterion is defined by the equation (2.29):

$$C_\psi = \int_0^\infty \frac{|\Psi(\omega)|^2}{|\omega|} d\omega < \infty \tag{2.29}$$

where the term $\Psi(\omega)$ is the Fourier transform of the mother wavelet $\psi(t)$. This constraint is imposed so that the inverse Wavelet transform can exist.

The Discrete Wavelet Transform (DWT) is any transform in which the wavelet implemented is discretely sampled. As explained by Lee and Yamamoto (1994), in the discrete domain the scale and shift parameters are discretized as $a = a_0^m$ and $b = nb_0$ respectively. Consequently, the analyzing wavelets are also discretized as:

$$\psi_{m,n}(t) = a_0^{-m/2}\, \psi\left(\frac{t - nb_0}{a_0^m}\right) \tag{2.30}$$

where m and n are integer values. As a result, the DWT and its inverse transform are respectively defined by equations (2.31) and (2.32) as:

$$X_w(m, n) = \int_{-\infty}^{\infty} x(t)\, \psi_{m,n}(t)\, dt \tag{2.31}$$

$$x(t) = K_\psi \sum_m \sum_n X_w(m, n)\, \psi_{m,n}(t) \tag{2.32}$$

where K_ψ is a constant value for normalization. The main reason for its use is that, according to Daubechies (1992), in order to reconstruct the signal $x(t)$ it is unnecessary to use the full domain of $X_w(a, b)$. It is enough to use the discrete values of the dilation and translation parameters. An advantage of this transform is its temporal resolution capturing both frequency and time location information. By applying the DTW, a signal $x(t)$ can be represented by its approximations (A) and details (D) at different decomposition levels (j) as shown in equation (2.33). The low frequency (high scale) components of the signal are contained in the approximations term and the high frequency (low scale) components are contained in the details term.

$$x(t) = A_j + \sum_{i \leq j} D_i \tag{2.33}$$

This represents an advantage of the DWT because it is capable to segregate the discontinuities contained in the detail components embedded in the structural response from the original signal. With this information, it is possible to detect and locate structural damage.

Consequently, low frequency and high frequency analyses can be performed by implementing the Wavelet transform. By low frequencies it is meant in the range representative of the structure's modes of vibration. On the other hand, high frequencies are close to the signal's Nyquist frequency, which is defined as one half the sampling rate of the discrete signal. Both analyses aim to detect shifts in the vibration frequencies of a structure and to detect irregularities in the high frequency response of the structure. Todorovska and Trifunac (2007) analyzed inter-story drifts and frequency shifts using low frequency analyses on the Imperial County Services building damaged in 1979 after the M6.6 Imperial Valley earthquake. They found that a decrease in the structure's frequencies correlated well with the observed damage. This is due to the damaging process that a structure suffers during an earthquake, which causes permanent loss of stiffness while at the same time decreases its fundamental frequency (Michel and Gueguen, 2010). In a similar fashion, the implementation of high frequency analysis with the DWT allows the detection of anomalies in the structure's response because abrupt changes in stiffness are reflected on the high frequency range of the response signal.

2.5 Performance and Nonlinear Behavior of Structures

Civil structures such as buildings, bridges, and dams must be designed to withstand the destructive lateral forces generated from natural events such as earthquakes and hurricanes. Similarly, lateral forces generated from man-made events, such as explosions and impacts, can be even more destructive to these infrastructure systems. It is for that reason that structural designs must account for the inelastic deformations that a structure will undergo during extreme dynamic events. Current building codes prescribe the use of linear-elastic structural analysis procedures for the design of buildings and other structures. The inelastic effects in structural elements are accounted by providing them with enough ductility so that they can withstand forces that exceed their elastic strength limits while dissipating the energy imparted by the strong dynamic input forces without reaching their ultimate capacities. However, linear-elastic analyses do not provide a realistic scenario for aged existing structures, or for the assessment of new structures with asymmetrical configurations or that may have construction flaws or material deficiencies. In these and many other cases, it is necessary to evaluate the expected performance of the structure when subjected to probable dynamic expected loads, such as probable design earthquakes. The overall building behavior can be measured in terms of structural performance. For instance, strong dynamic excitations, such as earthquakes, can cause a structure to experience four different types of damages: total collapse, partial collapse, failure and falling of building components, and blocking of entry-exit routes, which prevents the execution of evacuation and rescue procedures.

In general, the earthquake performance of a structure can be related to the levels of damage in which the structure incurred. These damages are not only in structural elements but also in non-structural components. The United States Federal Emergency and Management Agency (FEMA) and the American Society of Civil Engineers (ASCE) periodically publish updated editions of their FEMA 356 pre-standard and ASCE41 standard, respectively, in which they provide information on the performance levels of structures. These performance levels describe the expected structure state after earthquake events and are summarized as follows.

1. **Operational (non-structural)**: Very light overall damage is observed in the structure, if existent. There is no permanent drift and the structure substantially retains its original strength and stiffness. Minor cracking of facades, parapets, and other non-structural components as well as structural elements may occur. All the important systems for normal operation are functional.

2. **Immediate Occupancy (IO)**: The post-earthquake damage is very limited, if existent, because the structure is expected to mainly, if not completely, behave elastically. It is expected to observe little to none yielding of steel, concrete cracking, and non-structural damage. As a result, the basic vertical and lateral force resisting systems in the structure retain nearly all their pre-event strength and stiffness. Therefore, the risk of life-threatening injuries due to structural damage is very low. Some minor damage is observed in the structure.
3. **Life Safety (LS)**: Moderate overall damage is observed in the structure. It has suffered significant damage but some margin against either partial or total collapse remains. Damage is limited in structural and non-structural elements so as to minimize the risk of life-threatening injuries or casualties to a low-level and to keep essential routes accessible. It should be possible to repair the structure although unpractical for its elevated costs. The structure does not have an imminent collapse risk; however, permanent or temporary structural repairs should be done.
4. **Collapse Prevention (CP)**: Severe overall damage is observed in the structure. There are damaged structural and non-structural components. Structural elements continue to support gravity loads without any margin against collapse. Structural deformations and forces must be limited to the onset of significant strength and stiffness degradation to minimizing the risk of partial or total building collapse.

Although earthquake-resistant design is based on linear-elastic analyses, modern building codes addresses earthquake performance objectives implicitly by providing design specifications that drives the structure to behave as listed below when subjected to earthquakes of different intensities.

- **Low-intensity**: The structure is expected to resist without *any* damage
- **Moderate-intensity**: The structure is expected to resist without *structural* damage but may experience *non-structural* damage.
- **High-Intensity**: The structure is expected to resist an earthquake of equal intensity as the strongest previously experienced earthquake or as the probable expected earthquake for its site characteristics without collapse. However, it is also expected to haver non-structural damage.

Hence, to assess the complete structure performance, more advanced analyses should be implemented beyond linear-elastic procedures. A nonlinear analysis results in a nonlinear relation

between the applied forces in the structure and its overall displacement. Contrary to a linear-elastic analysis where the stiffness matrix remains constant throughout the entire analysis, in a nonlinear analysis the global stiffness matrix is constantly changing due to the following nonlinear effects generated in the structure elements.

- **Geometric nonlinearities**: Refers to the changes in the structure's geometry as it deforms. These geometrical changes can be represented as large deformations and are considered in equilibrium as well as in constitutive equations.
- **Material nonlinearities**: Refers to the nonlinear behavior observed exclusively by the material due to a deformation state.
- **Contact nonlinearities**: This type of nonlinearity can occur when kinematic degrees of freedom are restricted on their movement.

Therefore, nonlinearities in structural systems are likely to occur at any moment and under different load scenarios. For this reason, there are two different analysis procedures to account these nonlinear effects in structures subjected to strong dynamic loads and which may be used for rehabilitation purposes or design upgrades.

1. **Nonlinear Static Analysis**: It is widely known as *pushover* analysis. In it, the structure is subjected to gravity loading and a monotonic force-controlled or displacement-controlled lateral load pattern which continuously increases through elastic and inelastic behavior until an ultimate condition is reached. The FEMA 356 provides specific procedures for its implementation. The two analysis methods are explained as follows.
    a. *Force-controlled*: The structure is pushed to a target force level and its performance based on displacement (or deformation) is measured.
    b. *Displacement-controlled*: The structure is pushed to a target displacement while the structural response is measured.

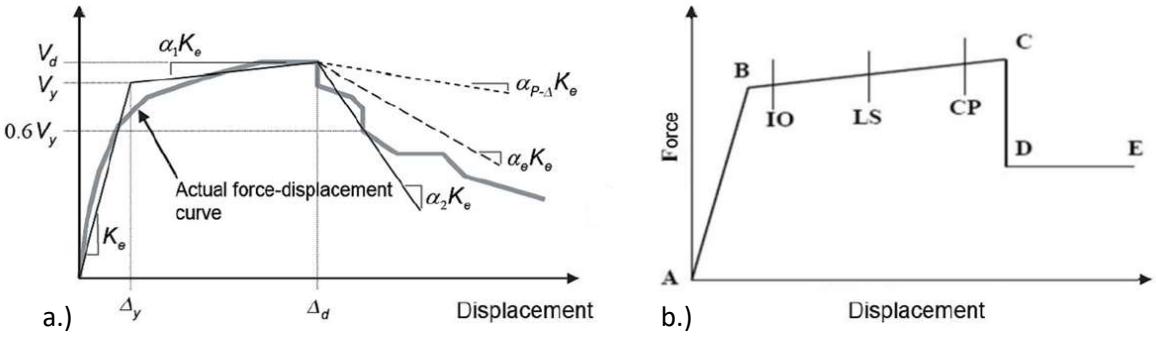


Figure 2-11: Pushover curves. a) Static Pushover curve with backbone (FEMA,2005). b) Idealized pushover curve

Figure 2-11a shows a static pushover curve and its idealized backbone curve. In Figure 2-11b, the performance objectives are located along the idealized curve.

2. **Nonlinear Dynamic Analysis**: The structure response is computed using inelastic time history dynamic analysis to determine the distribution of forces and corresponding internal forces and system displacements.

2.5.1 Inelastic Models for Structural Components

The structural components of a structure model should possess constitutive properties that make them behave in the most realistic manner by accounting for the inelastic effects that the imparted loads will generate in them. There are five idealized inelastic model types for simulating the inelastic response of beam-columns and wall elements. These models can be divided into two groups based on plastic distribution assumptions: concentrated and distributed plasticity. Figure 2-12 shows the five idealized models.

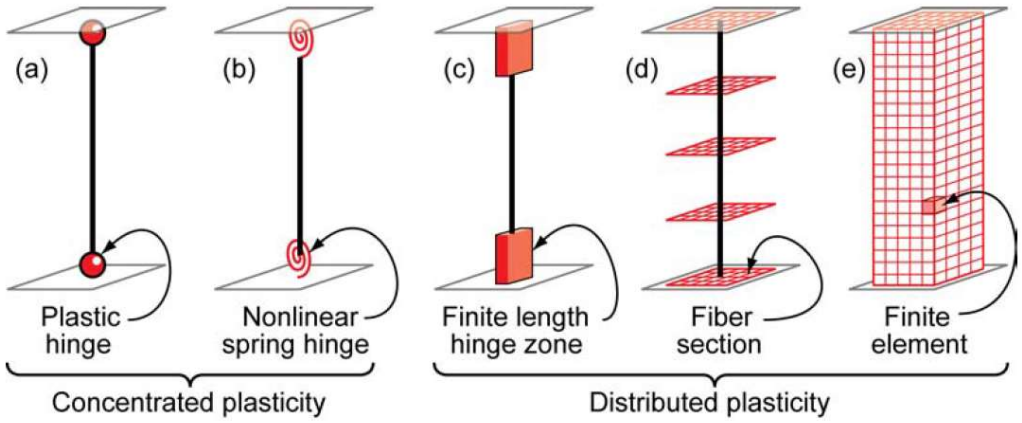


Figure 2-12: Idealized models of beam-column elements (Deierlein et al., 2010)

Concentrated plasticity models are the simplest and they assume that plasticity only occurs at the ends of each element. For this purpose, moment-rotation relationships are assigned to zero-length hinges at the extreme ends. On the contrary, distributed plasticity models consider a detailed variation of stress and strain through the section and along each member. The characteristics of the models in Figure 2-12 are summarized below.

1. **Concentrated Plasticity Models**
    a. *Plastic Hinge*: Model in which a rigid-plastic hinge with defined moment-rotation properties is assigned at the ends of the elements.

b. *Nonlinear Spring Hinge*: Model in which an inelastic spring with hysteretic properties is assigned at the ends of the elements.

2. Distributed Plasticity Models

c. *Finite Length Hinge Zone*: Model in which hinge zones are defined at the member ends. With the assumption that plane sections remain plane, moment-curvature relationships or explicit fiber-section integration are defined in the inelastic hinge zones. The hinge length is determined from the sectional moment-curvature characteristics and the axial force and moment gradient. This method facilitates the computation of hinge rotations in addition to better represent the spread of yielding along the hinge length.

d. *Fiber Section*: This method distributes plasticity through the cross section and along the length of the structural element by numerical integration. In order to capture nonlinear hysteretic axial stress-strain characteristics, uniaxial material models are defined throughout the cross section. Stress resultants (axial force and moments) and incremental moment-curvature obtained by the integration of the material fibers with the assumption that plane sections remain plane. The distributed fiber formulations do not generally report plastic hinge rotations, but instead report concrete and steel cross section fibers strain.

e. *Finite Element*: This model discretizes the element cross section into small finite elements along its length. These elements have nonlinear hysteretic constitutive properties with numerous input parameters. It is the most versatile level of modeling but the most computationally challenging.

2.5.2 Hysteretic Nonlinear Models

When subjected to cyclic loading, structures experience deformation responses that are characteristic of the system geometry and essentially of the material of its components. The cyclic behavior of structural elements and their ability to dissipate the input energy in the system through its deformation can be described by the material hysteretic property. This property refers to a hysteretic cycle that indicates material nonlinearity in the form of loops. In a hysteresis plot, the translational or rotational deformation is the independent variable and a strength-based parameter is plotted against the physical oscillation of the system. This property is convenient for the

dynamic response characterization under time-history inputs. Figure 2-13 displays a typical hysteresis loop with its backbone curve.

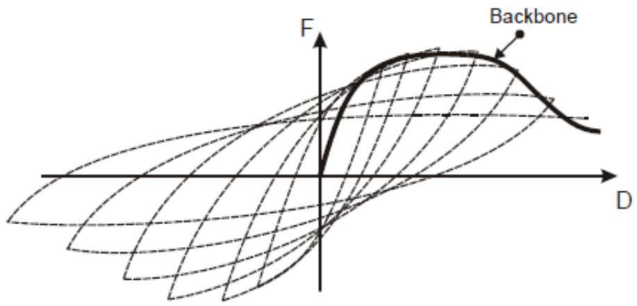


Figure 2-13: Nonlinear hysteresis loop curve with backbone

It is possible to notice the post-yielding typical behavior of a structural system or element. The strength and stiffness values change with respect to their initial relationship and continue to do so with additional cycles. The maximum strength value defined by the backbone curve is mainly caused by the system's hardening. Beyond that point, its strength and stiffness begin to decrease due to the system's degradation. As a result, the system's ductility can be estimated from its ultimate deformation value, that maintains a post-peak strength. Moreover, the energy dissipation in the system can be estimated by the shape pattern of the hysteresis loops. The wider the area enclosed in the loops, the more energy is being dissipated. In contrast, less energy is dissipated as the enclosed area by the hysteretic loops get more pinched. An illustration of the hysteresis stages is presented below in Figure 2-14.

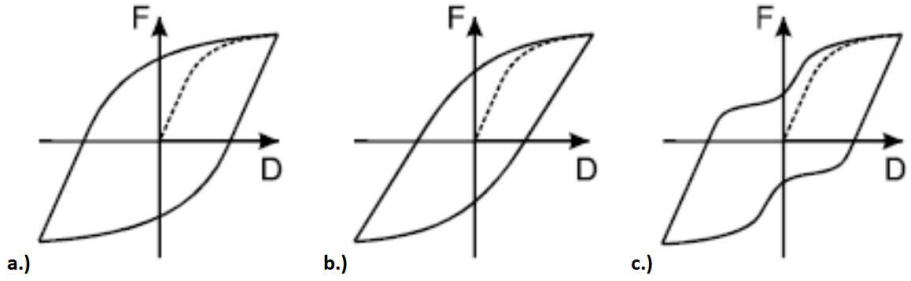


Figure 2-14: Hysteresis stages. a) Hysteresis loop without degradation. b) Hysteresis loop with degradation. c) Pinching effect

There are different hysteresis models that engineers use to better estimate the dynamic behavior of structural systems and hence provide better assessment of retrofit and rehabilitation solutions as well as for improvement of new designs before their construction. Many of those models are predefined in modern computational tools and software for the ease of analysis. However, the selection of a model depends on the structure material characteristics and what the engineer seeks

to observe or to specifically model. A list of commonly used hysteresis models in structural analysis is presented below. These models are available in SAP2000®, ETABS®, and CSIBridge®.

1. **Elastic Hysteresis Model**: This model follows a nonlinear elastic behavior. Therefore, loading and unloading of the material always occurs along the backbone curve. Consequently, no energy is dissipated. This hysteretic model is plotted in Figure 2-15.

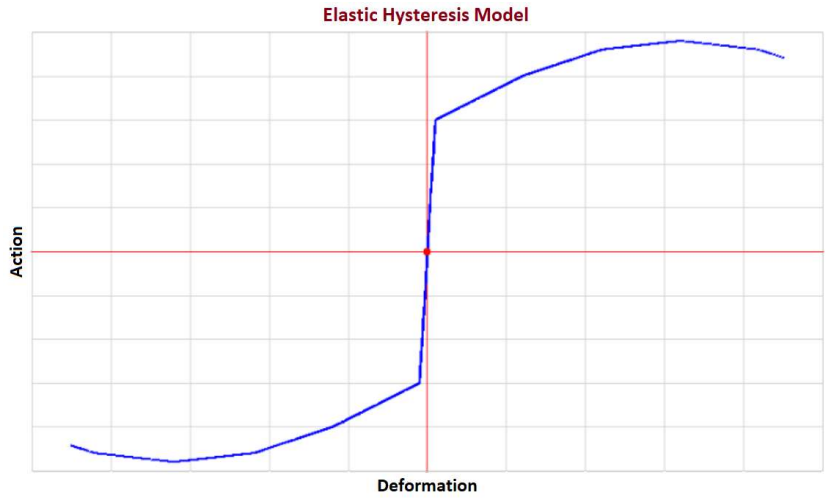


Figure 2-15: Elastic Hysteresis Model

2. **Kinematic Hysteresis Model**: It is based on kinematic hardening behavior. This model dissipates a significant amount of energy and is best suitable for use with metals or other ductile materials. This model forms the basis for other commonly used models. This hysteretic model is plotted in Figure 2-16.

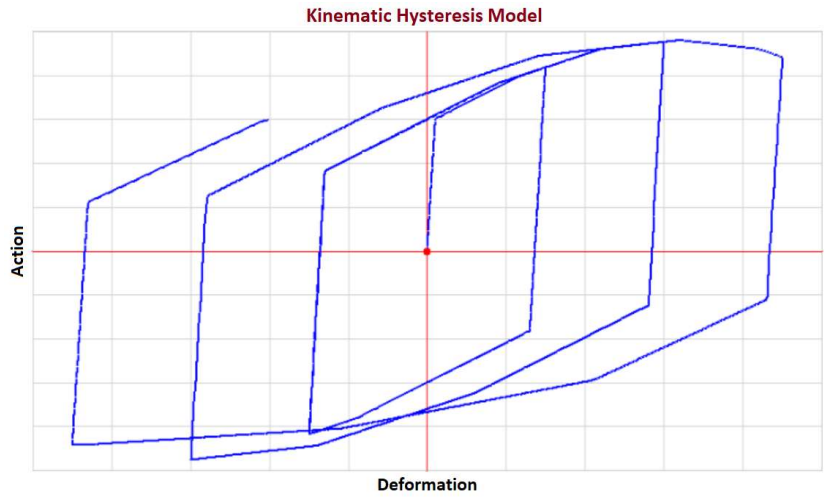


Figure 2-16: Kinematic Hysteresis Model

3. **Degrading Hysteresis Model**: It is similar to the Kinematic model. However, to account for decreasing energy dissipation and for unloading stiffness with increasing plastic deformation it uses a degrading hysteretic wool, as opposed to the kinemetric hysteretic model. This hysteretic model is plotted in Figure 2-17.

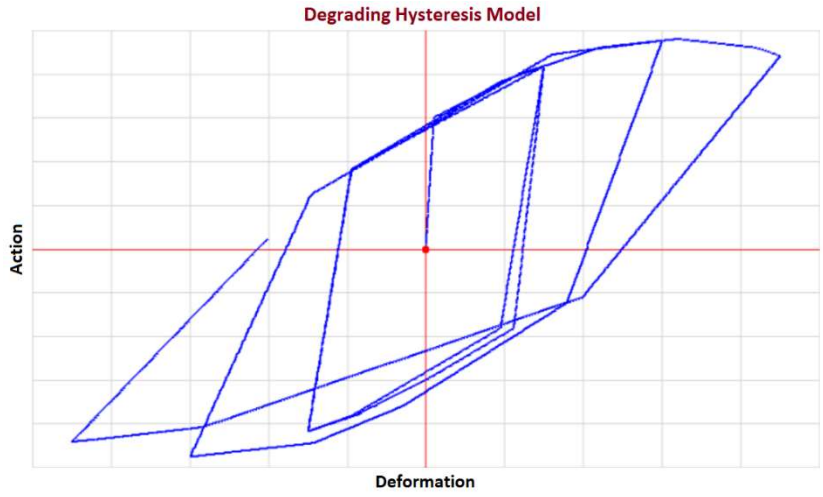


Figure 2-17: Degrading Hysteresis Model

4. **Takeda Hysteresis Model**: It is similar to the Kinematic model. However, it uses a degrading hysteretic loop model based on the Takeda model, described in Takeda, Sozen, and Nielsen (1970). Less energy is dissipated with this model with the Kinematic model. It is a simple model that is best suitable for reinforced concrete. This hysteretic model is plotted in Figure 2-18.

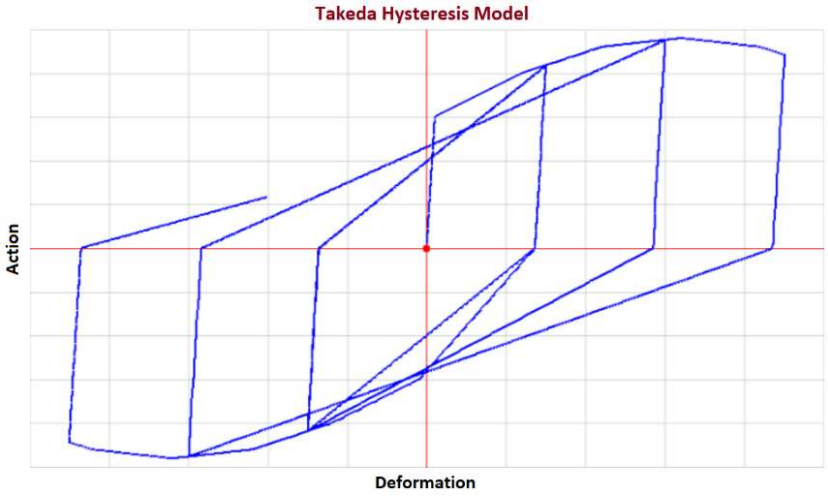


Figure 2-18: Takeda Hysteresis Model

5. **Pivot Hysteresis Model**: It is similar to the Takeda model with additional parameters to control the degrading hysteretic loop. Its unloading and reverse loading behavior tend to be directed toward specific "pivot" points in the action-deformation plane. This characteristic makes it particularly well-suited for reinforced concrete but not for unreinforced concrete. Its most common use is for moment-rotation analysis. The model is fully described in Dowell, Seible, and Wilson (1998). This hysteretic model is plotted in Figure 2-19.

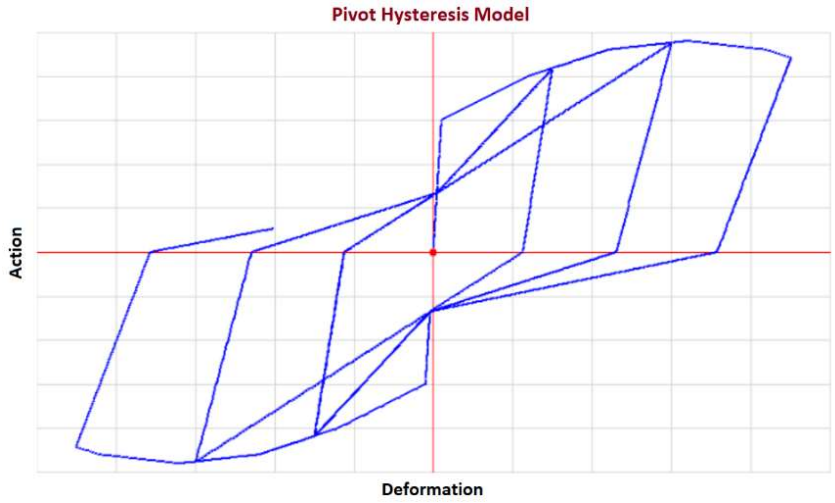


Figure 2-19: Pivot Hysteresis Model

6. **Concrete Hysteresis Model**: As opposed to previous models, the use of this model is intended to be for unreinforced concrete and similar materials. In it, the tension and compression behavior are different and independent. The primary purpose of this model is to describe axial behavior, although it can be applied to any degree of freedom. In this sense, the point with the largest absolute value of stress or force is considered to be in compression regardless of its sign. It is possible to represent a tension-only material that behaves similar to unconfined concrete in compression. This hysteretic model is plotted in Figure 2-20.

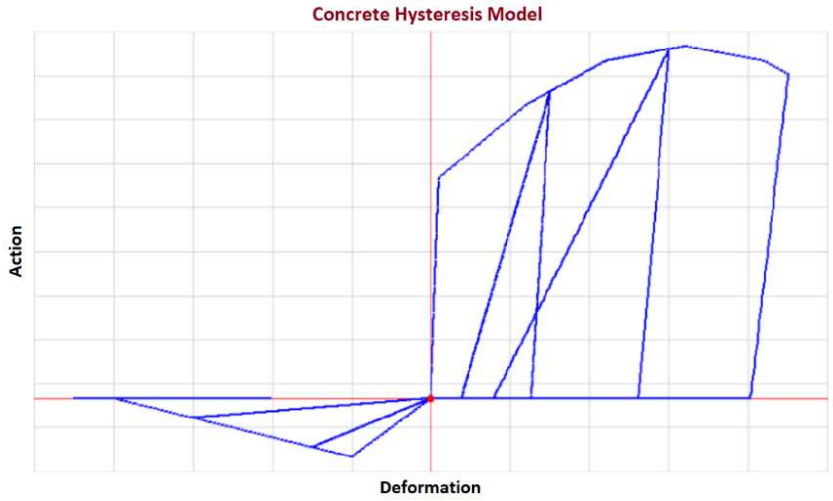


Figure 2-20: Concrete Hysteresis Model

7. **BRB Hardening Hysteresis Model**: It is similar to the Kinematic model with the variation that it accounts for the increasing strength caused by plastic deformation. This causes the hysteresis loops, and hence the backbone, to progressively grow in size. It is primarily intended for describing axial behavior, although it can be applied to any degree of freedom. During monotonic loading degradation does not occur. However, upon load reversal, the unloading and reverse loading curve for the opposite direction is modified in accordance to a hardening factor computed for the last deformation increment. This hysteretic model is plotted in Figure 2-21.

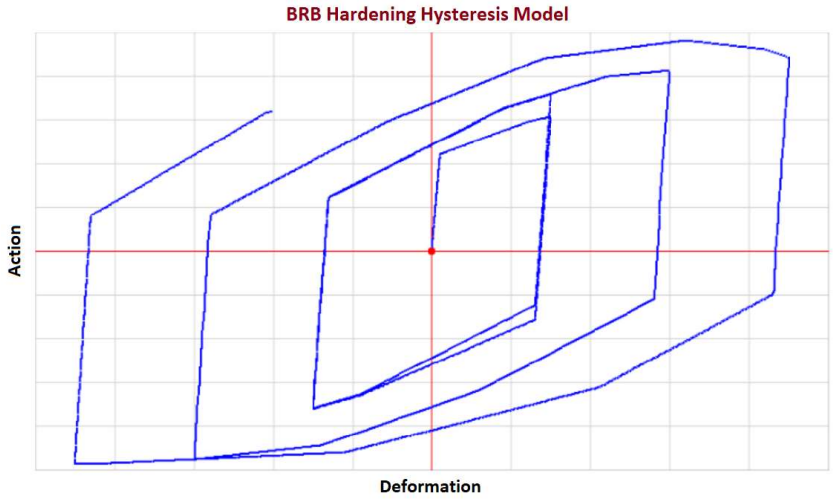


Figure 2-21: BRB Hardening Hysteresis Model

8. **Isotropic Hysteresis Model**: In this model, both directions increase simultaneously because plastic deformation in one direction pushes the curve in the other direction away from it. Here the backbone curve does not exhibit an increasing strength. The unloading and reverse loading action follows a path parallel to the elastic line. This occurs until the magnitude of the action (e.g. force or stress) in the reverse direction equals that of the backbone reverse direction. It then continues horizontally and secant to the backbone curve. This model dissipates the most energy of the presented earlier. This hysteretic model is plotted in Figure 2-22.

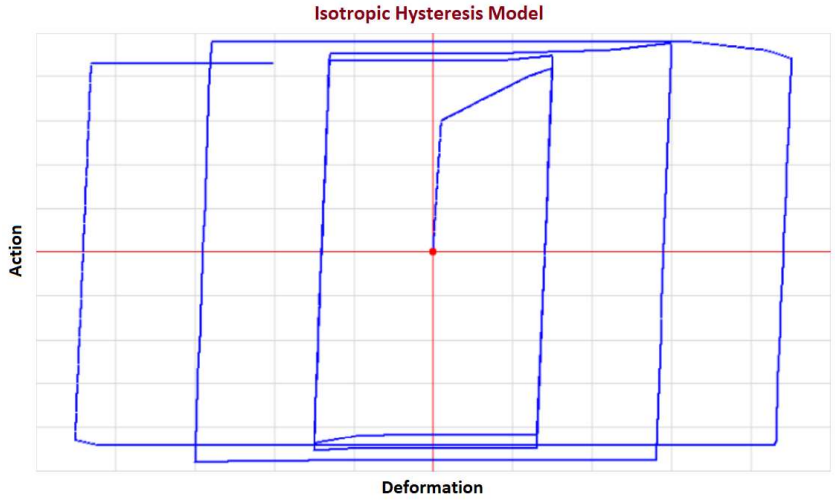


Figure 2-22: Isotropic Hysteresis Model

CHAPTER 3. STRUCTURAL SYSTEMS STUDIED

3.1 Ponce Highway Bridge Structure

Highway bridge No. 2348, shown in Figures 3-1 and 3-2, is a reinforced pre-stressed concrete bridge in the municipality of Ponce, PR and is part of the San Juan – Ponce PR-52 highway. Its exact location is $17°59'11.84"N$ and $66°36'33.24"W$, which is at $0.81\ miles$ normal from the southern coast of the island. It was designed by Guillermety, Ortiz & Associates Consulting Engineers in 1989 and its construction concluded in 1992. It is part of the National Highway System and is administered by the Puerto Rico Highway Authority under the Department of Transportation and Public Works.



Figure 3-1: Ponce Highway Bridge [ID: 2348] (Photo by the author)



Figure 3-2: Aerial view of Ponce Highway Bridge [ID: 2348] (Image from Google Earth Pro)

3.1.1 Bridge Description

The bridge has two spans with three lanes in each direction. It is composed by 18 AASHTO Type IV pre-stressed concrete beams supporting a 7.5 in thick skew concrete slab of 123.5 ft of width and 189 ft of length. The beams are connected at the middle of the bridge to a cap beam with a base of 4 $ft - 7$ in by 4 ft of height and length of 127 ft. The cap beam is supported by 8 columns of 3.6 ft of diameter with varying heights of 5 ft to 6 ft due to the bridge's camber of 2.81% as shown in Figures 3-3 and 3-4.

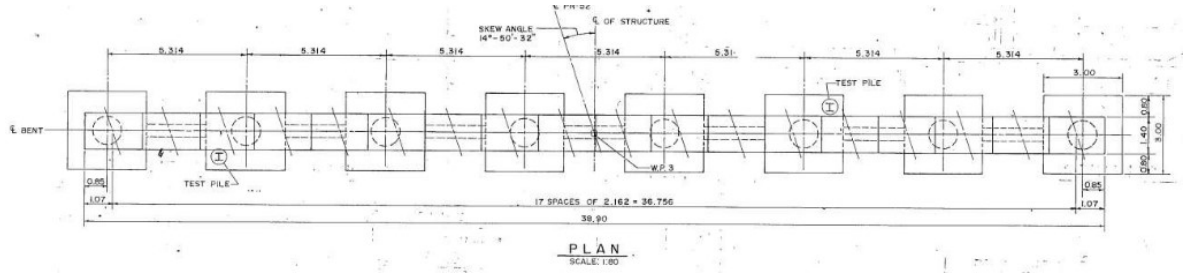


Figure 3-3: Schematic plan view of the eight columns supporting the bridge

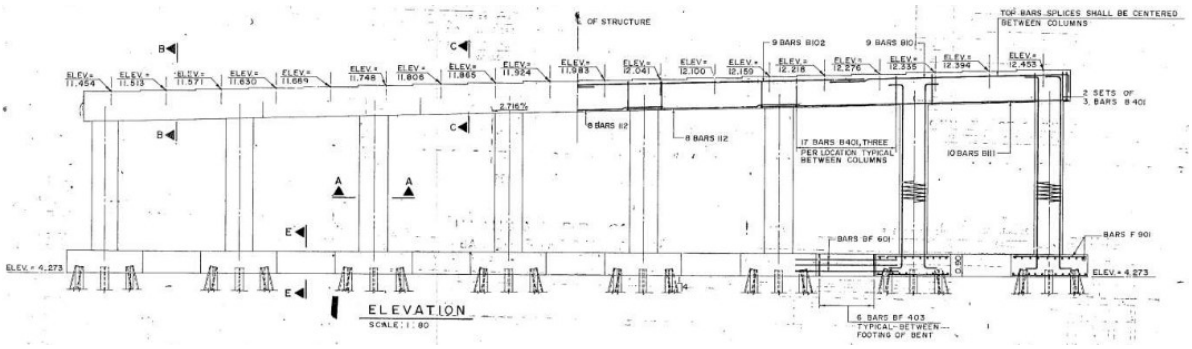


Figure 3-4: Schematic elevation view of the eight columns supporting the bridge

The bridge was designed to meet the traffic requirements of the highway. The design designations for the bridge design are outlined in Table 3-1.

Table 3-1: Traffic requirements for Ponce Highway Bridge [ID: 2348] design

Requirement	Designation
Control of Access	Full
ADT (2010)	30,931 vehicles
DHV	3,093 vehicles
D	50%
T	12%
V	70 mph

3.1.2 Bridge Instrumentation

Ponce Highway Bridge [ID: 2348] was instrumented in October of 2001. Its instrumentation consists of 12 sensor channels of Kinemetrics EpiSensor units. These sensors are distributed throughout the bridge structure at key locations, as shown in the bridge's instrument schematic layout shown in Figure 3-5.

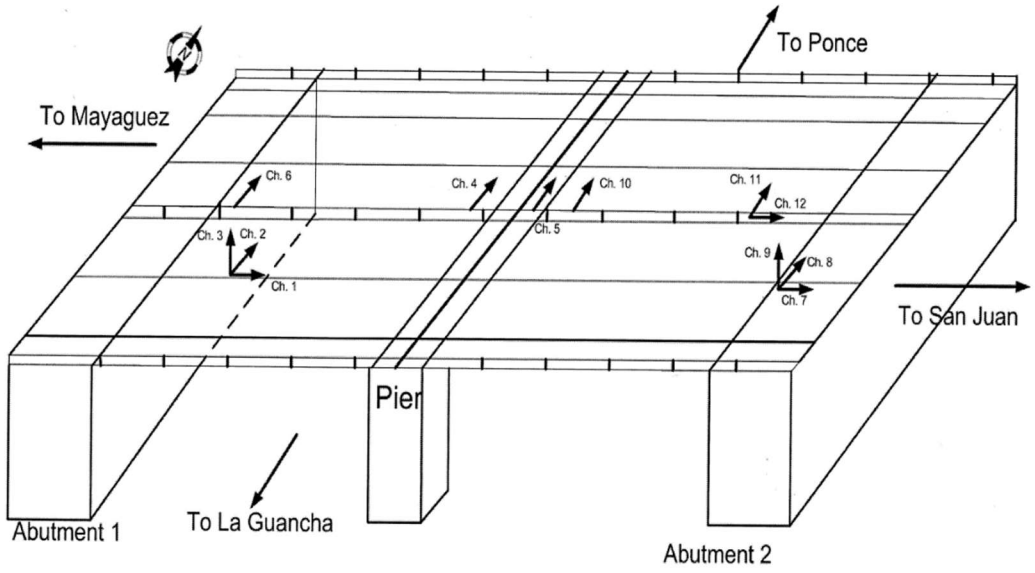
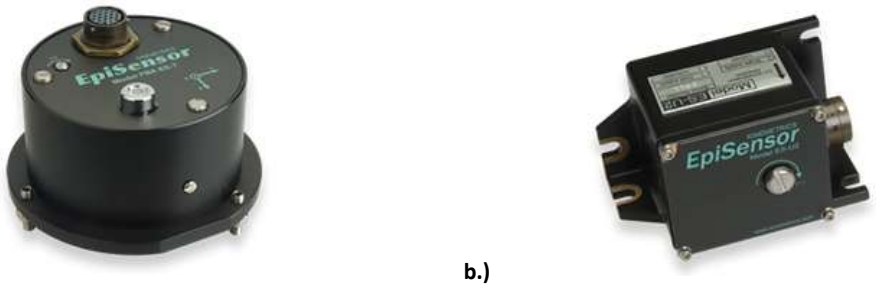


Figure 3-5: Schematic drawing with sensors layout

A triaxial unit is installed at each of the abutment walls at about a third of its height. These sensors (channels 1-3 and 7-9) account for longitudinal and transverse absolute and relative movements of the bridge extreme supports as well as any vertical movement in which the bridge may incur. These two triaxial sensor units are Kinemetrics EpiSensor ES-T model, which consists of three EpiSensor Force Balance Accelerometer modules mounted orthogonally in one small package as shown in Figure 3-6a. In addition, five uniaxial sensors (channels 4-6 and 10-11) account for transverse movements and one sensor (channel 12) accounts for longitudinal movements. These sensors are Kinemetrics EpiSensor ES-U2 model and is shown in Figure 3-6b.



a.) b.)

Figure 3-6: Kinemetrics EpiSensor accelerometers. a.) EpiSensor ES-T model; b.) EpiSensor ES-U2 model

3.2 High-Rise Residential Building

PRILA Condominium is a 20 stories residential building located in a densely populated coastal zone in the Puerto Rico metropolitan area. Its physical address is 70 Kings Court St., Condado, San Juan, PR and its exact location is $18°27'12"N$ and $66°03'42"W$, which is $500\ ft$ off the northern coast of the island. It was designed in 1963 by SAGMAC of Puerto Rico, Inc. -Engineers & Architects- and its construction concluded in the mid 1960's. The multi-story structure is shown in Figure 3-7.

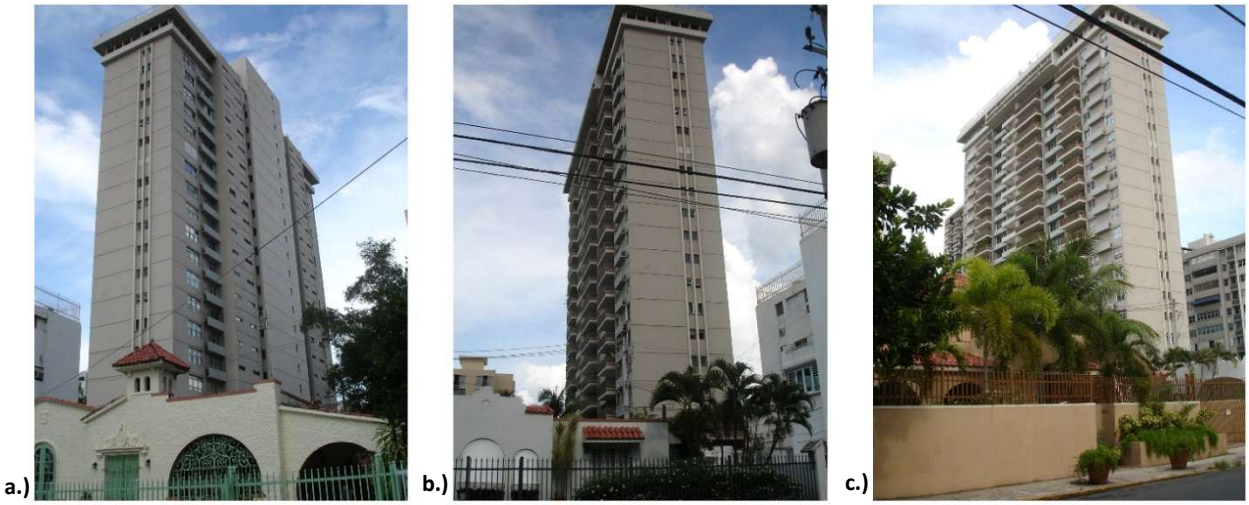


Figure 3-7: PRILA Condominium. a.) South view. b.) Side (west) view. c.) North view.

3.2.1 PRILA Condominium Description

PRILA is a reinforced concrete building with plan dimensions of $42' - 11"$ by $158' - 4"$ and a total height of $184\ ft$ above the ground. Its main force resisting system consists of a parallel shear walls arrangement with their strong axes parallel to the building's short direction. This arrangement is illustrated in Figure 3-8. The building has a shear wall area to floor area ratio of 3.72% in the $N - S$ direction and of 1.16% on the $E - W$ direction.

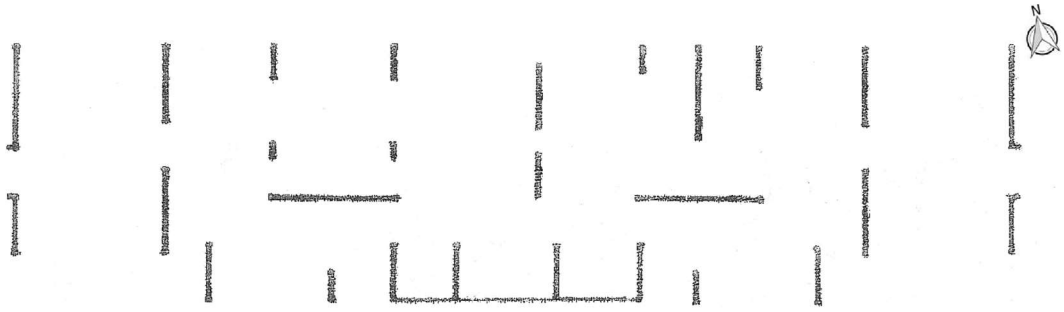


Figure 3-8: Shear walls layout in PRILA's typical stories

The 20^{th} story is the building's penthouse and above it there is a two-story roof top extension of the elevator core used as machinery and storage rooms. A geotechnical study of 7 borings determined that the structure was built on a predominantly sandy soil with traces of silt and clay and having a bearing capacity of $5{,}000\ psf$ at $15\ ft$ below natural grade. Its foundation system consists in a raft foundation with beams with a concrete compression strength of $3{,}000\ psi$ and steel reinforcement with a yield strength of $40{,}000\ psi$. The steel reinforcement arrangement in the mat consists in #6 rebars spaced at 12 in. Figure 3-9 shows the extent of the raft foundation.

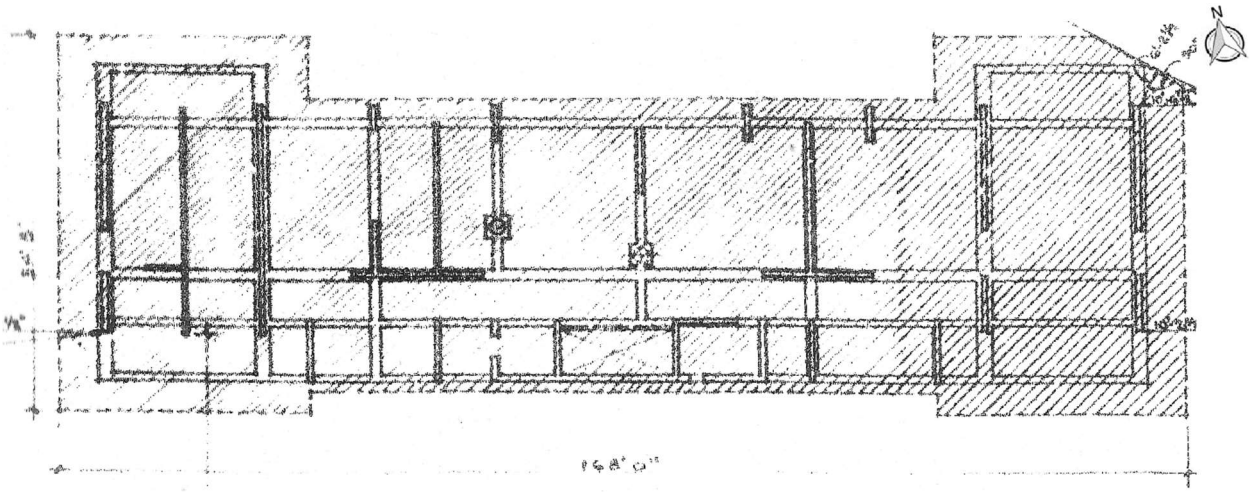


Figure 3-9: Footings location

3.2.2 Building Instrumentation

The PRILA Condominium was instrumented in October of 2012. Its instrumentation consists of 36 sensor channels of Kinemetrics EpiSensor units, shown in Figure 3-6. These accelerometers are distributed throughout the height of the building following the instrumentation model (e) and (f), as shown in Figure 2-1. The selected combination model possesses the characteristics outlined below.

- The instrumentation for this configuration typically includes at least 12 sensors distributed on three or more levels of the building.
- Three sensors are installed on each level, with a reference free-field station outside the building.
- Three sensors at the roof level to measure the translational and torsional motions.
- Extensive horizontal and vertical cablings are required to provide common recording of all channels in the building.

In addition to the building instrumentation, a free-field station consisting of a triaxial sensor accelerometer was installed at Robinson School in San Juan, PR. Figure 3-10 shows a schematic drawing of the south and east views of the PRILA Condominium with the location of the installed sensors throughout the height of the building.



Figure 3-10: Schematic drawing of PRILA Condominium's south and east views with the installed sensors' location

By considering the number of available sensors and following the instrumentation models as guidelines, a 3D computational model was created to perform modal analysis and obtain the optimal placement location for all sensors. This will be further explained in the next chapter.

CHAPTER 4. ANALYTICAL STRUCTURAL MODELS

4.1 Mathematical model for the Ponce Highway Bridge

The end goal of the system identification process is to create mathematical models of physical systems or to calibrate existing ones from experimental input-output data. This allows for increased accuracy in the behavior prediction of the systems studied. In this study, a mathematical model was initially developed to later predict the dynamic behavior of the highway bridge when subjected to different in-service horizontal vibration scenarios. The 2-span bridge was modeled as a single degree of freedom (SDOF) system using the equivalent mass and stiffness method. A simplified schematic drawing of the bridge's analytical model and boundary assumptions is presented in Figure 4-1.

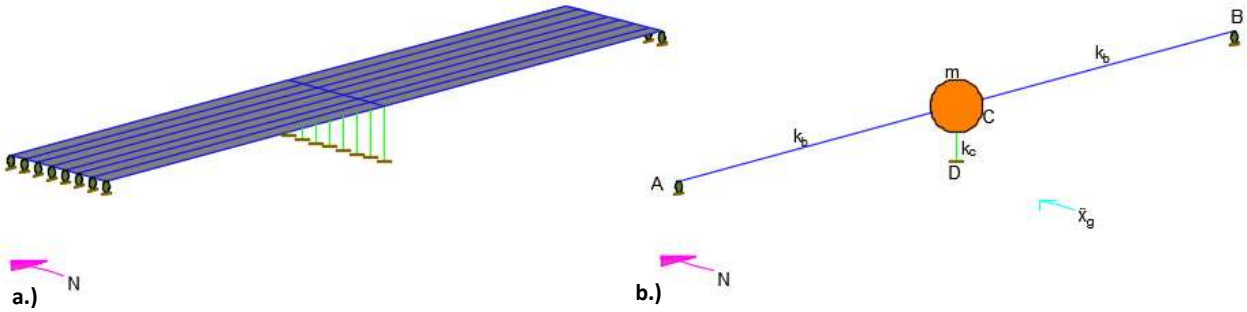


Figure 4-1: a.) Simplified drawing of the bridge structure. b.) Schematic description of the bridge's equivalent analytical model

The bridge physical structure was simplified as a lateral force resisting system composed of two equivalent beams whose outer ends are pinned to the abutments and their inner ends are connected at the middle of the bridge's total length by a pinned connection. Similarly, an equivalent column with fixed base is assumed to be connected at that middle pin connection supporting the two equivalent beams.

In vibration theory, the dynamic behavior of a SDOF system can be mathematically described by the second-order differential equation shown in (4.1).

$$m\ddot{u}(t) + c\dot{u}(t) + ku(t) = F(t) \tag{4.1}$$

In this SDOF dynamic model, the concentrated mass, m, represents part of the structure's total mass, k is a stiffness constant that corresponds to an equivalent spring, and c is a damping constant, which can be related to a simple linear viscous damping model, in which the damper's force is proportional to the velocity of the system's mass. An illustrated description of the development of the bridge analytical model is shown in Figure 4-2. It explains how the bridge's lateral force resisting system can be assumed to behave as a damped simple oscillator subjected to acceleration inputs.

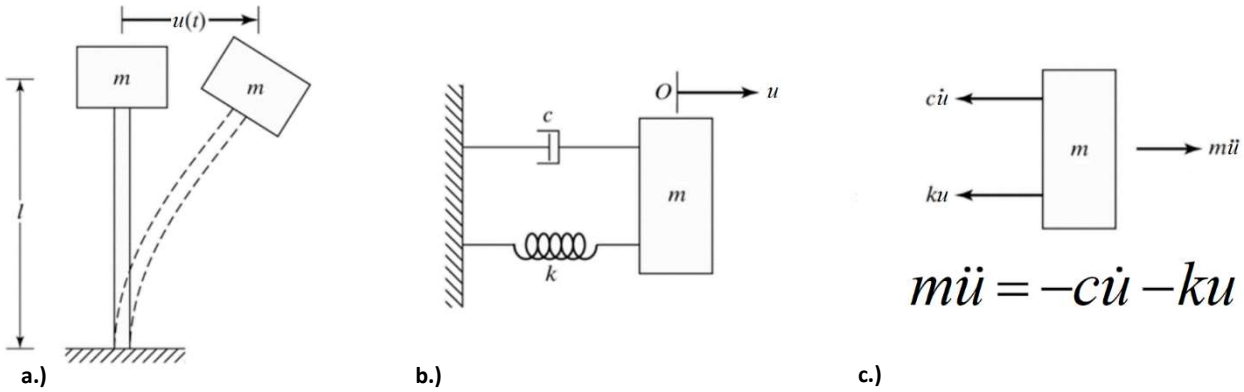


Figure 4-2: Sequence for analytical model development. a.) Simplified drawing of bridge's lateral system. b.) Damped simple oscillator assumption. c.) Free-body diagram of analytical model

The bridge dimensions and structural properties used for the development of the model were extracted from the original design drawings, which were provided by the Puerto Rico Highway Authority. The structure was designed using normal-weight concrete with a specified compressive strength of $f_c = 4{,}000\ psi$. This corresponds to a material's modulus of elasticity of $E_c = 3{,}605\ ksi$ in accordance to section *19.2.2.1* in *ACI 318-14*. A detailed description of the quantity of structural elements considered in this mathematical development with their respective physical properties is outlined in Tables 4-1 to 4-6.

Table 4-1: Physical properties for Type IV AASHTO concrete beams

AASHTO Concrete Beam [Type IV]							
Beams	**Length [ft]**	**Element Weight [kip]**	**Total Weight [kip]**	**I_y [in^4]**	**I_x [in^4]**	**k_y [k/in]**	**k_x [k/in]**
36	94.554	77.723	2,798.036	24,373	260,741	6.496	69.496

Table 4-2: Physical properties of the highway bridge piers

Columns					
ID	**Length [ft]**	**Volume [ft^3]**	**Weight [kip]**	**I_y [in^4]**	**k_y [k/in]**
1	16.951	173.397	26.010	172,665.58	887.486
2	17.224	176.193	26.429	172,665.58	845.892
3	17.498	178.990	26.849	172,665.58	806.857
4	18.045	184.584	27.688	172,665.58	735.707
5	18.591	190.177	28.527	172,665.58	672.682
6	18.865	192.974	28.946	172,665.58	643.857
7	19.138	195.770	29.366	172,665.58	616.656
8	19.685	201.364	30.205	172,665.58	566.682

Table 4-3: Physical properties of the highway bridge concrete deck

Reinforced Concrete Deck								
Thickness [in.]	**Width [ft.]**	**Length [ft.]**	**Volume [ft^3]**	**Weight [kips]**	**I_y [in^4]**	**I_x [in^4]**	**k_y [k/in]**	**k_x [k/in]**
7.5	123.408	189.108	14,547.62	2,182.143	2.02E+09	5,1654	1,873.6	0.0478

Table 4-4: Physical properties of the highway bridge concrete parapets

Concrete Parapets			
Number of Parapets	**Length [ft.]**	**Volume [ft^3]**	**Total Weight [kips]**
2	94.554	231.441	69.432

Table 4-5: Physical properties of the highway bridge concrete median barriers

Concrete Median Barrier		
Length [ft.]	**Volume [ft^3]**	**Total Weight [kips]**
94.554	351.435	52.715

Table 4-6: Physical properties of the bridge's cap bean located at joint B in figure 4-1b

Cap Beam				
Base [ft.]	**Height [ft.]**	**Length [ft.]**	**Volume [ft.]**	**Weight [kips]**
4.593	4.035	127.672	2366.451	354.968

The bridge's equivalent mass is assumed to be concentrated at joint C in Figure 4-1b. It was computed assuming a contribution of half of the mass for each connecting structural element at C, except for the cap beam, whose mass was considered to totally contribute due to its axial coincidence with joint C. The equivalent mass used for the model resulted in $93{,}731.06\ slugs$.

A detailed computation of the equivalent mass is shown below.

AASHTO Concrete Beams (Type IV) ..... 3,478.52 $slugs$

Columns ..... 43,447.83 $slugs$

Concrete Deck ..... 33,884.16 $slugs$

Concrete Parapets ..... 1,078.14 $slugs$

Concrete Median Barrier ..... 818.56 $slugs$

Cap Beam ..... 11,023.85 $slugs$

Total Mass ..... $93,731.06\ slugs$

When computing the equivalent spring stiffness coefficient, the assumed boundary conditions considered for the structural elements in their Y-axis are outlined in Table 4-7.

Table 4-7: Assumed boundary conditions for bridge's analytical model

Structural Element	Boundary Condition	Stiffness Formula
AASHTO Concrete Beams (Type IV)	Pinned-Pinned	$k_c = \frac{3\ EI}{L^3}$
Concrete Columns	Fixed-Fixed	$k_c = \frac{12\ EI}{L^3}$
Concrete Deck	Pinned-Pinned	$k_c = \frac{3\ EI}{L^3}$

The computed equivalent stiffness of the lateral (transverse) structural force resisting system of the bridge was $91{,}870.67\ kip/ft$.

Using the values of the equivalent mass and lateral stiffness of the bridge, it is possible to compute the natural frequency of the SDOF system. This is the most important quantity when studying any structural dynamic problem because it governs the dynamic behavior of a system under any excitation. Consequently, it ensures proper design considerations for new infrastructure developments and more accurate retrofitting alternatives in the case of existing structures. Equations (4.2), (4.3), and (4.4) define the natural frequency in Hertz and radians/seconds, and the period in seconds, respectively.

$$f_n = \frac{1}{2\pi}\sqrt{\frac{k}{m}} \quad [Hz] \tag{4.2}$$

$$\omega_n = \sqrt{\frac{k}{m}} = 2\pi f \quad \left[{}^{rad}/_{sec}\right] \tag{4.3}$$

$$T_n = \frac{1}{f} = \frac{2\pi}{\omega_n} \quad [sec] \tag{4.4}$$

While the mass and stiffness coefficients are very important in understanding the behavior of a dynamic system, the damping contribution intrinsic to that system is relevant to accurately model the system and predict its behavior under any external (forced) excitation. Therefore, it should be determined in the best possible way. However, determining the value of the damping coefficient, c, of a structural system in the simplified assumption of a viscous fluid model is technically impossible since the total damping comes from multiple sources. The only exception is when the damping comes solely from physical damper. For this reason, engineers and dynamic analysts prefer to use what is commonly known as the damping ratio, ξ, which is defined in equation (4.5).

$$\xi = \frac{c}{c_{crit.}} \tag{4.5}$$

Simply explained, it is a dimensionless value computed as the ratio between the actual damping coefficient, c, and its critical value, $c_{crit.}$. In a system that is assumed to behave as a damped simple oscillator, it is the minimum value of c that makes the response to damp out eliminating any decaying oscillation. It can be obtained from a system's characteristic equation and is defined as shown in equation (4.6).

$$c_{crit.} = 2\omega_n m \tag{4.6}$$

In this case study, the bridge can be classified as an underdamped structural system for which the value of $\xi < 1$. For concrete structures the values of ξ ranges from 0.01 to 0.025. Accordingly, the Ponce Highway Bridge must fall within this range. For this reason, a value of $\xi = 0.02$ will

be used to model the damping contribution in the system's model represented by equation (4.5). This will result in a value of damping coefficient of $c = 117{,}378.94\ lb \cdot s/ft$. The resulting motion equation of the model of the Ponce Highway Bridge [ID: 2348] presented in (4.1) can be rewritten as in equation (4.7):

$$93{,}731.06\,\ddot{u}(t) + 117{,}378.94\,\dot{u}(t) + 91{,}870{,}667.4\,u(t) = F(t) \qquad (4.7)$$

4.2 Computational Model for the PRILA Condominium

Analytical models for structural systems should represent their dynamic behavior to the best possible extent. However, since a model is a reduced order mathematical representation of a continuous system, the model reliability depends on the accuracy of the estimations of each constituent property, of the system's boundary conditions, and the size and geometric complexity of the real system. For these reasons, the structural model for PRILA Condominium was initially done as a 3D computational model using ETABS® analysis software. The main purpose of this model is to perform a modal analysis, in the most accurate way, to a structure whose dimensions are so large that the inaccuracies in approximating its real properties and boundary conditions, without any empirical data, could lead to large errors in the dynamic properties' prediction. In this case the minimization of errors is of special importance because the modes of vibration extracted from the analysis will dictate the optimal sensor placement throughout the entire structure.

With this purpose in mind, the 3D computational model was constructed *as-designed* in accordance to the original design drawings. The model included all structural elements made of reinforced concrete and masonry wythes with their gross section (uncracked) areas. Figure 4-3 shows the *as-designed* 3D computational model and its similarity to the real building.

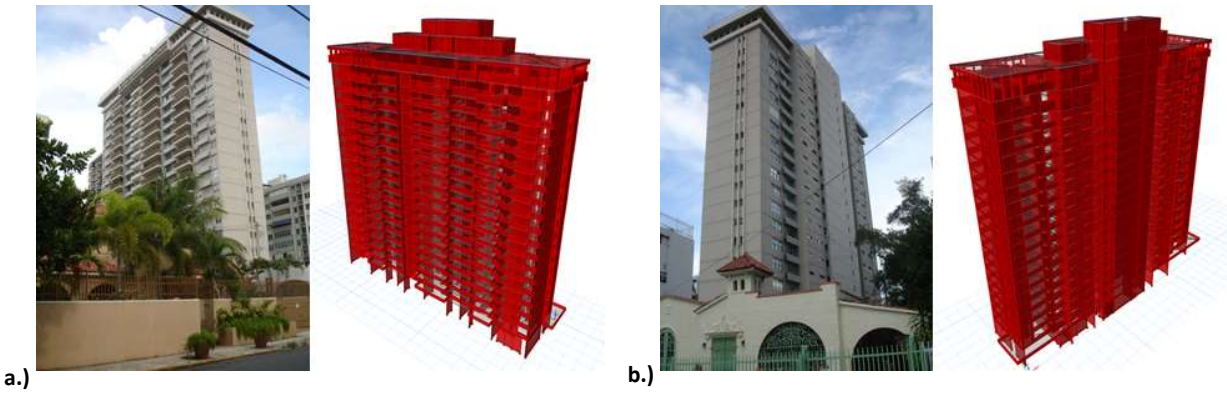


Figure 4-3: 3D model and real structure. a.) PRILA front view. b.) PRILA rear view

A modal analysis was performed to obtain the structure's resonant frequencies and its respective mode shapes. The stories with the maximum modal displacements in the first four modes of vibration were selected to install the accelerometers. The reason for this is because the structure, due to its geometric characteristics, tends to oscillate in its first (fundamental) mode of vibration when seismically excited. Due to the availability of 36 sensors for collecting the experimental data, points with maximum displacement for the first four modal shapes were selected as the optimal placement location. The amount and quality of information that can be extracted from an unknown system or structure is proportional to the quantity of sensors, their distribution throughout the structure, and their optimal placement. However, to have an extensive distribution of sensors, such as in PRILA, is not always possible. The total cost of the sensor network in PRILA, including all instruments, and labor was $106,000.

When performing the modal analysis in the 3D model of the building, torsional modes were noted in some of the lower modes of the structure. This is in accordance to its geometric characteristics, its mass and stiffness distribution, and its large dimensions. However, translational modes of vibrations in the model were selected to assess the placement of the accelerometers in the real structure. Figures 4-4 to 4-8 shows PRILA's first four translational modes of vibration and the selected stories for sensor placement. The corresponding frequencies of vibration for these mode shapes are summarized in Table 4-8.

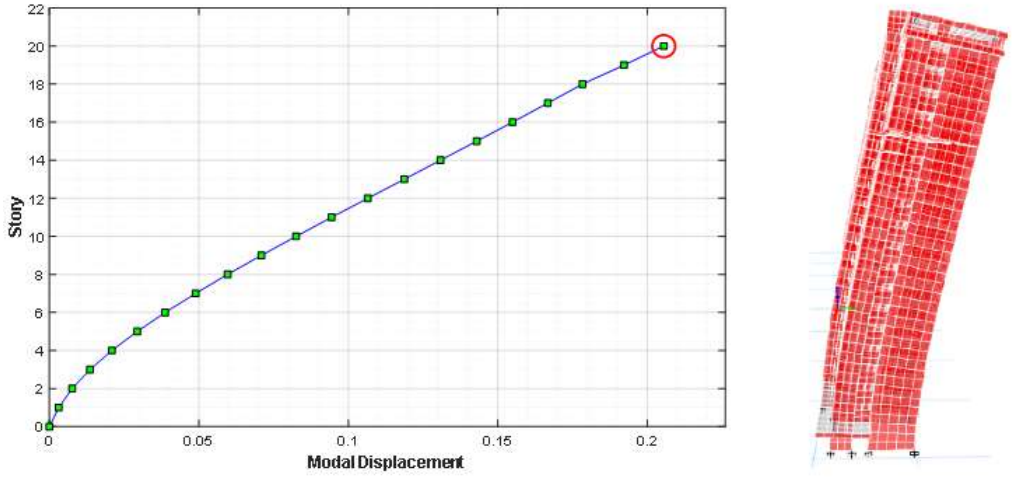


Figure 4-4: First translational mode shape for PRILA Condominium

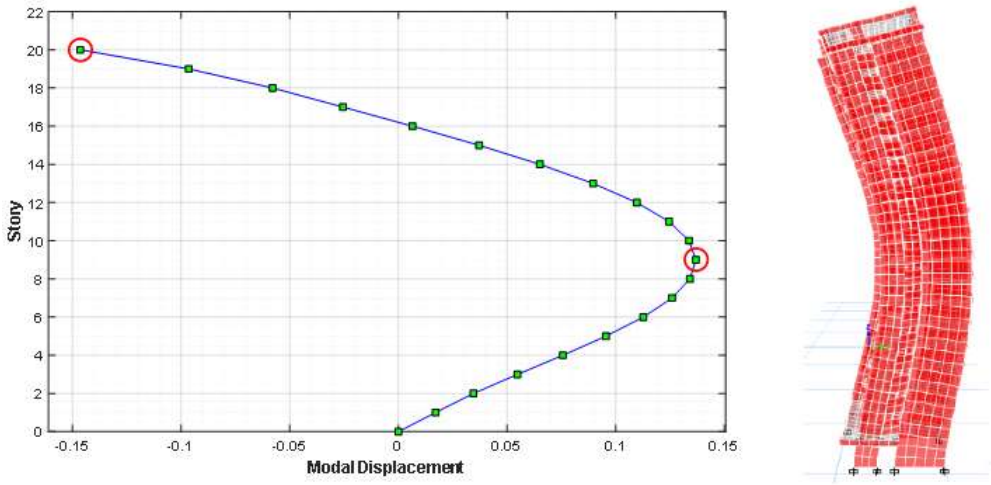


Figure 4-5: Second translational mode shape for PRILA Condominium

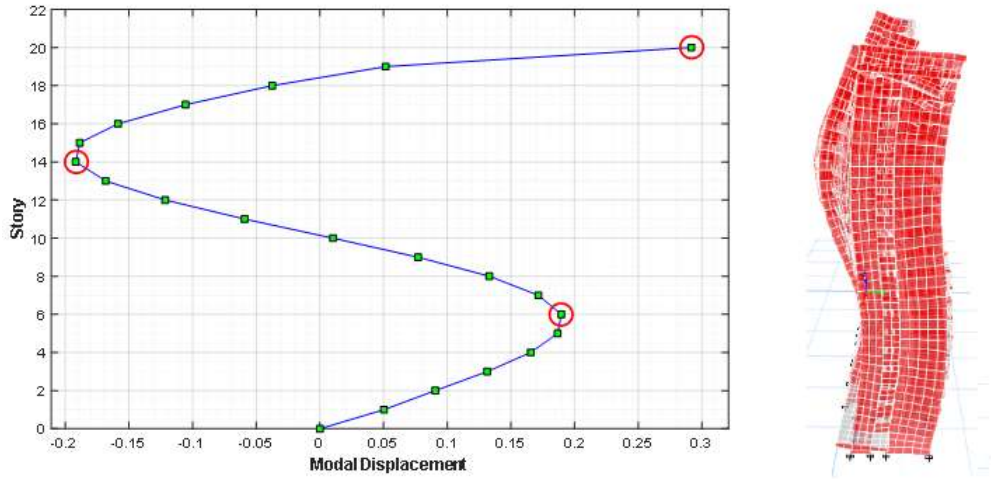


Figure 4-6: Third translational mode shape for PRILA Condominium

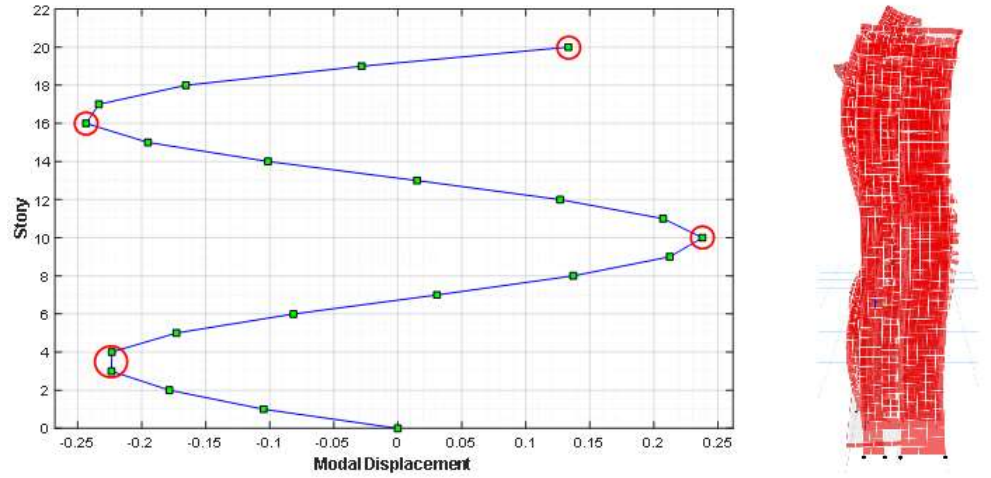
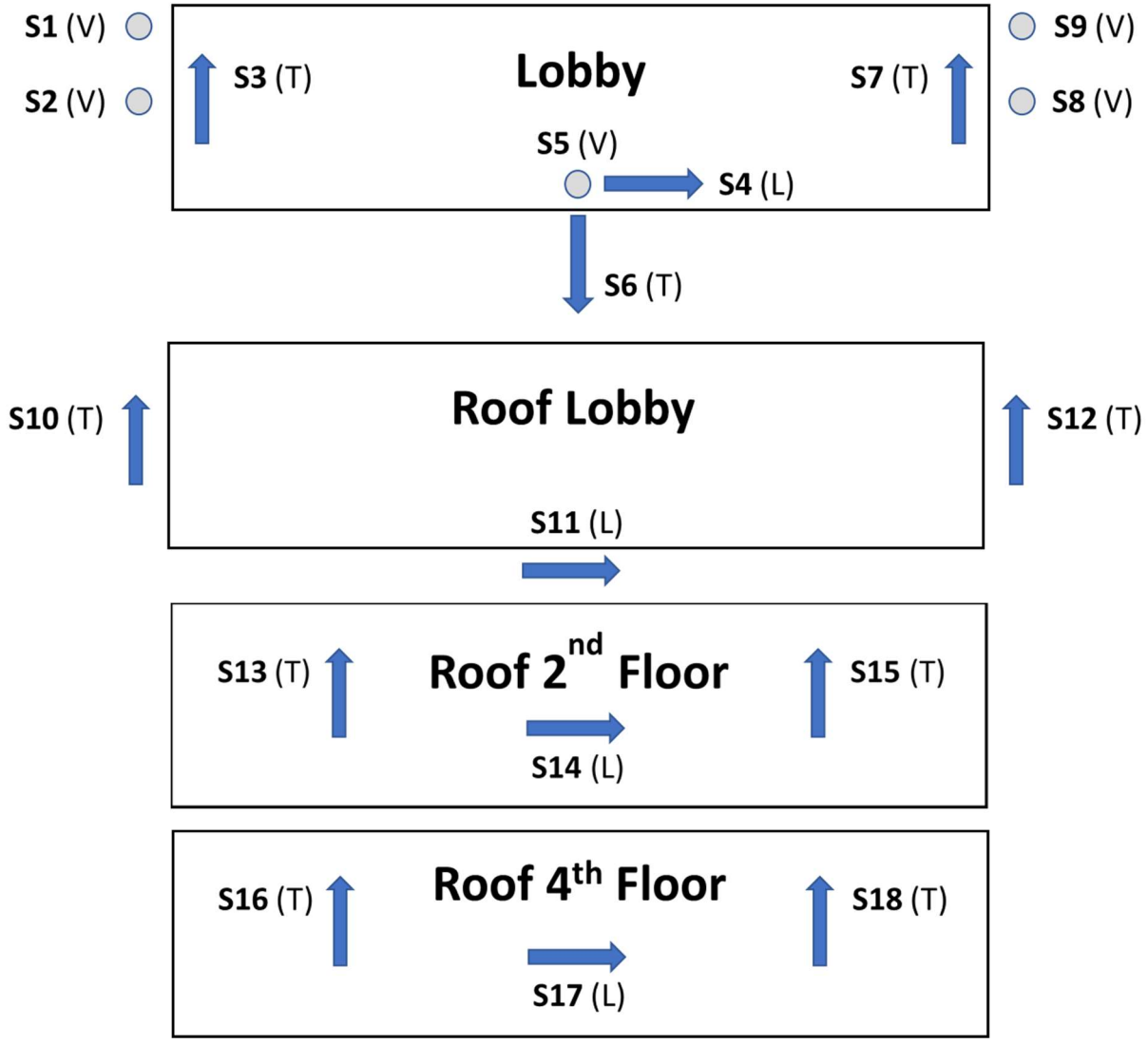


Figure 4-7: Fourth translational mode shape for PRILA Condominium

Table 4-8: Natural periods and frequencies of vibration for PRILA Condominium computational model

Model Mode	Classic Mode	T_n [sec]	f_n [Hz]
1	1	0.946	1.057
4	2	0.229	4.367
8	3	0.113	8.850
13	4	0.073	13.699

A pair of uniaxial sensors were placed at each story in the $N-S$ direction and one uniaxial sensor was placed in the elevator core at each selected story in the $E-W$ direction. The accelerometers' distribution in each selected story is shown in Figure 4-8.



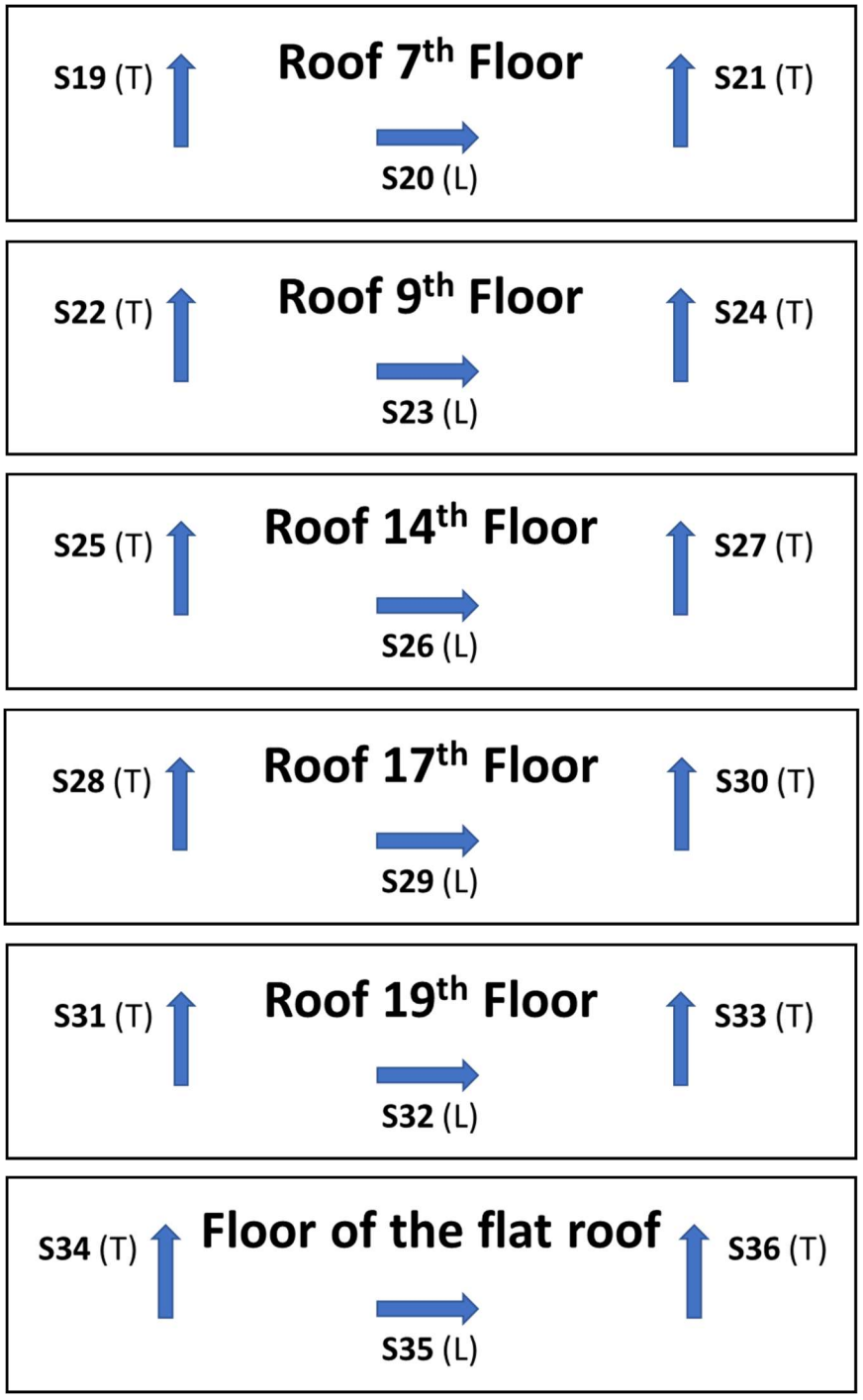


Figure 4-8: Sensor accelerometers' location per selected story

CHAPTER 5. EXPERIMENTAL DYNAMIC ANALYSES

Experimental dynamics is an applied field within structural dynamics that deals with the study of simulated or recorded dynamic actions and its effects on structural and mechanical systems by means of their recorded vibration responses. The information gathered allows engineers to truly understand the behavior and predict the performance of man-made structures when subjected to ground motions. In particular, engineers can define the actual forces acting on a system and the stresses they generate in it to subsequently determine if the structure's capacity is exceeded or not. Likewise, with this analysis approach, it is possible to estimate the maximum displacements induced in the structure by a strong motion and determine whether the structure is capable to maintain an acceptable performance during and after the event.

Theoretical structural dynamics provides the framework to formulate mathematical models to simulate the behavior of real structural systems. These models, when carefully developed, should be able to predict structural behavior in the linear-elastic range and assist in estimating damage occurrence that may increase the possibility of failure or collapse. In other words, they must describe the capacity of a structure to undergo sequences of randomly varying cyclic deformations by accounting for its stiffness and strength loss. However, the reliability of a model depends on the accuracy by which the structure's materials, mechanical properties, and surrounding conditions are determined or assumed. Factors such as the contribution of non-structural components, soil-structure interaction, and the *as-designed* versus the *as-built* conditions for structural components and their properties greatly influence in the deviation of the modeled response from the actual (or recorded) structural response. A major problem in reinforced concrete structures is not necessarily the loss of strength but the degradation of its component's stiffness and their energy capacities with cyclic actions. In fact, the quantification of these detrimental effects from mathematical models, which is already difficult to predict, becomes unreliable with the lack of enough and reliable information on the *as-built* structural properties. For this reason, the use of experimental methods jointly applied with the theory of structural dynamics has increasingly popularized among analysts in the past decades to accurately determine the essential properties that allows to adjust unreliable mathematical models to produce more realistic dynamic responses. This process,

denoted as *system identification*, converts experimental recorded data to system's characteristics which are later employed in model updating.

In the past decades, extensive work has been done in the field of system identification. Researchers have developed two main analysis approaches. In the first one, the system's parameters are estimated in non-linear differential equations. Different types of non-linear differential equations with varying parameters' values are compared by correlation analyses of predicted and measured responses. The parameters' values and the equations that provide the best correlation results are selected as the identified system's model. On the other hand, in the second analysis approach a linear-elastic model is assumed to be valid to compute the dynamic response of a system. The system's dynamic parameters are identified for different time intervals of the recorded experimental response. The identification of these parameters is carried out implementing time-domain and frequency-domain analysis to the selected segments of the recorded response measurements. The parameter values determined at different stages of the system's life cycle serve to update the initially developed mathematical model at different stages of the structure's service life and provide immediate assessment of its structural health after an earthquake or any other significant dynamic action that may have affected the structure's integrity and consequently its future performance and functionality. For this study, the second method will be implemented for determining the dynamic parameters of the Ponce Highway Bridge [ID: 2348] and the PRILA Condominium to update their previously developed analytical models.

This work focuses on the determination of the structures' natural frequencies of vibration, ω_n, and their corresponding damping factors, ξ, from recorded acceleration measurements. For this purpose, several numerical approaches in both the time and frequency domains are applied to experimental recorded data and the results are presented in the following sections. In the frequency domain, the analysis was performed using the Fast Fourier Transform, and in the time-domain, the Random Decrement Technique was implemented. In addition, a combined Time-Frequency domain approach was performed using the Continuous Wavelet Transform with the Complex Morlet Wavelet as its mother wavelet function. Small amplitude acceleration measurements from ambient vibrations were used to compute both structures' dynamic parameters. Furthermore, four low intensity earthquake motions that were recorded in the Ponce Highway Bridge [ID: 2348] in 2010 and 2014 were analyzed with these mathematical tools to study their respective frequency spectra. All acceleration records were provided by the PRSMP.

5.1 Ponce Highway Bridge [ID: 2348]

5.1.1 Dynamic Assessment from Ambient Vibration Records

Small amplitude vibration measurements were recorded at the Ponce Highway Bridge [ID: 2348] on Wednesday, September 14, 2016 at 5:50 pm. The recording period lasted 18 hours and the data was simultaneously sampled at 200 Hz in twelve different sensor channels on $N-S$ and $E-W$ directions. However, for this case study, the sensor of interest for dynamic properties identification of the bridge's lateral force resisting system is sensor #5 as shown in Figure 3-5. For this reason, the identification analysis was executed solely on the output information provided by this sensor. Raw data was baseline corrected by a piecewise cubic spline and then converted to acceleration units as a fraction of the gravitational constant, g. Figure 5-1 shows the recorded acceleration signal which is implemented in the following analyses.

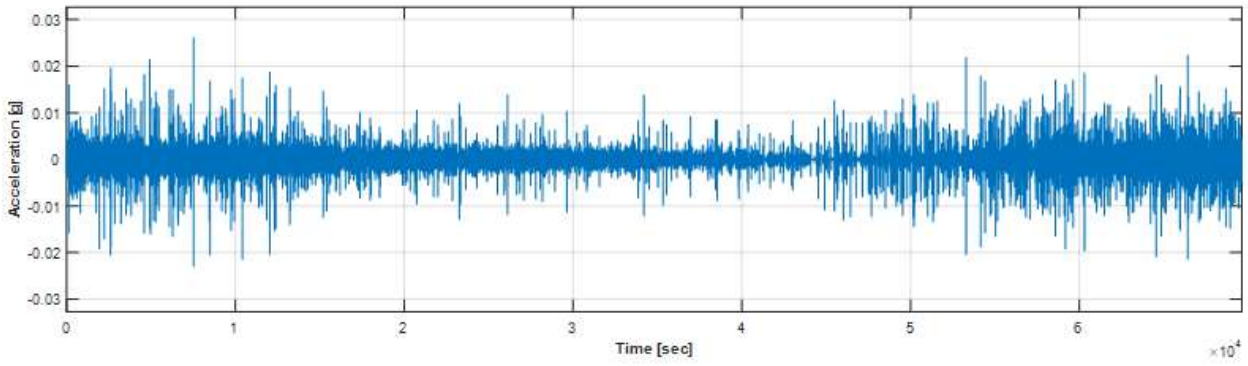


Figure 5-1: Eighteen hours of ambient vibrations recording in sensor #5 at Ponce Highway Bridge [ID: 2348]

5.1.1.1 Frequency-Domain Identification via FFT

The Fourier transform is the oldest method developed to decompose a transient signal into its constituent sinusoids. In addition, its most efficient version, the FFT, has proved to be the most reliable method for determining the frequency spectrum of any signal, and hence of any recorded system's response. For that reason, in this study the frequency spectrum obtained with the FFT will be used as a benchmark value to quantitatively measure the reliability of subsequent methods employed in this work.

The frequency spectrum for the measured signal in sensor #5 is shown in Figure 5-2. It can be easily noticed that the natural frequency of the bridge regarded as a SDOF system is $f_n = 3.271\ Hz$. In addition, the effect of road traffic on the bridge can be noticed to produce vibrations

approximately ranging from $11.5\,Hz$ to $20\,Hz$. On a study on the effect of measured traffic vibrations in buildings, Hunaidi (2000) states that road traffic tends to produce vibrations with frequencies ranging predominantly in the range from $5\,Hz$ to $25\,Hz$ in which the acceleration amplitude of the recorded vibrations ranges between $0.0005\,g$ and $0.2\,g$ ($0.005\ m/s^2$ and $2\,m/s^2$) and between $0.05\,mm/s$ and $25\,mm/s$ measured as velocity. These range values are consistent with the ones obtained in this study for traffic noise vibrations by means of the FFT.

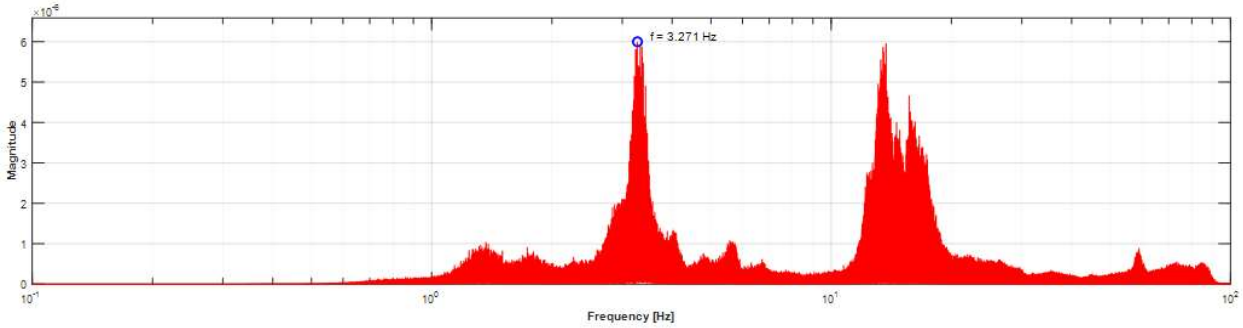


Figure 5-2: Frequency spectrum for eighteen hours of recorded ambient vibrations in sensor #5 at Ponce Highway Bridge

5.1.1.2 Time-Domain Identification via RDT

The Random Decrement Technique is a time-domain mathematical algorithm that extracts correlation functions from forced vibration responses of structural systems. These generated correlation functions resemble free vibration functions (exponentially decaying oscillations) and consequently allows the computation of dynamic properties of systems under forced vibrations excitations. The RDT functions correlate the response of a system under random excitations to the forcing function throughout the measured response period. A threshold condition must be selected from equations (2.3) to (2.7) to simulate an initial excitation. Then, through the averaging of N number of sub-segments of the same length, the randomness of the system response is averaged out leaving only the apparent response corresponding to the simulated initial condition excitation. The reason for this generated function to decay is that throughout the specified time of the sub-segments the effect that the simulated initial excitations (threshold condition selected) has on the system is decaying until it reduces to zero.

To identify the dynamic parameters of the Ponce Highway Bridge [ID: 2348], sensor #5 was used as the leading sensor in the random decrement analysis. In addition, the baseline corrected recorded response was split into 13,844 sub-segments of 5 seconds using equation (2.3) as the

threshold criterion. After averaging these sub-segments, the random decrement signature for the bridge response was obtained and is shown in Figure 5-3.

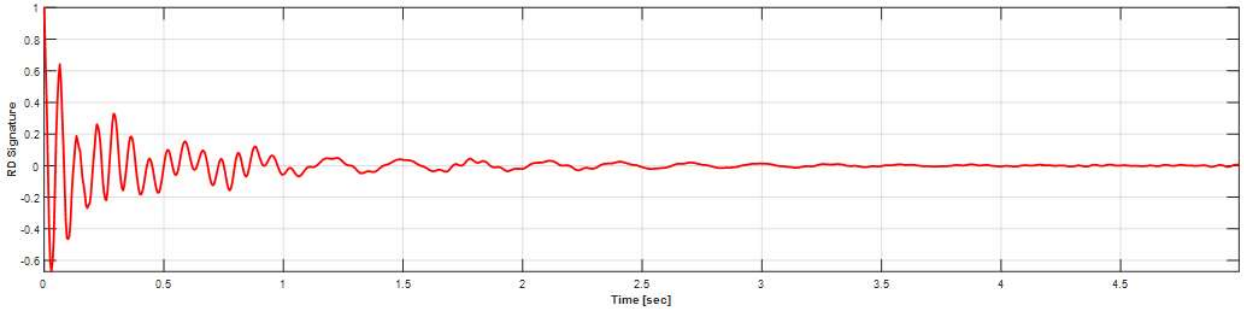


Figure 5-3: Random decrement signature for ambient vibration response at sensor #5

After generating the random decrement signature, it is possible to extract the system's dynamic parameters from it by applying time-domain concepts of classical structural dynamics. An idealized free vibration response of a SDOF system is shown in Figure 5-4. From it, some damped dynamic parameters can be explicitly extracted and then converted to the undamped dynamic parameters of interest by applying the corresponding mathematical relations outlined in Table 5-1.

Table 5-1: Mathematical relations between damped and undamped dynamic parameters

Classic Relations for Damped Systems	**Description**
$T_d = \frac{t_2 - t_1}{n};\ n = number\ of\ cycles$	Damped Period $[sec]$
$\omega_d = \frac{2\pi}{T_d}$	Damped Angular Frequency $[rad/sec]$
$\omega_n = \frac{\omega_d}{\sqrt{1-\xi^2}}$	Natural Frequency $[rad/sec]$
$f_n = \frac{\omega_n}{2\pi}$	Natural Frequency $[Hz]$
$T_n = \frac{1}{f_n} = \frac{2\pi}{\omega_n}$	Natural Period $[sec.]$

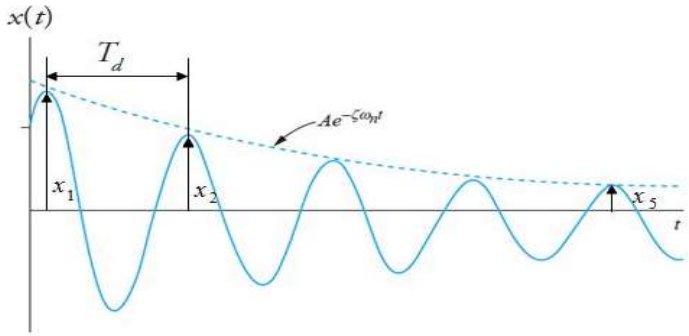


Figure 5-4: Idealized free vibration response of a SDOF system.

Equally important is the possibility of computing the system's modal damping factor from the generated random decrement signature. For this respect, the *Logarithmic Decrement Method* has proven to be a simple and efficient time-domain method to estimate the real damping in structures producing free vibration responses which have an apparent exponentially decaying envelope. This method consists in computing the logarithmic decrement, δ, by selecting two peaks x_1 and x_{1+n} in equation (5.1) in the free vibration response signal.

$$\delta = \frac{1}{n}\ln\left(\frac{x_1}{x_{1+n}}\right) \tag{5.1}$$

In the equation, n refers to the amount of cycles between peaks x_1 and x_{1+n} in which a decaying exponential function is assumed to be defined. This is applicable to any decaying vibration response, regardless of its nature. The relation between the logarithmic decrement, δ, and the damping factor, ξ, is shown in equation (5.2).

$$\delta = \frac{2\pi\xi}{\sqrt{1-\xi^2}} \tag{5.2}$$

For underdamped structures with little damping, the denominator in equation (5.3) approaches unity and consequently the damping ratio can be computed as

$$\xi = \frac{\delta}{2\pi} \tag{5.3}$$

However, in cases where it may be desired to compute ξ considering more than two peaks in the free vibration response, equation (5.1) and (5.3) can be mathematically manipulated to obtain a logarithmic linearization of the chosen response peaks, as shown in equation (5.4).

$$\ln(x_{1+n}) = -2\pi\xi n + \ln(x_1) \tag{5.4}$$

This equation makes it possible to compute the value of ξ in accordance to the numerical values corresponding to the coefficients of a linear equation of the form $y = mx + b$, where

$$y = \ln(x_{n+1}) \tag{5.5}$$

$$m = -2\pi\xi \tag{5.6}$$

$$b = \ln(x_1) \tag{5.7}$$

Equation (5.6) can be arranged as shown in equation (5.8) to ultimately compute ξ.

$$\xi = -\frac{m}{2\pi} \tag{5.8}$$

The logarithmic decrement method was applied to the generated random decrement signature from sensor #5 from the bridge using both the two-peaks selection approach and using all the peaks contained in the signal. With the two-peaks approach, two separate computations of dynamic parameters were performed with two different pairs of chosen peaks. Each pair of peaks was selected by observation of the signal behavior to compare the results obtained from the peak selection from different signal intervals. The pair of peaks selected for the first computation are shown in Figure 5-5 and are defined as $x_1 = 1$, $t_1 = 0$ and $x_9 = 0.1539$, $t_9 = 0.59$ with $n = 8$.

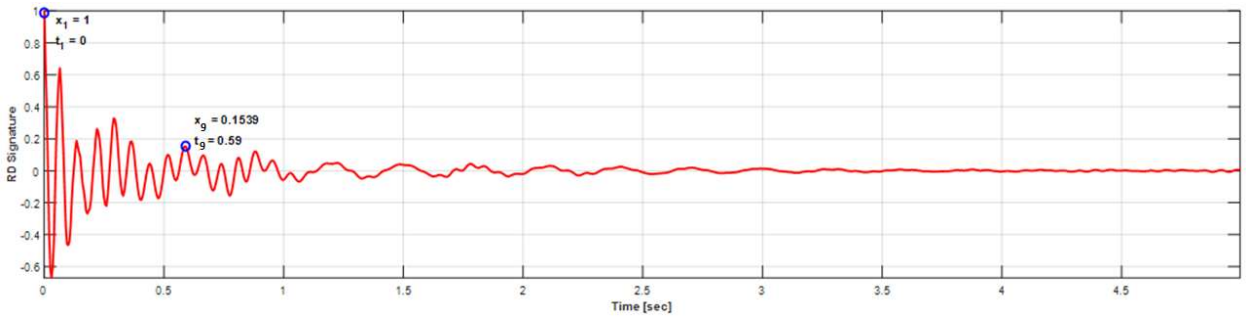


Figure 5-5: Random decrement signature with the 1st pair of selected peaks to implement the logarithmic decrement method.

For the second computation, the selected peaks are shown in Figure 5-6 and its respective values are defined as $x_1 = 0.04032$, $t_1 = 1.485$ and $x_5 = 0.01971$, $t_5 = 2.705$ with $n = 4$.

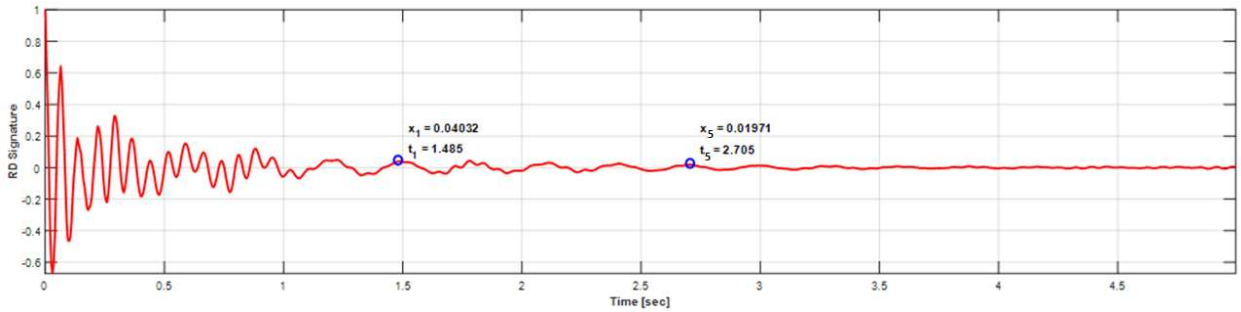


Figure 5-6: Random decrement signature with the 2nd pair of selected peaks to implement the logarithmic decrement method.

Table 5-2 shows the results for both computations that utilizes the two-peaks approach and for the computation that uses all the peaks of the free vibration response.

Table 5-2: Dynamic parameters results implementing the logarithmic decrement method

Dynamic Parameter	**Two-Peaks in Log. Decrement Analysis**		**All-Peaks in Logarithmic Decrement Analysis**
	1st Pair of Peaks	*2nd Pair of Peaks*	
$f_n\ [Hz]$	13.5687	3.28	16.0998
$\omega_n\ [rad/sec]$	85.2548	20.609	101.1582
$T_n\ [sec]$	0.073699	0.30488	0.062112
ξ	0.03723	0.028478	0.0096584

From Table 5-2, it can be easily noticed the large discrepancies between the values obtained for each dynamic parameter in each logarithmic decrement analysis approach. These discrepancies are the result of unfiltered noise traces embedded in the generated random decrement signature during the first second of duration. This phenomenon is commonly encountered at the beginning of many experimental random decrement signatures and its cause is intrinsic to the implementation of the RDT. It greatly depends on the amount of noise encountered in the signals and the effect is increased when closely spaced modes are encountered within a system's response. To reduce this noisy effect to the largest extent, the signals must be adequately baseline corrected and the recommendations presented in Section 2.4.1 should be followed. However, there are occasions in which even though these recommendations are considered in the analysis, reduced noise traces still exist embedded in the random decrement signatures, as is the case in this study. In those cases, the analyst judgement, based on experience and previous knowledge of the studied system, must be applied in deciding which peaks should be selected as representatives of the free vibration response of the system. As an illustration, the discrepancies shown in Table 5-2 corresponds to the peaks' selection criteria, in which it can be noticed that the best approximation of a free vibration curve corresponds to the cycles defined between the two peaks selected in the second selection of peaks for the logarithmic decrement analysis. Consequently, this makes these results the best estimates of the real dynamic parameters of the Ponce Highway Bridge [ID: 2348] when implementing the logarithmic decrement method to random decrement signatures generated from its ambient response measurements.

5.1.1.3 Time-Frequency Domain Identification via Wavelet Transform

In experimental dynamics, it is often desired to track the changes of a system's dynamic parameters to better asses its structural health. This allows engineers to determine the exact time of occurrence of any possible damage scenario reflected by dynamic changes during any strong excitation, such as earthquake motions or vehicle crashes into the structure. Furthermore, by tracking the dynamic changes through time it is possible to determine if these changes are permanent or transient; and if transient, how much time does it take for the structure to recover its original dynamic state if there is no significant structural damage. This approach provides a more complete picture of what is happening to the system and the possible causes of its health state. Consequently, this permits the engineer to have a better final assessment and diagnosis of the studied system.

For this purpose, and without underestimating the existing frequency domain and time domain methods, the emergence of new and powerful mathematical tools changed the way in which signals are analyzed and interpreted. In particular, the wavelet transform gained a lot of popularity among analysts, especially due to its capability of identifying dynamic properties in multicomponent signals. In fact, that is the main reason to choose this mathematical approach over the Hilbert Transform, which only works for monocomponent signals, and the Hilbert-Huang Transform, which requires to employ two companion methodologies for identifying multicomponent signals.

In this case study, the CWT is applied to the random decrement signature generated by using the RDT to ambient recordings from sensor #5 to compare the bridge's dynamic parameters from its equivalent free vibration response. In addition, a wavelet transform analysis is performed to the baseline corrected ambient response recorded from the same sensor. Both analyses show the capabilities of the wavelet transform and the feasibility of using it for the dynamic identification of forced and free vibration responses. In particular, all the time-frequency analyses presented in this work were performed using the Complex Morlet Wavelet as the basis function (or mother wavelet) in the CWT. This basis function is shown in Figure 5-7.

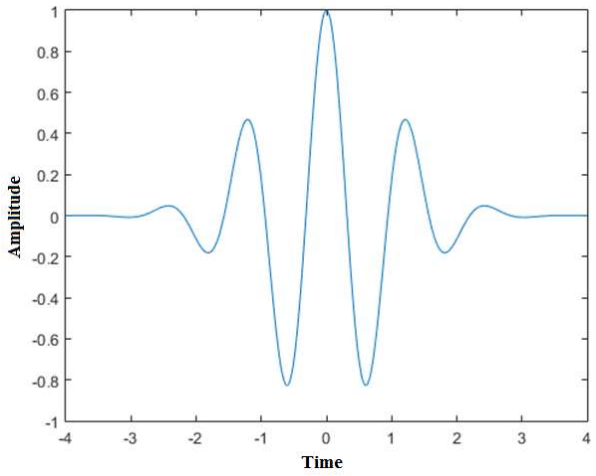


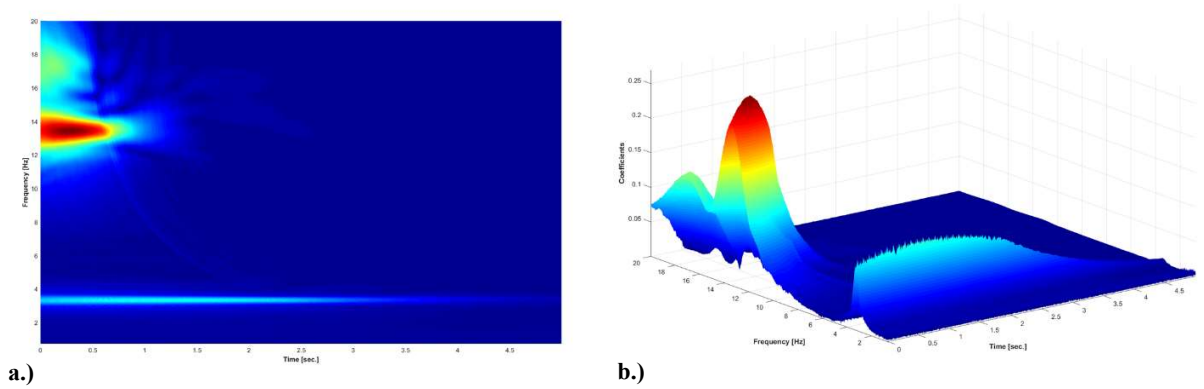
Figure 5-7: Graph of the Complex Morlet Wavelet basis function

It is defined by equation (5.9) in which f_b is a bandwidth parameter that controls the shape of the mother wavelet and f_c is the wavelet's central frequency. In this study, the values selected for these parameters were $f_b = 75$ and $f_c = 1$.

$$\psi(t) = \frac{1}{\sqrt{\pi f_b}} e^{if_c t} e^{-t^2/f_b} \tag{5.9}$$

5.1.1.3.1 Wavelet Transform Analysis of Random Decrement Signatures

The results of the time-frequency analysis of the computed random decrement signature, were plotted in a spectrogram, also known as a wavelet map. From it, is noted that the CWT worked as a filter. The results shown in Figure 5-8a display the presence of three main frequency components embedded in the random decrement signature. One frequency component is mostly concentrated in a frequency range from $12\,Hz$ to $15\,Hz$. Another component mostly contains a frequency content between $16\,Hz$ to $19\,Hz$. These two signal components correspond to the traffic vibrations generated in the bridge and does not represent the structure's fundamental frequency. These frequency components caused the discrepancies in the identification of dynamic parameters by directly applying the logarithmic decrement method to the random decrement signatures. The remaining, and noticeably the most influential frequency component embedded in the random decrement signature is localized between $3\,Hz$ and $4\,Hz$.



a.) b.)

Figure 5-8: Spectrogram for wavelet transform computed to random decrement signature of ambient response at sensor #5

In Figure 5-8b, it is easily noticed to resemble a free vibration curve corresponding to the generated random decrement signature. To emphasize this feature, a skeleton plot was generated for the frequency range in which the resemblance of the free decay curve is located. The plotted skeleton curve is shown in Figure 5-9. Hence, a more accurate frequency value was obtained. Skeletons for the other frequency components that are related to traffic vibrations were not computed in this part of the analysis because they do not represent the natural dynamic behavior for the bridge and they have proven to adversely affect the dynamic analysis.

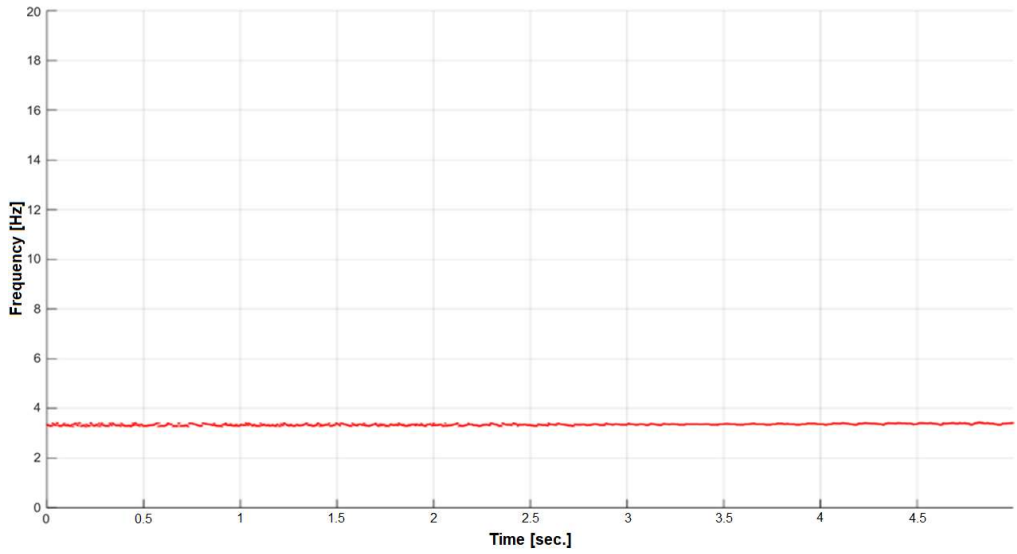


Figure 5-9: Skeleton curve from 3 Hz to 4 Hz corresponding to the computed wavelet map

A major advantage of using complex wavelet functions, such as the Complex Morlet Wavelet, in the CWT is that its resultant coefficients are complex. Therefore, these coefficient values extracted along the ridges that defines the skeleton plots for a specified frequency range possess real and imaginary components that are directly proportional to the signal content at that frequency

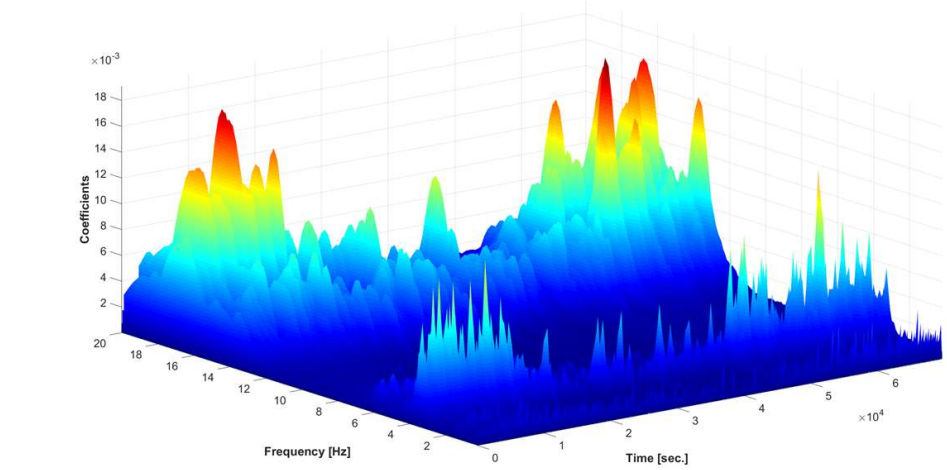
and its corresponding Hilbert Transform. Consequently, the wavelet coefficients along each ridge are used to construct the analytic signal for each component, allowing the identification of instant frequencies and damping ratios. The instant frequencies can be obtained by differentiating the phase of the analytic signal or by averaging the skeleton frequencies. In this study, the latter approach was implemented. With respect to the damping factor determination, it can be obtained by implementing the logarithmic decrement method to the analytic signal. In this study, all the peaks of the analytic signal generated from the wavelet transform were used in its computation. Thus, for the skeleton shown in Figure 5-9, the system's natural frequency of vibration resulted in $f_n = 3.345\ Hz$ and the corresponding damping factor resulted in $\xi = 0.02283$.

5.1.1.3.2 Wavelet Transform Analysis on Recorded Ambient Vibrations

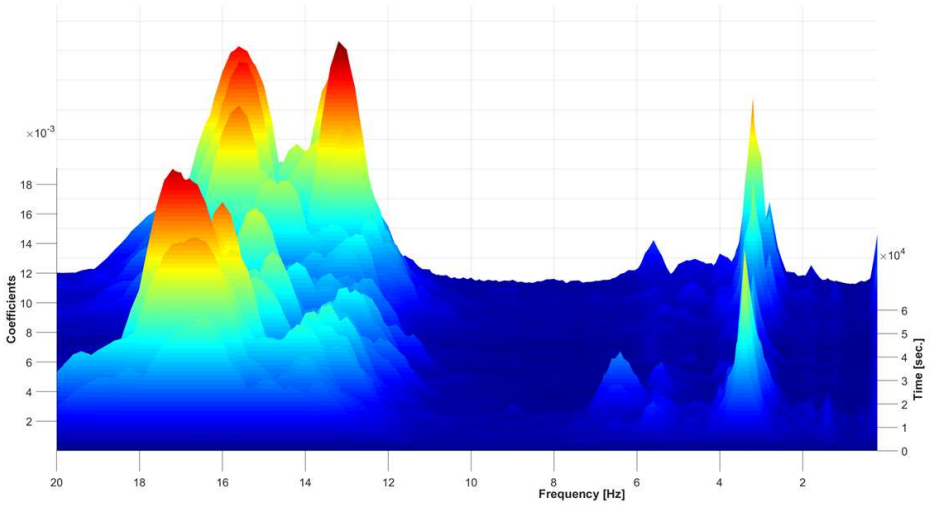
The use of Wavelet Transforms in time-frequency analysis of forced vibrations responses has been studied proving to produce reliable results for dynamic identification. However, a great majority of these analyses were implemented with recorded responses obtained from laboratory-controlled systems, in many cases under ideal conditions and without material or geometrical complexities. In other cases, simulated and idealized systems' responses were generated and analyzed. Likewise, windows of reduced lengths were typically analyzed, which in many cases may produce numerical inaccuracies especially when the shifted version of the basis wavelet does not fit the window length. The reasons for applying wavelet transform analyses to simplified systems and to short or moderate length signals is due to the numerical complexity intrinsic to the transformation, which typically requires high computational power while requiring extensive of computer memory. Consequently, little or no research has been done on Wavelet Transform analysis of in-service complex structures subjected to forced dynamic excitations.

This study intends the use of the CWT to simultaneously analyze in the time and frequency domains the 18-hours of recorded lateral responses from sensor #5 in the Ponce Highway Bridge [ID: 2348] while it is being dynamically excited by small amplitude ambient vibration and typical highway traffic vibrations. Figure 5-10 shows two 3D views of the generated spectrogram in which the wavelet coefficients are plotted with respect to time and frequency. A very important feature of the wavelet transform that is shown in Figure 5-9 and Figure 5-10 is the capability of identifying any amount of frequency components embedded in the analyzed signal without compromising the resolution or affecting the accuracy of the results. This is important to note

because if the same signal is analyzed with the Hilbert Transform, the frequency identified would be the average of the frequencies found per unit of time. This is a major reason for using wavelet transform in this study.



a.)



b.)

Figure 5-10: 3D spectrograms for ambient vibration records from sensor #5 at Ponce Highway Bridge

In addition, from Figure 5-10a it can be noticed that the wavelet transform is highly effective in tracing the behavior of the response signal for its complete duration. As an illustration, it is easy to notice that the wavelet coefficients' amplitudes, especially due to traffic vibrations, display higher values from around 6:00 pm (start of recording) to approximately 11:00 pm. This is the result to the highest traffic hours in the afternoons and nights. On the contrary, the approximate interval of 11:00 pm to 6:00 am shows a decrease in amplitudes which corresponds to the hours of less traffic. Finally, the coefficients' amplitudes increase from 8:30 am to 12:00 pm (end of

recording) as a result of the high daily traffic. Moreover, the bands corresponding to the response's dominant frequencies can be observed in Figure 5-10b. The effects of traffic excitation produce bridge vibrations with a frequency content of 16 Hz to 20 Hz. The frequencies within this range seem to be scattered and higher amplitude coefficients are noticed at random locations in both time and frequency domains. These high amplitude peaks may be caused by impact vehicle loads from normal traffic conditions. On the other hand, a much narrower and defined alignment of peaks throughout the entire response length is observed within a frequency range from 2.5 Hz to 4 Hz. These lower amplitude peaks correspond to the bridge's natural frequency of vibration. For this reason, a skeleton plot was generated to locate in the frequency domain the maximum amplitude peaks contained within the dominant frequency range per unit of time. Figure 5-11 shows the skeleton only obtained for the specified frequency range. By averaging the computed maximum values, a frequency of vibration of $f_n = 3.246\ Hz$ is obtained.

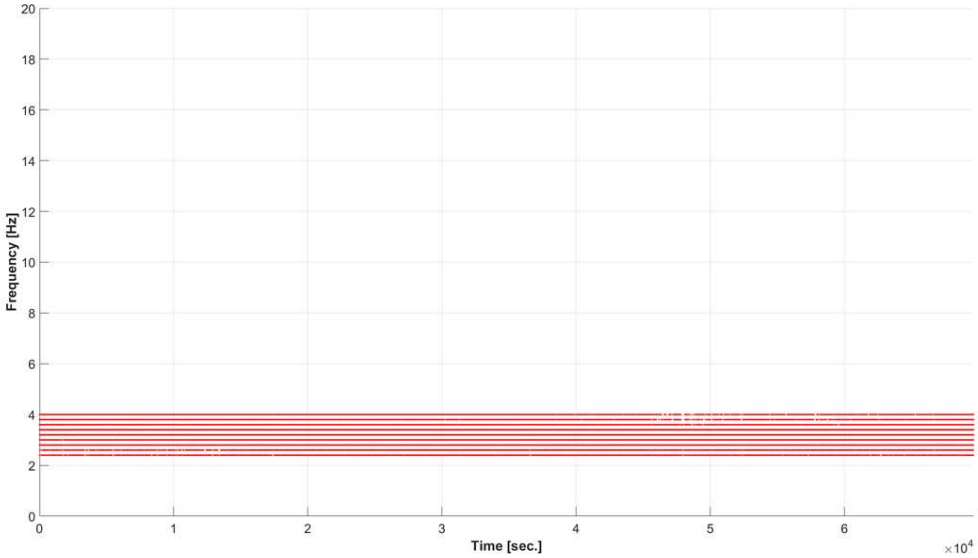


Figure 5-11: Skeleton curve from 2.5 Hz to 4 Hz corresponding to the computed ambient recording's wavelet map

5.1.2 Model Updating from Ambient Vibration Analyses

After implementing various time and frequency domain analyses to experimentally recorded ambient vibration data it is necessary to update the mathematical model developed in Chapter 4. By doing so, it will be possible to accurately describe the dynamic behavior of the bridge when it undergoes any type of excitation, whether it is of low or strong intensity. Table 5-3 summarizes the obtained results of natural frequencies and damping ratios for each implemented methodology.

Table 5-3: Summary of results for bridge's identified dynamic parameters

Method	f_n [Hz]	ω_n [rad/sec]	ξ
FFT	3.271	20.552	------
WT	3.246	20.395	------
RDT-WT	3.345	21.017	0.02283
RDT-Log. Dec.	3.28	20.609	0.028478
Average	**3.2865**	**20.6434**	**0.025654**

With the calculated dynamic parameters, it is possible to compute the updated coefficient values for the bridge's motion equation.

From the computed natural frequency, ω_n, it is possible to compute an updated equivalent mass or an updated equivalent stiffness. Hence, for this study it was decided to compute an updated equivalent stiffness and keep the originally computed equivalent mass. The reason for this decision relies in the fact that the mass, although estimated for a SDOF system, was obtained from the original design plans. On the contrary, the stiffness was computed by assuming ideal boundary conditions and linear-elastic material assumptions. However, the assumed scenario may not be true at present. There is a possibility of boundary conditions degradation due to aging and environmental effects. In addition, the stiffness of the soil beneath the structure was not considered in the original analysis assumptions and its interaction with the structure influences the bridge dynamic behavior. Thereby, from equation (4.3), the updated equivalent bridge stiffness as an approximated SDOF system can be obtained by

$$K = m\omega_n^2 \tag{5.10}$$

Substituting the computed equivalent mass and the experimentally obtained natural frequency, the resultant updated bridge's stiffness is $K = 3{,}328.623\ k/in$.

Similarly, the updated damping coefficient, C, can be obtained by substituting in equations (4.5) and (4.6) the computed equivalent mass value and the experimentally obtained natural frequency and damping ration. This will result in a value for the updated damping coefficient of $C = 99{,}277.27\ {}^{lb\cdot s}/_{ft}$. Therefore, the resulting updated motion equation for Ponce Highway Bridge [ID: 2348] is expressed as:

$$93{,}731.06\,\ddot{u}(t) + 99{,}277.27\,\dot{u}(t) + 39{,}943{,}479.276\,u(t) = F(t) \tag{5.11}$$

5.1.3 Dynamic Assessment from Earthquake Records

The PRSMP, who has a network of instrumented structures in Puerto Rico and the Caribbean, registered four earthquake motions felt in the island's southern region and therefore recorded the bridge acceleration response histories in Ponce Highway Bridge [ID: 2348]. The information for each ground motion was provided by the PRSMP and is shown in Table 5-4. From a seismological point of view, the distances shown in the table are not exact and may contain a tolerated approximation error. With the acceleration responses, it was desired to evaluate the frequency content of the pre-event motions, the strong motions, and the post-event motions. The main purpose for this staged analysis was to evaluate the dynamic properties of the bridge before the main shock and compare them to the values obtained after the event. Especially if the strong motion possessed a frequency range in which the bridge's resonant frequency is contained.

Table 5-4: Information on the ground motions received by Ponce Highway Bridge [ID: 2348]

ID	Date	Time [UTC]	Lat. [°]	Lon. [°]	Focal Depth [km]	Epicentral Dist. [km]	Magnitude
EQ-1	5/16/2010	5:16:11 AM	18.40	-67.07	113.1	66.9	5.8
EQ-2	12/24/2010	11:43:45 PM	18.26	-66.14	102.9	58.6	5.4
EQ-3	1/13/2014	4:01:04 AM	19.14	-66.82	36	129.5	6.4
EQ-4	5/28/2014	9:15:06 PM	18.05	-68.35	90	184.3	5.8

However, a difficulty for assessing the earthquakes' responses is that no sensor was installed at the ground beneath the structure. Knowing that the response measured at sensor #5 is the result of contributions from motions in both abutments as well as from the ground beneath the columns supporting the cap bean (where sensor #5 is installed), it is very difficult to determine if the frequency content of a measured ground motion adversely influenced the lateral response of the bridge or not. In addition, the measurements provided by the PRSMP just exhibits the earthquakes' responses and do not show enough sampling period before and after the event to allow for dynamic parameters comparisons. Because of this lack of information, the analysis is limited to only evaluate the frequency content of the pre-event, the strong motion, and the post-event by implementing FFT and Wavelet transforms to compare the efficacy of both mathematical tools. Consequently, it is possible to compare the results with the bridge's natural frequency previously identified from more recent recordings of ambient vibrations and presented in Section 5.1.

A more detailed information of the recorded responses at sensor #5, located in the bridge's cap beam, at sensors #6 and #11, located at the top of the left and right abutments respectively, and at sensors #2 and #8, located at the mid-height of the left and right abutments respectively, is shown in Tables 5-5 to 5-8.

Table 5-5: Acceleration, velocity, and displacement responses' peak values for EQ-1 recorded in sensors #2, #5, #6, #8, and #10

Event ID: EQ-1					**Recorded Duration: 70 sec.**	
Sensor	*Acceleration [g]*		*Velocity [in/s]*		*Displacement [in]*	
	Time	Peak	Time	Peak	Time	Peak
S2	23.2	0.01662	23.04	0.7359	70	3.218
S5	24.89	0.03545	28.24	0.7771	70	4.017
S6	27.07	0.03718	23.03	0.8871	70	3.937
S8	23.23	0.0184	23.08	0.67	73.53	2.055
S11	24.89	0.02982	27.37	0.7019	73.5	2.311

Table 5-6: Acceleration, velocity, and displacement responses' peak values for EQ-2 recorded in sensors #2, #5, #6, #8, and #10

Event ID: EQ-2					**Recorded Duration: 68 sec.**	
Sensor	*Acceleration [g]*		*Velocity [in/s]*		*Displacement [in]*	
	Time	Peak	Time	Peak	Time	Peak
S2	23.96	0.008316	24.08	0.2343	68	0.735
S5	24.24	0.02341	24.14	0.5513	65.25	0.8032
S6	24.2	0.0186	24.13	0.4726	67.52	0.9628
S8	23.79	0.008007	24.12	0.2404	68	0.2295
S11	24.05	0.02561	24.13	0.5897	67.51	0.5373

Table 5-7: Acceleration, velocity, and displacement responses' peak values for EQ-3 recorded in sensors #2, #5, #6, #8, and #10

Event ID: EQ-3					**Recorded Duration: 79 sec.**	
Sensor	*Acceleration [g]*		*Velocity [in/s]*		*Displacement [in]*	
	Time	Peak	Time	Peak	Time	Peak
S2	31.36	0.02217	39.7	0.9287	79	1.729
S5	31.37	0.04307	31.27	1.119	79	1.955
S6	31.37	0.04328	31.27	1.162	79	2.058
S8	25.29	0.01962	39.7	0.8999	79	1.01
S11	31.37	0.0386	25.15	1.104	79	2.178

Table 5-8: Acceleration, velocity, and displacement responses' peak values for EQ-4 recorded in sensors #2, #5, #6, #8, and #10

Event ID: EQ-4					**Recorded Duration: 69 sec.**	
Sensor	*Acceleration [g]*		*Velocity [in/s]*		*Displacement [in]*	
	Time	Peak	Time	Peak	Time	Peak
S2	29.41	0.01151	29.3	0.382	68.64	1.133
S5	29.46	0.02373	29.57	0.5669	68.61	1.581
S6	29.67	0.01823	29.59	0.557	66.86	0.6261
S8	22.36	0.01054	26.15	0.381	70	1.632
S11	26.3	0.02571	26.22	0.5662	69.61	2.114

The characteristics of the earthquakes' response measurements show that the four ground motions to which the bridge was subjected were small and possibly of a low intensity. Although there are no recorded ground motions, sensors #2 and #8 give an idea of the motion received by the bridge from the ground by assuming that both abutments are rigidly enough for not to significantly alter the amplitudes of the ground accelerations experienced by the bridge. In Sections 5.3.1 and 5.3.2 the FFT and the Wavelet transforms are respectively implemented to analyze the frequency spectra of the complete earthquake responses in sensor #5 to evaluate their performance. In Section 5.3.3, the FFT will be applied to the strong motion segment of each recorded earthquake response at sensor #5. Complete earthquakes' responses in that sensor are shown from Figure 5-12 to 5-15.

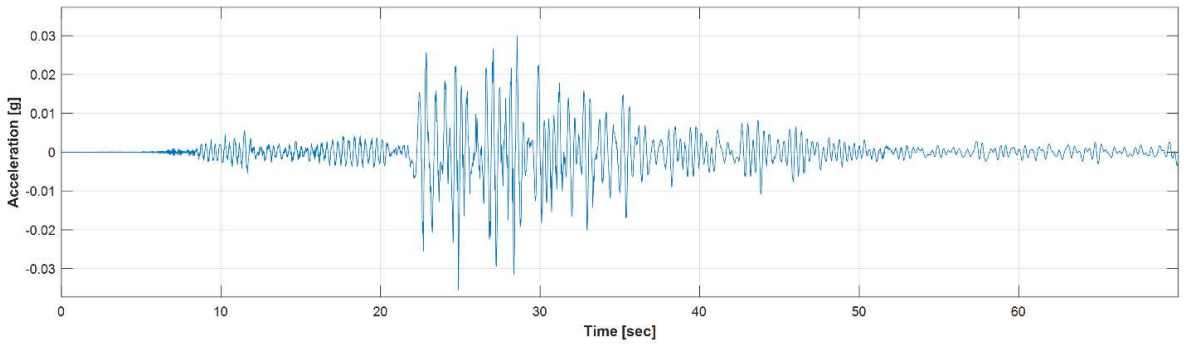


Figure 5-12: Acceleration response EQ-1 recorded at sensor #5 on May 16, 2010

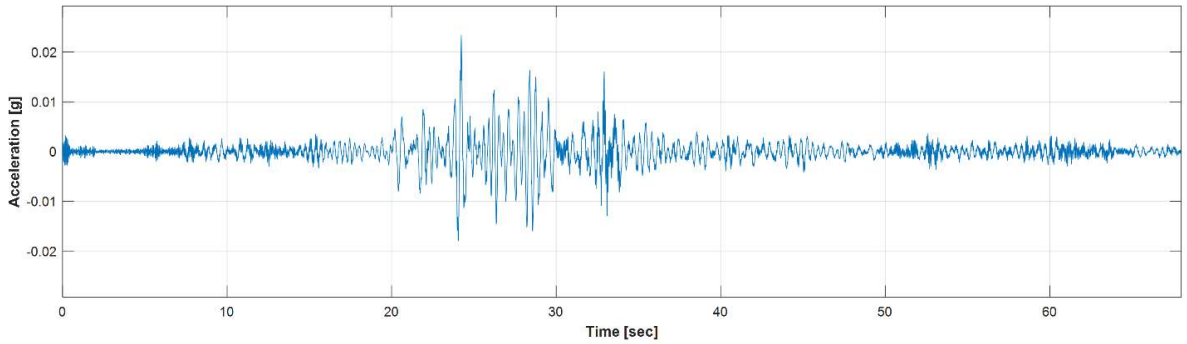


Figure 5-13: Acceleration response EQ-2 recorded at sensor #5 on December 24, 2010

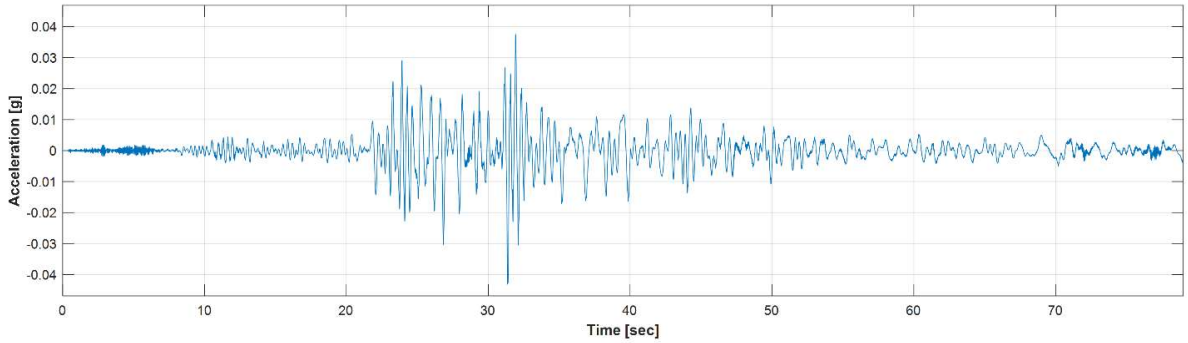


Figure 5-14: Acceleration response EQ-3 recorded at sensor #5 on January 13, 2014

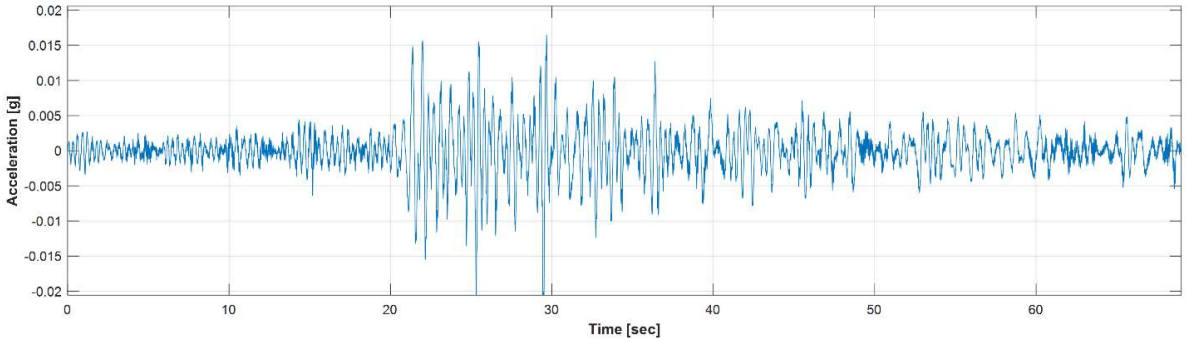


Figure 5-15: Acceleration response EQ-4 recorded at sensor #5 on May 28, 2014

The signal-to-noise ratio (SNR) is a measure that describes how much noise is embedded in a signal. In this study, it compares the strength level of a desired earthquake response to the level of background noise recorded. It is usually measured in decibels (dB) and defined as shown in equation (5.12), in which for this case $s(t)$ refers to an earthquake response and $n(t)$ refers to ambient vibration recordings. It is necessary that both signals have the same length and is recommended to avoid zero-padding because it alters real SNR values. Table 5-9 shows the results.

$$SNR = \frac{P_{signal}}{P_{noise}} = \frac{\sum_{i=1}^{N} s(t)}{\sum_{i=1}^{N} n(t)} \tag{5.12}$$

Table 5-9: Computed Signal-to-Noise ratios for each of the recorded earthquake responses

Response ID	SNR	SNR_{dB}
EQ-1	95.128	19.783
EQ-2	27.39	14.376
EQ-3	104.317	20.183
EQ-4	43.6116	16.396

5.1.3.1 Frequency Spectrum Identification via FFT

By computing the frequency spectrum of recorded responses, it is possible to get an idea of the frequency content of the unknown ground motion. When a certain system is responding to forced dynamic excitations, its vibratory behavior tends to reflect the characteristics of the exciting forces and particularly its frequency content. Therefore, the frequency spectra of complete earthquake responses allow the engineer to check if the identified natural frequencies of an excited system are contained within the apparent dominant frequency content of the input excitation. Due to the absence of a free-field station and of a sensor at the columns' supports, the frequency spectrum is computed for each of the four earthquakes' responses. In this section the FFT was implemented.

Currently, the FFT is the best mathematical tool to identify the complete frequency content of a signal's total sinusoidal constituents. Hence, it is sensitive to the effect of unwanted and disturbing small amplitude oscillations embedded in the signal, commonly known as noise. However, as noted from Table 5-9, the computed SNR for the responses are not small enough as to mask the needed frequency content. Although the noise content in this case does not adversely affect the capabilities of the FFT and its sensitivity in showing what is desired to reveal, this is something that can negatively affect the results with small SNRs. In the analyses, the frequency spectra were computed with a frequency resolution of $\Delta f = 0.00013889\ Hz$. It was obtained by zero padding each of the recorded earthquake responses to a signal's length of two hours sampled at $200\ Hz$. This was done because the poor frequency resolution provided by the original responses' lengths displayed distorted frequency spectra in which it was not clear which were the dominant frequencies' ranges. Figures 5-16 to 5-19 show the generated frequency spectrum for each of the complete earthquake responses after zero padding.

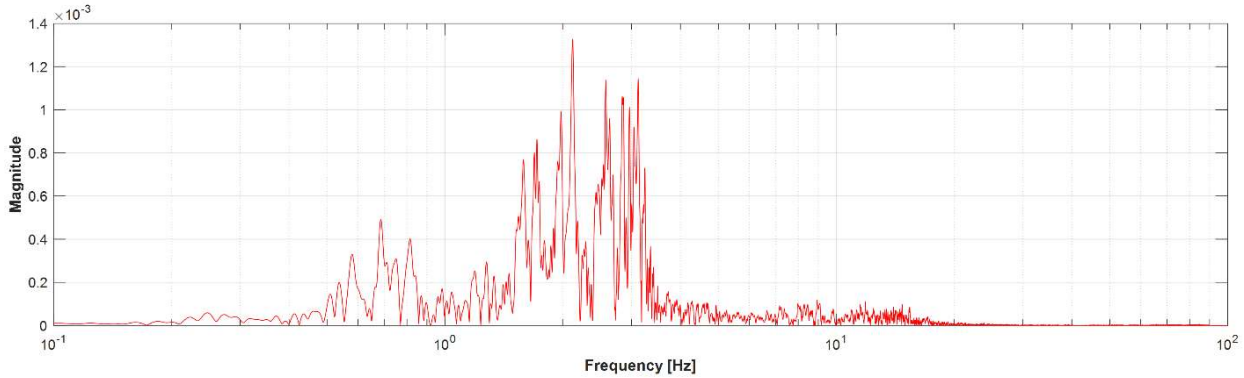


Figure 5-16: Frequency spectrum for earthquake response EQ-1 recorded at sensor #5 on May 16, 2010

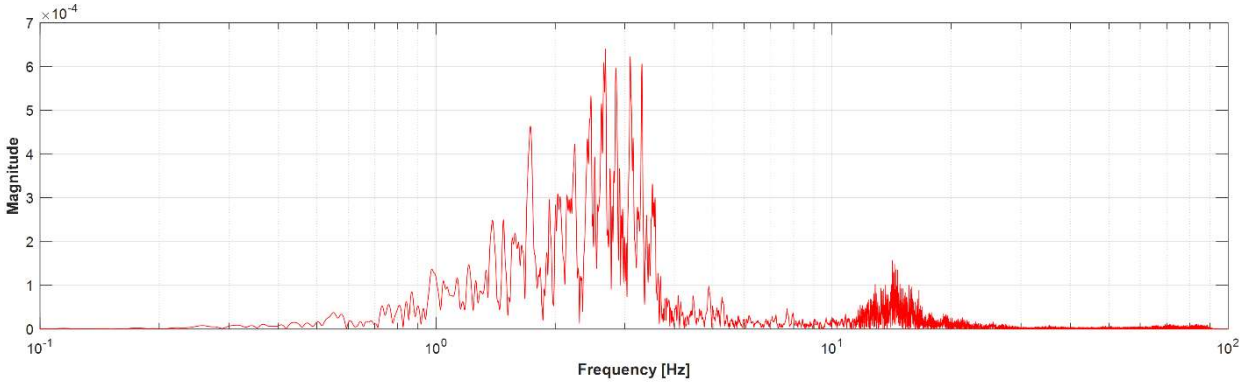


Figure 5-17: Frequency spectrum for earthquake response EQ-2 recorded at sensor #5 on December 24, 2010

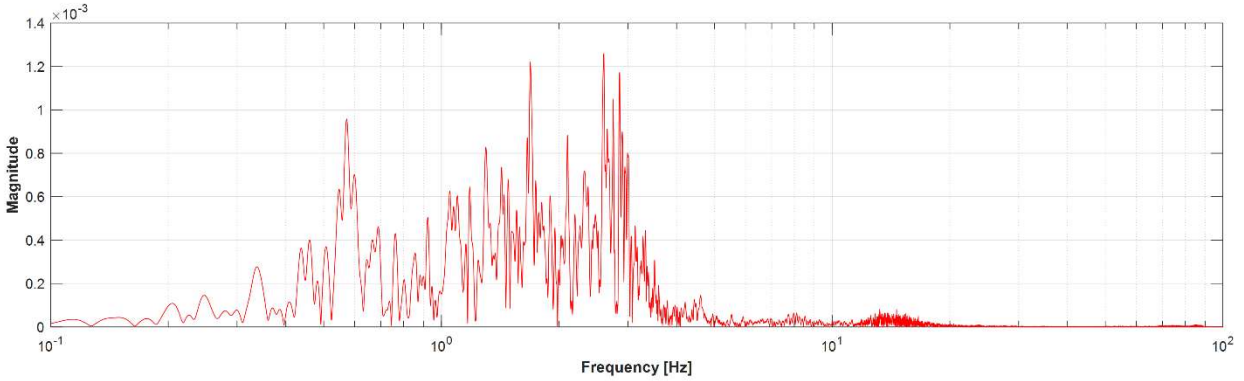


Figure 5-18: Frequency spectrum for earthquake response EQ-3 recorded at sensor #5 on January 13, 2014

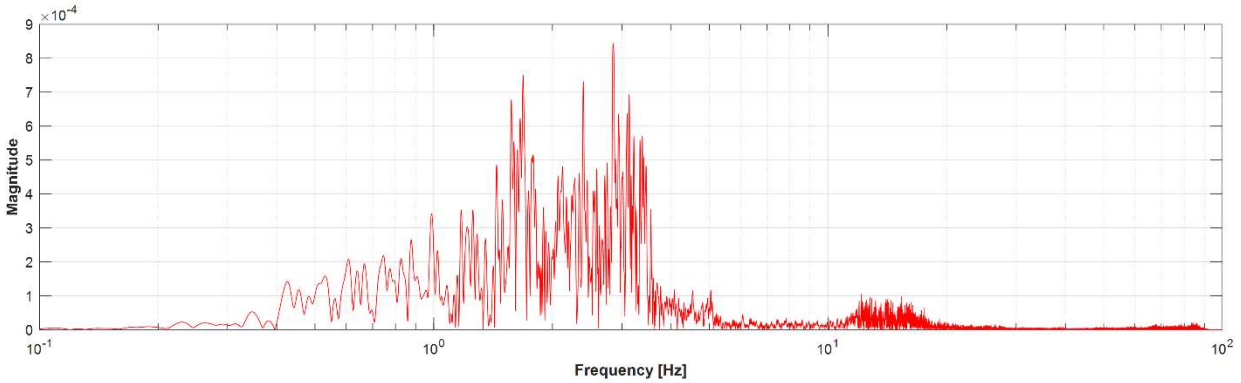


Figure 5-19: Frequency spectrum for earthquake response EQ-4 recorded at sensor #5 on May 28, 2014

From the results presented in the Figures, it can be noticed that the traffic vibration noise is present in the four recordings and is consistent with the range obtained in Section 5.1. Earthquakes' responses EQ-1, EQ-2, and EQ-4 display wider dominant frequency spectra, approximately ranging from 0.4 Hz to 3.5 Hz. On the contrary, EQ-2 displays a narrower spectrum with dominant frequencies approximately ranging from 1.5 Hz to 3.5 Hz. In addition, frequencies contained close to the bridge's identified natural frequency seems to show more power within the response than on the other three responses. This may infer the presence of a dominant frequency within the input ground motions that is close the bridge's resonant frequency of vibrations.

5.1.3.2 Frequency Spectrum Identification via Wavelet Transforms

The implementation of wavelet transforms to the recorded earthquakes' responses provides an improved description of the structure's dynamic behavior. It allows to trace the dynamic changes through the recorded time interval and hence let the analyst know the exact instant in which each constituent frequency of the response is being reflected by the system's motions. Figures 5-20 to 5-27 shows two 3D views of the generated wavelet maps for each of the earthquakes' responses recorded at sensor #5. In all of them, it is possible to see small traces of the frequencies corresponding to traffic vibration responses in the same range as determined in the previous frequency analyses. These observed low amplitude wavelet coefficients mean that the total structure's response when the earthquake is exciting the bridge is, to the most extent, influenced by it than by the ambient or traffic vibrations. However, the wavelet transform is capable to identify all the frequency components simultaneously regardless of the excitation's amplitude or source and through all the response duration. This intrinsic characteristic highlights the transform's sensitivity when properly applied and its reliability for identification purposes.

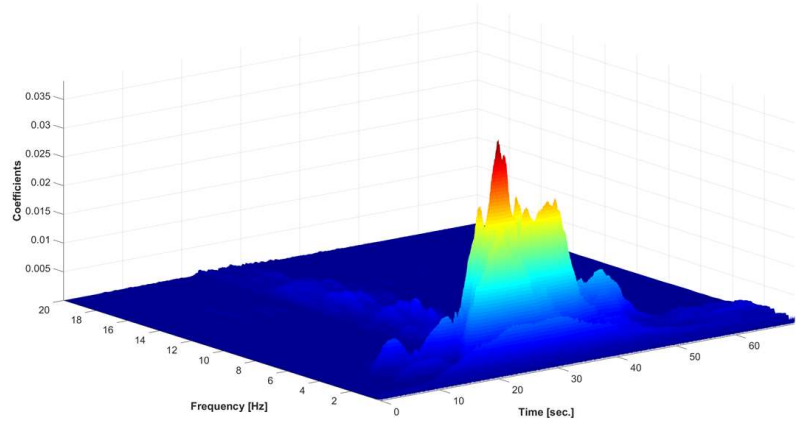


Figure 5-20: 3D wavelet map for earthquake response EQ-1 recorded in sensor #5 on May 16, 2010

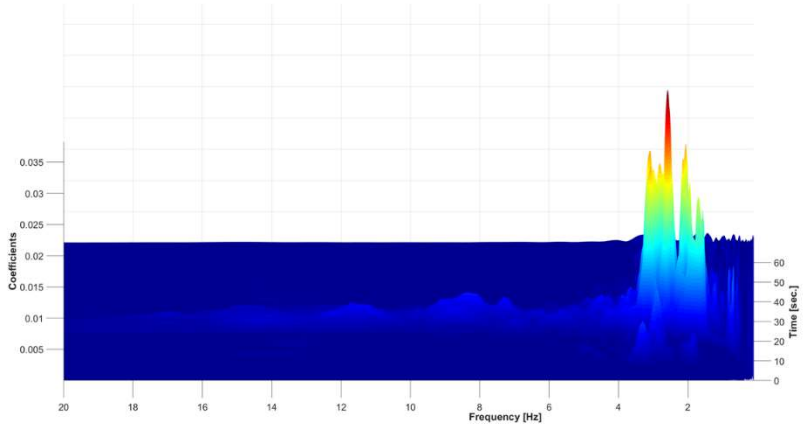


Figure 5-21: Dominant frequencies for earthquake response EQ-1 recorded in sensor #5 on May 16, 2010

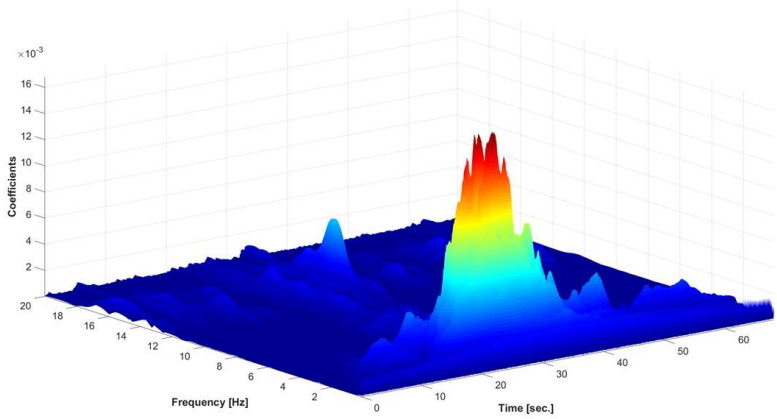


Figure 5-22: 3D wavelet map for earthquake response EQ-2 recorded in sensor #5 on December 24, 2010

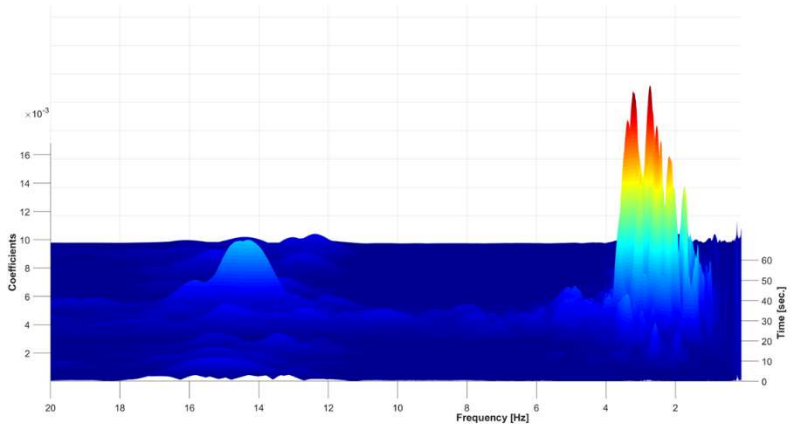


Figure 5-23: Dominant frequencies for earthquake response EQ-2 recorded in sensor #5 on December 24, 2010

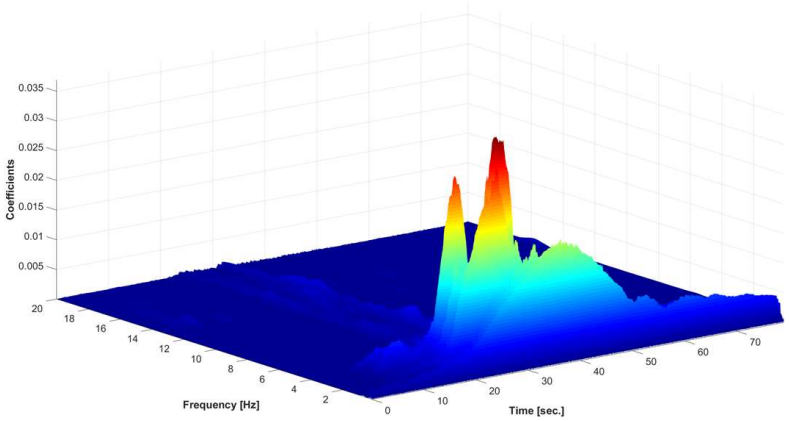


Figure 5-24: 3D wavelet map for earthquake response EQ-3 recorded in sensor #5 on January 13, 2014

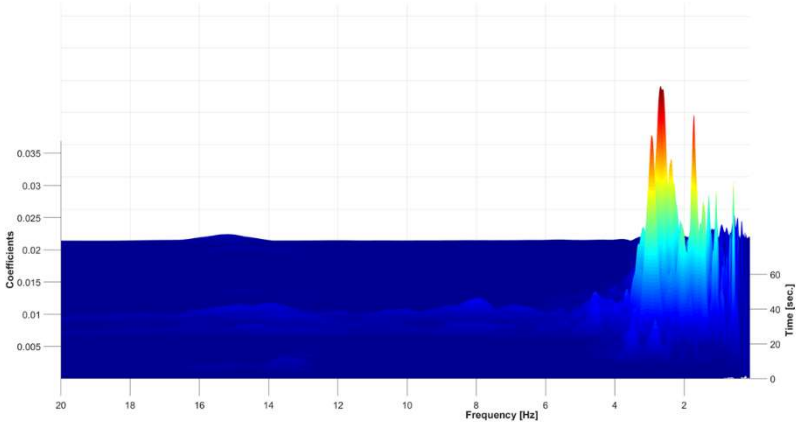


Figure 5-25: Dominant frequencies for earthquake response EQ-3 recorded in sensor #5 on January 13, 2014

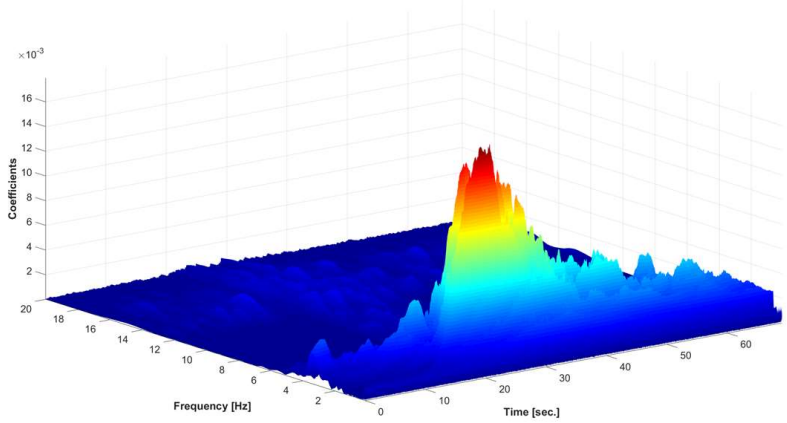


Figure 5-26: 3D wavelet map for earthquake response EQ-4 recorded in sensor #5 on May 28, 2014

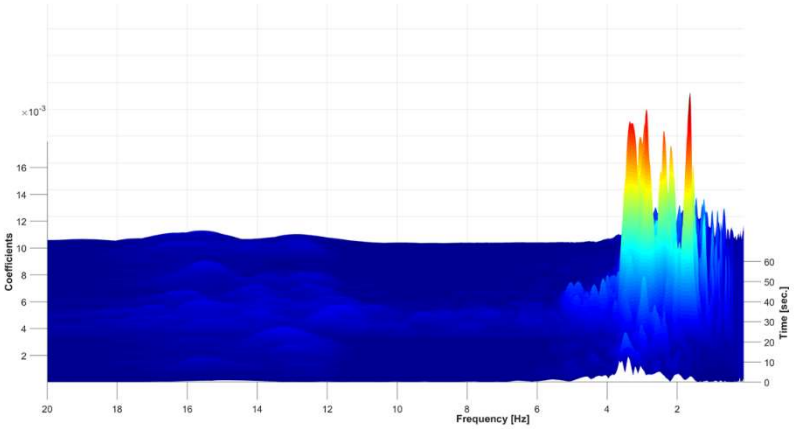


Figure 5-27: Dominant frequencies for earthquake response EQ-4 recorded in sensor #5 on May 28, 2014

In particular, this special feature is of great benefit when assessing damaged structures after a strong excitation. Frequently, structural damage scenarios are associated with abrupt changes observed within the response's instant frequencies in a structure subjected to strong dynamic excitations. However, this is not always true. With sufficiently extensive recordings capable of capturing an earthquake while being recording ambient vibrations, it is possible to track the response frequencies' behavior in time. This provides the chance to compare the dynamic properties before and after the shaking, especially after an abrupt instant frequency change. In the cases where a shift in frequencies is detected, this tool provides the advantage of monitoring the altered natural frequencies for long periods of time allowing to determine if the dynamic changes are transient or permanent. If after a determined amount of time the natural frequency is restituted to its original value, it was a transient dynamic change with other causes not necessarily associated with structural damage, such as soil nonlinearities or environmental changes. If the dynamic

change is permanent it may have a relation with the observed abrupt frequency shift during the excitation. In both cases, visual inspections must be performed to validate the dynamic analysis results and possible findings.

5.1.3.3 Frequency Spectrum of Strong Motion Responses

In the field of earthquake engineering, it is a common practice to extract the time segment of the strong motion of an earthquake to better relate the structural response to the strong motion's frequency content and peak accelerations. A simple and commonly used measure of strong motion duration is one known as the *bracketed duration*. It consists in the shaking duration above a certain threshold acceleration value, commonly taken as $0.05g$ or $0.1g$, although it is based on the analyst's judgement. Simply explained, an earthquake's strong motion duration is defined as the time between the first and last peaks of motion that exceeds the established threshold value. However, his method relies on threshold values selected on qualitative judgement after the observation of the recorded earthquakes. Moreover, this method has been successfully implemented on ground motion recordings of moderate and strong earthquakes but not on low intensity motions. The peak accelerations experienced by the bridge in the four earthquakes were less than the minimum recommended threshold value of $0.05g$. Accordingly, this may be the result of ground motions with less acceleration amplitudes. In addition, because there is no direct recording of ground motions for the four events it is difficult to concisely determine what is the contribution of each strong motion to the bridge's respective responses. For this reason, an alternate method for determining the bridge's strong motion response duration should be implemented. Consequently, this will allow to determine a better estimate of the effects of the imparted strong motion in terms of the frequency content exhibited in the response's strong motion. To this end, the *significant duration* of the recorded earthquake responses is computed in this study.

The *significant duration* can be defined as the time interval across which a specified amount of energy is dissipated within the structure. For this research, the bridge's dissipated energy due to the earthquakes' excitation is related to the Arias Intensity (Arias, 1970), defined by

$$I_A = \frac{\pi}{2g}\int_0^T a^2(t)\,dt \tag{5.13}$$

in which $a(t)$ is the acceleration time histories of the earthquakes' responses, g is the gravity's acceleration constant, and T represents the complete duration of the recorded accelerations. The results are then presented in Husid plots, which are used to track the build-up of dissipated energy in time. The significant duration is commonly determined as the time interval between 5% - 75% or 5% - 95% of the computed system's Arias Intensity. The decision to use the significant duration to define the strong response motion was based on the need of a quantitative approach in which stable results could be obtained for low-intensity motions from small earthquakes. In addition, the use of the Arias Intensity integral for computing significant duration of ground motions has increasingly popularized among earthquake analysts.

Hence, the Arias Intensity was computed for each of the four earthquakes' responses. For this study, the significant duration for each recorded response is defined by the time interval corresponding to 5% and 95% of the correspondent Arias Intensity measure. From Figures 5-28 to 5-31 it is possible to observe the Husid plots in which the Arias Intensity for each event's response is displayed with markers denoting the cutting points that define the time interval for each response strong motion. Similarly, Table 5-10 shows the time intervals that defines each significant duration.

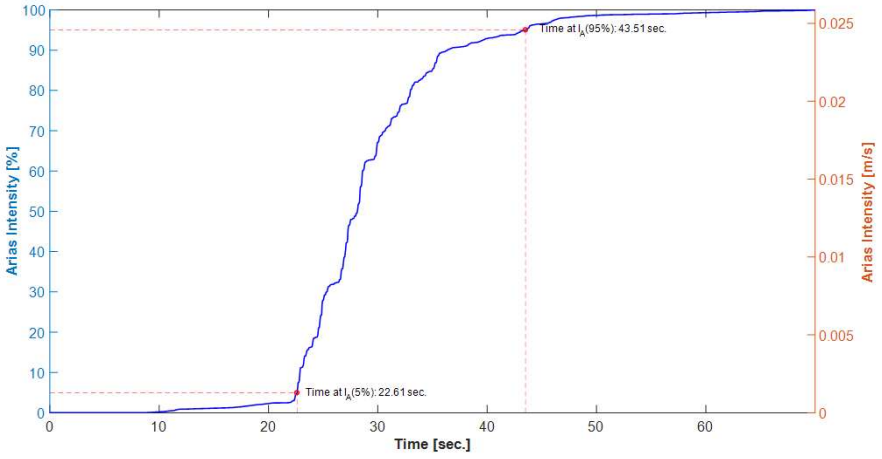


Figure 5-28: Arias intensity delimiting the interval where 90% of the imparted energy was dissipated by the bridge in EQ-1

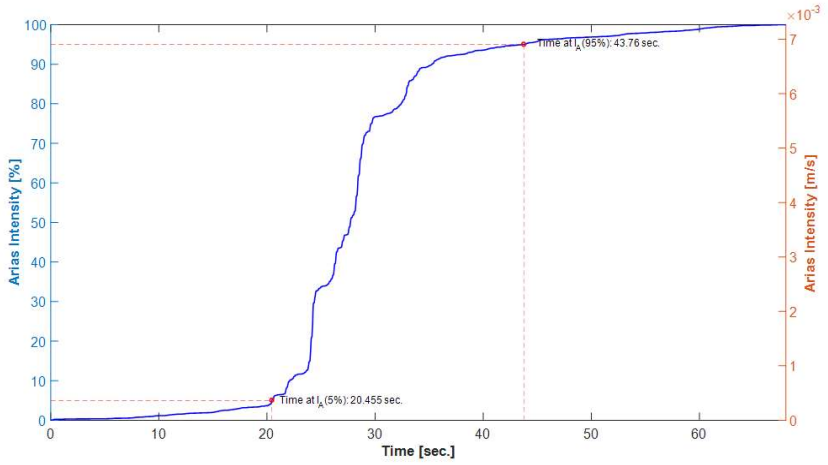


Figure 5-29: Arias intensity delimiting the interval where 90% of the imparted energy was dissipated by the bridge in EQ-2

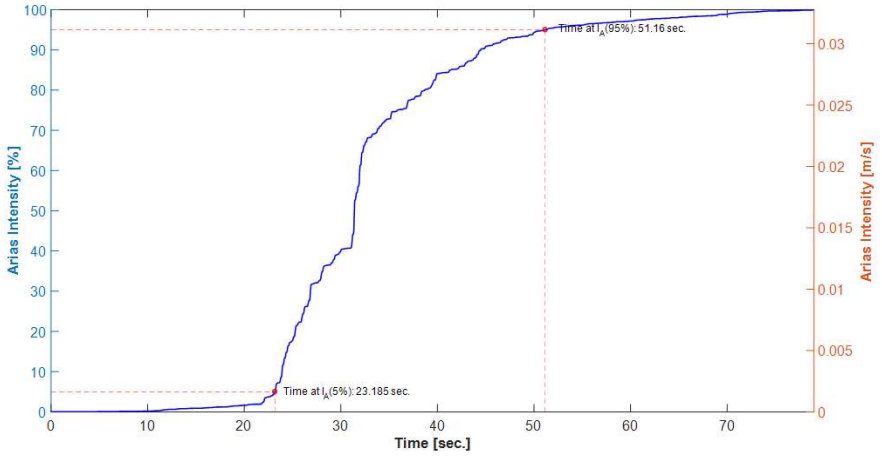


Figure 5-30: Arias intensity delimiting the interval where 90% of the imparted energy was dissipated by the bridge in EQ-3

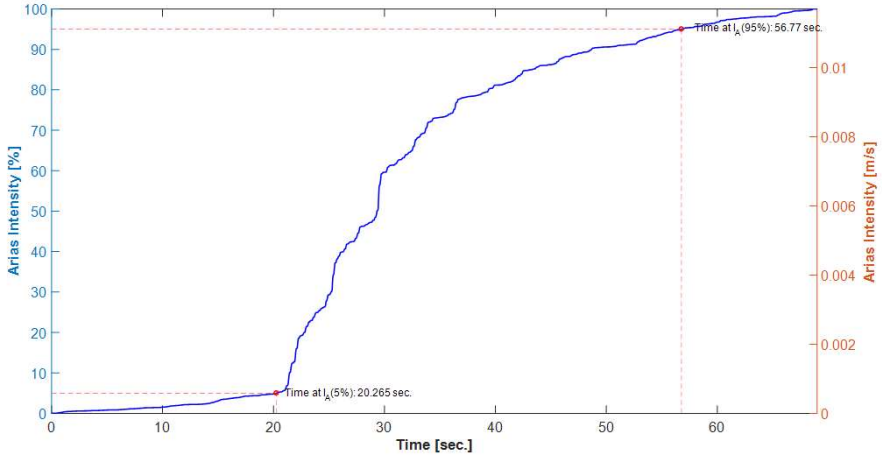


Figure 5-31: Arias intensity delimiting the interval where 90% of the imparted energy was dissipated by the bridge in EQ-4

Table 5-10: Significant duration for each of the recorded earthquake responses in sensor #5

Response ID	$t_{5\%}$ [sec.]	$t_{95\%}$ [sec]
EQ-1	22.61	43.51
EQ-2	20.445	43.76
EQ-3	23.185	51.16
EQ-4	20.265	56.77

With the time intervals obtained for the significant durations it is possible to extract the response's strong motion for each earthquake from its original record. Once defined, their individual frequency spectrum can be computed with any of the frequency analyzers previously presented. For this analysis, the FFT is used with the same frequency resolution as for the previous frequency domain analysis, $\Delta f = 0.00013889\ Hz$. Figures 5-32 to 5-35 show the original recorded responses for each earthquake with the computed significant duration interval delimited by two vertical lines. A second plot in each figure displays its corresponding frequency spectrum.

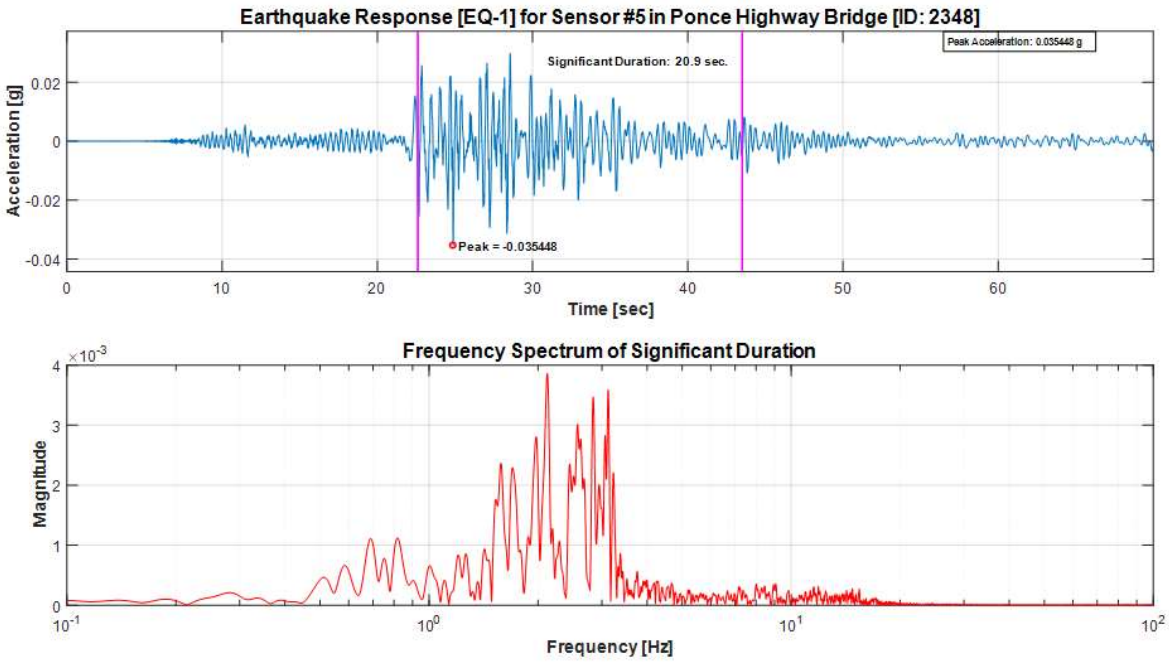


Figure 5-32: Significant duration of 20.9 seconds in earthquake response EQ-1 and its corresponding frequency spectrum

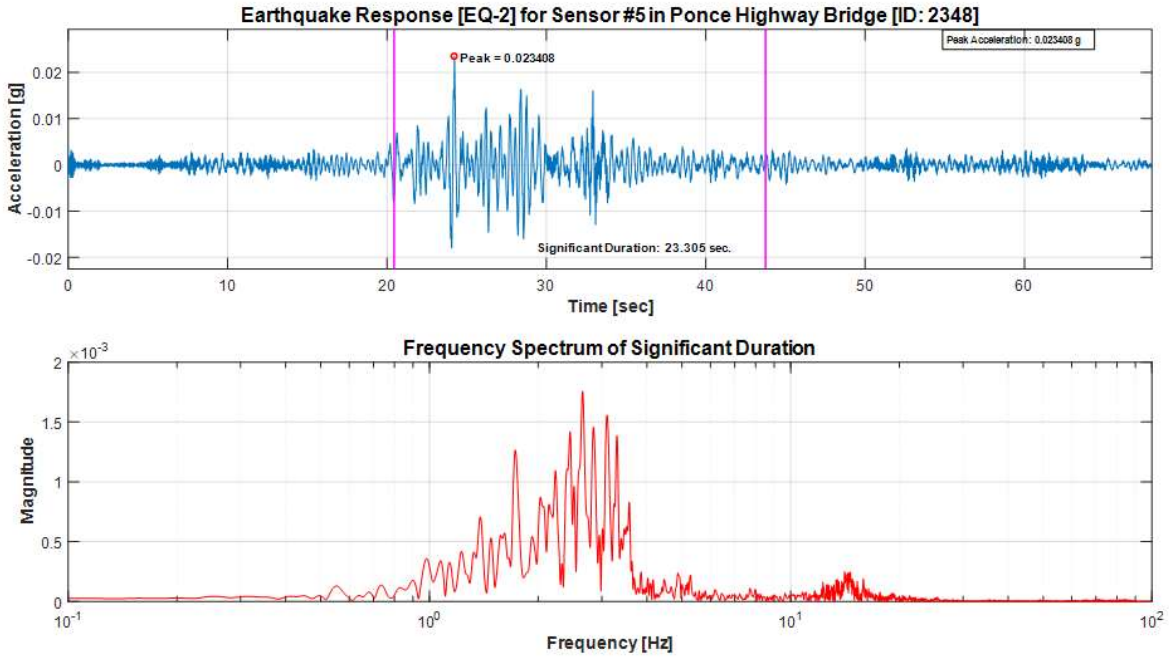


Figure 5-33: Significant duration of 23.305 seconds in earthquake response EQ-2 and its corresponding frequency spectrum

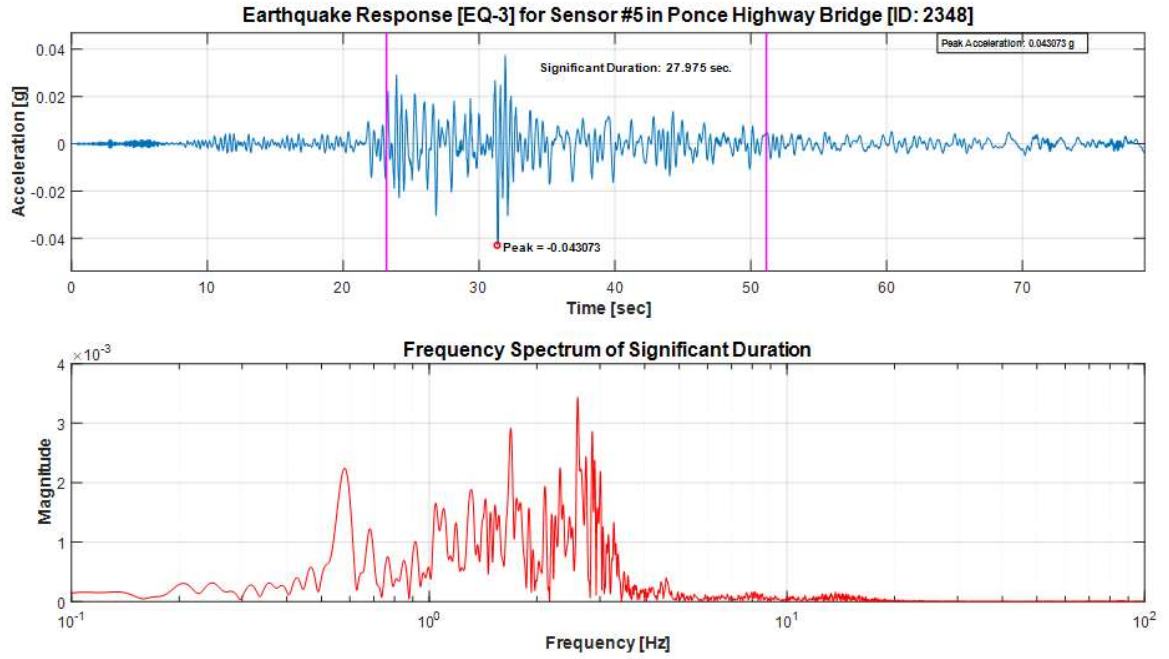


Figure 5-34: Significant duration of 27.975 seconds in earthquake response EQ-3 and its corresponding frequency spectrum

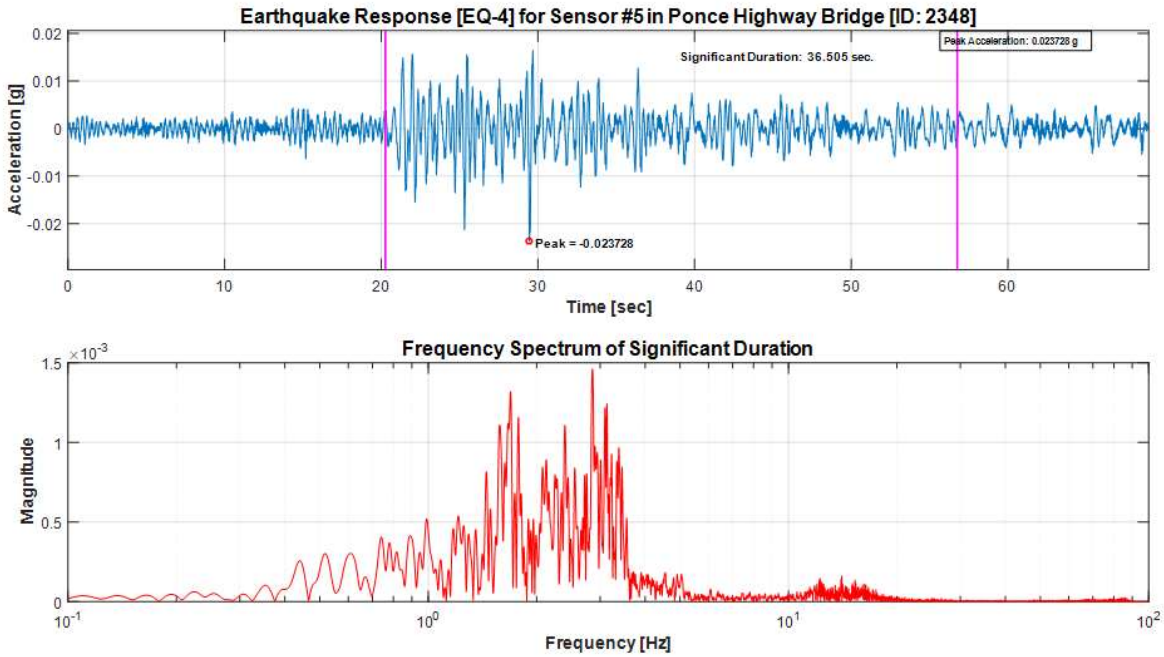


Figure 5-35: Significant duration of 36.505 seconds in earthquake response EQ-4 and its corresponding frequency spectrum

It can be observed that their computed frequency spectra are very similar to the frequency spectra of the original responses. The reason for this similitude is because the complete response recording for each earthquake contains only the earthquake response, without small amplitude responses due to ambient vibrations. Furthermore, in earthquake response EQ-4 it seems as if it has not finished by the end of its time history. Besides almost having the same frequency spectra both the significant duration interval and the complete response, this short record adversely influences the values of the beginning and end of the significant duration. The reason is because if the recording time would have been made longer by including segments of ambient responses before the start and after the complete end of the recorded event it is guaranteed that the structure is at rest at the beginning of the recording and at its end. Therefore, the cumulative dissipated energy computed by the Arias Intensity integral of equation (5.13) may reflect a 5% and a 95% of dissipated energy at time instants different from the ones currently obtained. With this change in significant duration may be possible to have a more accurate description of the frequency content of the most influential response segment in addition to be able to measure possible fundamental frequency shifts by comparing pre-and-post event spectra.

5.2 PRILA Condominium

5.2.1 Dynamic Assessment from Ambient Vibration Records

Small amplitude vibration measurements were recorded at PRILA Condominium on Thursday, November 19, 2015 at 12:00 am. The recording period lasted 24 hours and the data was simultaneously sampled at $200\,Hz$ in 36 different sensor channels on the $N-S$, $E-W$, and vertical directions. However, for this study the sensors of interest were the ones in the $N-S$ direction, which is the slender dimension of the building, making it its weak axis. A total of 20 accelerometer sensors are evenly distributed throughout the height of the building at the sides of each instrumented floor slab. This was illustrated in Figure 4-8. Raw data was baseline corrected by piecewise cubic spline and converted to acceleration units as a fraction of the gravitational constant, $\boldsymbol{g}$. Figure 5-36 shows the recorded acceleration signal for sensor #33, located at the 19th floor slab on the east side of the building. This signal is a typical representation of the recorded signals in the other sensors. All the acceleration signals recorded in the $N-S$ direction are used in the following analyses.

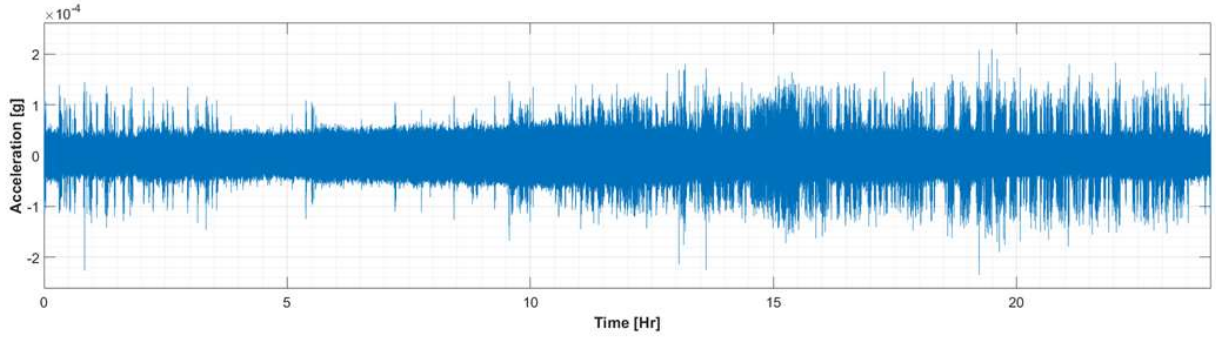


Figure 5-36: Twenty-four hours of ambient vibrations recording in sensor #33 at PRILA Condominium

5.2.1.1 Frequency Domain Identification via Power Spectral Density

The power spectral density (PSD) of a signal describes its power distribution per frequency component. It provides a measure of the energy per unit frequency embedded in a segment of a recorded signal, therefore showing the energy variation of the frequency content or how the average power of a signal is distributed with frequency. Mathematically, it is the Fourier transform of the signal's autocorrelation function. The PSD applies to signals existing over all time or over a large enough time interval. The summation (i.e., integration) of the spectral components yields

the total power. This is analogous to integrating the squared of the time series, over the time domain, as dictated by Parseval's theorem. For continuous and discrete signals, the PSD can be defined as equations (5.14) and (5.15), respectively.

$$S(\omega) = \left[\int_{-\infty}^{\infty} x(t)\, e^{-j\omega_o t}\, dt\right]^2 \tag{5.14}$$

$$S[k] = \left[\sum_{n=0}^{N-1} x[n]\, e^{-j\omega_k n}\right]^2 \tag{5.15}$$

For the purpose of frequencies' identification of a signal, the results obtained by implementing the PSD are no different than the results that the FFT generates. However, an advantage of implementing the PSD instead of the FFT is that the PSD generates a spectrum in which the system's frequencies peaks are denoted with a much higher magnitude (i.e., power) than the embedded frequencies that do not intrinsically corresponds to the studied system, such as is the case of noise embedded in the signal. This is of particular help when identifying the natural frequency content of systems with multiple degrees of freedom through their vibration responses and in which their higher frequencies do not get excited as the lower frequencies do. In addition, when lower magnitude random vibrations are continuously present in the forced structural response, the PSD greatly helps to unmask the natural systems frequencies by drastically reducing the magnitude of the non-natural frequencies. For these reasons, the PSD is implemented in the frequency analysis for the PRILA Condominium. The generated PSD for sensor #33 is illustrated in Figure 5-37 as an example. Tables 5-11 and 5-12 shows the identified natural frequencies for the building per sensor for the east and west sides of the structure, respectively.

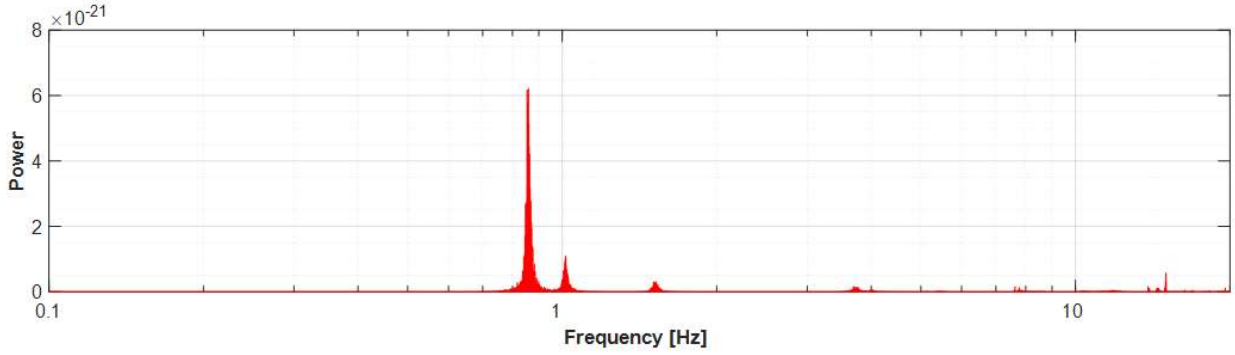


Figure 5-37: PSD for twenty-four hours of recorded ambient vibrations in sensor #33 at PRILA Condominium

Table 5-11: Identified natural frequencies from east-side sensors in PRILA

East Side [N-S]				
Sensor	f_1	f_2	f_3	f_4
S12	0.860	3.697	7.626	11.780
S15	0.860	3.697	7.628	11.760
S18	0.860	3.697	7.628	11.760
S21	0.860	3.697	7.628	11.760
S24	0.860	3.697	7.628	11.760
S27	0.860	3.697	7.628	11.780
S30	0.860	3.697	7.628	11.760
S33	0.860	3.697	7.628	11.760
S36	0.860	3.697	7.766	11.770
Average	**0.860**	**3.697**	**7.643**	**11.766**

Table 5-12: Identified natural frequencies from west-side sensors in PRILA

West Side [N-S]				
Sensor	f_1	f_2	f_3	f_4
S10	0.854	3.753	7.628	11.780
S13	0.854	3.753	7.628	11.770
S16	0.854	3.753	7.628	11.770
S19	0.854	3.753	7.628	11.760
S22	0.854	3.753	7.628	11.770
S25	0.854	3.753	7.628	11.810
S28	0.854	3.753	7.628	11.760
S31	0.854	3.753	7.628	11.770
S34	0.854	3.753	7.628	11.940
Average	**0.854**	**3.753**	**7.628**	**11.792**

The average of the identified natural frequencies for each sensor was computed in order to identify the overall natural frequencies of the structure. The values of the first four natural frequencies and periods identified by the PSD for the PRILA Condominium are displayed in Table 5-13. Only the first four natural frequencies were confidently identified because the amounts of sensors provided for installation in PRILA were placed to record accurate responses up to the fourth mode of vibration. However, other peaks were noticed in the frequency spectrum range up to the Nyquist frequency, but their experimental modal shapes were unable to be accurately identified to validate it is a natural frequency, as presented in Chapter 6.

Table 5-13: Summary of first four identified natural frequencies and periods by PSD

$Mode$	f_n[Hz]	$\omega_n\ [rad/s]$	$T\ [sec.]$
1	0.857	5.384	1.167
2	3.725	23.405	0.268
3	7.636	47.976	0.131
4	11.779	74.009	0.085

5.2.1.2 Wavelet Transform Analysis on Random Decrement Signatures

A combined analysis approach was performed to PRILA's response signals in order to obtain its natural frequencies and corresponding damping ratios for the first four modes of vibration. By generating a random decrement signature from the ambient vibration response of the Ponce Highway Bridge [ID: 2348], the effectiveness of the Random Decrement Method on obtaining the system's dynamic parameters was demonstrated. However, the best estimate of the damping ratio was through the initial implementation of the Wavelet transform to the generated signature. This is because the Wavelet transform acts as a filter when constructing the analytical signal, thus segregating and reducing the effect of other frequency components that may be embedded in the recorded response and consequently improving its generated random decrement signature. Some of the unwanted frequency components may correspond to noise or to other frequencies intrinsic to MDOF systems. Because the PRILA Condominium is a MDOF system, it is convenient to implement this identification approach used on the Ponce Highway Bridge [ID: 2348].

First, it is intended to generate a random decrement signature for the ambient vibration responses recorded in each of the sensors in the $N-S$ direction. The Wavelet transform, with the Complex Morlet Wavelet used as its basis function, was applied to each of the random decrement signatures in order to separate all the frequencies' traces that may be embedded in them and that may correspond to higher order vibration modes of the system. Then the fundamental frequency of the building was computed by averaging the generated skeleton values from the wavelet map. Likewise, from the analytical signal generated for this identified frequency, the damping ratio was computed by applying the *Logarithmic Decrement Method* to all the points of the signal. Figure 5-38 shows the random decrement signature for sensor #33 as an example. In addition, Figures 5-39 and 5-40 show its spectrogram and its corresponding skeleton plot, respectively.

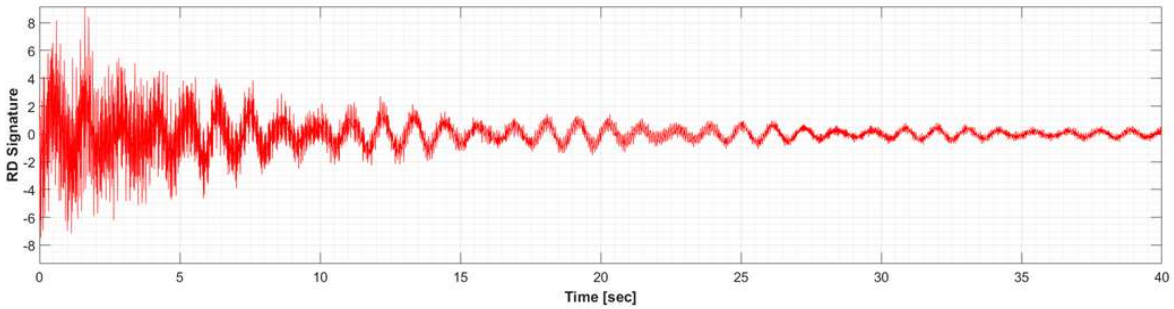


Figure 5-38: Random decrement signature for ambient vibration response at sensor #33

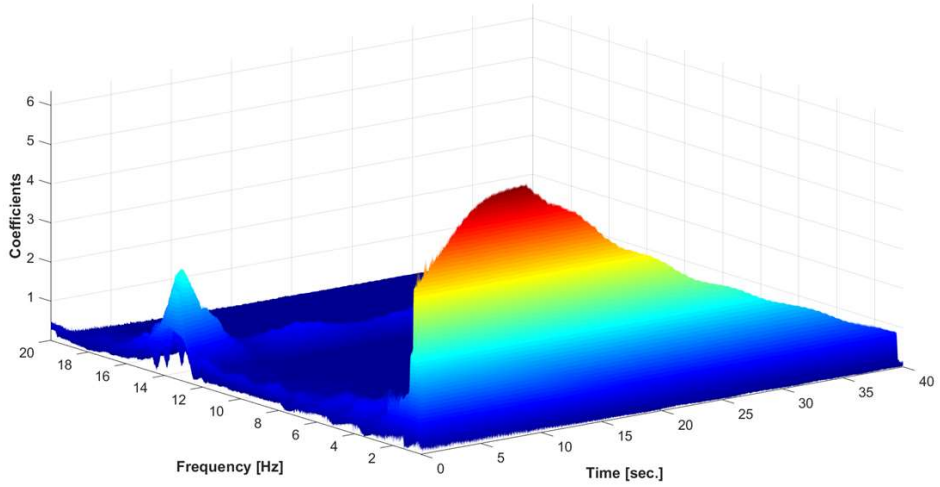


Figure 5-39: Spectrogram for wavelet transform computed to random decrement signature of ambient response at sensor #33

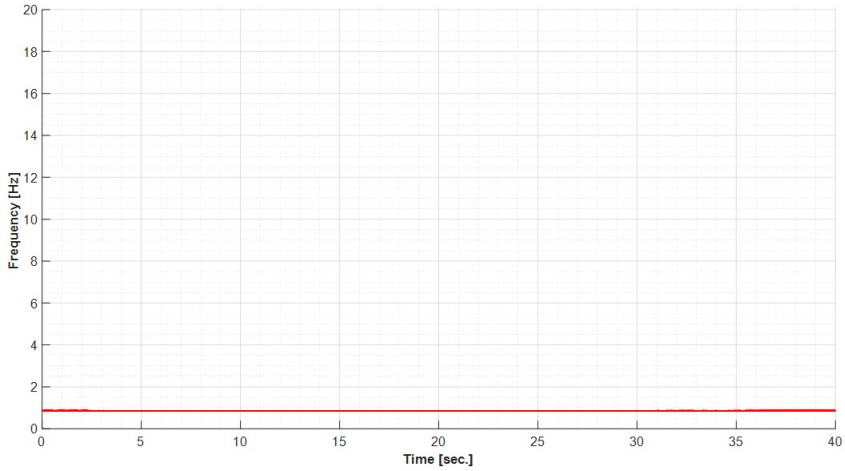


Figure 5-40: Skeleton curve from 0.5 Hz to 1.5 Hz corresponding to the computed wavelet map

The results obtained with this combined identification approach for each sensor in the $N-S$ direction is shown in Table 5-14. These values correspond to the fundamental mode of PRILA.

Table 5-14: PRILA's fundamental frequency identified by wavelet transform on RDS

West Side [N-S]				**East Side [N-S]**		
Sensor	f_n *[Hz]*	ξ		*Sensor*	f_n *[Hz]*	ξ
S10	0.8514	0.0169		S12	0.8481	0.0140
S13	0.8571	0.0091		S15	0.8623	0.0091
S16	0.8598	0.0086		S18	0.8612	0.0086
S19	0.8598	0.0085		S21	0.8599	0.0085
S22	0.8591	0.0085		S24	0.8599	0.0085
S25	0.8600	0.0086		S27	0.8600	0.0085
S28	0.8601	0.0085		S30	0.8596	0.0085
S31	0.8600	0.0085		S33	0.8609	0.0084
S34	0.8579	0.0088		S36	0.8569	0.0090
Average	**0.8584**	**0.0096**		**Average**	**0.8588**	**0.0092**

In addition to finding the fundamental dynamic properties of the building, this combined approach was used to compute modal properties corresponding to higher modes. This was executed by applying a band-pass frequency filter to each of the recorded response signals. For each recorded response signal in the $N-S$ direction, four filtered signals were generated. Each of these four filtered signals has a frequency band containing the natural frequency corresponding to each of the first four modes of vibration of the building. These frequency bands were selected by observation after inspecting the frequency spectrum obtained from each of the signals' PSD, such as the one for sensor #33 shown in Figure 5-37. These frequency bands are listed in Table 5-15.

Table 5-15: Frequency bands for each mode

Mode	**Frequency Band [Hz]**
1	0.75 - 0.95
2	3.60 - 3.80
3	7.60 - 7.65
4	11.35 - 12.35

The proposed combined time-frequency identification approach was implemented to the complete sets of signals to obtain the first four natural frequencies and their corresponding damping ratios, which were computed by applying the *Logarithmic Decrement Method* to all the points of the signal as it was previously computed for the building's fundamental mode damping ratio extracted from the unfiltered data. Results for each modal frequency are displayed in Tables 5-16 to 5-19.

Table 5-16: PRILA's 1st natural frequency identified by wavelet transform on RDS of filtered signal

West Side [N-S]				East Side [N-S]		
Sensor	f_n *[Hz]*	ξ		*Sensor*	f_n *[Hz]*	ξ
S10	0.8618	0.0105		S12	0.8606	0.0112
S13	0.8622	0.0107		S15	0.8606	0.0109
S16	0.8622	0.0106		S18	0.8608	0.0109
S19	0.8622	0.0107		S21	0.8607	0.0109
S22	0.8623	0.0107		S24	0.8607	0.0110
S25	0.8623	0.0106		S27	0.8607	0.0110
S28	0.8623	0.0106		S30	0.8608	0.0110
S31	0.8622	0.0107		S33	0.8607	0.0110
S34	0.8621	0.0106		S36	0.8607	0.0111
Average	**0.8622**	**0.0106**		**Average**	**0.8607**	**0.0110**

Table 5-17: PRILA's 2nd natural frequency identified by wavelet transform on RDS of filtered signal

West Side [N-S]				East Side [N-S]		
Sensor	f_n *[Hz]*	ξ		*Sensor*	f_n *[Hz]*	ξ
S10	3.720	0.0123		S12	3.722	0.0141
S13	3.726	0.0128		S15	3.725	0.0139
S16	3.731	0.0128		S18	3.726	0.0139
S19	3.736	0.0128		S21	3.727	0.0139
S22	3.738	0.0127		S24	3.727	0.0139
S25	3.744	0.0128		S27	3.728	0.0140
S28	3.767	0.0120		S30	3.764	0.0104
S31	3.733	0.0127		S33	3.726	0.0137
S34	3.742	0.0124		S36	3.727	0.0135
Average	**3.737**	**0.0126**		**Average**	**3.730**	**0.0135**

Table 5-18: PRILA's 3rd natural frequency identified by wavelet transform on RDS of filtered signal

West Side [N-S]				East Side [N-S]		
Sensor	f_n *[Hz]*	ξ		*Sensor*	f_n *[Hz]*	ξ
S10	7.622	0.0015		S12	7.614	0.0014
S13	7.622	0.0015		S15	7.622	0.0014
S16	7.622	0.0015		S18	7.622	0.0015
S19	7.622	0.0015		S21	7.621	0.0016
S22	7.622	0.0015		S24	7.624	0.0014
S25	7.622	0.0015		S27	7.622	0.0015
S28	7.622	0.0015		S30	7.622	0.0015
S31	7.622	0.0015		S33	7.623	0.0016
S34	7.622	0.0015		S36	7.610	0.0017
Average	**7.622**	**0.0015**		**Average**	**7.620**	**0.0015**

Table 5-19: PRILA's 4th natural frequency identified by wavelet transform on RDS of filtered signal

West Side [N-S]				East Side [N-S]		
Sensor	f_n *[Hz]*	ξ		*Sensor*	f_n *[Hz]*	ξ
S10	11.700	0.0173		S12	11.760	0.0114
S13	11.900	0.0150		S15	11.950	0.0150
S16	11.850	0.0153		S18	11.970	0.0140
S19	12.170	0.0160		S21	11.820	0.0157
S22	11.920	0.0157		S24	11.860	0.0153
S25	11.950	0.0178		S27	11.780	0.0150
S28	12.160	0.0165		S30	11.810	0.0157
S31	11.820	0.0155		S33	11.810	0.0131
S34	12.200	0.0133		S36	11.820	0.0144
Average	**11.963**	**0.0158**		**Average**	**11.842**	**0.0144**

From these results, it can be observed that there is no significant discrepancy from the results obtained for the complete unfiltered response signal and the results obtained for the filtered signal corresponding to the first mode of vibration. This demonstrates that the proposed method is capable to successfully identify the fundamental dynamic properties of a complex multi-degree of freedom system with no significant error. Likewise, it is possible to successfully identify higher order modal properties when this proposed methodology is implemented to filtered signals with a frequency band that has the frequency of interest. It is important to note that the Random Decrement Method will generate signatures that reflects the lowest influential frequency embedded in the signal, with some traces of higher frequencies. Therefore, an iterative identification process should be performed in cases where the analyst does not know the approximate location of the system's natural frequencies within the complete spectrum. Figure 5-41 shows the experimental damping ratio curve for the first four modes of vibration of the building.

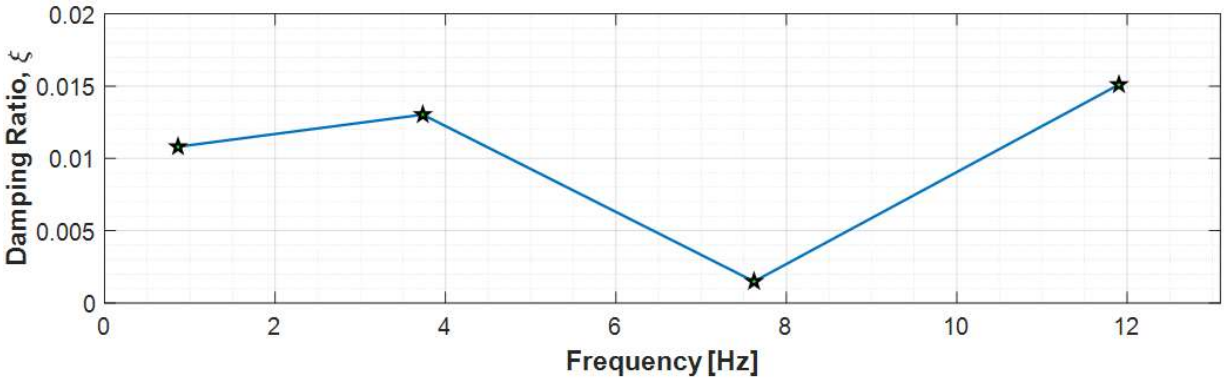


Figure 5-41: Experimental Damping Ratio Identified for PRILA's 1st, 2nd, 3rd, and 4th modes of vibration

5.2.2 Updated Linear-Elastic Models for PRILA Condominium

After implementing the dynamic identification tools and procedures presented and discussed in Section 5.2.1, PRILA's dynamic properties were obtained. Table 5-20 summarizes the results obtained of natural frequencies and damping ratios for each implemented methodology.

Table 5-20: Summary of results for PRILA Condominium's identified dynamic parameters

Mode	f_n [Hz]	T_n [sec.]	ξ
1	0.859	1.164	0.0108
2	3.729	0.268	0.0130
3	7.628	0.131	0.0015
4	11.841	0.084	0.0151

With the computed dynamic properties, it is possible to generate a simplified updated computational model in order to better perform future nonlinear dynamic analyses which produces reliable results for structural assessments. In addition, with an updated computational model of the building it is possible to compute a realistic stiffness matrix for the MDOF system. This stiffness matrix, together with the previously obtained experimental dynamic properties of the building are used to assemble a simplified mathematical model of PRILA which effectively predicts its dynamic behavior in the linear-elastic range. This can be of particular interest for future assessment of the structure if used as a reference, (i.e., no damage) health state when compared to future experimental data collected after any natural or manmade event that could represent a threat to PRILA's structural integrity and consequently the safety and wellbeing of its residents.

5.2.2.1 PRILA's Simplified Updated Computational Model

For the purpose of effectively representing the dynamic behavior of PRILA Condominium and to drastically reduce the computational cost when performing future nonlinear dynamic analyses to assess its prognosis, a simplified MDOF model was created in the commercial software SAP2000®. In the model, the complete structure was represented by a vertical column with a height of $184\ ft - 2\ in$ and having condensed masses at each story height. The mass of each story was computed from the design drawings and then was condensed at the slab's levels. Each condensed mass consists in a tributary mass corresponding to half of the mass of the upper and lower stories with respect to each level slab, in addition to the slab's mass. Table 5-21 shows the masses for each of the stories.

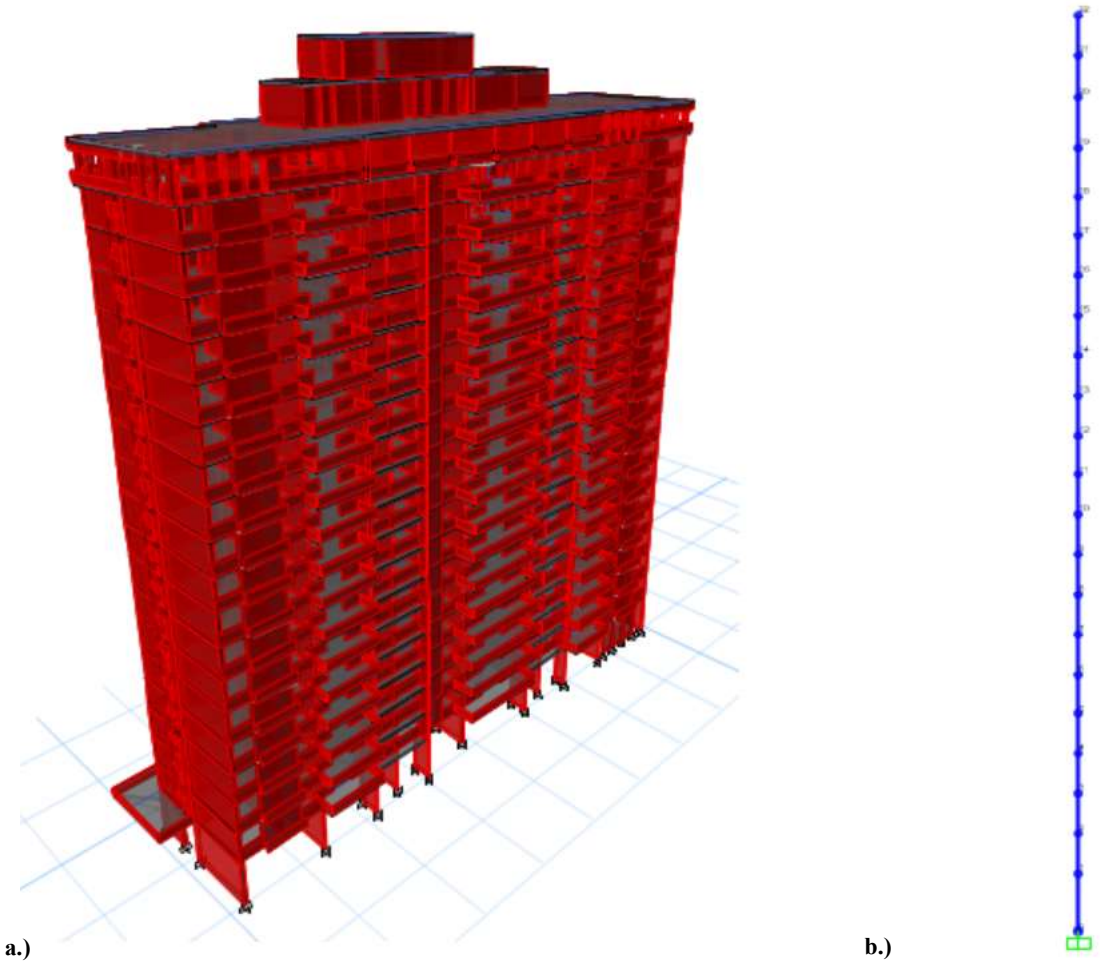
Table 5-21: Tributary mass and weight for each story

Story	Elevation [ft-in]	Mass [slugs]	Weight [kips]
1	11'-9"	35,336.04	1,136.90
2	19'-9"	32,689.91	1,051.77
3	27'-9"	32,689.91	1,051.77
4	35'-9"	32,689.91	1,051.77
5	43'-9"	32,689.91	1,051.77
6	51'-9"	32,689.91	1,051.77
7	59'-9"	32,689.91	1,051.77
8	67'-9"	32,689.91	1,051.77
9	75'-9"	32,689.91	1,051.77
10	83'-9"	32,689.91	1,051.77
11	91'-9"	32,689.91	1,051.77
12	99'-9"	32,689.91	1,051.77
13	107'-9"	32,689.91	1,051.77
14	115'-9"	32,689.91	1,051.77
15	123'-9"	32,689.91	1,051.77
16	131'-9"	32,689.91	1,051.77
17	139'-9"	32,689.91	1,051.77
18	147'-9"	35,432.21	1,140.00
19	157'-6"	39,328.25	1,265.35
20	167'-6"	28,690.77	923.10
21	175'-10"	8,002.05	257.46
22	184'-2"	3,176.83	102.21

Figure 5-42 shows the initial 3D model of the building and the simplified 2D model with a condensed mass per story. After the 2D model assembly, it was updated with the identified dynamic properties outlined in Table 5-20 by modifying the vertical elements' flexural rigidity between joints. The first four natural frequencies of this simplified model were updated to match the experimental results with an error of less than 5% for each mode of interest. Likewise, the identified modal damping ratios were added to the 2D model of the building. An outline of the experimental and the updated natural frequencies in the 2D model is presented in Table 5-22.

Table 5-22: Comparison between natural frequencies from experiments and from updated model

Mode	Experimental			Updated 2D Model			Error
	f_n [Hz]	ω_n [rad/sec]	T_n [sec.]	f_n [Hz]	ω_n [rad/sec]	T_n [sec.]	[%]
1	0.859	5.398	1.164	0.825	5.186	1.212	3.968
2	3.729	23.433	0.268	3.909	24.566	0.256	4.836
3	7.628	47.930	0.131	7.290	45.806	0.137	4.431
4	11.841	74.398	0.084	11.28	70.876	0.089	4.734



a.) b.)

Figure 5-42: a.) PRILA Condominium 3D model in ETABS; b.) PRILA 2D model in SAP2000

The PRILA Condominium's simplified computational model has 22 joints, each with a condensed mass and two degrees of freedom (vertical displacements are ignored). PRILA's lateral force resisting system consists of shear walls, which due to their aspect ratios, deforms in flexure modes when resisting lateral loads. Therefore, each joint will have a lateral displacement degree of freedom in the short direction and a rotational degree of freedom. Consequently, a simplified mathematical model of the structure has forty-four degrees of freedom. Accordingly, to effectively represent the dynamic behavior of PRILA Condominium, the simplified mathematical model represented by equation (4.1) should be modified to represent a MDOF system in which each system's matrix should have a dimension of 44×44. This model is shown in equation (5.16).

$$[M]_{44\times44}\{\ddot{u}(t)\}_{44\times1} + [C]_{44\times44}\{\dot{u}(t)\}_{44\times1} + [K]_{44\times44}\{u(t)\}_{44\times1} = \{F(t)\}_{44\times1} \qquad (5.16)$$

5.2.2.2 Updated Stiffness and Mass Matrices for PRILA Mathematical Model

The mathematical model established for PRILA Condominium and defined in equation (5.16) can conveniently be reduced. This will greatly reduce the amount of computational effort in future analyses and avoid singularities when solving it due to the null terms in the mass matrix. For this reason, it is necessary to *condense* the terms in the stiffness matrix corresponding to rotations and therefore express the matrix in terms of the displacement only. Consequently, a reduced system of second order differential equations will result with system matrices with sizes of 22×22, as shown in equation (5.17).

$$[M]_{22\times22}\{\ddot{u}(t)\}_{22\times1} + [C]_{22\times22}\{\dot{u}(t)\}_{22\times1} + [K]_{22\times22}\{u(t)\}_{22\times1} = \{F(t)\}_{22\times1} \qquad (5.17)$$

To this end, the reduced stiffness matrix was extracted from the updated 2D computational model by implementing the Direct Stiffness Method. The resultant structure's stiffness matrix is shown in Table 5-23.

Once the system's stiffness matrix has been reduced, it is possible to accordingly reduce the system's mass matrix, $[M]$, by eliminating the null terms in its diagonal. The reduced mass matrix for the system's simplified mathematical model is shown in Table 5-24. This reduced size matrix has a dimension of 22×22.

In the case of the system's damping matrix, it is not possible to determine it because the system's total damping comes from multiple sources. However, PRILA's damping matrix, $[C]$, can be approximated by assuming that the structure possesses classical damping and hence it is possible to combine equations (4.5) and (4.6) to add damping terms that include the experimentally obtained damping ratios into an equivalent damping matrix diagonal, which also has a dimension of 22×22. This procedure uncouples the system's second order differential equations by using modal coordinates and will be presented in more detail in the next chapter.

Table 5-23: PRILA Condominium stiffness matrix, $[\boldsymbol{K}]$, [kip/in]

24,272,692.88	-21,309,750.31	9,410,437.91	-2,520,891.98	673,130.01	-171,628.06	33,663.13	-3,586.29	962.91	-265.36	81.48	-26.40	7.05	-1.81	0.37	-0.05	0.01	0.00	0.00	0.00	0.00	0.00
-21,309,750.31	31,806,599.85	-24,316,167.21	10,213,631.57	-2,727,249.71	695,367.27	-136,389.36	14,530.18	-3,901.33	1,075.15	-330.10	106.96	-28.57	7.34	-1.52	0.21	-0.05	0.01	0.00	0.00	0.00	0.00
9,410,437.91	-24,316,167.21	32,949,057.81	-24,613,407.92	10,260,136.45	-2,616,028.54	513,107.94	-54,663.71	14,677.13	-4,044.79	1,241.88	-402.39	107.50	-27.61	5.71	-0.78	0.20	-0.04	0.01	0.00	0.00	0.00
-2,520,891.98	10,213,631.57	-24,613,407.92	32,995,562.70	-24,502,186.75	9,768,746.89	-1,916,042.41	204,124.65	-54,807.17	15,104.03	-4,637.42	1,502.59	-401.42	103.09	-21.31	2.92	-0.76	0.16	-0.02	0.00	0.00	0.00
673,130.01	-2,727,249.71	10,260,136.45	-24,502,186.75	32,504,173.13	-22,647,849.66	7,151,061.68	-761,834.91	204,551.56	-56,371.33	17,307.81	-5,607.99	1,498.18	-384.75	79.55	-10.91	2.82	-0.60	0.08	-0.01	0.00	0.00
-171,628.06	695,367.27	-2,616,028.54	9,768,746.89	-22,647,849.66	25,578,214.33	-12,877,094.97	2,843,214.99	-763,399.07	210,381.29	-64,593.80	20,929.35	-5,591.32	1,435.91	-296.88	40.72	-10.53	2.23	-0.29	0.05	0.00	0.00
33,663.13	-136,389.36	513,107.94	-1,916,042.41	7,151,061.68	-12,877,094.97	11,366,065.23	-5,828,210.63	2,158,188.07	-594,764.13	182,611.66	-59,168.88	15,807.08	-4,059.44	839.31	-115.11	29.76	-6.29	0.81	-0.14	0.01	0.00
-3,586.29	14,530.18	-54,663.71	204,124.65	-761,834.91	2,843,214.99	-5,828,210.63	6,484,443.73	-4,277,862.39	1,787,895.86	-548,941.35	177,865.14	-47,517.01	12,202.90	-2,523.02	346.02	-89.47	18.92	-2.43	0.42	-0.02	0.00
962.91	-3,901.33	14,677.13	-54,807.17	204,551.56	-763,399.07	2,158,188.07	-4,277,862.39	5,423,294.87	-4,156,652.11	1,954,697.99	-633,351.14	169,200.96	-43,452.72	8,984.11	-1,232.13	318.60	-67.37	8.65	-1.48	0.06	-0.01
-265.36	1,075.15	-4,044.79	15,104.03	-56,371.33	210,381.29	-594,764.13	1,787,895.86	-4,156,652.11	5,999,602.61	-5,060,073.12	2,355,539.42	-629,286.85	161,607.96	-33,413.41	4,582.49	-1,184.94	250.55	-32.18	5.52	-0.23	0.04
81.48	-330.10	1,241.88	-4,637.42	17,307.81	-64,593.80	182,611.66	-548,941.35	1,954,697.99	-5,060,073.12	7,932,709.09	-7,069,881.22	3,364,597.92	-864,066.71	178,650.94	-24,501.10	6,335.49	-1,339.60	172.06	-29.53	1.21	-0.20
-26.40	106.96	-402.39	1,502.59	-5,607.99	20,929.35	-59,168.88	177,865.14	-633,351.14	2,355,539.42	-7,069,881.22	11,437,247.33	-9,337,964.08	3,816,834.03	-789,153.18	108,228.49	-27,985.68	5,917.40	-760.04	130.42	-5.35	0.89
7.05	-28.57	107.50	-401.42	1,498.18	-5,591.32	15,807.08	-47,517.01	169,200.96	-629,286.85	3,364,597.92	-9,337,964.08	12,906,134.94	-9,139,913.23	3,031,943.19	-415,816.15	107,521.58	-22,734.76	2,920.10	-501.09	20.56	-3.43
-1.81	7.34	-27.61	103.09	-384.75	1,435.91	-4,059.44	12,202.90	-43,452.72	161,607.96	-864,066.71	3,816,834.03	-9,139,913.23	10,645,043.93	-5,814,175.85	1,555,036.11	-402,100.63	85,021.64	-10,920.35	1,873.95	-76.88	12.81
0.37	-1.52	5.71	-21.31	79.55	-296.88	839.31	-2,523.02	8,984.11	-33,413.41	178,650.94	-789,153.18	3,031,943.19	-5,814,175.85	5,701,677.34	-3,230,662.12	1,168,702.01	-247,114.66	31,739.90	-5,446.63	223.45	-37.24
-0.05	0.21	-0.78	2.92	-10.91	40.72	-115.11	346.02	-1,232.13	4,582.49	-24,501.10	108,228.49	-415,816.15	1,555,036.11	-3,230,662.12	3,642,206.33	-2,319,312.67	762,962.71	-97,996.46	16,816.39	-689.90	114.98
0.01	-0.05	0.20	-0.76	2.82	-10.53	29.76	-89.47	318.60	-1,184.94	6,335.49	-27,985.68	107,521.58	-402,100.63	1,168,702.01	-2,319,312.67	2,620,222.22	-1,445,462.19	351,224.53	-60,270.85	2,472.65	-412.11
0.00	0.01	-0.04	0.16	-0.60	2.23	-6.29	18.92	-67.37	250.55	-1,339.60	5,917.40	-22,734.76	85,021.64	-247,114.66	762,962.71	-1,445,462.19	1,347,447.62	-635,788.31	156,233.91	-6,409.60	1,068.27
0.00	0.00	0.01	-0.02	0.08	-0.29	0.81	-2.43	8.65	-32.18	172.06	-760.04	2,920.10	-10,920.35	31,739.90	-97,996.46	351,224.53	-635,788.31	546,039.62	-202,222.39	18,740.05	-3,123.34
0.00	0.00	0.00	0.00	-0.01	0.05	-0.14	0.42	-1.48	5.52	-29.53	130.42	-501.09	1,873.95	-5,446.63	16,816.39	-60,270.85	156,233.91	-202,222.39	123,319.12	-39,147.64	9,239.98
0.00	0.00	0.00	0.00	0.00	0.00	0.01	-0.02	0.06	-0.23	1.21	-5.35	20.56	-76.88	223.45	-689.90	2,472.65	-6,409.60	18,740.05	-39,147.64	36,362.85	-11,491.22
0.00	0.00	0.00	0.00	0.00	0.00	0.00	0.00	-0.01	0.04	-0.20	0.89	-3.43	12.81	-37.24	114.98	-412.11	1,068.27	-3,123.34	9,239.98	-11,491.22	4,630.58

Table 5-24: PRILA Condominium mass matrix, $[\boldsymbol{M}]$, [slugs]

35,336.04	0	0	0	0	0	0	0	0	0	0	0	0	0	0	0	0	0	0	0	0	0
0	32,689.91	0	0	0	0	0	0	0	0	0	0	0	0	0	0	0	0	0	0	0	0
0	0	32,689.91	0	0	0	0	0	0	0	0	0	0	0	0	0	0	0	0	0	0	0
0	0	0	32,689.91	0	0	0	0	0	0	0	0	0	0	0	0	0	0	0	0	0	0
0	0	0	0	32,689.91	0	0	0	0	0	0	0	0	0	0	0	0	0	0	0	0	0
0	0	0	0	0	32,689.91	0	0	0	0	0	0	0	0	0	0	0	0	0	0	0	0
0	0	0	0	0	0	32,689.91	0	0	0	0	0	0	0	0	0	0	0	0	0	0	0
0	0	0	0	0	0	0	32,689.91	0	0	0	0	0	0	0	0	0	0	0	0	0	0
0	0	0	0	0	0	0	0	32,689.91	0	0	0	0	0	0	0	0	0	0	0	0	0
0	0	0	0	0	0	0	0	0	32,689.91	0	0	0	0	0	0	0	0	0	0	0	0
0	0	0	0	0	0	0	0	0	0	32,689.91	0	0	0	0	0	0	0	0	0	0	0
0	0	0	0	0	0	0	0	0	0	0	32,689.91	0	0	0	0	0	0	0	0	0	0
0	0	0	0	0	0	0	0	0	0	0	0	32,689.91	0	0	0	0	0	0	0	0	0
0	0	0	0	0	0	0	0	0	0	0	0	0	32,689.91	0	0	0	0	0	0	0	0
0	0	0	0	0	0	0	0	0	0	0	0	0	0	32,689.91	0	0	0	0	0	0	0
0	0	0	0	0	0	0	0	0	0	0	0	0	0	0	32,689.91	0	0	0	0	0	0
0	0	0	0	0	0	0	0	0	0	0	0	0	0	0	0	35,432.21	0	0	0	0	0
0	0	0	0	0	0	0	0	0	0	0	0	0	0	0	0	0	39,328.25	0	0	0	0
0	0	0	0	0	0	0	0	0	0	0	0	0	0	0	0	0	0	28,690.77	0	0	0
0	0	0	0	0	0	0	0	0	0	0	0	0	0	0	0	0	0	0	8,002.05	0	0
0	0	0	0	0	0	0	0	0	0	0	0	0	0	0	0	0	0	0	0	3,176.83	0

CHAPTER 6. FREQUENCY RESPONSE FUNCTIONS

The dynamic behavior of structural systems can be estimated by mathematical models in which a discretized version of the real system provides accurate dynamic results. In Chapter 4, the Ponce Highway Bridge [ID: 2348] and the PRILA Condominium were simplified as a SDOF and a MDOF system, respectively, and as such was the estimation of their physical properties. For that reason, discretized structural models need to be updated with experimental data analyses to provide the best possible predictions of dynamic behavior. This procedure was successfully applied in Chapter 5 by experimental dynamic analyses. Once the system's model as a function of time is updated with the field experiments, it is possible to describe it in the frequency domain by what is known as its *Frequency Response Function* (FRF). This function, defined by modal analysis, is of special importance because it allows to algebraically compute a system's response to any input excitation, as shown in equation (6.1), instead of solving a system of differential equations of motion, as follows:

$$Y(\omega) = H(\omega) \cdot F(\omega) \tag{6.1}$$

In the above equation, $Y(\omega)$ represents the system's response in the frequency domain, $F(\omega)$ is the input excitation (e.g. force) in the frequency domain, and $H(\omega)$ is the system's FRF.

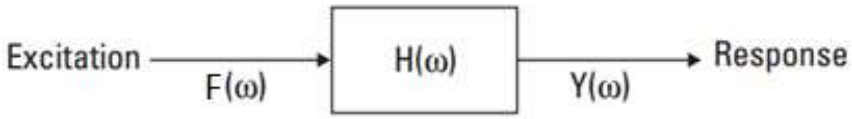


Figure 6-1: Block diagram for an input-output system (adapted from Agilent Technologies, 2000)

A FRF is a frequency based measurement function that is used to describe or identify, in the case of experimental dynamics, the natural frequencies, damping ratios, and mode shapes of a physical structure. It is the mathematical representation of the relationship between any input and the corresponding output of a linear time-invariant system in the frequency domain. A block diagram representation of this relationship is depicted in Figure 6-1. The FRF is mathematically defined as the Fourier transform of the output divided by the Fourier transform of the input, as defined by

$$H(\omega) = \frac{Y(\omega)}{F(\omega)} \tag{6.2}$$

It is often mistakenly confused with the Transfer Function, which is also an input-output relationship of a system. However, the FRF is related to a system's Transfer Function as simply the Transfer Function measured along the complex axis, $j\omega$, of the s-plane as shown in Figure 6-2.

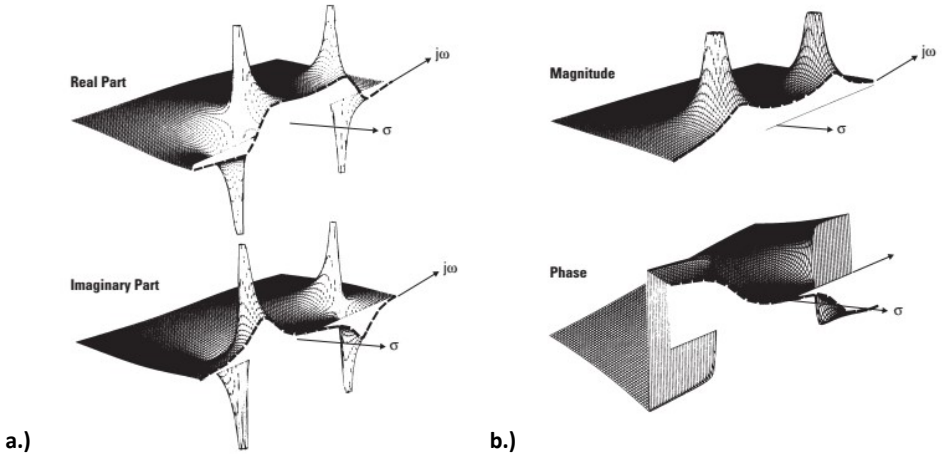


Figure 6-2: 3D Laplace Representation. The surface represents the Transfer Function and the dashed line represents the FRF. a.) Representation by real and imaginary parts; b.) Representation by magnitude and phase (Agilent Technologies, 2000)

The response coordinates can be displacements, velocities, or accelerations. Nevertheless, acceleration is the preferred and most used variable because the responses of structural systems are typically measured as accelerations. FRFs are capable to relate any input to any output (i.e., response) variable but the most popular variations of FRFs in mechanical and structural systems are outlined in Table 6-1.

Table 6-1: Variations in frequency responses

Definition	FRF	Variables
Compliance	$\frac{H_u(\omega)}{F(\omega)}$	$\frac{Displacement}{Force}$
Mobility	$\frac{H_v(\omega)}{F(\omega)}$	$\frac{Velocity}{Force}$
Accelerance	$\frac{H_a(\omega)}{F(\omega)}$	$\frac{Acceleration}{Force}$

In this study, the accelerance for the Ponce Highway Bridge [ID: 2348] and for the PRILA Condominium are analytically developed and experimentally computed for identification of earthquake excitations and for assessing its capabilities in the identification of the structures' natural dynamic properties.

6.1 FRF Dynamic Analyses for the Ponce Highway Bridge [ID: 2348]

6.1.1 FRFs from updated mathematical model of the bridge

The FRF of a damped dynamic system, described by the 2nd order differential equation in (4.1) is the steady-state response to a complex harmonically varying force. Therefore, to obtain the FRF describing the system response, the forcing function, $F(t)$, must be related to a ground motion excitation, as an example, and should be defined as

$$F(t) = -mA_g e^{i\omega t} \tag{6.3}$$

In the above equation, m is the computed bridge's equivalent mass, A_g is the excitation amplitude, and the term $e^{i\omega t}$ is the complex harmonic function describing the excitation. Hence, equation (4.1) can be re-written as

$$m\ddot{u}(t) + c\dot{u}(t) + ku(t) = -mA_g e^{i\omega t} \tag{6.4}$$

In an analogous way, the steady-state displacement of the system due to $F(t)$ can be defined as

$$u(t) = Ae^{i\omega t} \tag{6.5}$$

Consequently, by substituting equations (4.3), (4.5), (4.6), and (6.5) into equation (6.4) it is possible to define the constant A as shown in the equation given below.

$$A = \frac{-A_g}{\omega_n^2 - \omega^2 + i2\xi\omega_n\omega} \tag{6.6}$$

In it, A represents the amplitude of the system's relative displacement response. Therefore, by substituting equation (6.6) in equation (6.5) the system's relative displacement function results in

$$u(t) = \frac{-1}{\omega_n^2 - \omega^2 + i2\xi\omega_n\omega} A_g e^{i\omega t}. \tag{6.7}$$

In equation (6.7), the FRF that relates the input acceleration (e.g. ground motions) to the structure's relative displacement output is known as the *compliance* function and is defined as

$$H_u(\omega) = \frac{-1}{\omega_n^2 - \omega^2 + i2\xi\omega_n\omega} \tag{6.8}$$

Similarly, by substituting equation (6.6) into the first and second derivatives of equation (6.5), it is possible to respectively compute the system's relative velocity response, in which the *mobility* function is defined in equation (6.9), and the system's relative acceleration response, in which the *accelerance* function is defined in equation (6.10).

$$H_v(\omega) = \frac{-i\omega}{\omega_n^2 - \omega^2 + i2\xi\omega_n\omega} \tag{6.9}$$

$$H_a(\omega) = \frac{\omega^2}{\omega_n^2 - \omega^2 + i2\xi\omega_n\omega} \tag{6.10}$$

The accelerance function for the Ponce Highway Bridge [ID: 2348] is shown in Figure 6-3. It is easy to notice that the bridge's natural frequency is $\omega_n = 20.6434\ rad/sec$ or $f_n = 3.285\ Hz$.

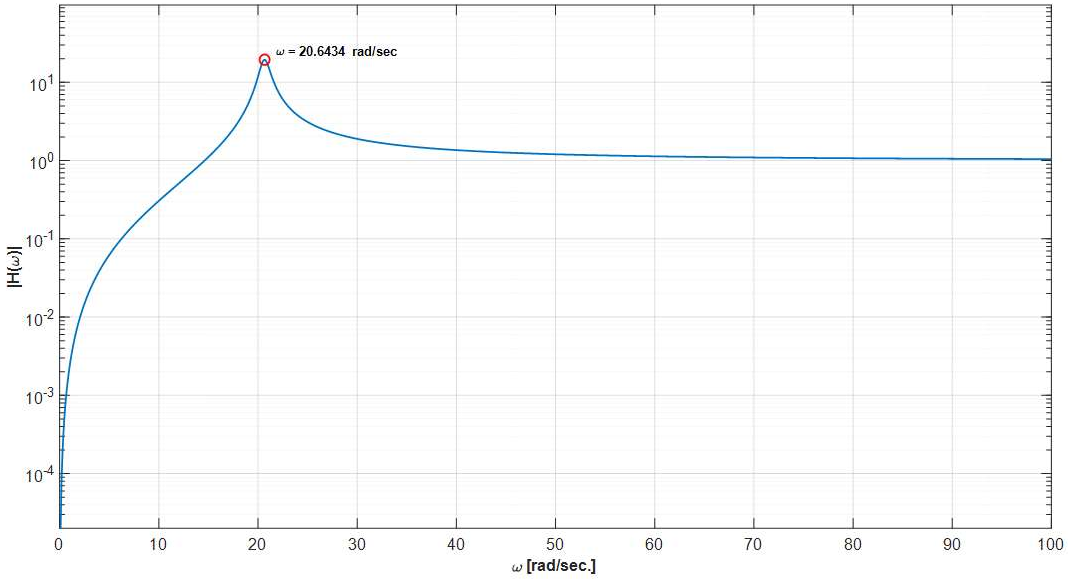


Figure 6-3: Accelerance function for updated mathematical model of the bridge

6.1.2 Experimental FRFs from recorded ambient vibrations in the bridge

For cases in which a mathematical model that describes the dynamic behavior of a structural system is available, the identification process is straightforward because it will produce good, although idealized, results of a physical system's motion. However, when no dynamic model is available, the identification process becomes complex and cumbersome. This case is common in older structures for which there is little to none available information on its original design, on any structural modification it may have had, or even on the soil profile supporting it. For this and other similar scenarios, the determination of experimental FRFs acquires particular importance. For this purpose, the studied structure should be instrumented with sensors placed in optimal locations from which the best description of the system's motion can be recorded. In the case of bridge structures, accelerometers are the recommended sensors and the recommendations presented in Section 2.1 should be followed. It is important to remember that real structures are continuous systems with infinite degrees of freedom. Therefore, it is also possible to describe its dynamic behavior in terms of wave propagation throughout the system's medium. In fact, this type of analysis reveals traits of the vibrating structure that are not possible to detect under discretized dynamic analyses due to that same limitation. The implementation of the FFT in the generation of FRFs from experimentally recorded data is what allows to obtain a description of the resonant frequency content of a physical structure by evaluating the frequency content of all the waves that enter the studied system by means of any external excitation. For that reason, the most cost-efficient alternative to excite a physical structure for generating FRFs is via ambient vibrations.

6.1.2.1 Properties of Recorded Ambient Vibrations

Ambient vibrations are small amplitude oscillations transmitted through a medium such as the ground, water, and air. They are produced by nearby human activity, such as vehicular traffic and operating machinery, by atmospheric phenomena, such as wind and rain, by ocean waves, and by high levels of sound, among others. Its most important characteristic, and what makes it very attractive for its use in dynamic identification problems is that it has very similar properties to *white noise*, which is a random signal having equal intensity at a theoretical infinite frequency bandwidth. Simply explained, a signal can be considered white noise if it is observed to have a flat spectrum. Likewise, some other statistical properties of an ideal white noise signal are a zero-mean normal distribution of samples with zero variance, zero skewness, and a kurtosis of three.

Figure 6-4a shows a simulated ideal white noise signal of 30 seconds of duration with its frequency spectrum and Figure 6-4b shows a histogram and its most relevant statistical properties.

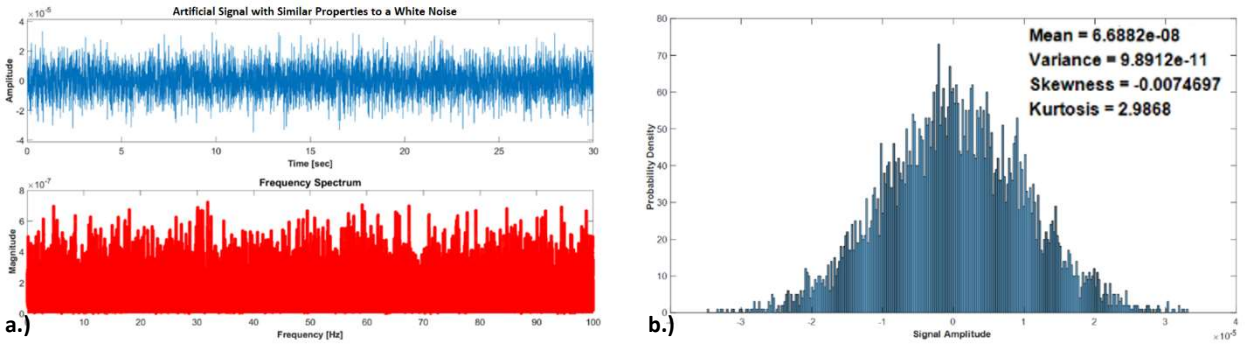


Figure 6-4: Artificial close-to-ideal white noise signal. a.) Signal and its frequency spectrum; b.) PDF and its statistical moments

Recorded ambient vibrations should possess similar statistical properties. However, during the recording process, instrumentation issues, external conditions, as well as sudden impulses or forced excitations could affect the measurements inducing trends. Implementing appropriate baseline correction techniques helps to enhance the signals. This is of special importance because the farther the measurements' properties are from idealized white noise, the higher the possibility of erroneous results. This is because most of the mathematical theories and tools used for non-parametric dynamic identification with ambient vibrations work effectively under this assumption. It is highly recommended to perform an adequate piecewise cubic spline baseline correction when working with experimental measurements of ambient vibrations. Figure 6-5a shows a 30 seconds' segment of experimentally recorded ambient vibrations at sensor #2 in the Ponce Highway Bridge [ID: 2348] and its frequency spectrum. Figure 6-5b, shows the signal's statistical properties.

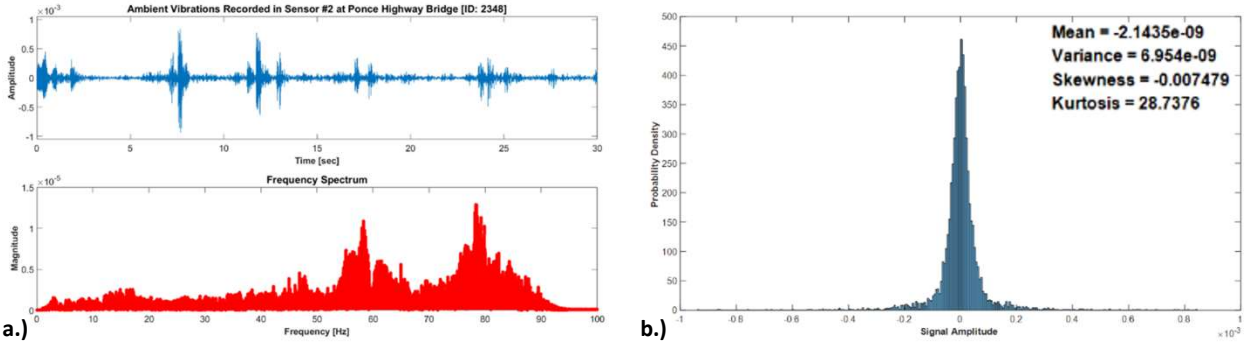


Figure 6-5: Signal recorded at sensor #2. a.) Recorded signal and its frequency spectrum; b.) PDF and its statistical moments

From the figure, it can be observed that the signal's frequency spectrum covers almost all the frequencies capable of being captured (i.e., up to the Nyquist frequency). However, it does not

have a flat frequency spectrum. In addition, there are some higher peaks at some frequency ranges due to external excitations and conditions. Similarly, all its statistical properties do not exactly match the ones for an ideal white noise. The signal has zero mean, zero variance, near zero skewness, and but a high value of kurtosis. Skewness is sensitive to an asymmetry being introduced into an initially symmetric system. For example, in damage identification, a displacement skewness may indicate the emergence of inelastic excursions in an initially linear system. However, the value for this recording segment is small enough as to indicate that possibility. On the other hand, the kurtosis measures the peaked nature of the recorded response distribution. In this case, the high value obtained reflects the impulses produced by the vehicles when they travel over the east abutment and enters the bridge deck. These are common values of ambient vibrations recorded in bridge structures. That is one of the reasons to install a free-field station outside the interacting area of vehicles and the studied structure. In addition, by recording free-field station measurements it is possible to avoid the recording of a signal that is contaminated with natural frequencies that may correspond to other interacting systems, such as the filler-soil and abutment interaction in this case where sensor #2 is placed at mid-height of the east abutment.

6.1.2.2 Bridge's FRF and a Proposed Approach for Improving its Fidelity

After presenting the characteristics of recorded ambient vibrations and understanding its most important similitudes and differences with ideal white noise signals, it is possible to compute the bridge's experimental FRFs and better interpret the identification results. For this case, as there is not a sensor directly beneath sensor #5 of a free-field station capable of recording undisturbed ambient vibration measurements, recordings at sensor #2 are going to be used as the input excitations to the bridge as to produce the responses recorded at sensor #5. In accordance to equation (6.2), the FFT is computed for ambient vibrations recorded at sensors #2 and #5. The next step is to algebraically divide the output (sensor #5) by the input (sensor #2), both already in the frequency domain, in order to obtain the experimental FRF, $H(f)$, for the Ponce Highway Bridge [ID: 2348]. It is important to remember that $H(f)$ is a complex function, with real and imaginary components. This means that it is possible to plot the function in its real and imaginary parts or in its magnitude and phase components, each separately. For this study, the first set of graphs are presented. Figure 6-6a shows the real and imaginary components for the bridge's experimental FRF by using recordings at sensor #2 as input and recordings at sensor #5 as output.

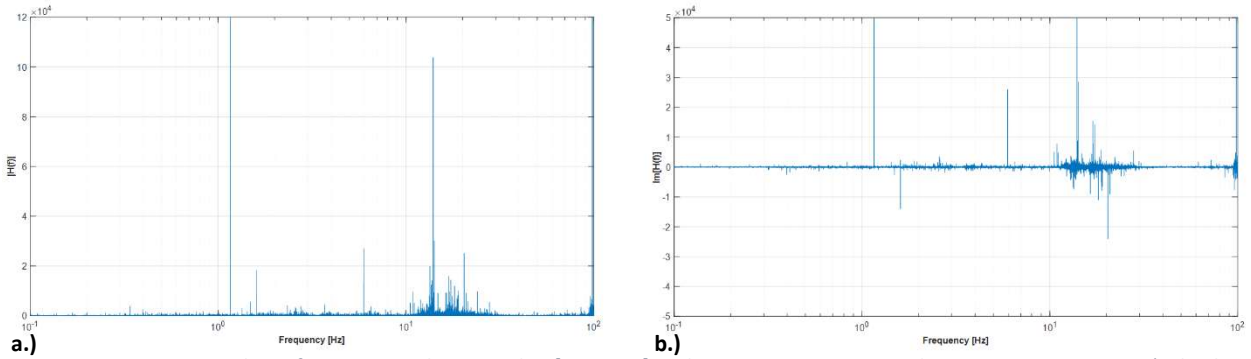


Figure 6-6: Experimental FRF for Ponce Highway Bridge [ID: 2348] with sensor #2 as input and sensor #5 as output. a.) Absolute value of real part of FRF; b.) Imaginary part of FRF

As it is observed from the figure, a notable frequency content is located between $10\ Hz$ and $20\ Hz$. These frequencies correspond to the vehicular traffic in the bridge. Besides that, there is not a resonant frequency that can be considered the bridge's natural frequency of vibration in its transverse direction. In fact, there is no other trace of additional dominant frequencies in both real and imaginary parts of the experimental FRF. This may be caused due to the fact that measurements at sensor #2 are not representative of the actual excitation sources for sensor #5. In addition, another source of problem may be that the measurements in sensor #2 (and in sensor #8) could be contaminated by localized excitations or that because of its location (at mid-height of the abutment) its recording captures the response of the abutment as influenced by the back filler-soil. However, an alternative approach is proposed to solve this issue and unmask the bridge's natural frequency embedded on the response measurements recorded at sensor #5 while at the same time increasing the fidelity of the results. By observing equation (6.2), it is easier to think of the FRF as an amplification factor. In the general case, dynamic input excitations have amplitudes smaller than their corresponding responses. In theory, if the input excitation has a broad frequency spectrum with all (or almost all) of the frequencies capable of being recorded, when the structure gets excited by the input its resonant frequency will get excited. Hence, it will notably produce larger amplitude values with respect to the input. In the same way, this is reflected in their frequency spectrum. Consequently, in the FRF an amplified peak in the natural frequency being excited will be observed. However, if the input excitation does not contain in its frequency spectrum the natural frequencies of the structure, the FRF will not display them. In the same way, the FRF will not display the structure's natural frequencies of vibration if, although they exist in the input frequency spectrum, its magnitude is greater than its magnitude in the output frequency spectrum. This may occur when measurements from sensors used as inputs do not considerably

contribute to the output measured responses. The proposed alternative is useful for these cases and for cases in which no input was recorded or no direct exciting source was recorded. It consists in generating an artificial signal of the same length as the response with comparable amplitudes containing close-to-ideal white noise properties and use it as if it is the input signal. Even though the output response does not correspond to the simulated white noise signal used as input, the natural frequencies of the structure will get amplified when computing the FRF and therefore displayed when $H(f)$ gets plotted. The result for this proposed approach after its implementation to the ambient vibration responses recorded in sensor #5 is displayed in Figure 6-7.

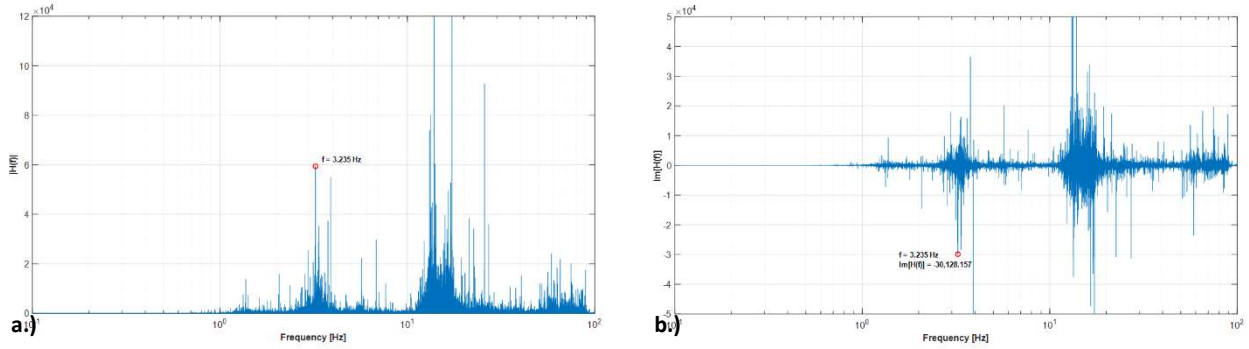


Figure 6-7: Experimental FRF for Ponce Highway Bridge [ID: 2348] with simulated white noise used as input and sensor #5 as output. a.) Absolute value of real part of FRF; b.) Imaginary part of FRF

From the above figure, two different frequency ranges can be observed to contain dominant frequencies. However, the first major gathering of peaks in Figure 6-7a corresponds to the resonant frequency of the bridge in which the highest peak has a frequency of $f_n = 3.325Hz$. This value is very close to the values obtained by implementing time and frequency analyses as presented in Chapter 5. The other cluster of peaks between $10\ Hz$ and $20\ Hz$, corresponds to the traffic of vehicles traveling over the bridge, analogous to the peaks shown in Figure 6-6a. The imaginary component of the FRF shown in Figure 6-7b has a value of $Im[H(f)] = -30{,}128.157$ corresponding to the identified natural frequency of the bridge. With the values of amplitude of the imaginary part of the FRFs it is possible to compute the mode shapes of the structure. However, due to the noise embedded in experimentally recorded measurements from real physical in-service structures and minor numerical errors generated when computing these experimental FRFs, mode shapes may not accurately represent what they mathematically should under ideal conditions. In this study, experimental mode shapes were not computed for the reasons stated and because, as a SDOF system simplification, the bridge will only have one mode that oscillates as an inverted pendulum when being excited.

6.1.2.3 Identification of Equivalent Ground Motions

As explained in Section 5.1.3, the response measurements recorded in sensor #5 at the Ponce Highway Bridge [ID: 2348] are the result of equivalent earthquake motions in which there is contribution from motions at the top of both abutments as well as from the ground beneath the columns supporting the cap beam. This means that the ground motion received by the bridge may not be exactly the same than the response at sensor #5 reflects. The structural elements supporting the bridge and its corresponding boundary conditions (e.g., joints connecting both abutments with the bridge deck) may have changed, to a little or great extent, the characteristics of what originally was the imparted excitation. In Section 6.1.1 the updated model's FRF was obtained and it is proposed in this study to use it to compute an equivalent earthquake motion that corresponds to the recorded response at sensor #5. The accelerance function, $H_a(\omega)$, in equation (6.10) is defined for the system's relative acceleration response. However, an accelerance function capable of relating the absolute acceleration response to an equivalent earthquake is needed because sensor accelerometers measure absolute accelerations instead of relative. This new function can be derived by defining the absolute acceleration recorded at sensor #5 as

$$\ddot{u}_{abs}(t) = \ddot{u}_r(t) + A_g e^{i\omega t} \tag{6.11}$$

in which $\ddot{u}_r(t)$ is the relative acceleration at sensor #5 defined as the second derivative of equation (6.5) and A_g is the excitation amplitude. Then by substituting equation (6.10) into equation (6.11) and re-organizing terms, the system's absolute acceleration can be defined as

$$\ddot{u}_{abs}(t) = \frac{{\omega_n}^2 + j2\xi\omega_n\omega}{\omega_n^2 - \omega^2 + i2\xi\omega_n\omega} A_g e^{i\omega t} \tag{6.12}$$

From equation (6.12), the accelerance function for the recorded absolute acceleration at the bridge is shown below.

$$\widetilde{H}_a(\omega) = \frac{{\omega_n}^2 + i2\xi\omega_n\omega}{\omega_n^2 - \omega^2 + i2\xi\omega_n\omega} \tag{6.13}$$

For the Ponce Highway Bridge [ID: 2348], the absolute accelerance function is illustrated in Figure 6-8. In addition, it can be observed that the bridge's natural frequency is $\omega_n = 20.6434\ rad/sec$ or $f_n = 3.285\ Hz$.

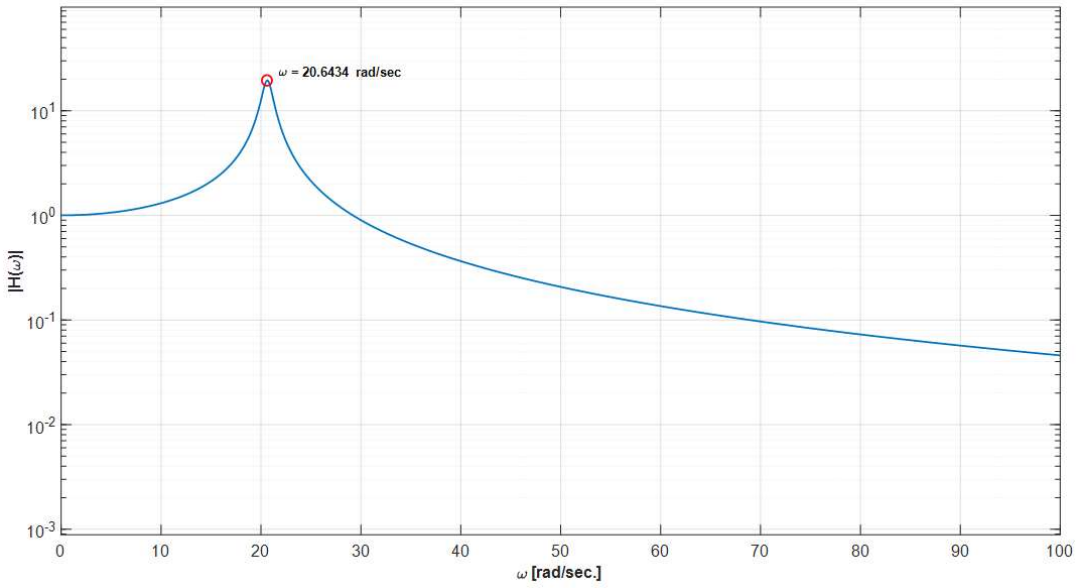


Figure 6-8: Absolute accelerance function for updated mathematical model of the bridge

After the absolute accelerance function, $\widetilde{H}_a(\omega)$, is computed it is possible to re-organize equation (6.1) and solve for an unknown acceleration input excitation, $F_a(\omega)$, as defined by equation (6.14), in which $Y_a(\omega)$ is the response acceleration measurements.

$$F_a(\omega) = \frac{Y_a(\omega)}{\widetilde{H}_a(\omega)} \tag{6.14}$$

Once the unknown input is obtained in the frequency domain, it is possible to compute its inverse Fourier transform (or IFFT in this case) in order to finally obtain an equivalent excitation from which the responses at sensor #5 were generated. This is of great importance in this study because there was not a direct recording of input earthquake excitations. Hence, it was not possible to completely assess the earthquakes responses without knowing the characteristics of this input excitations, such as their frequency content and peak ground accelerations. In this study, four equivalent earthquake excitations were generated for the four measured responses by implementing this proposed methodology. However, the earthquake responses had to be low-pass filtered at a cutting frequency of $f_{cut} = 10\ Hz$. By doing it, the contribution of the vehicular traffic vibrations was eliminated. This filtering process is important to perform since the FRF was developed for an ideal SDOF system updated model. This means that when computing the quotient in equation (6.14), an error will be produced at frequencies over $10\ Hz$ because the output response has high peaks in that frequency region due to vehicles constantly traveling over the

bridge, and not due to a second degree of freedom, for which $\widetilde{H}_a(\omega)$ was not developed. Figures 6-9 to 6-12 show the equivalent earthquakes and their corresponding frequency spectrum plotted below 10 Hz.

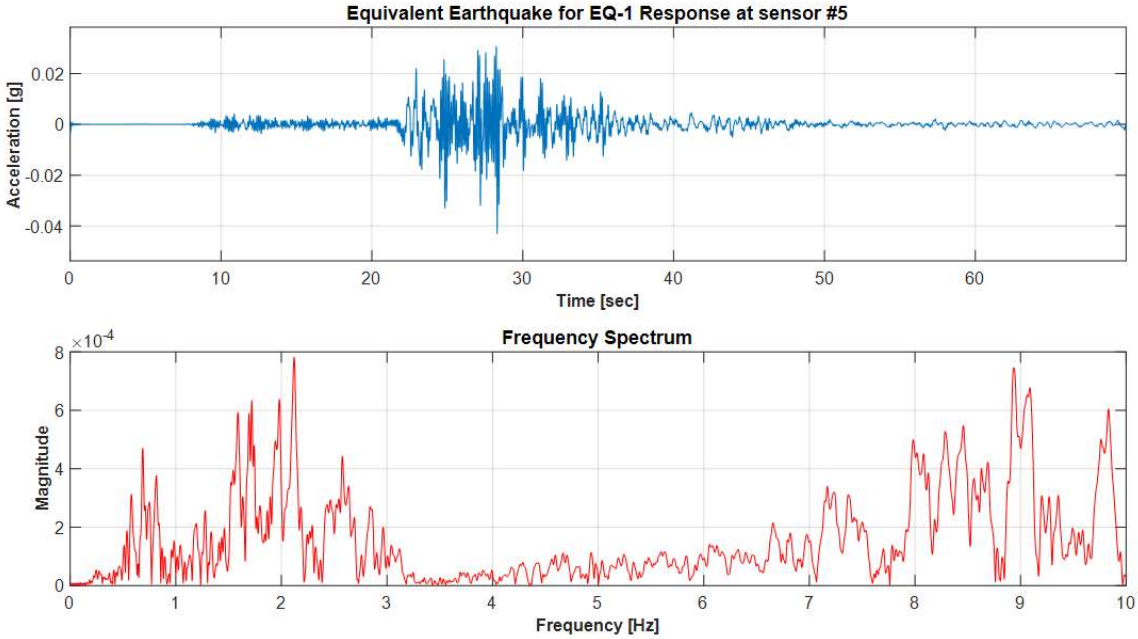


Figure 6-9: Equivalent earthquake EQ-1 and its frequency spectrum

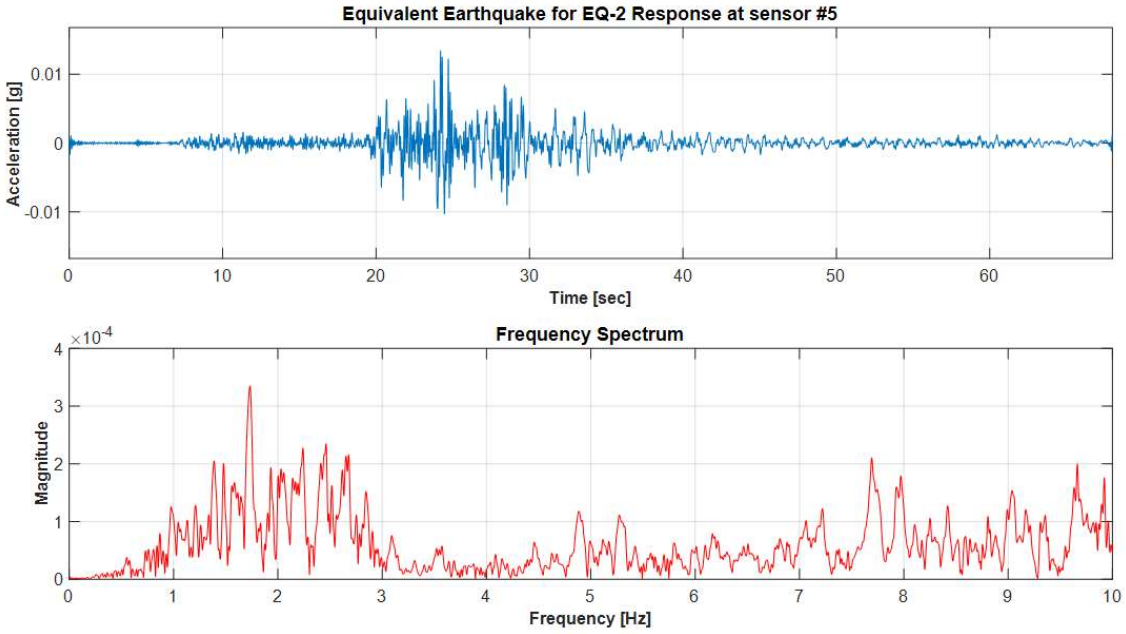


Figure 6-10: Equivalent earthquake EQ-2 and its frequency spectrum

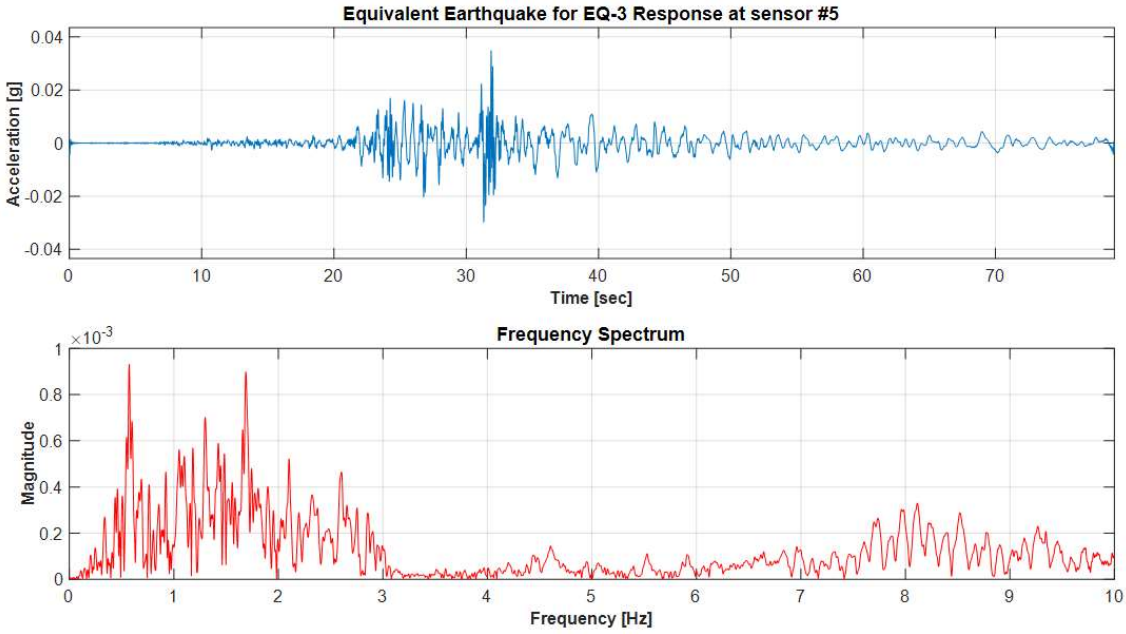


Figure 6-11: Equivalent earthquake EQ-3 and its frequency spectrum

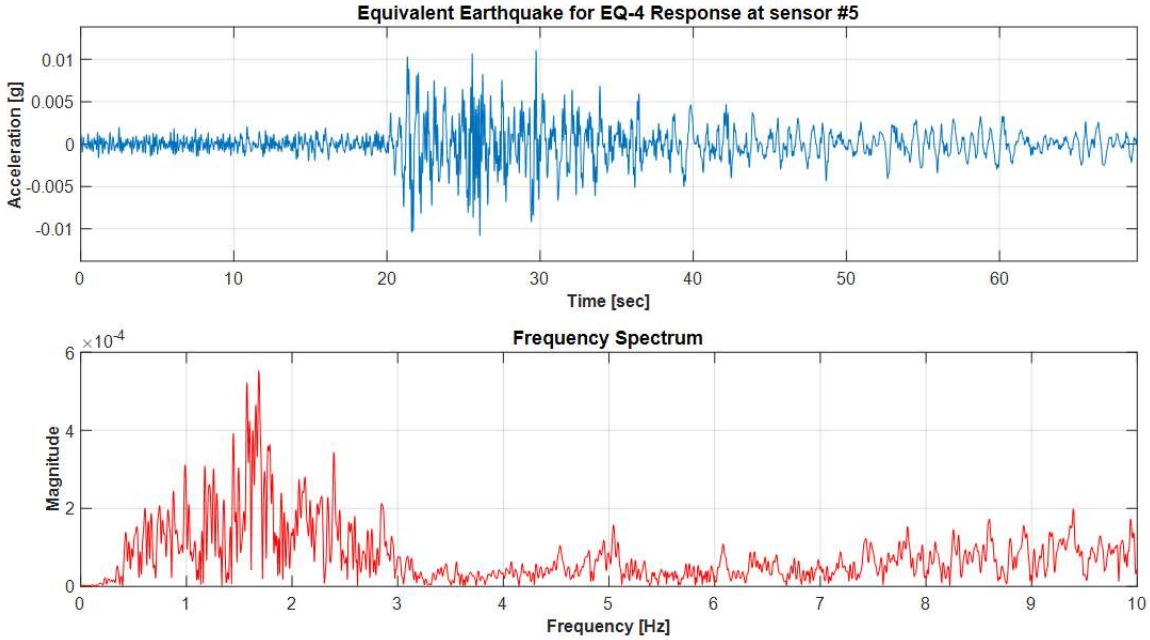


Figure 6-12: Equivalent earthquake EQ-4 and its frequency spectrum

From the Figures, it can be noted that for all the generated equivalent earthquakes the dominant frequency content does not coincide with the experimentally obtained resonant frequency of vibration for the bridge. The equivalent earthquakes' dominant frequencies are approximately located between 0.5 Hz and 3 Hz. For the equivalent earthquake EQ-1, there is another notable

dominant frequency content between located 7 Hz and 10 Hz. Similarly, that frequency content is observed in equivalent earthquakes EQ-2, EQ-3, and EQ-4, although with much less magnitudes than in equivalent earthquake EQ-1. These low frequency contents may be due to the distances between the epicenter of each earthquake and Ponce Highway Bridge [ID: 2348]. The earthquakes' information is outlined in Table 5-4. Most of the higher frequencies on an earthquake are filtered by the soil layers in the epicenter surroundings, leaving low frequency waves to travel much larger distances. The observed frequency content between 7 Hz and 10 Hz with the higher magnitudes correspond to the two earthquakes with the shortest epicentral distances. In addition, stiffening of the soil, among other localized environmental or incidental conditions may have affected the observed frequencies for each earthquake at the bridge. Table 6-2 displays the peak accelerations, velocities, and displacement values for the computed equivalent earthquakes.

Table 6-2: Peak acceleration, velocity, and displacement values for equivalent earthquakes

Equivalent Earthquake	**Acceleration [g]**		**Velocity [in/s]**		**Displacement [in]**	
	Time [sec.]	*Peak*	*Time [sec.]*	*Peak*	*Time [sec.]*	*Peak*
EQ-1	28.31	0.04302	22.99	0.6426	70	0.8008
EQ-2	24.21	0.01341	24.16	0.2828	67.53	1.503
EQ-3	31.89	0.0348	39.72	0.8861	77.73	3.294
EQ-4	29.74	0.01105	21.48	0.3397	68.64	1.213

6.2 FRF Dynamic Analyses of the PRILA Condominium

6.2.1 FRFs from updated mathematical model of the building

It is possible to obtain the FRF for a structural system of "n" degrees of freedom and that is represented in matrix form by the following set of coupled 2nd order differential equations described

$$[M]\,\ddot{u}(t) + [C]\,\dot{u}(t) + [K]\,u(t) = F(t) \tag{6.3}$$

where,

- $[M]$: mass matrix, $(n \times n)$
- $[C]$: damping matrix, $(n \times n)$
- $[K]$: stiffness matrix, $(n \times n)$

- $F(t)$: vector of harmonic forces, $(n \times 1)$
- $u(t)$: vector of physical displacements, $(n \times 1)$
- $\dot{u}(t)$: vector of physical velocities, $(n \times 1)$
- $\ddot{u}(t)$: vector of physical accelerations, $(n \times 1)$

Vectors $u(t)$, $\dot{u}(t)$, and $\ddot{u}(t)$ are obtained by adding the contribution of each of the "n" modes of the structure in the following form:

$$u(t) = \sum_{j=1}^{n} \{\phi_j\} \eta(t) \tag{6.4}$$

$$\dot{u}(t) = \sum_{j=1}^{n} \{\phi_j\} \dot{\eta}(t) \tag{6.5}$$

$$\ddot{u}(t) = \sum_{j=1}^{n} \{\phi_j\} \ddot{\eta}(t) \tag{6.6}$$

where,

- $\{\phi_j\}$: j[th] vibration mode of the structure
- $\eta_j(t)$: j[th] modal coordinate of the structure

These modal coordinates, $\eta_j(t)$, $\dot{\eta}_j(t)$, and $\ddot{\eta}_j(t)$, are the solution of the system of uncoupled 2[nd] order differential equations arranged in matrix form that is obtained by assuming that the structural system possess classical damping. For the uncoupled system of equations, matrix $[C]$ can be approximated with a matrix whose diagonal elements are of the form in equation (6.7).

$$\hat{c}_j = 2\xi_j \omega_j m_j^* \tag{6.7}$$

where,

- $\hat{c}_j$: damping coefficient corresponding to mode "j"
- ξ_j : damping ratio corresponding to mode "j"
- ω_j : natural angular frequency in rad/sec of the structure corresponding to mode "j"

- m_j^* : modal mass of the structure for mode "j"

Therefore, under the assumption of a dynamic system with classical damping, its uncoupled equations of motion will have the following form.

$$[M]\,\ddot{\eta}(t) + \left[\hat{C}\right]\dot{\eta}(t) + [K]\,\eta(t) = F(t) \tag{6.8}$$

In order to obtain equation (6.8) the matrices in the coupled equation of motion shown in (6.3) should be normalized by pre-multiplying each term by $\{\Phi\}^T$ and substituting $u(t)$, $\dot{u}(t)$, and $\ddot{u}(t)$ by $\eta_j(t)$, $\dot{\eta}_j(t)$, and $\ddot{\eta}_j(t)$ respectively, as defined by equations (6.4), (6.5), and (6.6). This transformation is shown in equation (6.9) as

$$\{\phi_j\}^T[M]\{\phi_j\}\,\ddot{\eta}(t) + \{\phi_j\}^T\left[\hat{C}\right]\{\phi_j\}\,\dot{\eta}(t) + \{\phi_j\}^T[K]\{\phi_j\}\,\eta(t) = \{\phi_j\}^T F(t) \tag{6.9}$$

where,

- $\{\phi_j\}^T[M]\{\phi_j\} = \begin{bmatrix} \ddots & & \\ & I & \\ & & \ddots \end{bmatrix}$ (6.10)

- $\{\phi_j\}^T\left[\hat{C}\right]\{\phi_j\} = \begin{bmatrix} \ddots & & \\ & \hat{c}_j & \\ & & \ddots \end{bmatrix}$ (6.11)

- $\{\phi_j\}^T[K]\{\phi_j\} = \begin{bmatrix} \ddots & & \\ & \omega_j^2 & \\ & & \ddots \end{bmatrix}$ (6.12)

- $\{\phi_j\}^T F(t) = N_j(t)$ (6.13)

Consequently, each uncoupled 2nd order differential equation of motion can be written as shown in equation (6.14).

$$\ddot{\eta}(t) + 2\xi_j\omega_j\dot{\eta}(t) + \omega_j^2\eta(t) = N_j(t) \tag{6.14}$$

By assuming that a base excitation is acting on the structure, the modal force term on the right of equation (6.14) can be expressed as

$$N(t) = -\{\phi_j\}^T [M]\{r\}\ddot{X}_g(t) \tag{6.14}$$

where,

- $\ddot{X}_g(t)$: base acceleration (e.g., as measured at the base of a building), $A_g e^{i\Omega t}$
- $\{r\}$: influence vector
- $\{\phi_j\}$: vibration mode "j" of the structure

Similarly, it is convenient to define a new variable, A_q, for the "j^{th}" mode as

$$A_{q,j} = \{\phi_j\}^T [M]\{r\}A_g \tag{6.15}$$

Therefore, the uncoupled motion equation shown in (6.13) can be redefined as in (6.16).

$$\ddot{\eta}(t) + 2\xi_j\omega_j\dot{\eta}(t) + \omega_j^2\eta(t) = -A_{q,j}e^{i\Omega t} \tag{6.16}$$

Accordingly, to obtain the particular (i.e., steady-state) solution of the 2nd order differential equation in (6.16), the following solution is proposed.

$$\eta(t) = A_j e^{i\Omega t} \tag{6.17}$$

$$\dot{\eta}(t) = i\Omega A_j e^{i\Omega t} \tag{6.18}$$

$$\ddot{\eta}(t) = -\Omega^2 A_j e^{i\Omega t} \tag{6.19}$$

By substituting equation (6.17), (6.18), and (6.19) into equation (6.16) and rearranging terms it is possible to obtain

$$A_j = \frac{-A_{q,j}}{\omega_j^2 - \Omega^2 + i2\xi_j\omega_j\Omega} \tag{6.20}$$

Then, by substituting equation (6.20) into equations (6.17), (6.18), and (6.19) it is possible rewrite these equations in the following form:

$$\eta(t) = \frac{-1}{\omega_j^2 - \Omega^2 + i2\xi_j\omega_j\Omega} A_q e^{i\Omega t} \tag{6.21}$$

$$\dot{\eta}(t) = \frac{-i\Omega}{\omega_j^2 - \Omega^2 + i2\xi_j\omega_j\Omega} A_q e^{i\Omega t} \tag{6.22}$$

$$\ddot{\eta}(t) = \frac{-\Omega^2}{\omega_j^2 - \Omega^2 + i2\xi_j\omega_j\Omega} A_q e^{i\Omega t} \tag{6.23}$$

Equations (6.21), (6.22), and (6.23) can be substituted into the vectors with physical coordinates defined in equations (6.4), (6.5), and (6.6) to obtain the corresponding relative displacements, velocities, and accelerations, which are shown below.

$$u(t) = \sum_{j=1}^{n} \frac{-\{\phi_j\}}{\omega_j^2 - \Omega^2 + i2\xi_j\omega_j\Omega} A_q e^{i\Omega t} \tag{6.24}$$

$$\dot{u}(t) = \sum_{j=1}^{n} \frac{-i\Omega\{\phi_j\}}{\omega_j^2 - \Omega^2 + i2\xi_j\omega_j\Omega} A_q e^{i\Omega t} \tag{6.25}$$

$$\ddot{u}(t) = \sum_{j=1}^{n} \frac{-\Omega^2\{\phi_j\}}{\omega_j^2 - \Omega^2 + i2\xi_j\omega_j\Omega} A_q e^{i\Omega t} \tag{6.26}$$

In addition, a modal participation factor, γ_j, can be defined as shown in equation (6.27) and in which $\{r\}$ is an influence vector such that the variable A_q can be redefined as in equation (6.28).

$$\gamma_j = \{\phi_j\}^T [M]\{r\} \tag{6.27}$$

$$A_{q,j} = \gamma_j A_g e^{i\Omega t} \tag{6.28}$$

Consequently, the physical displacements, velocities, and accelerations can be redefined as shown in the following equations.

$$u(t) = \sum_{j=1}^{n} \frac{-\{\phi_j\}\gamma_j}{\omega_j^2 - \Omega^2 + i2\xi_j\omega_j\Omega} A_g e^{i\Omega t} \tag{6.29}$$

$$\dot{u}(t) = \sum_{j=1}^{n} \frac{-i\Omega\{\phi_j\}\gamma_j}{\omega_j^2 - \Omega^2 + i2\xi_j\omega_j\Omega} A_g e^{i\Omega t} \tag{6.30}$$

$$\ddot{u}(t) = \sum_{j=1}^{n} \frac{\Omega^2\{\phi_j\}\gamma_j}{\omega_j^2 - \Omega^2 + i2\xi_j\omega_j\Omega} A_g e^{i\Omega t} \tag{6.31}$$

Therefore, it is possible to define the system's *relative* FRFs in its *compliance*, *mobility*, and *accelerance* forms in equations (6.32), (6.33), and (6.34), respectively. In these equations, the subscript "r" indicates the eigenvector row that represents the place in the physical structure from which it is desired to extract the system's response from an installed sensor and the subscript "b" refers to the base of the structure.

$$H_{r,b}(\Omega) = \sum_{j=1}^{n} \frac{-\phi_{r,j}\ \gamma_j}{\omega_j^2 - \Omega^2 + i2\xi_j\omega_j\Omega} \tag{6.32}$$

$$H_{r,b}(\Omega) = \sum_{j=1}^{n} \frac{-i\Omega\ \phi_{r,j}\ \gamma_j}{\omega_j^2 - \Omega^2 + i2\xi_j\omega_j\Omega} \tag{6.33}$$

$$\boldsymbol{H_{r,b}(\Omega) = \sum_{j=1}^{n} \frac{\Omega^2\ \phi_{r,j}\ \gamma_j}{\omega_j^2 - \Omega^2 + i2\xi_j\omega_j\Omega}} \tag{6.34}$$

Likewise, if the FRF needs to be computed given an *absolute* response recorded in a sensor in the structure, such as in cases where the dynamic excitation is located at the base of the structure (e.g., tremors, ambient vibrations, etc.), the uncoupled motion equation in (6.16) should be rearranged as shown in equation (6.35).

$$\ddot{\eta}(t) + \gamma \ddot{X}_g(t) = -2\xi_j \omega_j \dot{\eta}(t) - \omega_j^2 \eta(t) \tag{6.35}$$

From it, the *absolute acceleration* due to vibration mode "*j*" can be defined as:

$$a_j(t) = -2\xi_j \omega_j \dot{\eta}(t) - \omega_j^2 \eta(t) \tag{6.36}$$

Then, by substituting equations (6.17) and (6.18) into equation (6.35) it is possible to redefine the expression for the *absolute acceleration*, as shown below.

$$a_j(t) = -i2\xi_j \omega_j \Omega A_j e^{i\Omega t} - \omega_j^2 A_j e^{i\Omega t} \tag{6.37}$$

It is possible to define a *total*, or *absolute*, acceleration's vector as expressed in equation (6.38).

$$\{a_T(t)\} = \sum_{j=1}^{n} \{\phi_j\} a_j(t) = -\sum_{j=1}^{n} \{\phi_j\} \left(i2\xi_j \omega_j \Omega A_j e^{i\Omega t} + \omega_j^2\right) A_j e^{i\Omega t} \tag{6.38}$$

By replacing the variable "A_j" in equation (6.38) by its expression in equation (6.20) the *total*, or *absolute*, accelerations vector is redefined as follows.

$$\{a_T(t)\} = \sum_{j=1}^{n} \frac{\{\phi_j\}\left(\omega_j^2 + i2\xi_j \omega_j \Omega\right)}{\omega_j^2 - \Omega^2 + i2\xi_j \omega_j \Omega} A_{q,j} \tag{6.39}$$

Accordingly, a new variable, A_b, can be defined as shown in equation (6.40) to be able to redefine equation (6.39) for the response at the degree of freedom "*r*" due to base excitations, as established in the expression below.

$$A_{b,j} = \gamma_j \, A_g \tag{6.40}$$

$$a_{rT}(t) = \sum_{j=1}^{n} \frac{\phi_{r,j}\left(\omega_j^2 + i2\xi_j\omega_j\Omega\right)}{\omega_j^2 - \Omega^2 + i2\xi_j\omega_j\Omega} A_{b,j} e^{i\Omega t} \tag{6.41}$$

Consequently, the *absolute accelerance* FRF is defined in equation (6.42).

$$\boldsymbol{H_{r,b}(\Omega) = \sum_{j=1}^{n} \frac{\phi_{r,j}\left(\omega_j^2 + i2\xi_j\omega_j\Omega\right)}{\omega_j^2 - \Omega^2 + i2\xi_j\omega_j\Omega}} \tag{6.42}$$

A plot of the *absolute accelerance* FRF defined in equation (6.42) for the updated mathematical model of the PRILA Condominium is shown in Figure 6-13 for a response measured at the 22nd story, as an example. The graph on Figure 6.13a displays the FRF with the complete range of computed frequencies. However, in order to better illustrate the natural frequencies of interest for this study, the graph shown in Figure 6.13b shows only the range where the first four natural frequencies of the building are located.

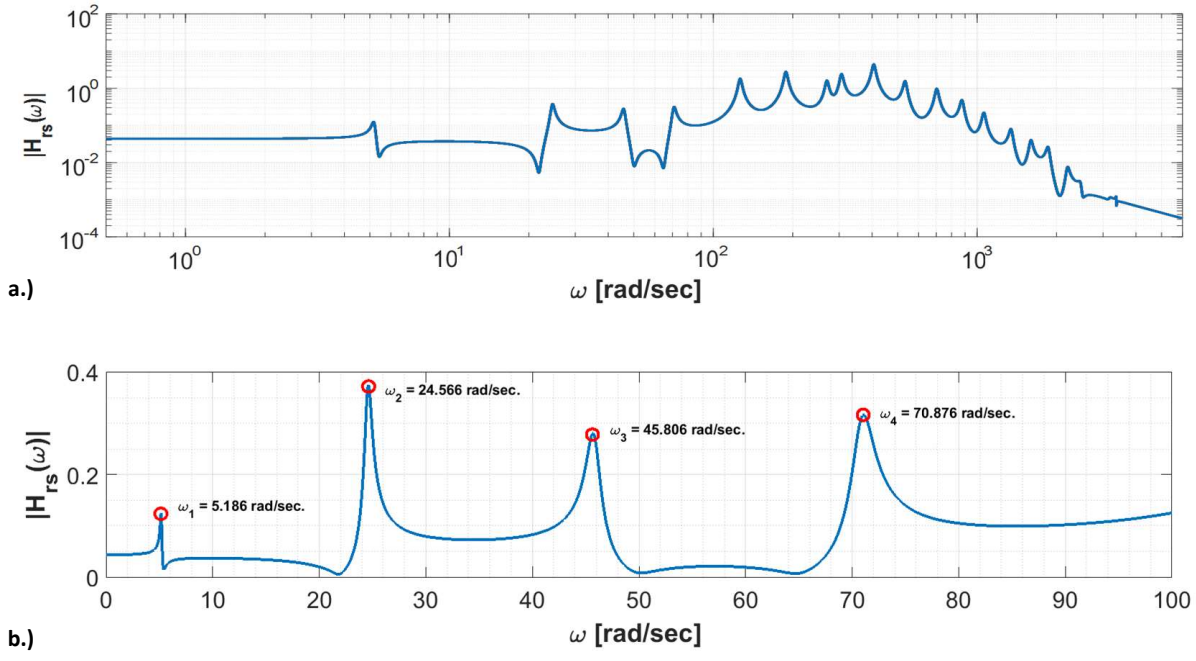


Figure 6-13: Absolute accelerance FRF for PRILA; a.) FRF defined over all frequencies range; b.) FRF in the range of the first four natural frequencies

6.2.2 Experimental FRFs from recorded ambient vibrations

Experimental FRFs provide valuable information about a dynamic system and, when properly extracted and analyzed, can result in a better assessment of the structural system. When generating FRFs from recorded ambient vibrations in a structural system, besides identifying the natural frequencies of the system, it is possible to identify its damping, via the half-power method, and its modal shapes, which acquires special importance in MDOF systems. Because ambient vibrations possess a broad frequency spectrum, they ideally can excite all the structure's frequency content. However, this premise is not entirely, or at least physically, true due to several reasons. First, it assumes white noise properties on the recorded ambient vibrations, which can never be true because it is a theoretical idealization. Second, the sensor type and sensitivity may be an issue that limits the recording to the manufacturer's specified range. Third, although ideally an input wave can freely propagate through a continuous medium, it is also true that it can be attenuated through the medium by other waves or by the medium itself so that its amplitude may not allow its recording by the available sensors in the system. Fourth, the quantity and optimal placement of the sensors throughout the structure play a significant role in the amount and quality of information that can be revealed of the system. Fifth, the recording memory available and the time availability to retrieve these recordings in most cases controls the sampling frequency, which limits the capability of recording a range of frequencies higher than the established Nyquist frequency. As a result, lower frequencies of a system are easier and more reliable to identify through frequency domain experimental methods such as the FRF.

Furthermore, depending on the extent and complexity of the studied structural system and on the location of the measurement sensors, the identified natural frequencies may have slight-to-noticeable differences in each sensor. Similarly, when the mass and stiffness arrangement of a system produces closely spaced natural frequencies, their identification can be more difficult and tedious, especially if high levels of unwanted noise are embedded in the recorded signal. For these and similar scenarios, the analyst experience in the dynamic identification field is highly valuable. In complex and large structural systems being identified by experimental FRFs, peaks corresponding to specific natural frequencies could be masked by higher peaks or peaks with comparable magnitude corresponding to noise effects or to vibration frequencies belonging to a distant effect. This distant effect bay be caused by a structural assembly or subsystem with a nearby frequency of vibration within the spectrum and having the same mode shape, with maybe a

different phase angle. For these cases, and after its recognition, it is useful to extract the system's experimental modal deformed shapes by means of its experimental FRFs.

The PRILA Condominium is a complex structural system with large dimensions. Hence, the structure can be divided into three coupled dynamic subsystems: the east wing, the west wing, and the central core, which corresponds to the elevator shaft. Due to the global structure geometry and its extent, each of these subsystems is able to dynamically behave with the same modal shape, but with slightly different frequencies of vibration while in addition its response oscillations may contain a different phase angle. Accordingly, the sensors' layout in PRILA Condominium include sensors in the 1st and 20th stories placed at the opposite extreme ends of the slabs in order to capture each subsystem's 1st mode of vibration. Likewise, a vertical arrangement of sensors was installed at the other stories attached closer to the elevator shaft, to capture its modal behavior. Consequently, the interaction between the three subsystems may be observed in the generated experimental FRFs of the system as a cluster of peaks in the region of interest. For cases like these, by extracting the modal deformed shape corresponding to each candidate natural frequency located in a region of interest in the spectrum it is possible to determine which frequency corresponds to the mode shape in that specific location and which doesn't.

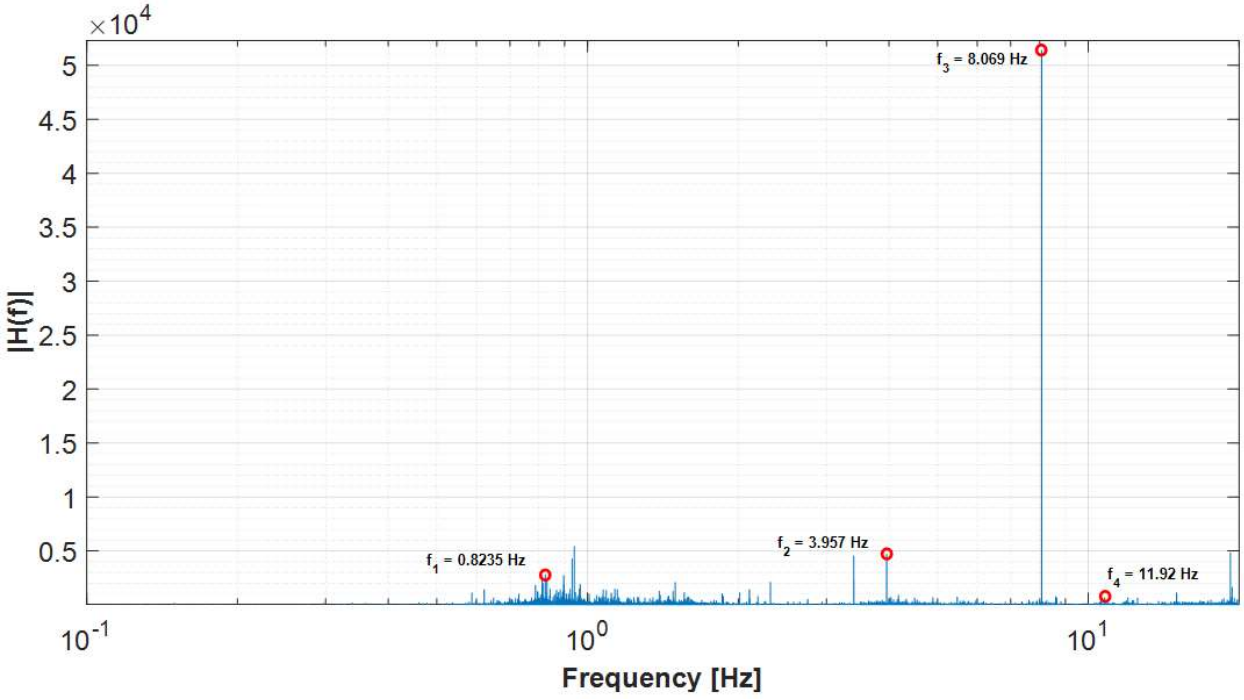


Figure 6-14: Example of experimental FRF computed for output sensor #33

With this in mind, it is important to generate experimental FRFs in the proper way in order to facilitate the extraction of information. The experimental FRFs measured for the PRILA Condominium were computed by applying the FFT to 24 hours of recorded ambient vibration and substituting the input and output measurements in equation (6.2). The signals recorded in sensors #3 and #7 were used as inputs in the west and east sides, respectively. Figure 6-14 displays an illustrative example of the FRF computed with an output measurement recorded at sensor #33. When plotting the generated FRFs, for visual convenience, its absolute value is displayed. However, to extract the modal shape of a selected frequency, only the imaginary part of the FRF was plotted. In order to completely extract a mode shape of a specific frequency defined throughout the height of the structure, the following procedure must be performed.

1. Compute the FRFs for all the sensors located in a vertical layout, preferably using as input signal the measurement recorded at the base of the building.
2. Plot the FRFs absolute values, $|H(f)|$, and in each plot select the dominant peaks, which may correspond to the frequency of interest.
3. Plot the imaginary part of all the FRFs, $Im[H(f)]$, and select, in each graph, the peaks corresponding to the frequencies, previously selected in the $|H(f)|$ plots.
4. For each selected frequency, plot the sensors' elevation versus their value of $Im[H(f)]$.

This generates a plot of the apparent modal deformed shape of each selected frequency of interest.

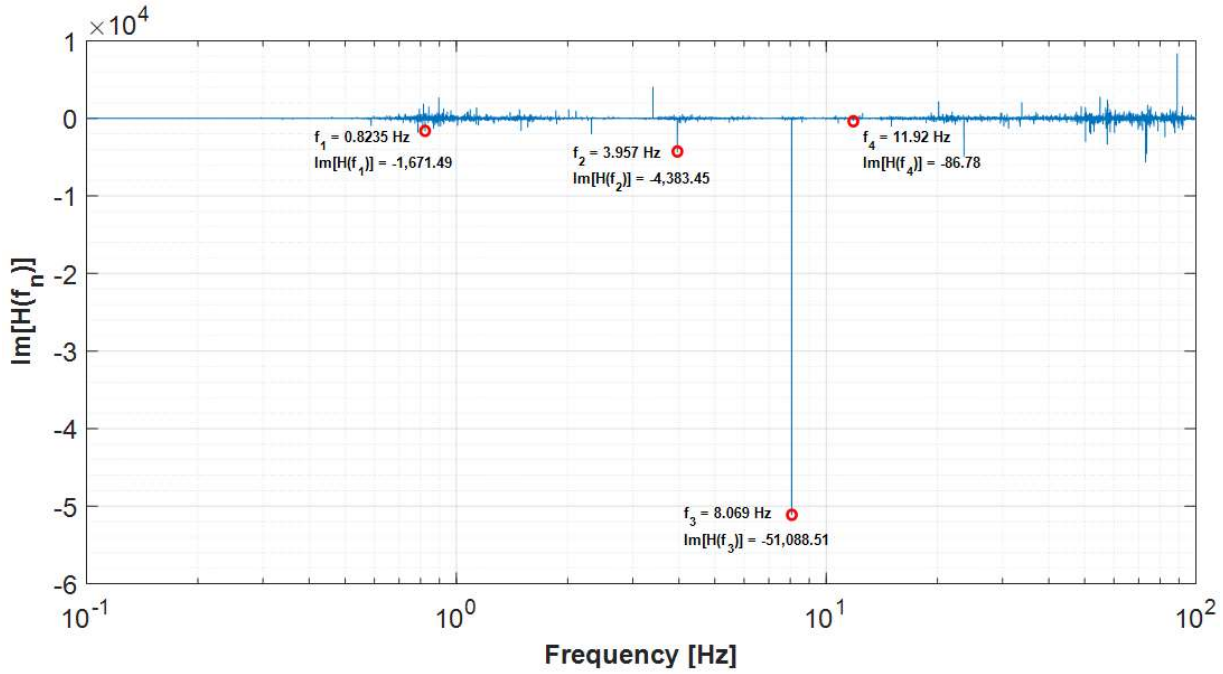


Figure 6-15: Imaginary part of experimental FRF computed for output sensor #33

Through visual inspection, and maybe several iterations, it is possible to determine which is the natural frequency of vibration according to the best possible representation of the mode of interest. If for a specific candidate frequency (pre-selected), the plotted modal shape does not completely represent the desired mode, it shall be discarded and another candidate frequency should be checked. This procedure should be repeated until the best representation of the mode is found for a frequency. Figure 6-15 shows a plot of $Im[H(f)]$ with selected peaks belonging to the frequencies of interest.

It is important to note that this procedure only gives the deformed shape of a mode and is not the mode shape vector, $\{\phi_j\}$, of the structure. However, the experimental values of $Im[H(f)]$ can be mathematically related to compute an approximated experimental mode shape vector. Tables 6-3 and 6-4 display PRILA's first four natural frequencies extracted by the Experimental FRF method and its respective values of $Im[H(f)]$.

Table 6-3: Experimental natural frequencies and modal deformed shapes extracted from FRFs on east side of PRILA

Sensor	Elevation [ft]	f_1 [Hz]	Im[H(f_1)]	f_2 [Hz]	Im[H(f_2)]	f_3 [Hz]	Im[H(f_3)]	f_4 [Hz]	Im[H(f_4)]
S7	0	—	0	—	0	—	0	—	0
S12	11.75	0.8235	-58.75	3.957	1,218.19	8.069	-32,910.04	11.92	-27.31
S15	19.75	0.8235	-228.40	3.957	2,877.26	8.069	-123,086.73	11.92	-214.20
S18	35.75	0.8235	-466.15	3.957	4,505.10	8.069	-147,039.22	11.92	-129.35
S21	59.75	0.8235	-651.56	3.957	6,025.37	8.069	-84,655.45	11.92	154.20
S24	83.75	0.8235	-788.03	3.957	5,463.76	8.069	39,844.43	11.92	213.72
S27	115.75	0.8235	-1,188.31	3.957	2,745.02	8.069	94,737.77	11.92	-50.29
S30	139.75	0.8235	-1,427.15	3.957	574.02	8.069	72,200.45	11.92	-196.61
S33	157.5	0.8235	-1,671.49	3.957	-4,383.45	8.069	-51,088.51	11.92	-86.78
S36	167.5	0.8235	-763.07	3.957	-8,274.63	8.069	-84,773.84	11.92	240.64
AVERAGE		**0.8235**	**---**	**3.957**	**---**	**8.069**	**---**	**11.92**	**---**

Table 6-4: Experimental natural frequencies and modal deformed shapes extracted from FRFs on west side of PRILA

Sensor	Elevation [ft]	f_1 [Hz]	Im[H(f_1)]	f_2 [Hz]	Im[H(f_3)]	f_3 [Hz]	Im[H(f_3)]	f_4 [Hz]	Im[H(f_4)]
S3	0	—	0	—	3.689	—	0	—	0
S10	11.75	0.8657	-547.63	3.689	3588.91	7.6	-23785.49	11.9	-1270.02
S13	19.75	0.8657	-1872.16	3.689	11574.33	7.6	-97534.25	11.9	-6640.39
S16	35.75	0.8657	-3623.45	3.689	18369.23	7.6	-130100.73	11.9	-2661.99
S19	59.75	0.8657	-6767.27	3.689	24060.95	7.6	-86590.05	11.9	8321.96
S22	83.75	0.8657	-3938.51	3.689	8282.99	7.6	9149.37	11.9	3761.2
S25	115.75	0.8657	-14515.2	3.689	11609.58	7.6	100940.75	11.9	-5019.74
S28	139.75	0.8657	-17140.2	3.689	1512.84	7.6	90822.95	11.9	-11865.2
S31	157.5	0.8657	-20687.3	3.689	-16911.57	7.6	-25214.17	11.9	-2953.19
S34	167.5	0.8657	-23071.8	3.689	-23442.89	7.6	-89131.11	11.9	11849.71
AVERAGE		**0.8657**	**---**	**3.689**	**---**	**7.6**	**---**	**11.9**	**---**

Experimental deformed shapes corresponding to the first four modes of vibration are shown below. The values are extracted from Tables 6-3 and 6-4 and plotted as part of the iterative selection process of determining the correct natural frequency per sensor. The east and west sides' deformed experimental shapes of PRILA are displayed in Figures 6-16 to 6-19 and 6-20 to 6-23, respectively.

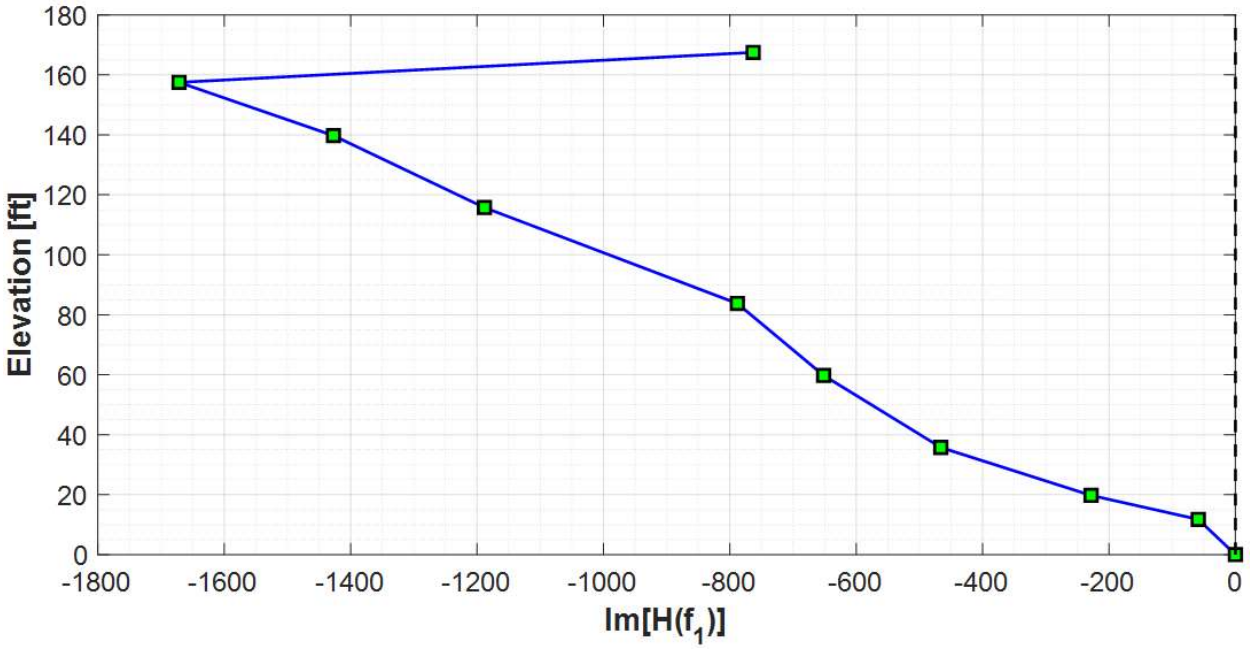


Figure 6-16: Experimental deformed shape for PRILA's 1st mode of vibration recorded at its east side

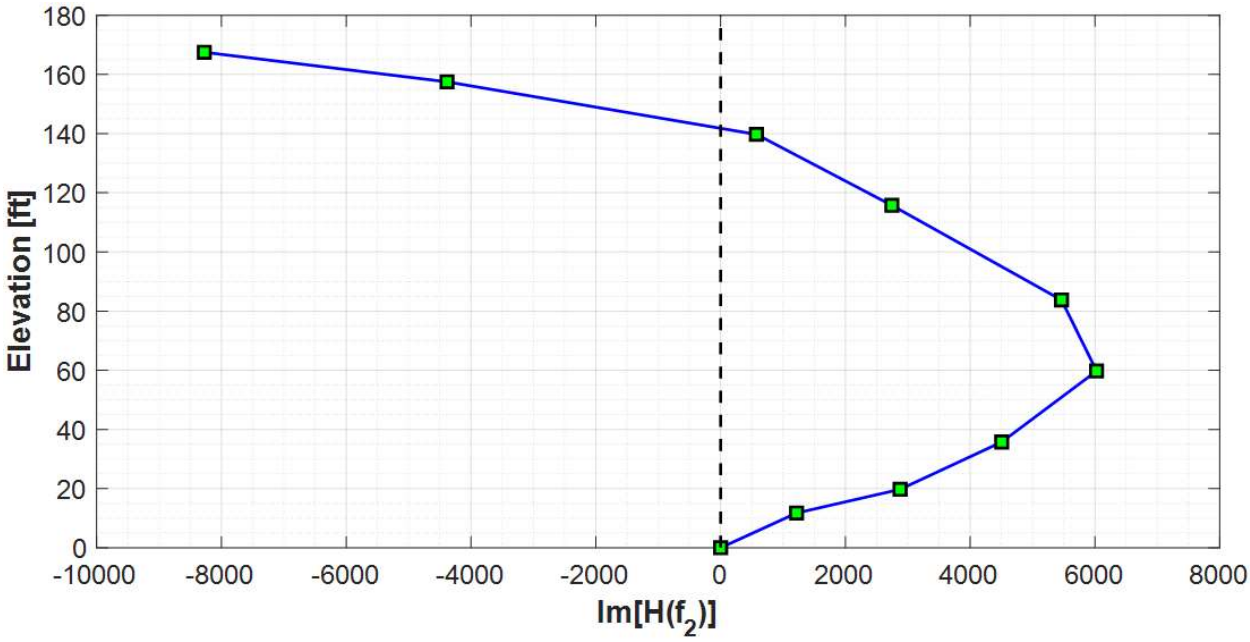


Figure 6-17: Experimental deformed shape for PRILA's 2nd mode of vibration recorded at its east side

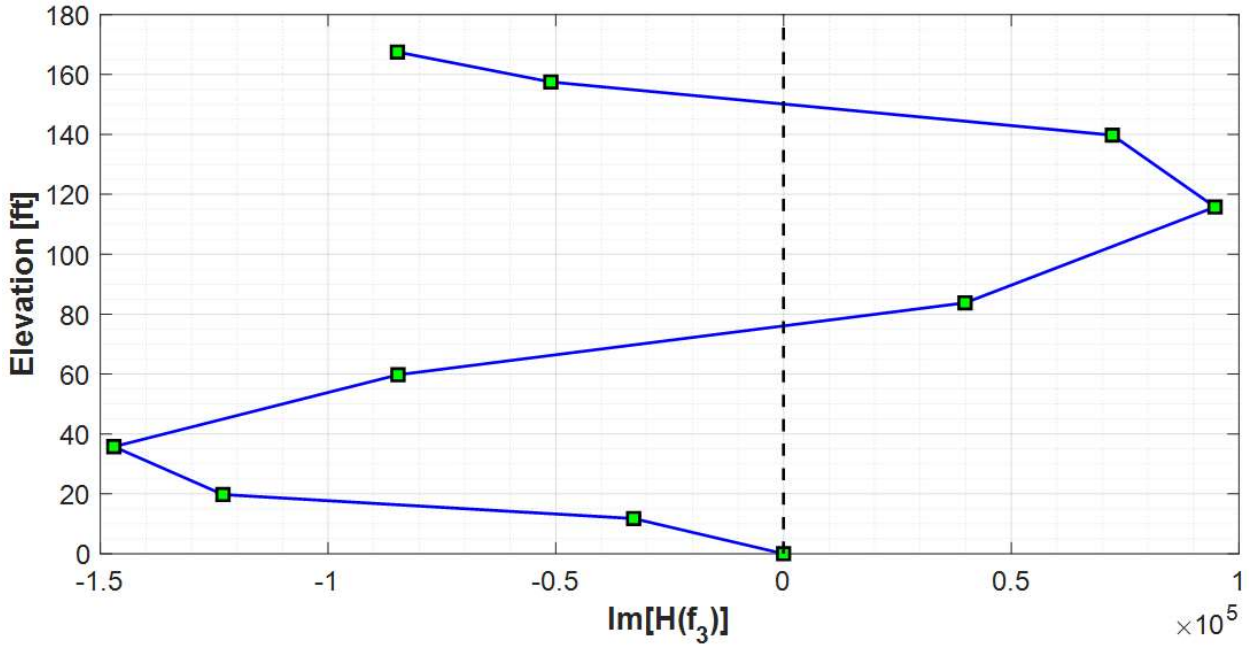


Figure 6-18: Experimental deformed shape for PRILA's 3rd mode of vibration recorded at its east side

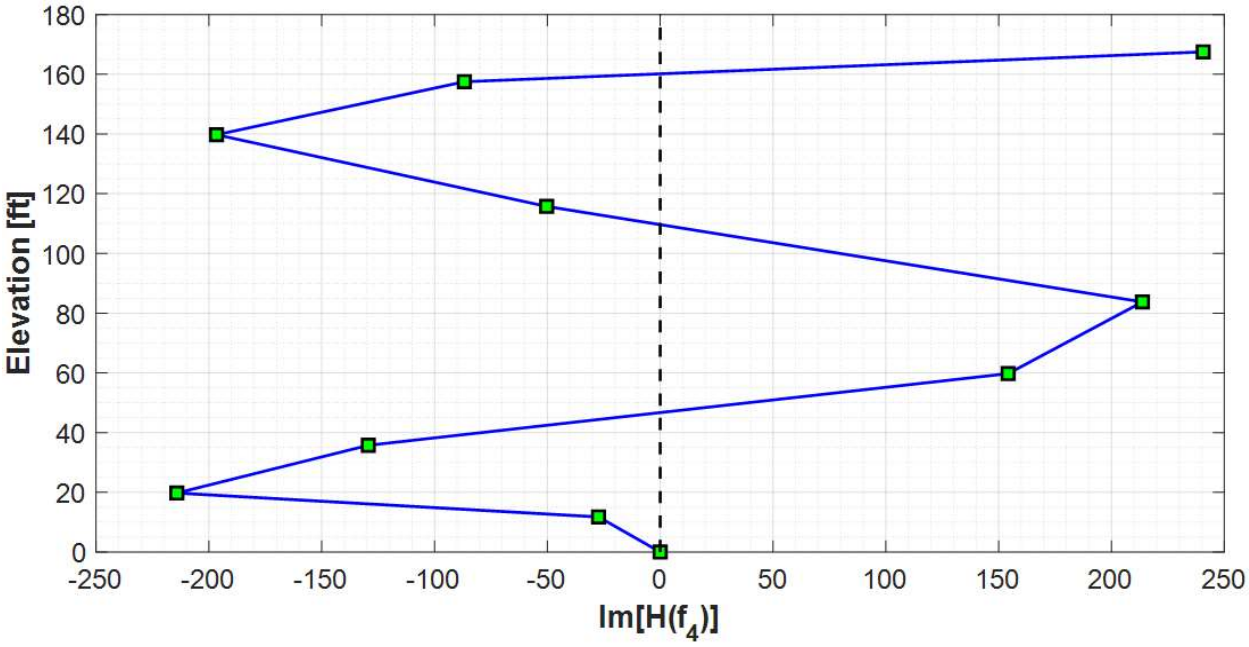


Figure 6-19: Experimental deformed shape for PRILA's 4th mode of vibration recorded at its east side

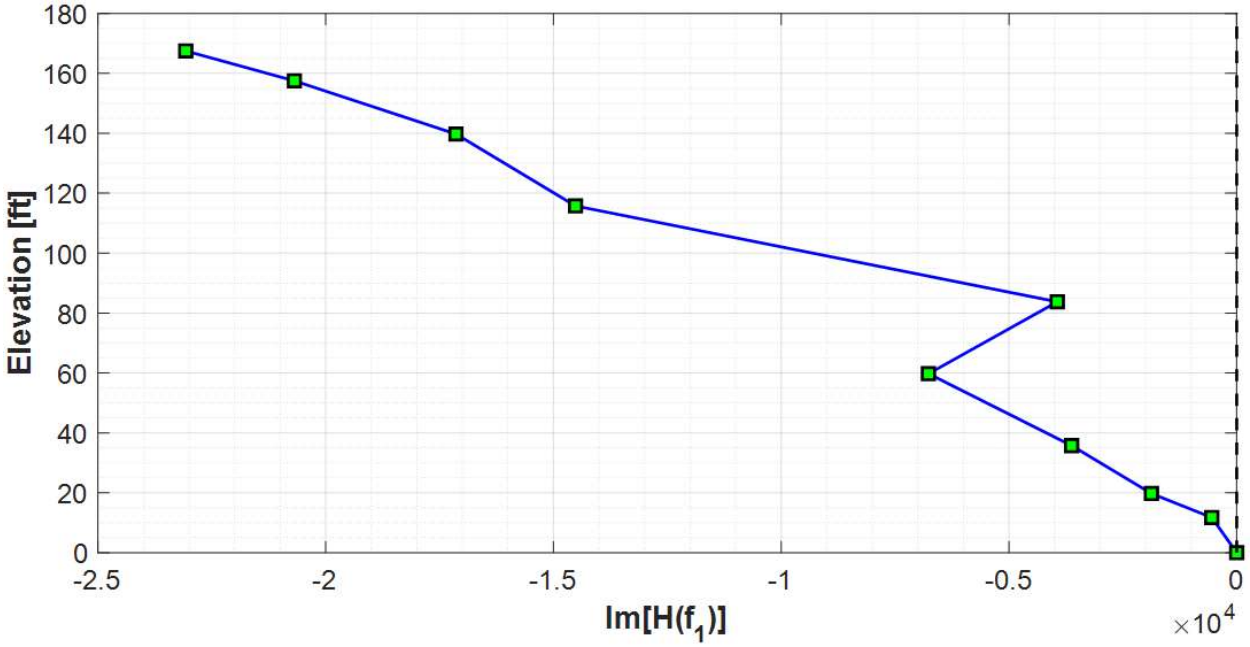


Figure 6-20: Experimental deformed shape for PRILA's 1st mode of vibration recorded at its west side

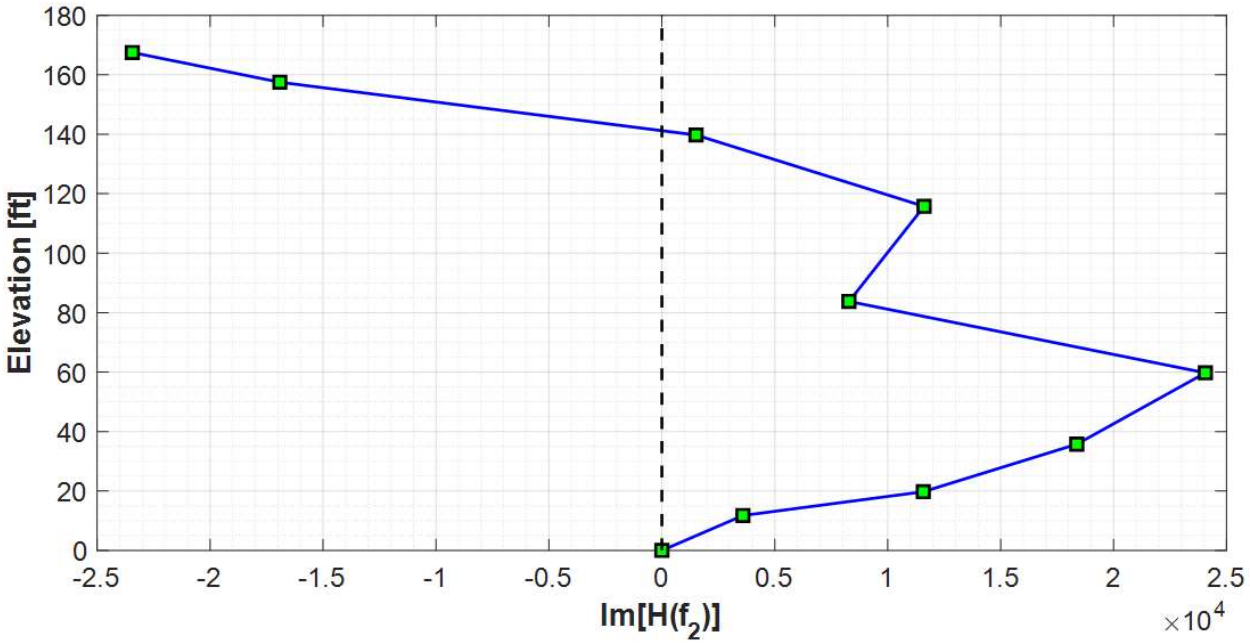


Figure 6-21: Experimental deformed shape for PRILA's 2nd mode of vibration recorded at its west side

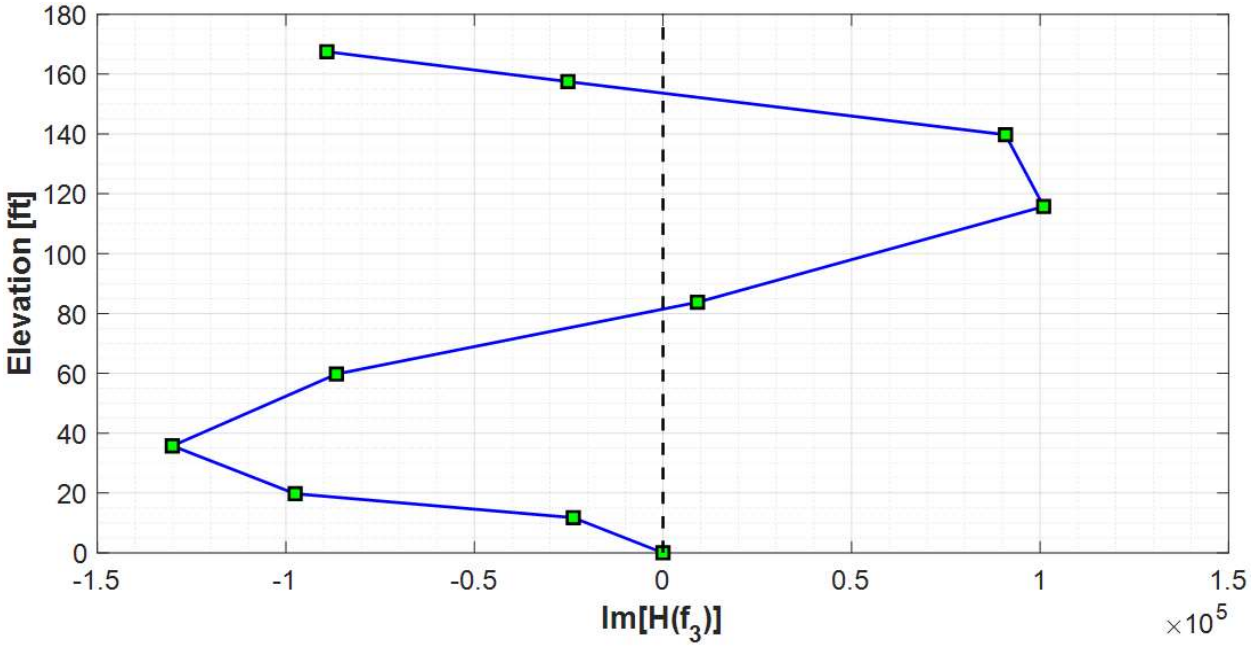


Figure 6-22: Experimental deformed shape for PRILA's 3rd mode of vibration recorded at its west side

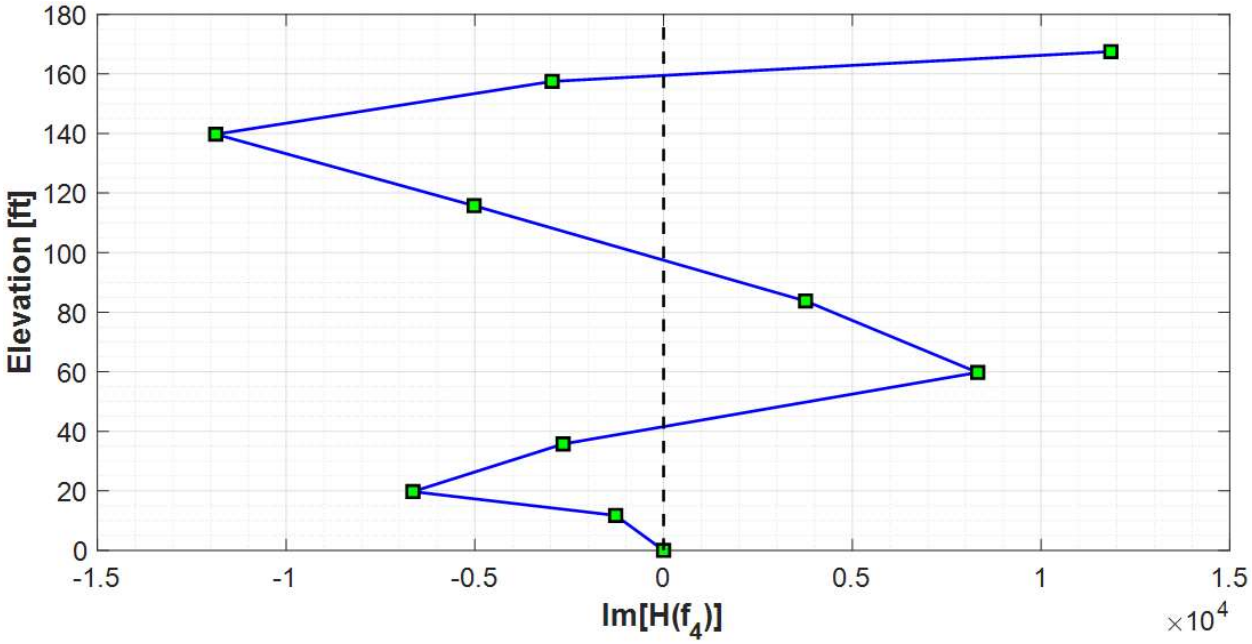


Figure 6-23: Experimental deformed shape for PRILA's 4th mode of vibration recorded at its west side

CHAPTER 7. EARTHQUAKES AND NONLINEAR ANALYSES FOR ASSESSMENT

7.1 Seismicity in the Puerto Rico Region and Probable Earthquakes

Puerto Rico, as many other countries and cities in the United States, is in a highly active seismic zone. The island is located between latitudes $18.0°N$ and $18.5°N$ and longitudes $65.5°W$ and $67.5°W$. Therefore, it is in the border of the Caribbean plate next to the North American plate and stands west of a subduction zone near strike-slip zones. Figure 7-1a shows a map of the Caribbean plate with some of its fault mechanisms and Figure 7-1b displays its most seismic regions.

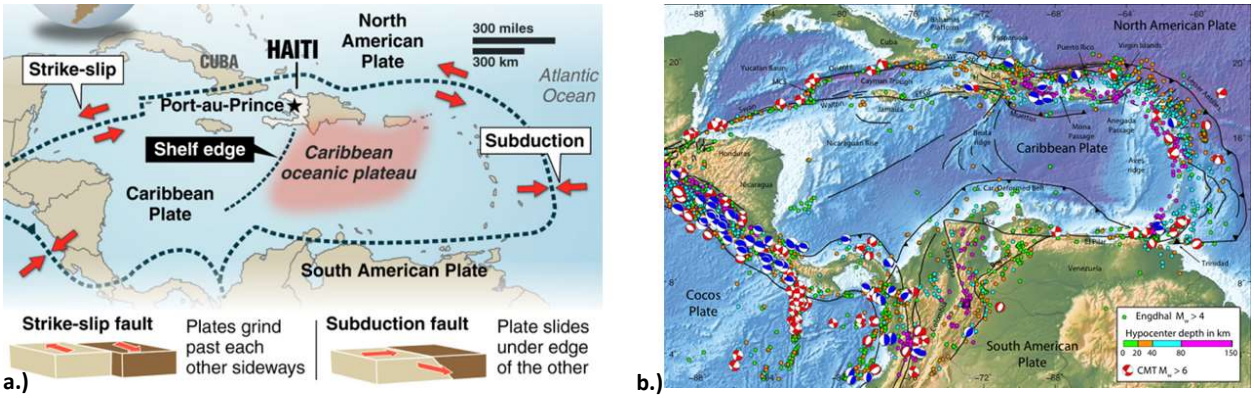


Figure 7-1: Seismicity in the Caribbean. a.) The Caribbean tectonic plate's relative movements and its faults. (Caribbean Studies Course) b.) The most active seismic zone on the Caribbean plate is at its borders. (E. Calais, Caribbean Active Tectonics)

As noticed in the Figures, the great majority of the seismic activity occurs in the borders of the Caribbean plate. In fact, the North American plate is bent down to the south and the Caribbean plate is bent down to the north, which means that they maybe in contact beneath the islands. There is scientific evidence of oblique subduction and lateral displacement between the two plates. The island's seismic activity is concentrated in eight main zones:

- The Puerto Rico Trench (to the North)
- The Northern and Southern Slope Faults (to the North)
- El Sombrero Seismic Zone (to the Northeast)
- The Mona Passage (to the West)
- The Mona Trough (to the West)

- The Virgin Islands and the Anegada Trough (to the East)
- The Muertos Trough (to the South)
- Puerto Rico's southwest region

Puerto Rico is currently surrounded by more than ten known inland and marine faults, although recent geophysical studies have revealed the existence of several more inland faults. These and other studies are still in progress and hence have not been completely incorporated in the design codes. Figure 7-2 is a map adapted from the Puerto Rico Seismic Network (PRSN) displaying the most active known faults in the island's region. USGS research indicates an equal probability for damaging ground motion for Mayagüez in western Puerto Rico as for Seattle, Washington. A study from McCann (1987) concluded that the probability of occurrence of a strong intensity earthquake is 33 - 50% within a 50 years' timeframe. In fact, the PRSN has registered more than 2,000 tremors per year since 2006.



Figure 7-2: The archipelago of Puerto Rico and most of its active known seismic faults

The recording of seismic activity in the island of Puerto Rico has been increasing in the last several decades. In the mid-1980s, the PRSN registered around 500 tremors per year. By 2017 this number increased to more than 3,000 tremors per year, with its highest record on 2016 with almost 4,000 registered tremors. In simple terms, the seismic activity registered in the Puerto Rico region has increased between 6 and 8 times since it started being documented. Figure 7-3 shows the registered seismic activity in the Puerto Rico region per year in the last three decades.

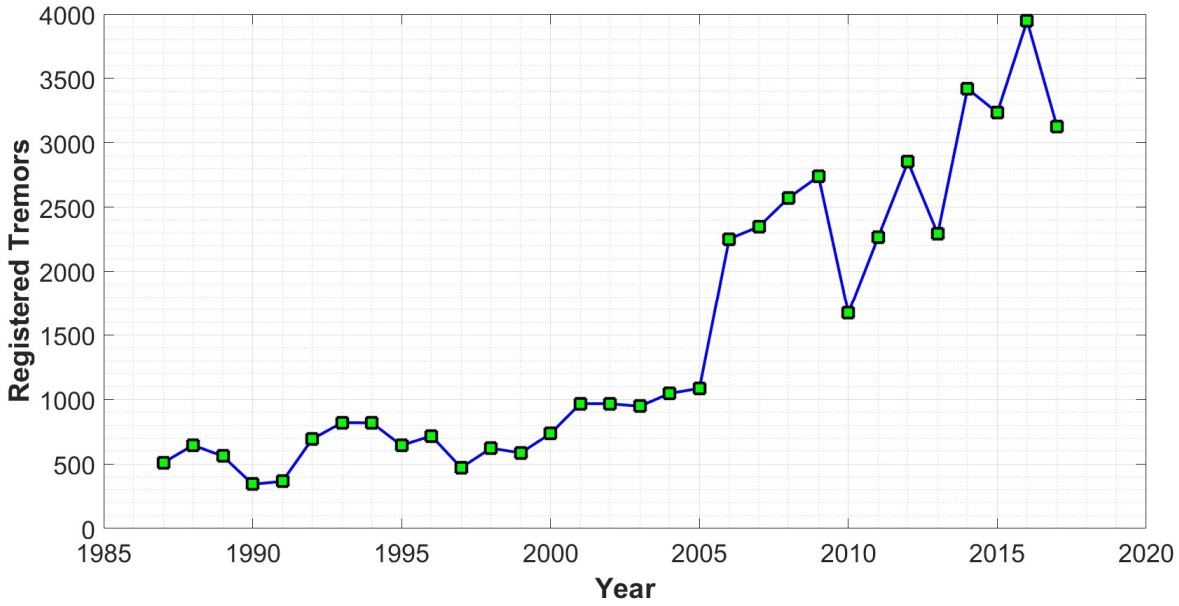


Figure 7-3: Registered seismic activity in the Puerto Rico region (data from PRSN)

It is important to note that more and better instrumentation has been acquired and installed in more locations throughout the years. However, the data trend as depicted in Figure 7-3, may create the public thinking that the seismic activity is expected to further increase which may not be the case. Furthermore, no strong intensity earthquake has been recorded in the island since the PRSN foundation in 1974. For instance, from the 1600s to 2018, only four significant and destructive earthquakes have been documented. Table 7-1 provides details of each event.

Table 7-1: Historic destructive earthquakes in the Puerto Rico region

Name	Date	Magnitude [M_w]	MMI	Epicenter	Comments
---	1670	Unknown	Unknown	West Coast	Significant damage in San German and the west coast of PR
Boricua Earthquake	05.02.1787	8	Unknown	Puerto Rico Trench	Felt in all PR. Major damages in all PR, including El Morro & San Cristobal Forts.
---	11.18.1867	7.3	X	Anegada Passage	Major damage in the east of PR. Produced a tsunami with 5 ft high waves.
San Fermín Earthquake	10.11.1918	7.3	IX	Mona Canyon	Major damage in the west coast of PR. Produced a tsunami with 20 ft high waves.

These historic records show cycles ranging from 51 to 117 years, from which an average period of recurrence of 83 years can be computed for destructive earthquakes. However, because each of these earthquakes were generated in different faults, other factors such as geological structures and activeness of faults, among others, may adjust that previously computed average recurrence period.

Furthermore, due to the lack of recorded strong earthquakes in the Puerto Rico region in recent times, earthquake-resistant analysis and design of structures must be performed by importing recorded earthquakes from around the world.

A study by Irizarry (1999) concluded that the maximum credible magnitude for earthquakes generated from geological faults located off the coast of Puerto Rico is 7.5 M, except for the fault located in the Puerto Rico Trench, whose earthquakes can reach 8.0 M. Similarly, inland geological faults can generate earthquakes with a maximum credible magnitude of 6.5 M. Her study was primarily based on historic earthquakes' records, faults' lengths, and geological formations. On her study, a set of 7 earthquakes were ultimately selected for each of the three main metropolitan cities of Puerto Rico: San Juan, Ponce, and Mayagüez. With these earthquake records she generated elastic response spectra for these cities, from which a final elastic design response spectrum was obtained and suggested for each municipality from a smooth envelope. More information on the details of this study can be found in Irizarry (1999) and in Martínez, Irizarry, and Portela (1999). The earthquakes selected in her study for the municipalities of San Juan and Ponce are used in the current study to perform a dynamic seismic assessment of the Ponce Highway Bridge [ID: 2348] and the PRILA Condominium. Tables 7-2 and 7-3 show specific information of these selected earthquakes for each city. These imported earthquakes are mathematically transformed and modified to meet the expected soil accelerations and amplifications specified in ASCE7-16 for the municipalities of Ponce, PR and San Juan, PR. Consequently, a set of artificial probable earthquakes that are compatible with the site's elastic design response spectrum were generated for each of the two cities.

Table 7-2: Earthquake records selected for Ponce, PR

Earthquake Name	Date	Depth [km]	Magnitude	Station Name	Epicenter [km]	PGA [g]	Filename
San Salvador	10.10.86	8	5.4 M_S	Geotechnical Investigation Center	4.3	0.420	CIG.EW
San Salvador	10.10.86	8	5.4 M_S	Hotel Sheraton	7	0.301	HSH.EW
San Salvador	10.10.86	8	5.4 M_S	National Geographical Institute	5.7	0.535	IGN.EW
San Salvador	10.10.86	8	5.4 M_S	Institute of Urban Construction	6	0.387	IVU.EW
San Salvador	10.10.86	8	5.4 M_S	Universidad Centro Americana	4	0.417	UCA.EW
Coyote Lake	08.06.79	6	5.8 M_L	Gilroy Array #6, San Ysidro	10	0.357	USACA18.033
Morgan Hill	04.24.84	9	6.2 M_L	Gilroy Array #6, San Ysidro	37	0.286	USACA36.011

Table 7-3: Earthquake records selected for San Juan, PR

Earthquake Name	Date	Depth [km]	Magnitude	Station Name	Epicenter [km]	PGA [g]	Filename
Japanese Earthquake	06.12.68	31	6.4 M_w	Miyako Harbor Works, Ground	103	0.167	JAP03.104
Miyagi Prefecture	06.12.78	40	6.3 M_w	Ofunato Harbor, Jetty	103	0.226	JAP03.173
Michoacán Aftershock	09.23.85	20	7.6 Ms	Papanoa	83	0.226	MEX03.112
Northridge	01.17.94	18	6.7 M_w	Pacoima, Kagel Canyon	43	0.301	pacoimaw.v2
Northridge	01.17.94	18	6.7 M_w	Rolling Hills Estates, Rancho Vista School	50	0.116	rollhill.v2
ADAK	05.02.71	38	6.8 M_S	Adak Naval Base (Hand Dig.)	67	0.187	USAAK02.067
Loma Prieta	10.18.89	11	7.1 M_w	Apeel Array #9, Crystal Springs Res.	62	0.108	USACA66.001

Throughout the years, building codes have evolved to adopt constant changes that respond to state-of-the-art research. These adaptation have led to improved design practices in the United States and Puerto Rico. In the 1920s the United States started to develop seismic codes and their use was voluntary. A decade later, in the 1930s, a mandatory building code was enforced in the state of California. However, it was during the 1950s and 1960s that the first modern seismic codes were applied in regions of high seismicity. Finally, in the 1980s, states enforced the new and improved detailing requirements for ductility specified in the building codes. In the case of Puerto Rico, the first building code was the "Reglamento de Edificación de Puerto Rico (No. 7)" and it had three versions, in 1954, 1968, and 1987. It was the 1987 version that included the first seismic provisions for the island. Then in 1999, the Puerto Rico Building Code (PRBC 1999) was created and enforced, using as a basis the Uniform Building Code of 1997 (UBC 1997). Later, in 2011, the Puerto Rico Building Code 2011 (PRBC 2011) was adapted using as basis the International Building Code of 2009 (IBC 2009). Lastly, the Puerto Rico Building Code 2018 (PRBC 2018) was developed using as a basis the International Building Code 2018 (IBC 2018), which in turn uses as a basis the ASCE7-16, among other Standards. It was enforced by the government of Puerto Rico starting on November 15, 2018 and is used in the development of this study. For the purpose of this study, and to compare the seismic requirements of the elastic design response spectra in the Puerto Rico Building Codes, Figure 7-4 and Figure 7-5 shows the Elastic Design Response Spectra for soil type D in the municipalities of Ponce, PR and San Juan, PR, respectively.

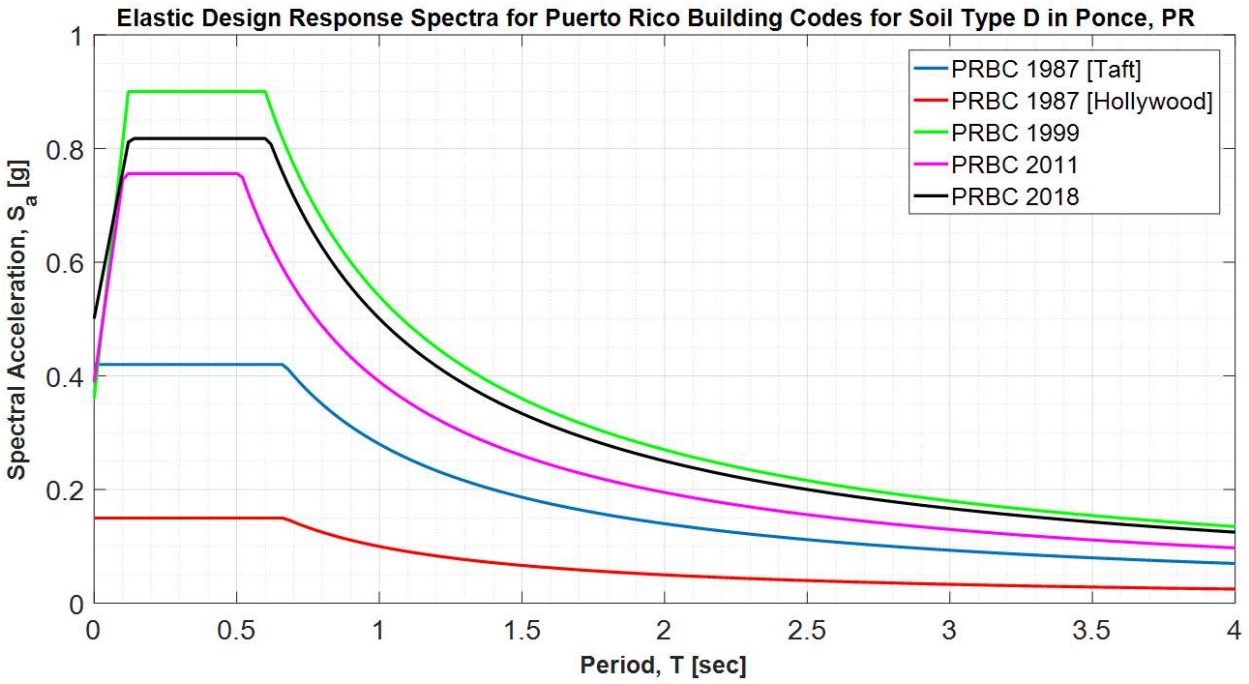


Figure 7-4: Elastic Design Response Spectra for Puerto Rico Building Codes for Soil Type D in Ponce, PR

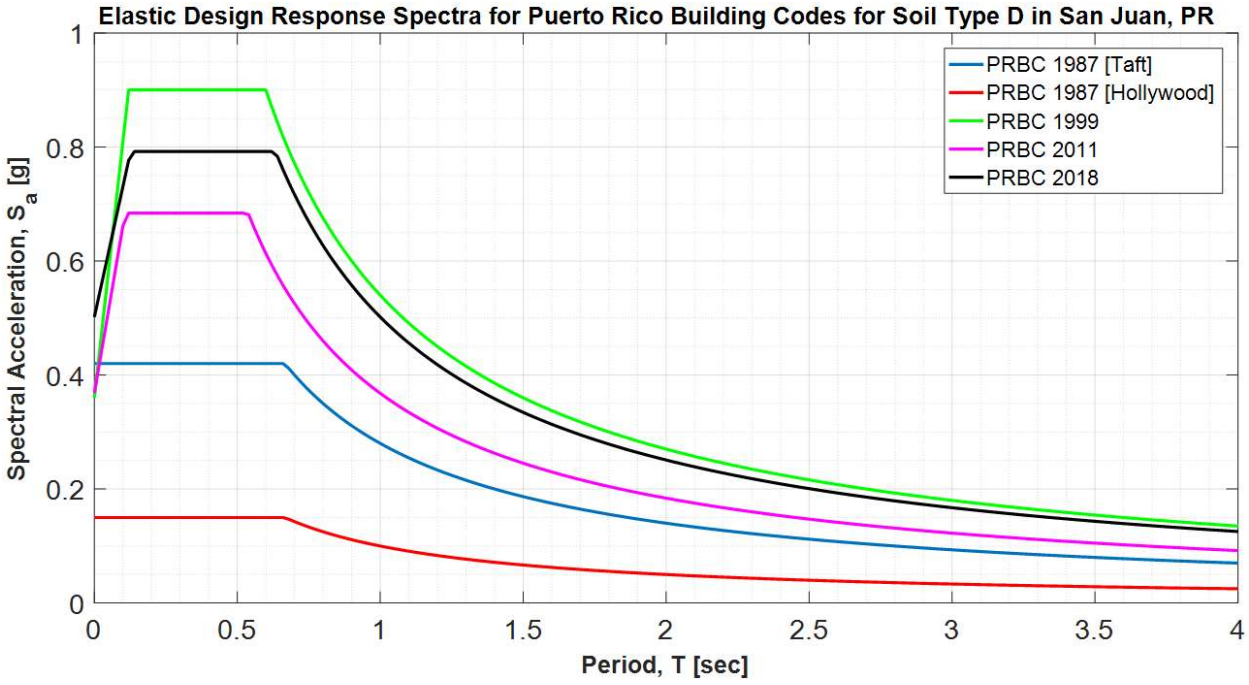


Figure 7-5: Elastic Design Response Spectra for Puerto Rico Building Codes for Soil Type D in San Juan, PR

7.1.1 Probable earthquakes generation for Ponce, PR

A set of seven artificial earthquakes was generated for the municipality of Ponce, PR. Although the purpose of this study is to assess the dynamic behavior and structural health of the Ponce Highway Bridge [ID:2348] with this set of artificial earthquakes, they can be used to assess any other structure within the municipality. For this purpose, two important conditions must be fulfilled. First, the generated earthquakes must be compatible with an elastic design response spectrum for the site's soil type as specified in Section 11.4 of ASCE7-16. Second, the PGA must consider site class effects as applicable and as specified in Section 11.8 of ASCE7-16. Another important aspect that should be taken into consideration before generating the artificial earthquakes is to use a transformation method that causes the least distortion in the shape of each of the original earthquakes' signals used as seeds. In Irizarry (1999), artificial strong motion earthquake records were generated by using the proposed elastic response spectra curves and the target design ground accelerations as inputs to SIMQKE®, which is a program for artificial motion generation. It is based on Fourier series and transforms that derive the Fourier spectrum iteratively from a target response spectrum and generates a series of sinusoids which are then added to obtain a desired artificial motion. However, the generated artificial earthquakes do not necessarily represent the shape of an earthquake that may be produced from the region's geologic faults system, such as the selected historic earthquakes. The generated artificial strong motion record for Ponce, PR, published in Irizarry (1999) is shown in Figure 7-6.

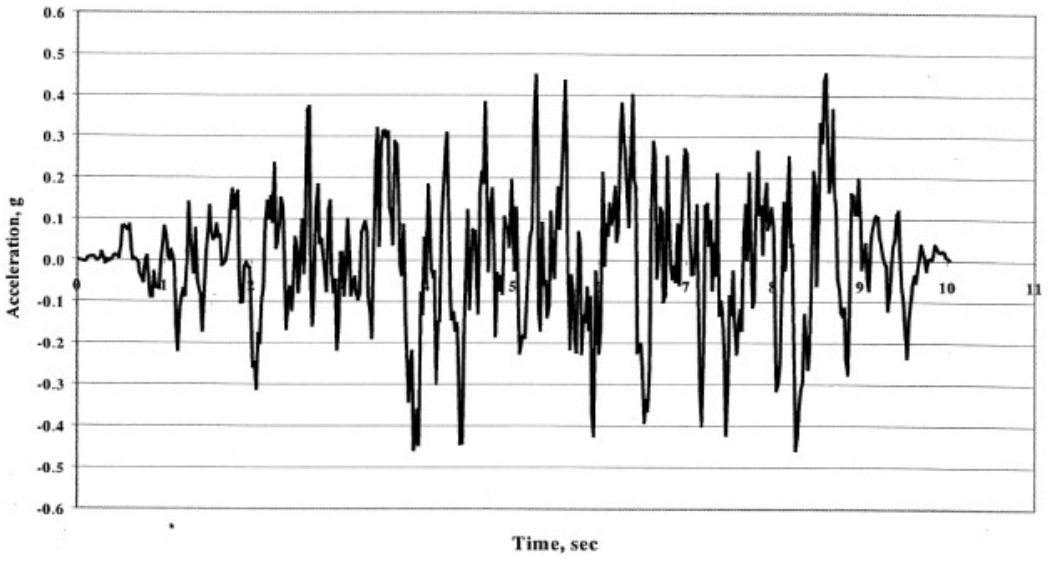


Figure 7-6: Artificial Strong Motion Record Recommended for Ponce, PR and Mayagüez, PR (Irizarry, 1999)

Its spiky characteristics may excessively punish any structure that is subjected to it, and consequently, the observed damage may not predominantly be a result of a realistic frequency content or the PGA. The problem particularly relies in the sequence of appearance of the frequency content in the artificial earthquake, which is not representative of the sequence in a real earthquake. Therefore, for this study the generation of artificial earthquake motions is performed by using ArtifQuakeLet II®. This is a MATLAB program code by Montejo and Suárez (2015) for artificial motion generation that implements the continuous wavelet transform (CWT) to modify historic earthquake records to obtain spectrum compatible records. The implementation of a wavelet-based approach in the program code produces artificial earthquake records with a trace that is more representative of the seed earthquakes.

For the probable earthquakes' generation, the elastic design response spectrum is computed for Ponce, PR in accordance to ASCE7-16. For this purpose, a soil classification of D is selected for the procedure because there is no available data on the soil type for the bridge site, as required by Chapter 20 of the Standard. Likewise, a summary of parameters for a current design of a highway bridge in the same location according to ASCE7-16 is shown in Table 7-4.

Table 7-4: Seismic design details for the structure's analysis in Ponce, PR as per ASCE7-16

Risk Category	IV
Importance Factor	1.5
Target Reliability	2.50%
Seismic Design Category	D

The Maximum Considered Earthquake (MCE_R), 5% damped, spectral response acceleration parameter at short periods, S_s, and the MCE_R, 5% damped, spectral response acceleration parameter at a period of 1 second, S_1, can be interpolated from the maps in Figure 22-6 in Chapter 22 of ASCE7-16 or can be alternatively obtained from the U.S. Seismic Design Maps on the USGS website: https://earthquake.usgs.gov/designmaps/us/application.php. For this case, S_s is taken as $1.022\ g$ and S_1 is taken as $0.394\ g$. As a result, the elastic design response spectrum used to generate probable earthquake records compatible to ASCE7-16 for soil type D is displayed below.

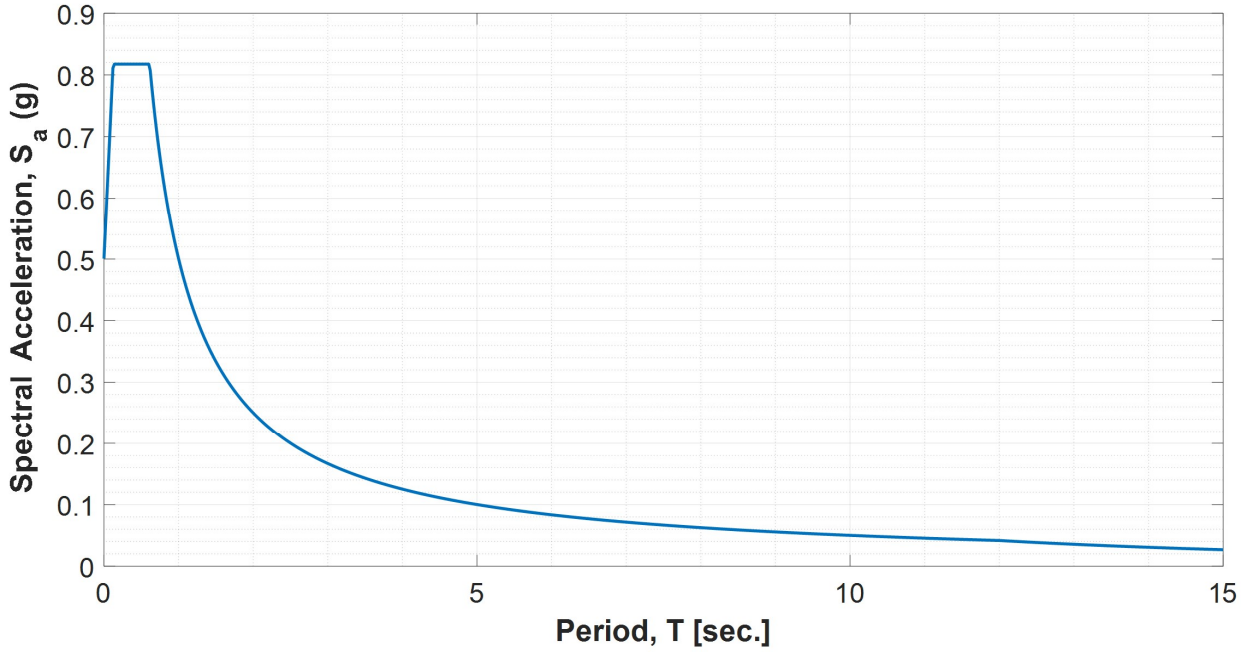


Figure 7-7: Elastic design response spectrum for soil type D in Ponce, PR as per ASCE7-16

Furthermore, additional requirements for seismic design category D should be fulfilled when generating the compatible probable earthquakes for the site. In this regard, the PGA must consider site class effects. Hence, the PGA can be determined from equation (7.1), as specified in Section 11.8.3 of ASCE7-16. The PGA_M is used for evaluation of liquefaction, lateral spreading, seismic settlements, and other soil-related issues.

$$PGA_M = F_{PGA} \cdot PGA \tag{7.1}$$

where,

- PGA_M : Maximum Considered Earthquake Geometric Mean (MCE_G) peak ground acceleration adjusted for site class effects.
- PGA : mapped MCE_G peak ground acceleration
- F_{PGA} : site coefficient from Table 11.8-1 of ASCE7-16

The PGA for Ponce, PR can be interpolated from the map in Figure 22-12 in Chapter 22 of ASCE7-16 or alternatively obtained from the U.S. Seismic Maps on the USGS website: https://earthquake.usgs.gov/designmaps/us/application.php. For the studied highway bridge location in Ponce, PR the PGA obtained is $0.408\ g$. Accordingly, the value of F_{PGA} from Table 11.8-1 in Section 11.8.3 of ASCE7-16 is 1.2. Therefore, the computed value of PGA_M for the

bridge location in Ponce, PR results in $0.49\,g$. Once all the required information and data is obtained, it is added as input to ArtifQuakeLet II® to generate the probable earthquakes compatible with ASCE7-16 for Ponce, PR. Figures 7-8 to 7-14 display the seven artificially generated earthquake records that will be used for further seismic analyses, with their corresponding Fourier spectrum.

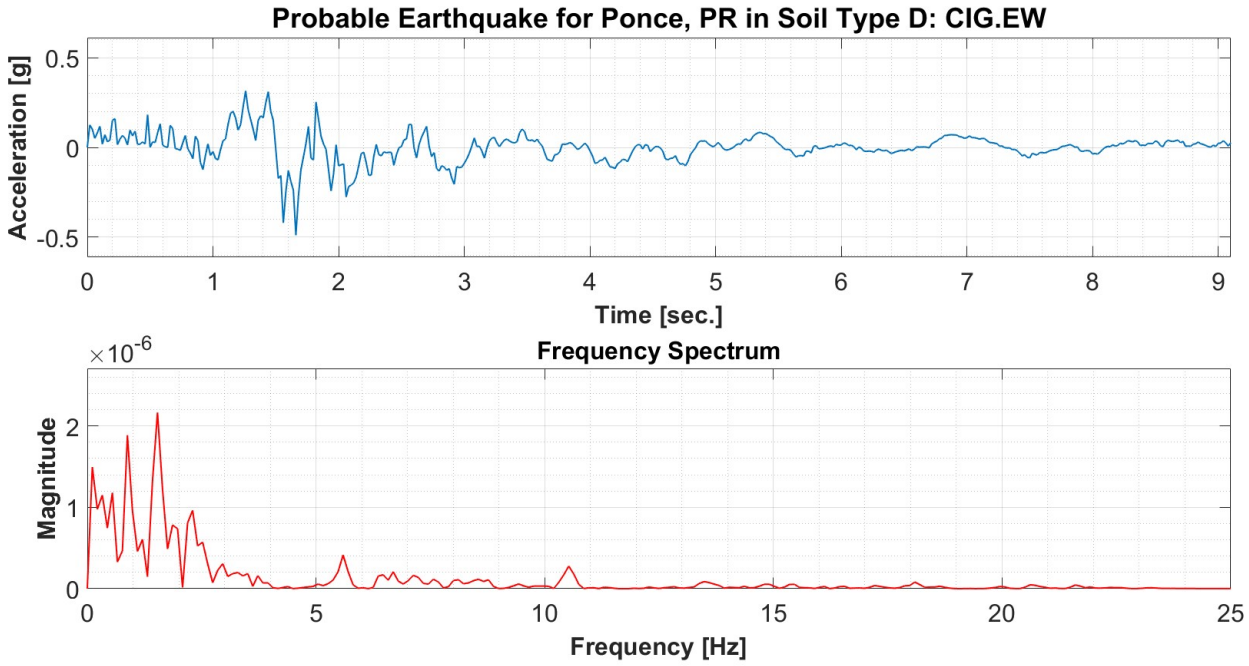


Figure 7-8: Probable Earthquake CIG.EW for Ponce, PR for soil type D as per ASCE7-16 and its frequency spectrum

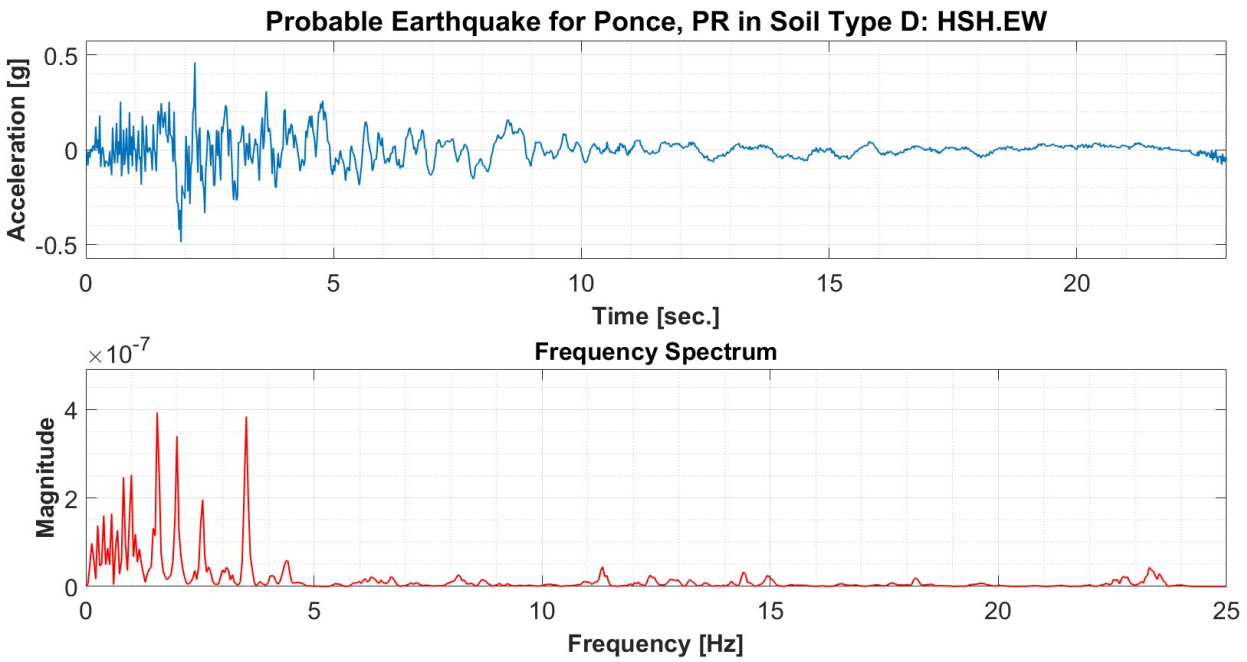


Figure 7-9: Probable Earthquake HSH.EW for Ponce, PR for soil type D as per ASCE7-16 and its frequency spectrum

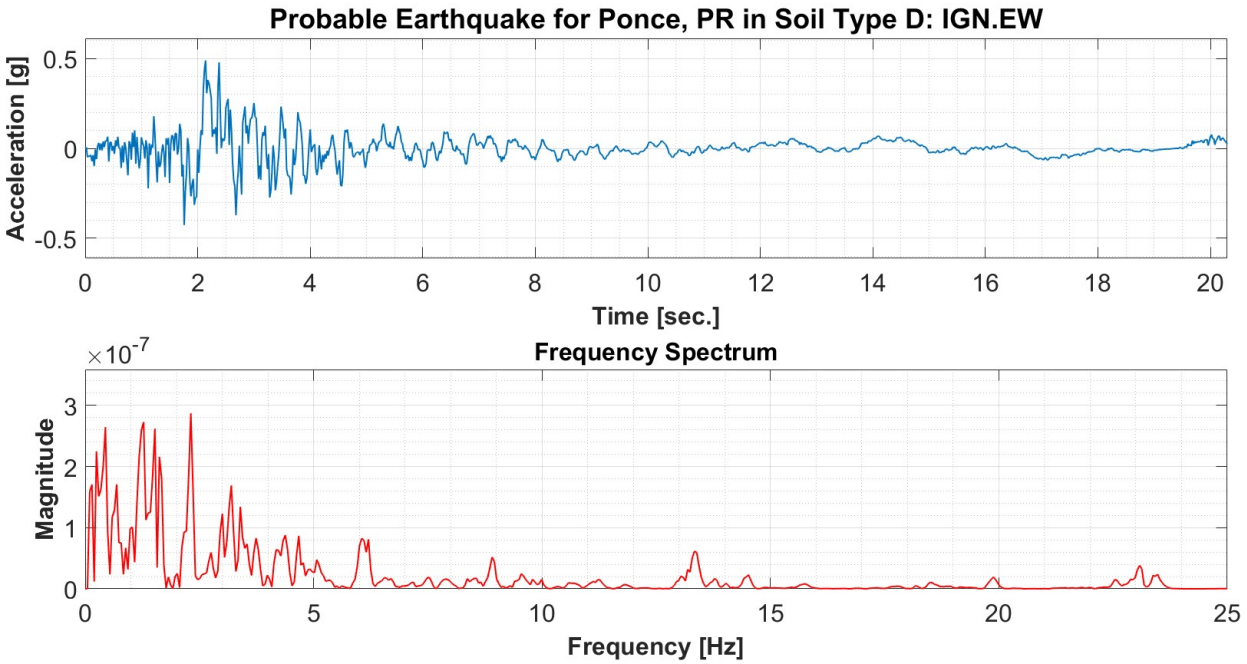


Figure 7-10: Probable Earthquake IGN.EW for Ponce, PR for soil type D as per ASCE7-16 and its frequency spectrum

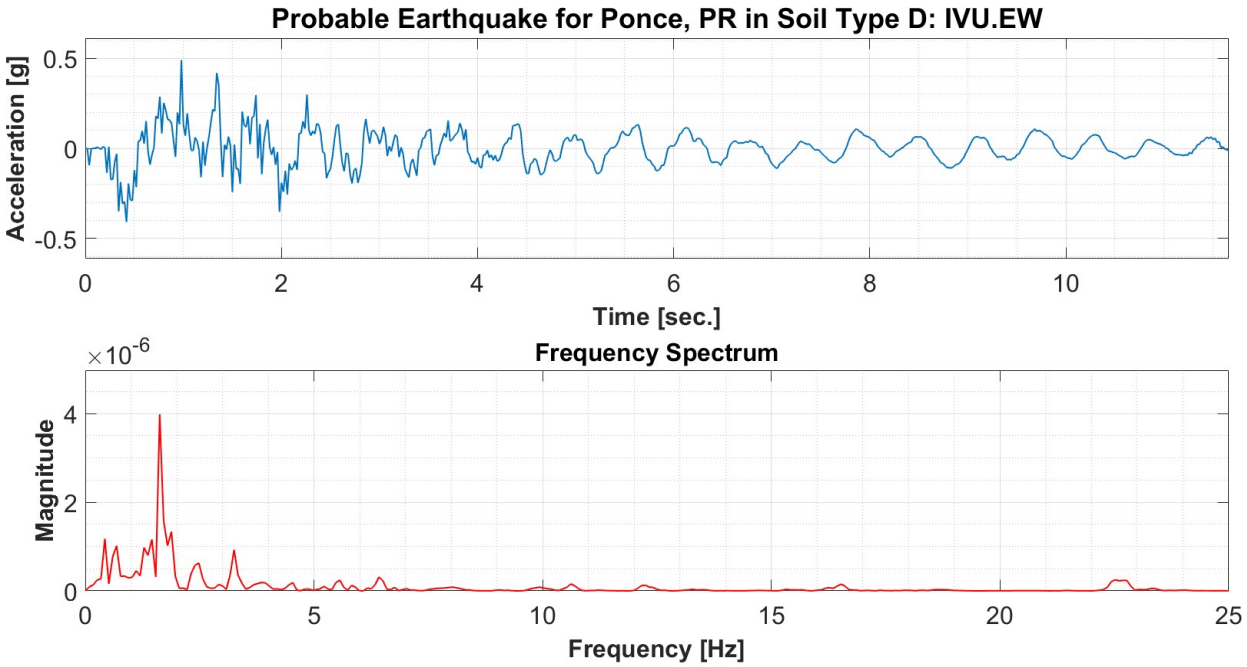


Figure 7-11: Probable Earthquake IVU.EW for Ponce, PR for soil type D as per ASCE7-16 and its frequency spectrum

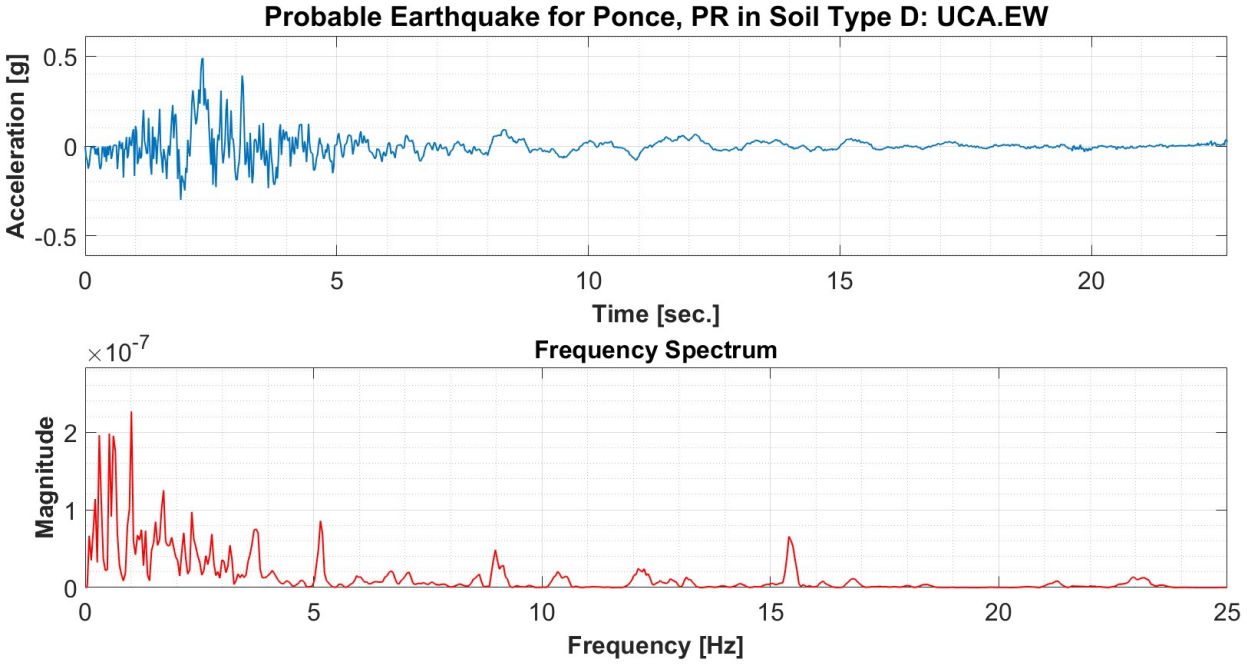


Figure 7-12: Probable Earthquake UCA.EW for Ponce, PR for soil type D as per ASCE7-16 and its frequency spectrum

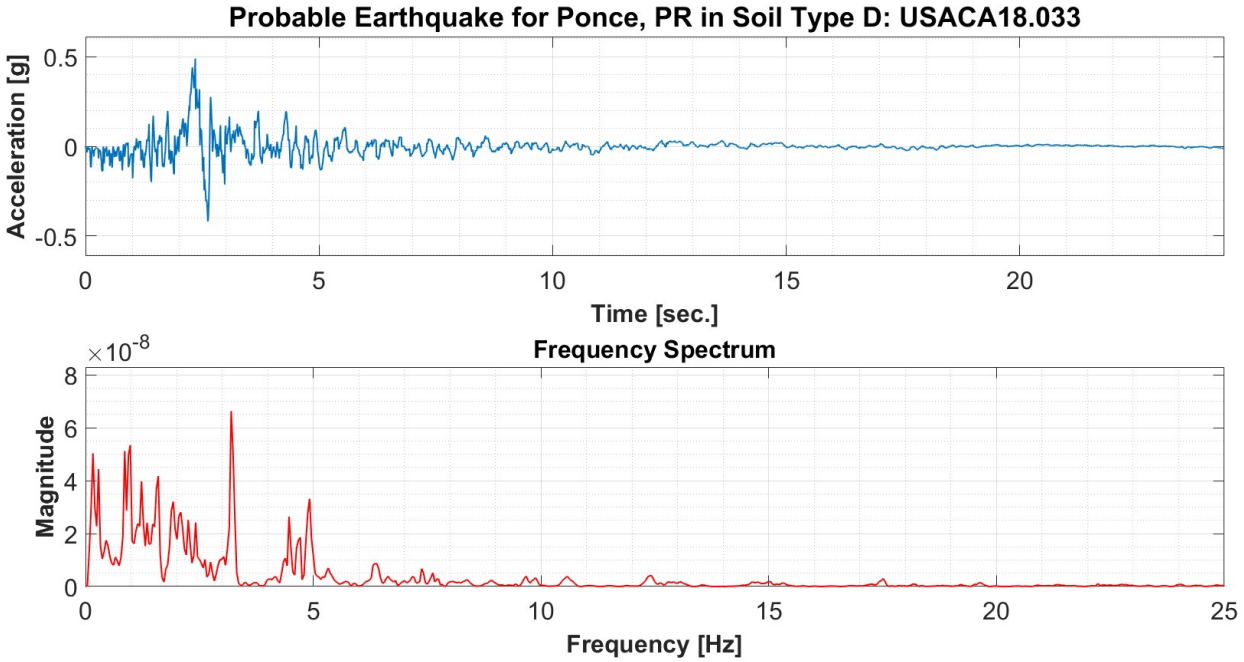


Figure 7-13: Probable Earthquake USACA18.033 for Ponce, PR for soil type D as per ASCE7-16 and its frequency spectrum

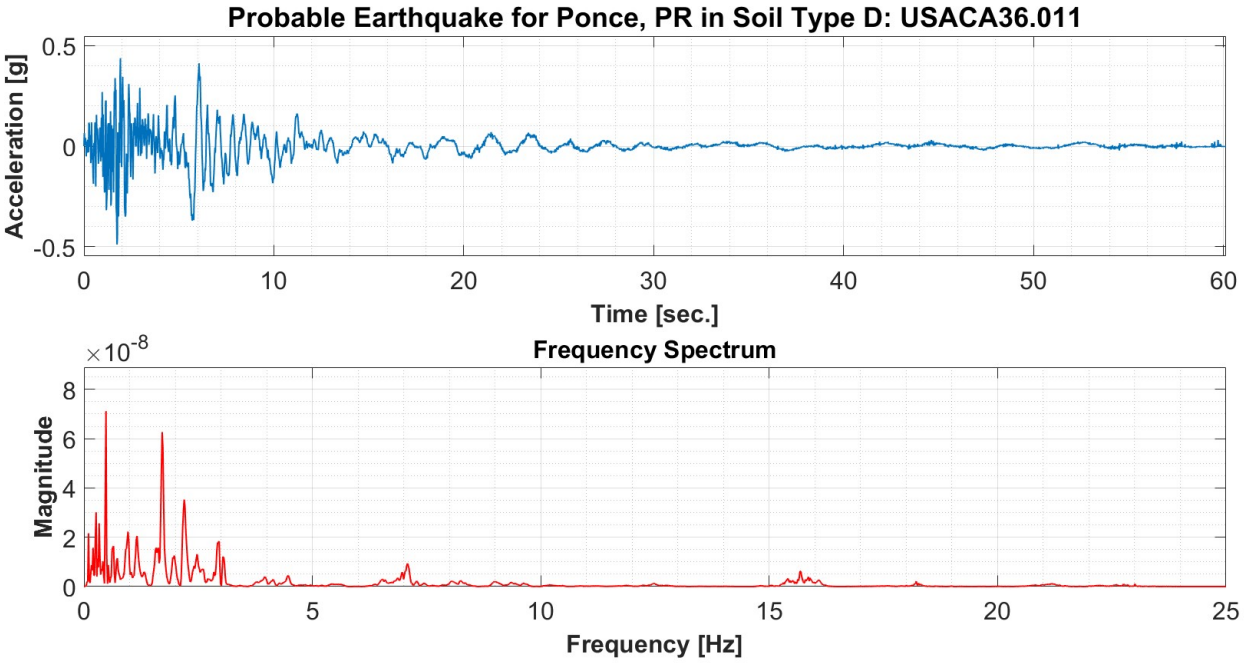


Figure 7-14: Probable Earthquake USACA36.011 for Ponce, PR for soil type D as per ASCE7-16 and its frequency spectrum

7.1.2 Probable earthquakes generation for San Juan, PR

For the municipality of San Juan, PR, the same procedure implemented for Ponce, PR is performed to generate its probable earthquakes. The study by Irizarry (1999) recommended an artificial strong motion record for San Juan, PR, which was generated with SIMQKE® using as its input the selected historic earthquakes for the city, the target design ground accelerations, and her proposed elastic response spectrum curve. However, the recommended record in her study possess spiky characteristics that do not completely represent the selected earthquakes. The generated artificial strong motion record for San Juan, PR published in her study is depicted in Figure 7-15.

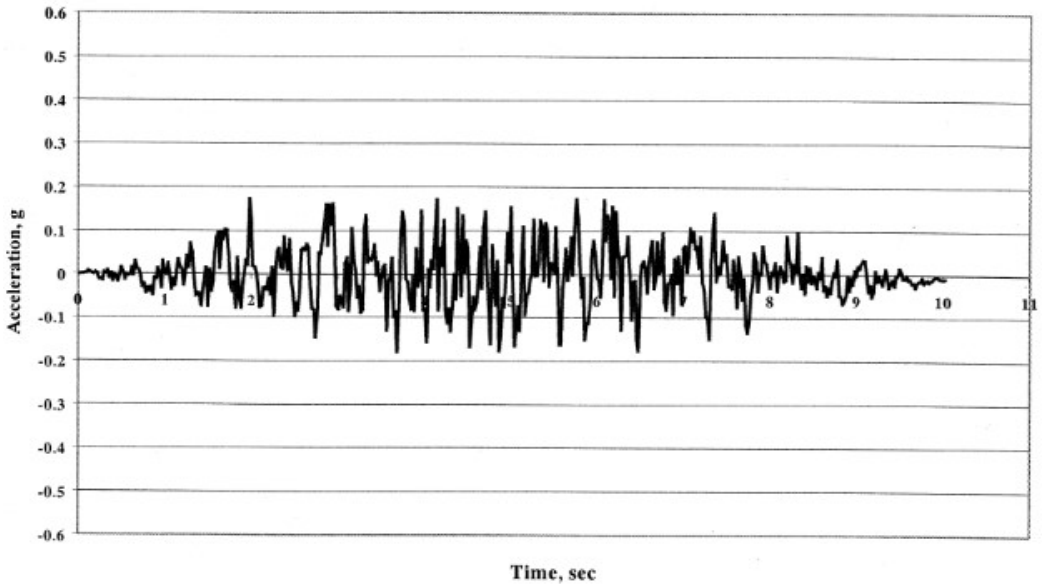


Figure 7-15: Artificial Strong Motion Record Recommended for San Juan, PR (Irizarry, 1999)

For this reason, and in the same way as it was performed to Ponce, PR, ArtifQuakeLet II® is used in this study to generate the probable earthquakes for San Juan, PR in compatibility to ASCE7-16.

Likewise, for the probable earthquakes' generation, the elastic design response spectrum is computed for San Juan, PR in accordance to ASCE7-16. Due to unavailable data on the soil properties or its type on the PRILA Condominium site, a soil classification of *D* is selected for this purpose as required by Chapter 20 of the Standard. A summary of parameters for a current design of a residential building in the same location as per ASCE7-16 is presented in Table 7-5.

Table 7-5: Seismic design details for the structure's analysis in San Juan, PR as per ASCE7-16

Risk Category	III
Importance Factor	1.25
Target Reliability	5 %
Seismic Design Category	D

For the municipality of San Juan, PR, the values of S_s and S_1 are taken to be 0.99 g and 0.395 g, respectively. They can be obtained from the U.S. Seismic Design Maps on the USGS website: https://earthquake.usgs.gov/designmaps/us/application.php or from the maps in Figure 22-6 in Chapter 22 of ASCE7-16. Accordingly, the elastic design response spectrum used to generate probable earthquakes in compatibility with ASCE7-16 for soil type D is displayed in Figure 7-16.

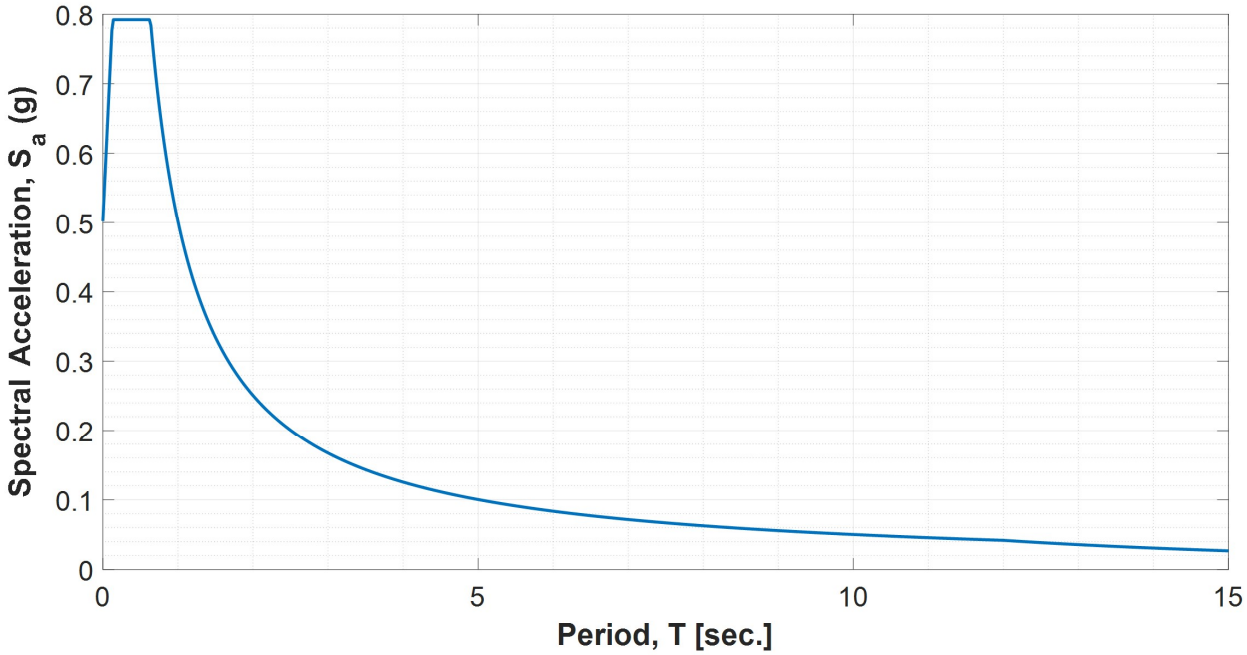


Figure 7-16: Elastic design response spectrum for soil type D in San Juan, PR as per ASCE7-16

To consider soil amplification effects, among other soil-related issues, the mapped PGA is adjusted for site class effects. The PGA for San Juan, PR, obtained from the map in Figure 22-6 in Chapter 22 of ASCE7-16 or alternatively from the U.S. Seismic Maps on the USGS website: https://earthquake.usgs.gov/designmaps/us/application.php, is 0.404 g. Accordingly, the value of F_{PGA} computed from Section 11.8.3 of ASCE7-16 is 1.2. Hence, the computed value of PGA_M for PRILA Condominium in San Juan, PR results in 0.484 g, as computed from equation (7.1). With the previous required data and the selected historic earthquakes for San Juan, PR used as

seed, the probable earthquakes compatible with ASCE7-16 for the city are generated with ArtifQuakeLet II®. Figures 7-17 to 7-23 display the seven artificially generated earthquake records that can be used for further seismic analyses with their corresponding Fourier spectrum.

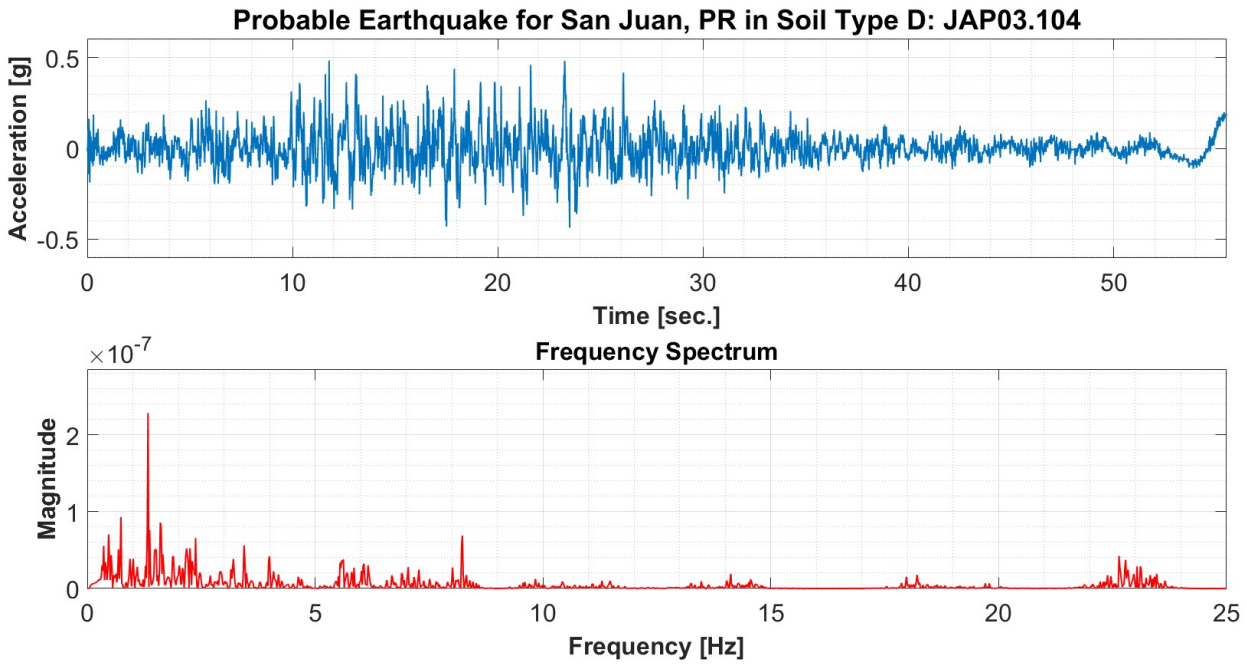


Figure 7-17: Probable Earthquake JAP03.104 for San Juan, PR for soil type D as per ASCE7-16 and its frequency spectrum

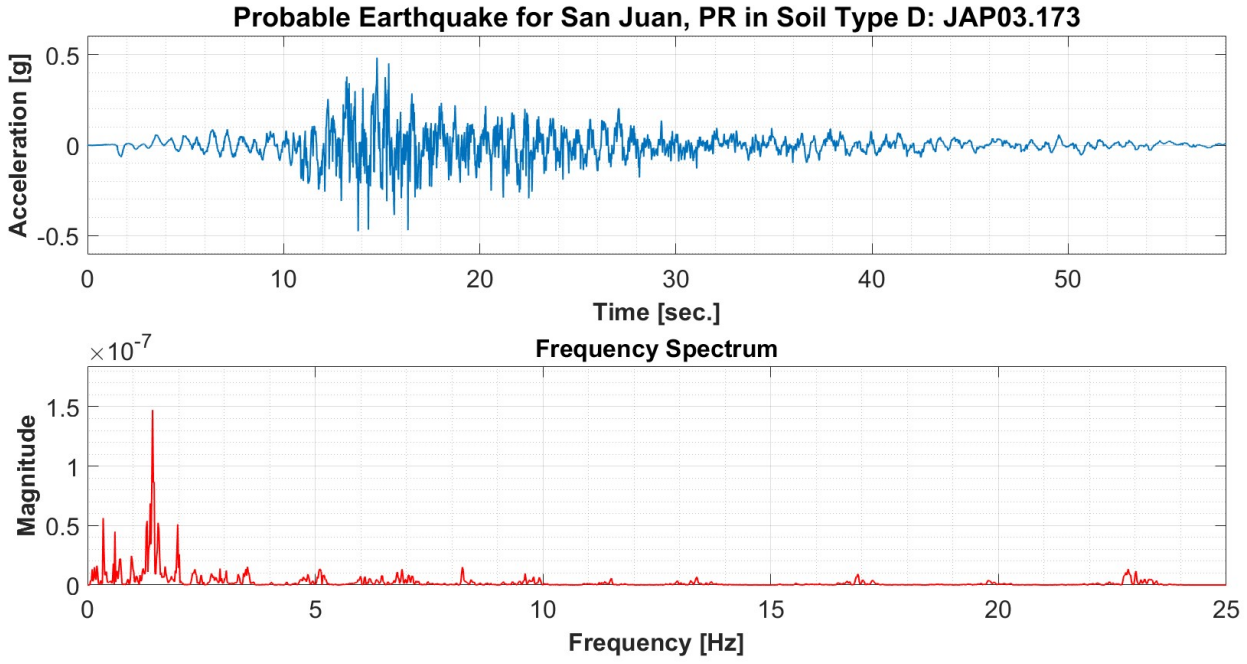


Figure 7-18: Probable Earthquake JAP03.173 for San Juan, PR for soil type D as per ASCE7-16 and its frequency spectrum

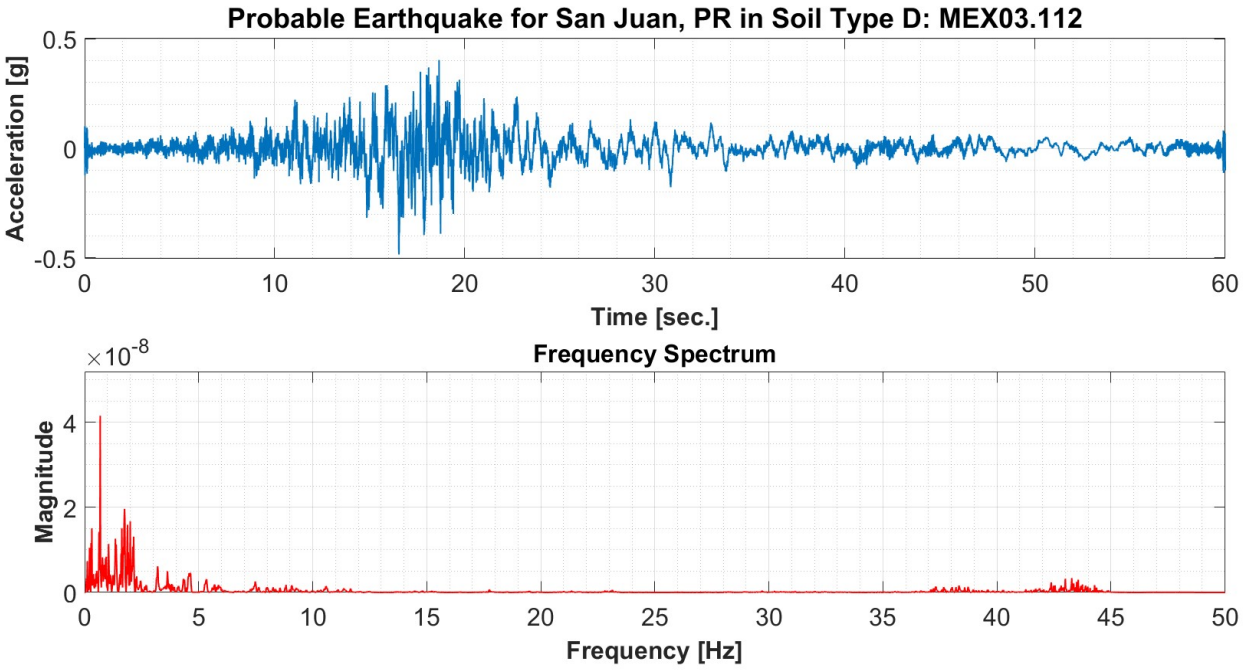


Figure 7-19: Probable Earthquake MEX03.112 for San Juan, PR for soil type D as per ASCE7-16 and its frequency spectrum

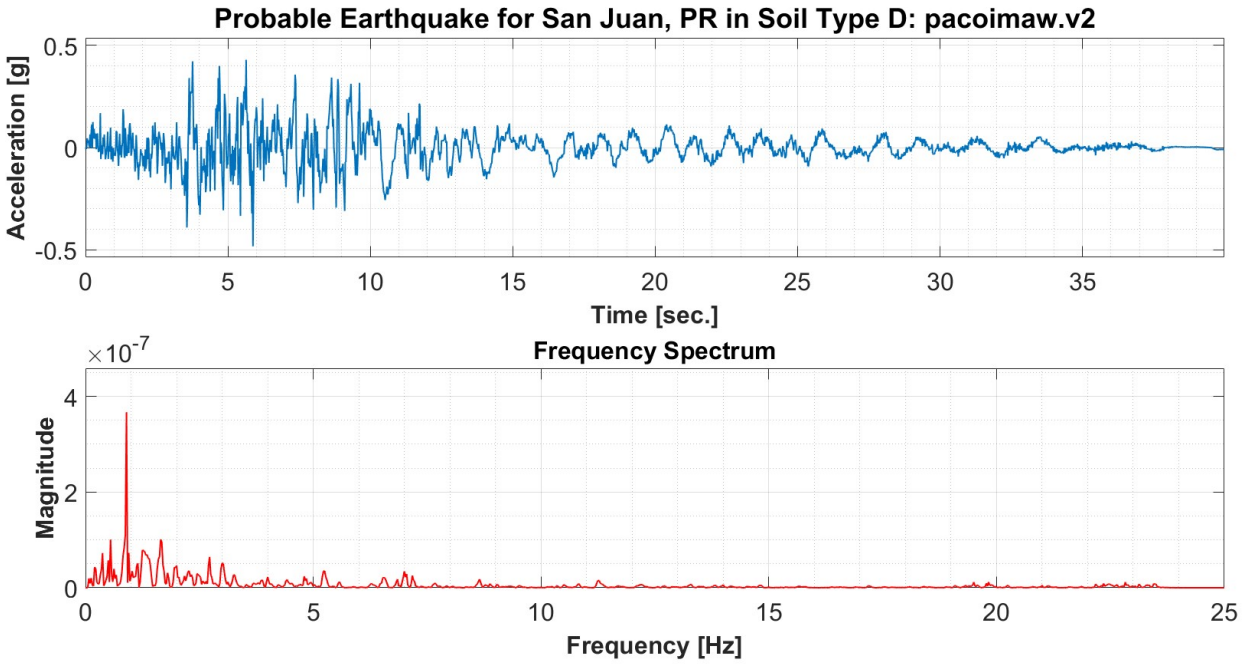


Figure 7-20: Probable Earthquake pacoimaw.v2 for San Juan, PR for soil type D as per ASCE7-16 and its frequency spectrum

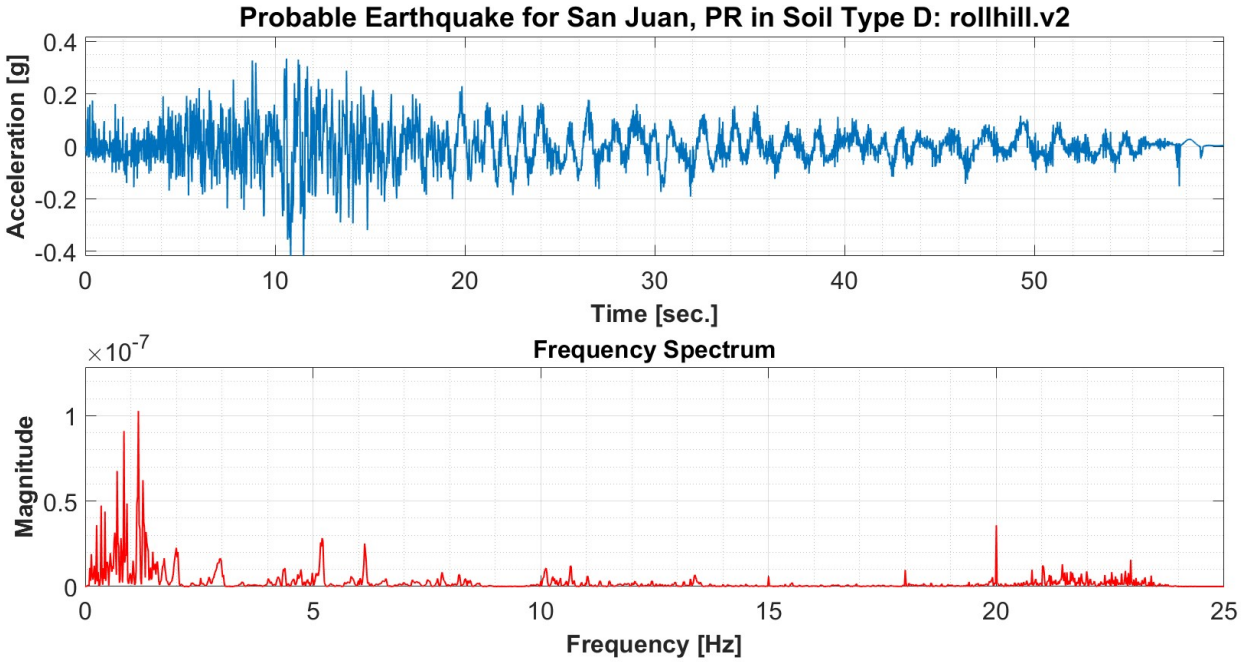


Figure 7-21: Probable Earthquake rollhill.v2 for San Juan, PR for soil type D as per ASCE7-16 and its frequency spectrum

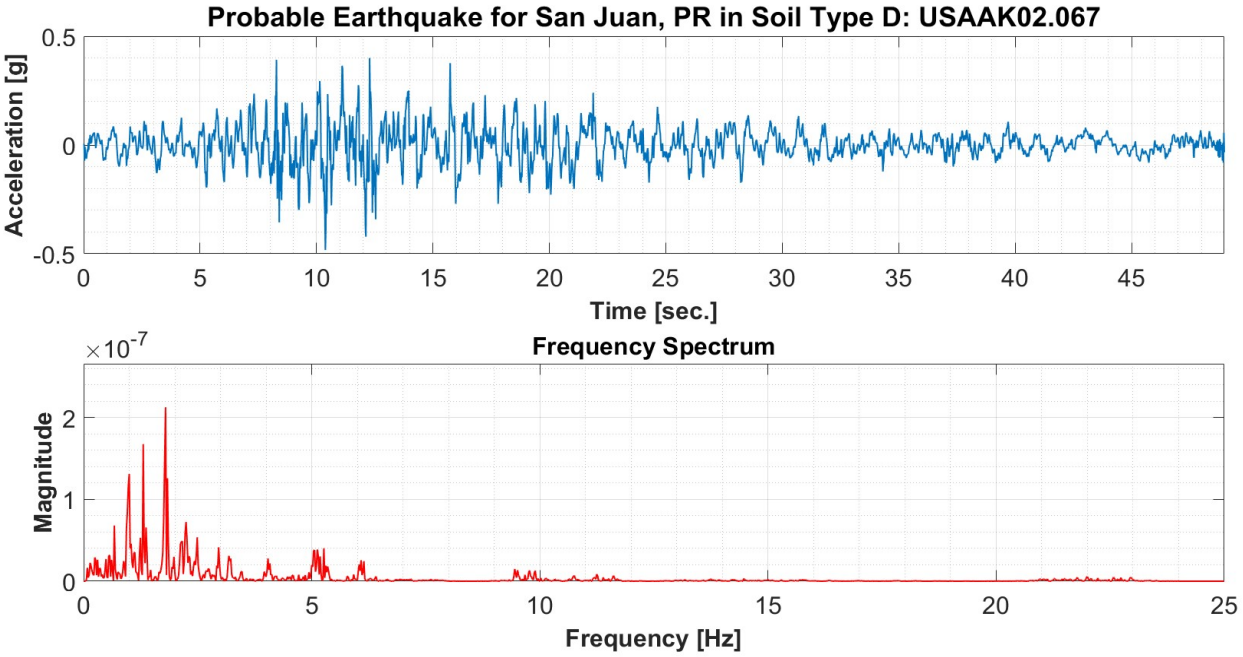


Figure 7-22: Probable Earthquake USAAK02.067 for San Juan, PR for soil type D as per ASCE7-16 and its frequency spectrum

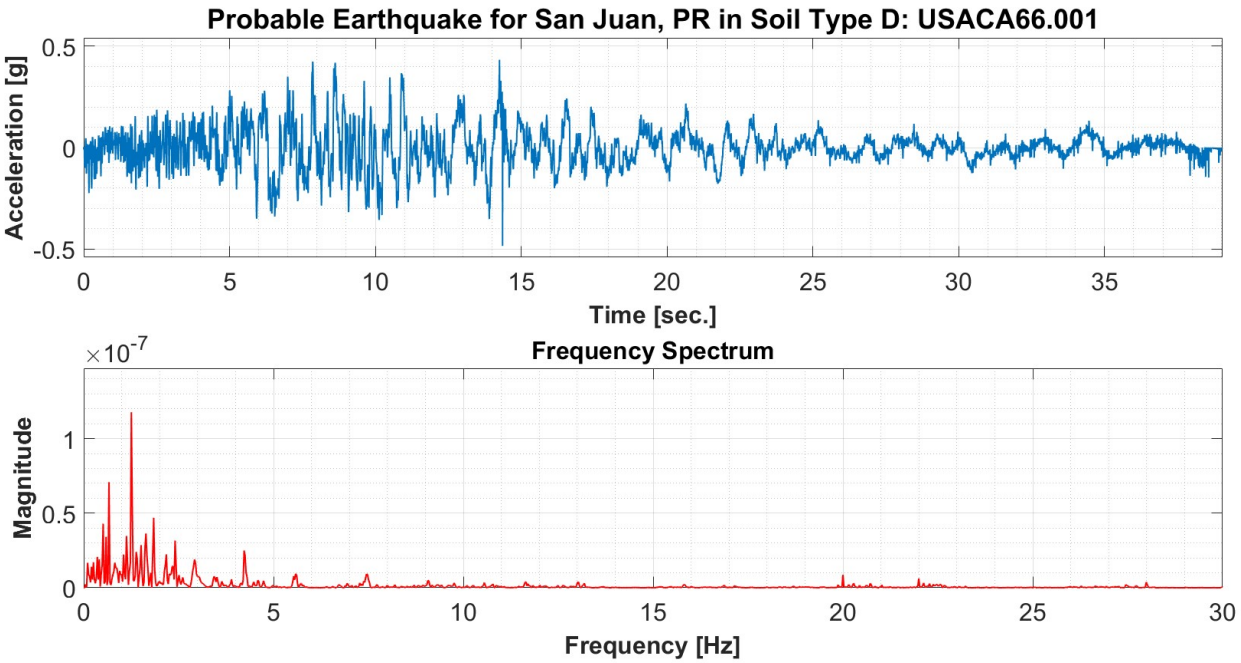


Figure 7-23: Probable Earthquake USACA66.001 for San Juan, PR for soil type D as per ASCE7-16 and its frequency spectrum

7.2 Nonlinear Assessment of the Ponce Highway Bridge [ID: 2348]

To completely assess the seismic performance of a structure, besides evaluating its dynamic properties associated to specific states in its lifespan, it is necessary to perform a nonlinear structural analysis. This type of analysis allows to determine the force and displacement capacities of a studied structural system and hence provides a complete understanding of its expected performance and behavior from a limit state perspective. Therefore, the observed performance can be compared against the expected behavior, based in Codes compliance or other related criteria. The results of a nonlinear analysis provide a view of the prognosis of a structural system and allows to find the right retrofitting solutions to recover its structural health and consequently extend its life cycle. Yet, nonlinear analyses tend to be time consuming and require extensive computational capabilities. Hence, it is convenient to develop a simplified structural model that approximately represents the physical system and that allows to reduce the time and computational need required to obtain reliable results from a nonlinear analysis.

For the Ponce Highway Bridge [ID: 2348], a simplified and experimentally updated computational model was created in SAP2000® to ease the procedure and accelerate the generation of results. This computational model is a 2D representation of the bridge as a SDOF system. It

was assembled by using the *as-designed* properties presented in Chapter 4. Minor updating was done to the SAP2000® model to match the experimentally identified natural frequency, f_n. Likewise, the identified damping ratio, ξ_n, of the system was added to the 2D computational model of the bridge. Figure 7-24 shows a simplified schematic representation of the Ponce Highway Bridge [ID: 2348] and its corresponding updated computational model.

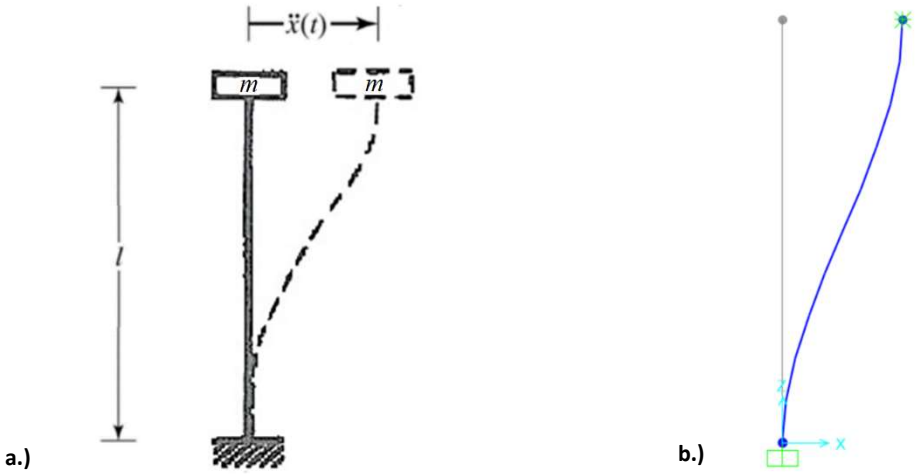


Figure 7-24: SDOF model for Ponce Highway Bridge [ID: 2348]; a.) Simplified schematic representation; b.) SAP2000 2D model

7.2.1 Moment-curvature relation for bridge's lateral force resisting system

Once the updated linear-elastic 2D model of the Ponce Highway Bridge [ID: 2348] is developed, it is necessary to add nonlinear properties to its elements so that inelastic analyses can be performed. For this purpose, moment-curvature relationships are computed for each element's section located at a joint. A bilinear approximation for each section's moment-curvature relationship was computed and then a global equivalent moment-curvature bilinear relationship was generated to develop a one-component element that accurately represents the inelastic behavior of the entire lateral force-resisting system of the bridge. A one-component element has a linear-elastic middle segment bounded by two rotational springs and rigid zones located at the extreme ends of the elements. The length of the linear-elastic section is equal to the unsupported length of the element and its properties are computed once from the element's initial moment of inertia. The rigid zones can be viewed as links that remain rigid. Therefore, the element's stiffness variation comes solely from changes in the springs' stiffness. Consequently, the nonlinear behavior of the element is controlled by the springs. A detailed description on this subject and the procedure to compute the spring constant can be found in Giberson (1967) and in López (1988).

To define the hinges' capacity properties, the yield moment, M_y, in the equivalent global bilinear moment-curvature relationship of the one-component element's springs was computed by adding all the yield moment capacities of all the individual vertical elements resisting lateral forces. On the other hand, the corresponding yield curvature, ϕ_y, in the one-component element was computed by taking the highest yield curvature capacity of all the individual vertical elements that resist lateral forces. This responds to the fact that when a structural system, whose elements can be viewed as a spring system acting in a parallel arrangement, the system completely yields when its last element yields. However, although one or more elements of the system have yielded under the action of lateral loads, the system's hinges, undergo a complete yield rotation when its last hinge yields. Likewise, the same reasoning applies to compute the ultimate moment capacity, M_u, and its corresponding ultimate curvature capacity, ϕ_u. The moment-curvature curves of the individual elements with circular cross-section were computed with CUMBIA®, a set of MATLAB program codes by Montejo and Kowalsky (2007) that perform monotonic moment-curvature analysis and force-displacement responses of reinforced concrete members. Table 7-6 shows the hinge capacities that define the global moment-curvature bilinear curve of Figure 7-25.

Table 7-6: Equivalent Moment-Curvature Bilinear Approximation for Ponce Highway Bridge [ID: 2348]

Equivalent Bilinear $M-\phi$		
Limit State	$\phi\ [1/in]$	$M\ [Kip-ft]$
---	0	0
Yield	0.000119	17644.43
Ultimate	0.002396	23229.65

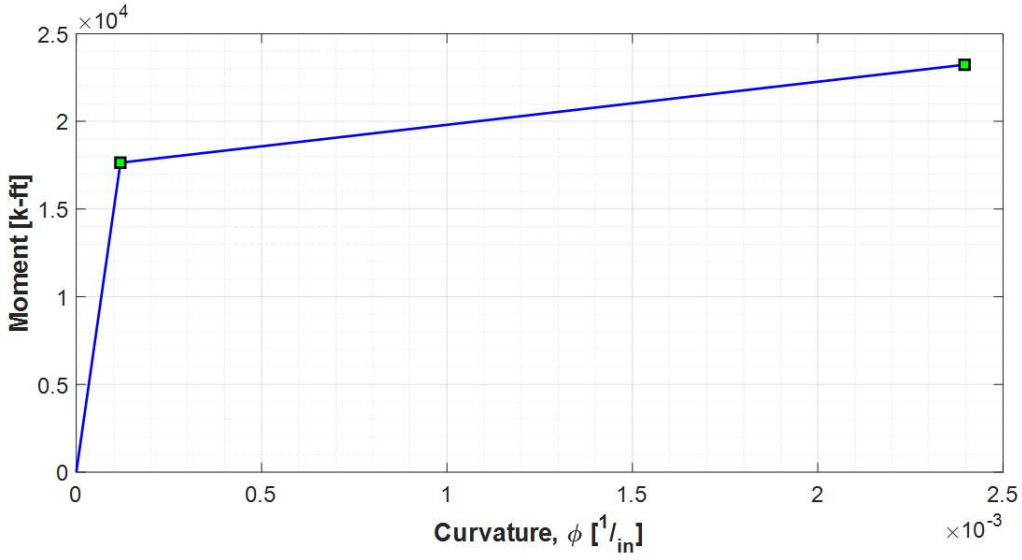


Figure 7-25: Equivalent moment-curvature bilinear approximation for SDOF model of Ponce Highway Bridge [ID: 2348]

7.2.2 Nonlinear time-history analysis of the bridge structure

Dynamic nonlinear time-history analyses of structural systems allow the engineering analyst to observe the dynamic structural behavior of the studied systems when subjected to a real scenario, if the input histories were experimentally recorded or are simulations of real past or possible future cases. Consequently, a more accurate and realistic assessment can be performed on the structural health and on the possible deficiencies observed in the system. For the nonlinear dynamic structural evaluation of the Ponce Highway Bridge [ID: 2348], its updated nonlinear simplified computational model was subjected to the seven probable earthquakes for the municipality of Ponce, PR. These earthquakes were artificially generated from the seed earthquakes listed in Table 7-2 as explained in Section 7.1.1. The nonlinear time-history analyses of the bridge were performed in SAP2000® as a direct integration nonlinear analysis and considering the $P-\Delta$ effect. In addition, the Takeda hysteretic model was implemented to model the cyclic behavior of the reinforced concrete. From the responses of the computational bridge model, demand parameters were evaluated to quantify the effect of each probable earthquake on the structure. The maximum values of the demand parameters for each computed response are presented in Table 7-7.

Table 7-7: Peak values of demand parameters and final condition for Ponce Highway Bridge [ID: 2348]

Parameters	CIG.EW	HSH.EW	IGN.EW	IVU.EW	UCA.EW	USACA18.033	USACA36.011
Peak Acceleration [g]	0.784	0.849	0.993	0.898	0.921	0.836	0.935
Peak Velocity [in/s]	14.417	14.295	17.572	16.553	16.451	15.633	19.328
Peak Displacement [in]	0.789	0.718	0.977	0.798	0.832	0.780	1.173
Max. Drift, δ_{max} [%]	0.360	0.328	0.446	0.364	0.380	0.356	0.535
Base Shear, V_{max} [kips]	2,420.79	2,391.97	2,432.05	2,421.37	2,424.48	2,420.30	2,443.70
Base Moment, M_{max} [k-ft]	3,681.62	43,653.48	44,384.95	44,189.94	44,246.68	44,170.48	44,597.58
Final condition	Minor Inelastic	Elastic	Minor Inelastic	Minor Inelastic	Minor Inelastic	Minor Inelastic	Minor Inelastic

The observed general response of the bridge before, during, and after each earthquake's strong motion was predominantly linear-elastic with spontaneous events of minor nonlinearities. These minor nonlinearities were detected at the joints' hinges with inelastic rotations values, quantified after exceeding the yield rotations, ranging from $0.000306\ 1/in$ up to $0.002505\ 1/in$. Table 7-8 shows the maximum inelastic rotations induced by each probable earthquake.

Table 7-8: Maximum inelastic curvatures for Ponce Highway Bridge [ID: 2348] due to probable earthquakes

EQ Filename	$\varphi\ [1/in]$
CIG.EW	0.000352
HSH.EW	Elastic
IGN.EW	0.00141
IVU.EW	0.000406
UCA.EW	0.000598
USACA18.033	0.000306
USACA36.011	0.002505

7.2.3 Static pushover analysis of the bridge structure

Inelastic analysis of structural systems provides valuable information on their expected behavior in response to specific conditions of excitation. However, the results obtained may not reveal a complete perspective of the system's health or prognosis. A dynamic nonlinear time-history analysis reveals the performance of the structure based on its response to these specific dynamic loads, which is greatly influenced by the frequency content of the input excitation and its peak acceleration, among others. Consequently, it is not possible to exactly determine the structural capabilities of the studied system. For this reason, it is always convenient to perform complementary nonlinear analyses in order to completely evaluate the system condition and in most cases determine the causes of observed damage or collapse. An alternate analysis approach for this purpose is to perform a static nonlinear analysis, commonly referred to as *pushover* analysis. This method of analysis consists in applying static lateral loads to the structure in an incremental predefined pattern while subjected to gravity loading until the ultimate state of the structure is attained. This procedure can be force-controlled or displacement-controlled. The applied lateral load represents the range of base shear induced by the earthquake loading. It is applied in a monotonic way, and the effects of cyclic behavior and load reversals are estimated by monotonic force-deformation criteria and an approximate damping.

A displacement-controlled pushover analysis was performed to the Ponce Highway Bridge [ID: 2348] to evaluate its lateral capacity until it reaches its ultimate state. The analysis was performed in SAP2000® with the same nonlinear simplified model used for the nonlinear dynamic analyses presented in Section 7.2.2. Table 7-9 displays the bridge's state capacity values and Figure 7-26 displays the pushover curve obtained for the bridge. The overall maximum values of the bridge's

displacement and base shear that resulted from the nonlinear dynamic analyses are also plotted in the same Figure as a red dot. These maximum values of displacement and base shear were obtained when the bridge was subjected to probable earthquake *USACA36.011* and can be observed in Table 7-7 as $\Delta_{max}= 1.173\ in$ and $V_{max} = 2{,}443.7\ Kips$.

Table 7-9: Ponce Highway Bridge [ID: 2348]'s state capacities

Bridge's Capacity Values		
State	*Δ [in]*	*F [Kips]*
Yield	0.720	2,397.905
Ultimate	13.440	3,150.414

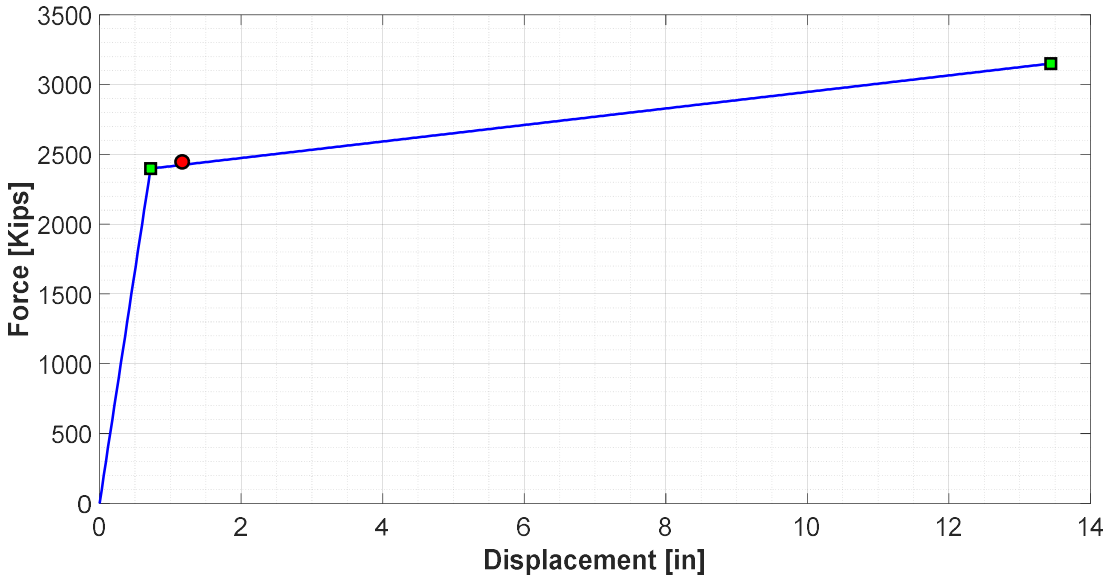


Figure 7-26: Pushover capacity curve for Ponce Highway Bridge [ID: 2348] and maximum base shear and displacement from nonlinear dynamic analyses (red dot).

7.3 Nonlinear Assessment of the PRILA Condominium

Nonlinear static and dynamic analyses of the PRILA Condominium were performed using the updated simplified computational model previously shown in Figure 5-42b. It is a 2D model that reduces PRILA to a dynamic system consisting of 44 degrees of freedom. Its first four lowest frequencies accurately represent the experimentally identified frequencies with less than a 5% error. Similarly, the respective modal damping ratios, ξ_i, for these frequencies were added to the computational model. The use of this model allows to completely perform the analyses in just a

couple of hours with less required computational power. Consequently, it is possible to make minor modifications, as required, and be able to perform all the established cases in several days.

7.3.1 Moment-curvature relation for PRILA's lateral force resisting system

To define a nonlinear model for the PRILA Condominium, its simplified 2D linear-elastic model was modified to include equivalent nonlinear hinges in each story. Analogous to the previously presented procedure for the Ponce Highway Bridge [ID: 2348], global equivalent moment-curvature bilinear relationships were computed for each story. This was done by computing the moment-curvature curves for each of the vertical elements in each story that resist lateral loads. Then, with the same approach used for Ponce Highway Bridge, an equivalente bilinear moment-curvature curve was generated per story to develop a corresponding one-component element. For each curve, the yield moment, M_y, was computed by adding all the yield moment capacities of all the individual vertical elements resisting lateral loads. On the other hand, the corresponding yield curvature, ϕ_y, in the one-component element was computed by taking the highest yield curvature capacity of all the individual vertical elements that resist vertical forces. Likewise, the same reasoning applies to compute the ultimate moment capacity, M_u, and its corresponding ultimate curvature, ϕ_u. The moment-curvature curves of the individual wall elements with rectangular cross-section were computed with a MATLAB program code developed by the author, which implements the Scott, Kent, and Park (1982) constitutive model for reinforced concrete and the Holzer (1975) constitutive model for steel. For the two circular columns of the ground to the first floor, the moment-curvature curves were computed with CUMBIA®. For the columns' section from the first to the nineteenth floor, the author's MATLAB code was applied. Table 7-10 shows the hinge capacities that define the global moment-curvature bilinear curve for each story.

Table 7-10: Hinge capacities defining the moment-curvature relationship per story for PRILA Condominium

Story	Limit State	ϕ [1/in]	M [kip-ft]	Story	Limit State	ϕ [1/in]	M [kip-ft]
1st	Yield	0.00092	88,194.82	12th	Yield	0.00057	28,514.30
	Ultimate	0.00594	100,967.23		Ultimate	0.00937	38,638.81
2nd	Yield	0.00085	65,294.30	13th	Yield	0.00057	28,514.30
	Ultimate	0.00659	76,197.67		Ultimate	0.00937	38,638.81
3rd	Yield	0.00085	62,366.94	14th	Yield	0.00057	27,060.85
	Ultimate	0.00659	71,598.67		Ultimate	0.00937	36,933.78
4th	Yield	0.00076	52,312.46	15th	Yield	0.00057	27,060.85
	Ultimate	0.00659	60,842.95		Ultimate	0.00937	36,933.78
5th	Yield	0.00076	52,312.46	16th	Yield	0.00057	27,060.85
	Ultimate	0.00659	60,842.95		Ultimate	0.00937	36,933.78
6th	Yield	0.00068	41,586.96	17th	Yield	0.00057	27,060.85
	Ultimate	0.00659	50,755.59		Ultimate	0.00937	36,933.78
7th	Yield	0.00068	41,586.96	18th	Yield	0.00057	27,060.85
	Ultimate	0.00659	50,755.59		Ultimate	0.00937	36,933.78
8th	Yield	0.00062	34,910.59	19th	Yield	0.00057	27,060.85
	Ultimate	0.00682	45,271.26		Ultimate	0.00937	36,933.78
9th	Yield	0.00062	34,910.59	20th	Yield	0.00057	3,386.42
	Ultimate	0.00682	45,271.26		Ultimate	0.00937	5,115.49
10th	Yield	0.00057	30,180.29	21st	Yield	0.00057	3,044.95
	Ultimate	0.00937	40,276.12		Ultimate	0.00937	4,616.25
11th	Yield	0.00057	30,180.29	22nd	Yield	0.00057	3,044.95
	Ultimate	0.00937	40,276.12		Ultimate	0.00937	4,616.25

7.3.2 Nonlinear time-history analysis of PRILA

For the nonlinear dynamic structural evaluation of the PRILA Condominium, its updated nonlinear simplified computational model was subjected to the seven probable earthquakes determined for the municipality of San Juan, PR. These earthquakes were artificially generated from the seed earthquakes listed in Table 7-3 as explained in Section 7.12. The nonlinear time-history analyses of the building were performed in SAP2000® as a direct integration nonlinear analysis and considering the $P-\Delta$ effect. For this purpose, the Takeda hysteretic model was selected to model the cyclic behavior of the reinforced concrete.

To quantify the effect of each probable earthquake on the structure, demand parameters were evaluated from the dynamic structural responses obtained with the PRILA Condominium nonlinear computational model. However, five of the seven probable earthquakes caused the

structure to collapse and the other two caused major damage producing excessive deformations. These two earthquakes are *rollhill.v2* and *USACA66.001*. The structural responses were set to be computed by SAP2000® for 180 seconds, to make sure that the complete response oscillations were captured until the motion stops. Although no collapse was observed when the *USACA66.001* record was applied to the PRILA model, the displacement response exhibited a tendency which may produce a collapse of the structure beyond the 180 seconds. Table 7-11 presents the maximum values of demand parameters obtained from the SAP2000® model response output. Only the peak values caused by the earthquakes that did not make the building collapse are included in the table.

Table 7-11: Peak values of demand parameters and final condition for PRILA Condominium

Parameters	JAP03.104	JAP03.173	MEX03.112	pacoimaw.v2	rollhill.v2	USAAK02.067	USACA66.001
Peak Acceleration [g]	---	---	---	---	21.68	---	36.21
Peak Velocity [in/s²]	---	---	---	---	54.07	---	52.18
Peak Displacement [in]	---	---	---	---	200.03	---	204.37
Base Shear, V_{max} [Kips]	---	---	---	---	16,851.3	---	20,660.5
Base Moment, M_{max} [K-ft]	---	---	---	---	120,512.63	---	236,893.52
Final condition	Collapse	Collapse	Collapse	Collapse	Perm. Def.	Collapse	Perm. Def. (Possible Collapse)

7.3.3 Static pushover analysis for PRILA

A displacement-controlled pushover analysis was performed to the PRILA Condominium to evaluate its lateral capacity until it reaches its ultimate state. The analysis was performed in SAP2000® using the same nonlinear simplified model employed for the nonlinear dynamic analyses presented in Section 7.3.2. Table 7-12 displays the building's state capacity and Figure 7-27 displays the pushover curve obtained for the PRILA Condominium. It can be noticed that the maximum base shear values of Table 7-11 far exceed the ultimate capacity of the building. However, the peak displacement values corresponding to the *rollhill.v2* and *USACA66.001* records, and which produced permanent deformations, are smaller than the displacement capacity displayed in the building's pushover curve.

Table 7-12: PRILA Condominium's state capacities

PRILA's Capacity Values		
State	*Δ [in]*	*F [Kips]*
1st Yield	1.392	747.707
Ultimate	462.792	881.264

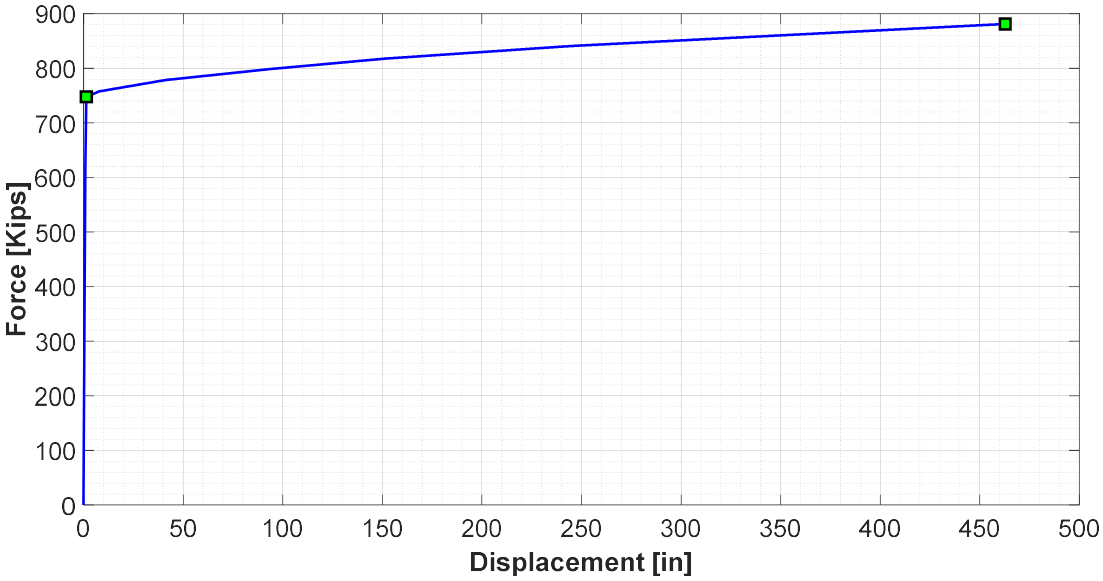


Figure 7-27: Pushover capacity curve for PRILA Condominium

CHAPTER 8. CONCLUSIONS AND RECOMMENDATIONS

Infrastructure deterioration is a serious issue that threatens every citizen's well-being and therefore must be pro-actively addressed through research to seek innovative solutions. This study effectively accomplished this goal by implementing state-of-the-art methodologies for structural health monitoring of aged and/or deficient infrastructure systems and by applying nonlinear computational methods and tools to assess their seismic vulnerability and prognosis. The feasibility in the implementation of the latest health monitoring techniques and proposed improved approaches addressing practical issues in experimental dynamic identification were presented as a comprehensive solution framework to encourage the adoption of these methodologies in similar infrastructure needs. Similarly, the methods and simplifications for seismic analyses and assessment were presented as an alternative approach to deliver accurate, fast, and reliable diagnostics on the current structural health of infrastructure systems. It is intended that this research project establishes a precedent in the current practice of this discipline in Puerto Rico and the United States by establishing sequential alternatives of implementation for various experimental identification methodologies and nonlinear seismic analyses procedures that could be selectively adapted to specific cases of comparable nature. It is important to note that this study took advantage of the PRSMP and its instrumented network of structures. The role that instrumentation networks, like this one in Puerto Rico and others in the United States, have is of great relevance in the advancement of new scientific developments to better improve our infrastructure's health and the safety of its users.

The focus of this research was to effectively implement and assess different non-parametric identification methodologies by implementing them to an in-service highway bridge in Ponce, PR, which contains deterioration traces and that has undergone several seismic events, and to an aged high-rise residential building, designed with mid-20th century building codes. For this purpose, the experimental analyses were performed to recorded ambient vibration measurements and earthquake responses. The experimental identification methodologies implemented for these recordings were the FFT, RDT, and Wavelet Transforms. In addition, probable earthquakes, compatible to ASCE7-16, were generated for Ponce, PR and San Juan, PR to perform nonlinear analyses to both structures. Concluding remarks with some recommendations for each

mathematical tool and its implementation are presented in Section 8.1. Likewise, conclusions and recommendations on the implementation and development of analytical and experimental FRFs is addressed in Section 8.2. Section 8.3 provides conclusions and recommendations for the nonlinear analyses and the proposed analysis approach. Finally, recommendations for future related research is presented in the last section.

8.1 Implemented Mathematical Identification Tools

8.1.1 Fast Fourier Transform

In the analyses of ambient and earthquake responses' recordings, the FFT proved to be the most efficient computational tool in identifying the frequency content embedded in the recorded responses. However, even though it is a fast computing tool and that it has proved to produce highly reliable results in identification applications, a notable drawback is its resolution issues when analyzing short length signals. The transform's frequency resolution increases with increased signal length. So, for short signals, such as the recorded earthquakes' responses, ranges of dominant frequency content may not accurately represent the actual values due to this resolution defect. This issue can be greatly reduced by increasing the number of samples in the signal by zero padding or by repeating the signal multiple times in the same vector. Another problem related to the FFT is that it reflects each frequency embedded in the signal regardless if it is an undesired frequency not intended to be captured in the recording or if it is the desired features that are wanted to identify. This makes the identification process difficult to interpret in cases where the analyst, at least, does not have an idea of the system's characteristic that he is looking for. This adverse effect can be mitigated by applying the FFT to windowed segments of data. Also, if the studied system is expected to contain the same dominant frequencies throughout the entire recording length, analyzing very long segments of data may reflect with more accuracy the featured frequency that is desired to disguise. Finally, the FFT provides no information on the instant of emergence of the embedded frequencies in the analyzed signals. In conclusion, when implementing the Fourier transform to an unknown system response signal it is important to follow the applicable recommendations according to the recorded signal's characteristics, such as its sampling frequency and recorded length to ensure better frequency content assessment.

8.1.2 Random Decrement Technique

As a time-domain identification tool, the RDT implemented on experimental ambient vibration recordings of ~~a~~ SDOF and MDOF systems produced a good quality correlation function (i.e., signature) from which it was possible to extract the dynamic parameters of the Ponce Highway Bridge and PRILA Condominium due to their resemblance to a damped system's free vibration response. In particular, the generation of RDSs for MDOF systems, such as PRILA Condominium, will substantially possess dynamic traits belonging to the fundamental mode of vibration of the system. Therefore, to identify higher modes' parameters it is necessary to apply a band-pass filter to the recorded response signals in which the cutting frequencies are obtained from an iterative process of visual inspection on the unfiltered signal's frequency spectra. Other methods, such as the generation of experimental FRFs and its corresponding modal shapes identification, can serve to validate that the intended frequency band is correctly identified for each higher mode. This approach is very useful when selecting the cutting frequencies of a response signal corresponding to a dynamic system possessing closely spaced modes. After proper selection of the cutting frequencies for each desired mode, a filtered time series can be reconstructed for each mode of vibration of interest and the RDT can be implemented to each reconstructed signal in order to satisfactorily generate a RDS for each of the modes intended to completely identify.

Furthermore, in order to produce quality decaying RDSs, the recorded responses must be adequately baseline corrected. This is because the RDT effectively works under the assumption of a signal response with characteristics similar to a white noise. Any trend encountered in the analyzed signal will negatively affect the generated RDS. In cases of high trends, the RDS will not even look as a SDOF free vibration response signal. Consequently, dynamic parameters' estimation will not produce reliable results, or in the worst cases, time domain identification will not be possible to perform. Therefore, a cubic spline piecewise correction is preferred and adequate visual inspection of the signal trends is highly recommended.

A drawback of the RDT when implemented to signals with considerable (i.e., moderate to high) noise levels, is the noise (or higher frequency) traces embedded in the initial portion of the generated RDS. As an example, the RDS generated for Ponce Highway Bridge [ID: 2348], shown in Figure 5-3 with a total duration of five seconds, displays traces of the traffic induced vibrations on its first second of duration. Therefore, when performing time domain identification procedures considering the peaks in that region, the computed frequency corresponds to the vehicles traveling

along the bridge and not to its natural frequency of vibration. This adverse effect was better illustrated in Figures 5-5 and 5-6 and in Table 5-2. Similarly, for PRILA Condominium, the generated RDS shown in Figure 5-38, displays a free decay correlation function with an extremely high level of noise traces embedded throughout the entire signature. In this case, Figure 5-39 shows that the implementation of the Wavelet transform on the generated signature separated the frequencies' components allowing the analyst to identify that the high noise in the RDS corresponds to the traffic vibrations and leaving a clean free decay signature corresponding to the fundamental dynamic properties of the building. Another limitation of the RDT is that recordings with enough length are required in order to produce an adequate averaging process with the recommended number of segments or more. Similarly, the threshold selection (Section 2.4.1) and its parameters is critical because from this criterion depends the number of segments selected for the averaging process. Moreover, the nature of the signal and its statistical properties (e.g., noticeable skewness or high kurtosis) may affect the effectiveness of the selected criteria on the final RDS quality.

In conclusion, the implementation of the RDT in recorded ambient responses of physical systems requires a high level of signal inspection and engineering judgement to successfully produce accurate and reliable results of dynamic identification. However, once the RDS is adequately generated, the adverse issues related to noise traces embedded in the signature and the problems that it may cause in applying time domain identification procedures to successfully compute accurate results of the system's dynamic parameters can be solved by applying another identification method that may be a lot less sensitive to this issues. Some sequential identification approaches after generating the RDS are the implementation of the Empirical Mode Decomposition, the Hilbert-Huang transform, or the Wavelet transform. In this study, the Wavelet transform was applied to the RDSs and consequently the system's dynamic parameters were successfully identified with much more ease, accuracy, and increased reliability.

8.1.3 Wavelet Transform

The implementation of the Wavelet transform in the identification of the dynamic parameters of Ponce Highway Bridge [ID: 2348] and of PRILA Condominium demonstrated its capabilities in producing quality results when used as a stand-alone tool or jointly with another technique as part of an identification framework. In this research, both approaches were tested and each

provided excellent parameters estimation. Firstly, the Wavelet transform was used in sequential combination with the RDT to recorded ambient vibration responses. For the case of Ponce Highway Bridge [ID: 2348], after the five seconds RDS shown in Figure 5-3 was generated, it was used as input signal to the Wavelet transform with the Complex Morlet Wavelet used as the basis function for the analysis. Due to the Wavelet transform capabilities in analyzing multicomponent signals, it behaved as a filter, in which the higher frequency signals embedded in the first second of the RDS, and corresponding to the vehicular traffic vibrations, were separated from the original RDS as noted in Figure 5-8. The use of a complex basis function in the analysis allowed the transform to reconstruct the analytic signal corresponding to each of the detected frequency components. This advantageous capability provided the great benefit of reconstructing a decaying signal equivalent to the original noise-contaminated RDS but without the noise traces embedded in it. Then, by using any traditional approach it is possible to successfully compute the bridge dynamic parameters with enhanced accuracy. Likewise, for PRILA Condominium, RDSs were generated for ambient vibrations' responses recorded in each of the sensors on the $N-S$ direction of the building. These signatures, such as the one shown in Figure 5-38 for sensor #33, were used as input to the Wavelet transform with the Complex Morlet Wavelet used as the basis function for the analysis. This allowed to separate noise traces from the signature and consequently generate an analytical signal of the free decay signature for each sensor's measured response to effectively extract the fundamental dynamic properties of the building by implementing time-domain procedure. In the same way, the Wavelet transform was used to identify the dynamic properties of PRILA Condominium corresponding to each of the first four modes of vibration. The input signals used for this purpose were the RDSs obtained from each of the previously band-pass filtered signals generated to capture each of these modes of vibration. The frequency content of each of the filtered signals used to generate RDS for each mode of vibration is shown in Table 5-15. As a result, each natural frequency of vibration and its corresponding damping ratio were effectively obtained for the four modes of vibration. These results are displayed in Table 5-20.

Similarly, the Wavelet transform was implemented to the recorded ambient responses measured at sensor #5 in the bridge. With this approach, it was possible to detect the dominant frequencies in an eighteen-hour recording interval. The Wavelet transform was capable to detect the frequencies corresponding to the traffic-induced vibrations, but most important, the bridge's natural frequency of vibration. In fact, the transformation results display a highly defined

dominant ridge corresponding to the natural frequency throughout the entire recording period. This is of great benefit when analyzing non-stationary transient signals because it allows to track the changes or shifts in frequencies of monocomponent or multicomponent signals. Furthermore, this feature makes the Wavelet transform an excellent tool for evaluating the possibilities of nonlinearities or inelastic emergence in structural systems subjected to strong dynamic excitations, such as high intensity earthquakes or vehicle crashes in the bridge's structural elements. In the case of PRILA Condominium, this approach was not performed because of the lack of computational memory to store and display the results from more sensors' responses with more recorded length.

Finally, the four recorded earthquakes' responses on Ponce Highway Bridge [ID: 2348] were analyzed with the Wavelet transform. For these and similar analyses of earthquakes, the transform results allow to detect the exact time instant in which one or more specific frequencies dominates the structure behavior. In a similar fashion, it is possible to continuously track the natural frequencies of the system immediately after the earthquake to detect any possible natural frequency shift and if so, determine if it is permanent or transient. This is better illustrated in Figures 5-20 to 5-27.

In conclusion, the Wavelet transform proved to be an excellent tool for determining and assessing the instantaneous frequency content of a physical SDOF or MDOF system from experimentally recorded measurements of ambient and earthquake responses. For this research study, the ambient recordings were baseline corrected although the Wavelet transform can be computed to trended signals. However, one notable drawback of this tool is its high computational power need. Similarly, the generation of spectrograms for displaying the results consumes too much computer RAM. Both situations are especially notable when working with long records. In addition, a good video card is highly recommended for this purpose. As a result, these computational needs limit the implementation of the Wavelet Transform in experimental dynamics identification purposes.

8.2 Frequency Response Functions

In this research study, FRFs for Ponce Highway Bridge [ID: 2348] and PRILA Condominium were analytically and experimentally obtained. For the bridge, the analytical FRF was derived from the updated SDOF model. The resultant FRF effectively describes the bridge dynamic

behavior in the frequency domain as an ideal SDOF system. This allows to predict how the system will behave in the linear-elastic regime, expressed in the form of a frequency domain output signal, by algebraically multiplying the computed FRF by any signal of interest, as expressed in equation (6.1). The generated output response can be transformed to the time domain if desired. Similarly, this approach was backwards implemented in this research. This FRF effectively worked in identifying input earthquake excitations that were not experimentally recorded. For this purpose, the recorded earthquake responses from sensor #5 at Ponce Highway Bridge [ID: 2348] were divided by the previously derived analytical FRF. This made it possible to generate four input earthquakes excitations that produced the response motions. Consequently, the frequency spectra of these generated equivalent earthquakes were computed to better assess the corresponding bridge responses and its frequency spectrum. It can be noticed from Figures 6-9 to 6-12 that the dominant frequencies in the equivalent earthquakes do not match the natural frequency of vibration of the bridge. Therefore, the chance of the bridge getting resonantly excited by the earthquakes, creating a possibility of damage, is little to none. Likewise, analytical FRFs were derived for PRILA Condominium. In particular, the absolute accelerance function was plotted to show the first four resonant frequencies from the updated mathematical model. This is displayed in Figure 6-3. This FRF effectively describes the dynamic behavior of the building in the linear-elastic regime and can be used as a dynamic prediction tool by using different input signals, such as probable seismic events or localized harmonic excitations.

On the other hand, experimental FRFs were computed for both structures in this study using their corresponding recorded ambient measurements. For Ponce Highway Bridge [ID: 2348], because there is no sensor installed at the base of the bridge piers or a free-field station, sensor #2 was used as the input excitation. Its selection was based on the fact that it was attached at mid height of the west abutment, which was initially assumed to be rigid enough as to transfer the ground motions with little to none distortion. However, the generated FRF, shown in Figure 6-6, did not displays any dominant frequency corresponding to the bridge. Therefore, the experimental FRF incorrectly describes the bridge. This may be caused do to the interaction of the abutment and its filling soil or to non-structural components affecting the vibration recordings. In this sense, this demonstrates the importance of the missing sensors. To solve this issue, it was proposed to generate a signal with ideal white noise characteristics, shown in Figure 6-4, and use it as input to the bridge. Consequently, this proposed approach produced accurate results with enhanced

fidelity. Even though the recorded bridge response does not correspond to the simulated signal used as input, it produces excellent results for the natural frequency identification. This FRF generated with the proposed approach is displayed in Figure 6-7. This proposed method can be used as an effective solution to structures with damaged or missing sensors at the base or when sensors are incorrectly placed. In the case of PRILA Condominium, experimental FRFs were generated from ambient vibrations response recordings using as its input signals the ones recorded at its base sensors #3 and #7 on the building west and east sides, respectively. Through their generation it was possible to obtain the structure's natural frequencies of vibration. However, because of the structure's extent, geometrical characteristics, and the characteristics of the noise embedded in the response signals, it was necessary to go further into the analysis by extracting the modal shapes of the building, according to its sensors' layout, for each peak possibly representing a natural frequency of vibration. With this approach the natural frequencies identification was successfully accomplished with increased reliability. These modal shapes are illustrated in Figures 6-16 to 6-23. In addition, the modal shapes identification through the imaginary component of the computed experimental FRFs allows the possibility to mathematically compute experimental modal vectors for the studied structural system. However, this approach was out of the scope of this study.

In conclusion, the computation of FRFs of a system provides valuable information and a deeper understanding on the actual or expected behavior of a dynamic system. Analytical FRFs from updated models are highly recommended to assess dynamic behaviors on proposed designs of structural systems as well as for assessment of structures after the possible occurrence of a damage state as a way of quantifying its extent, if any, by comparison with the reference (undamaged) state represented by the updated model FRF. Similarly, experimental FRFs are valuable tools to identify specific traits on the current health of the structure, from a global dynamic perspective. However, its interpretation may not be as trivial as when working with analytical FRFs. Issues such as inadequate alignment of sensors throughout the structure or lack of sensors in major input excitations locations may, with great possibility, produce unreliable results. In the case of MDOF systems, these situations can be worsened by inadequate baseline correction practices, proposed ambient vibrations' frequency content distribution and resolution, and quantity and location of sensors throughout the system. It is recommended that the implementation and interpretation of this method for dynamic assessment is carried out by experienced analysts, who can correctly

recognize how any of these mentioned possibilities is affecting the obtained results. Finally, analytical updated FRFs play a significant role in dynamic experimental assessments when there are no sensors recording input excitations. This was demonstrated in Section 6.1.2.3, when equivalent earthquakes were generated for the Ponce Highway Bridge [ID: 2348], based only on the recorded earthquake's responses at sensor #5. After computing those four equivalent input earthquakes, their corresponding frequency spectrum was computed with the FFT and it was concluded that they did not adversely affected the bridge's structural integrity, from a resonant excitation stand point.

8.3 Nonlinear Procedures and Analyses for Structural Assessment

In order to completely assess the structural capacity and the dynamic behavior of the Ponce Highway Bridge [ID: 2348] and of the PRILA Condominium, static and dynamic nonlinear computational analyses were performed to both structures. Due to the complexity of the physical structural systems and the computational limitations, a simplified modeling approach was proposed and implemented to satisfactorily perform both types of analyses and produce assessment results. The proposed simplification consisted in generating an equivalent one-component element per story, each containing an equivalent moment-curvature bilinear approximation computed from the corresponding lateral load-resisting elements of each story. To construct the bilinear moment-curvature relation for each story it is proposed to define each story's hinges' yield and ultimate moment capacity properties by adding all the corresponding moment capacities of all the individual elements acting in a parallel spring arrangement. On the other hand, each story hinge's yield and ultimate curvatures were defined by the highest curvature capacity of all the individual elements. Then a linear-elastic computational model of each structure, simplified as an equivalent vertical column with lumped masses at each story height, is modified with the nonlinear equivalent properties. With this simplified nonlinear model, it is possible to considerably reduce the analyses' time of execution and the required computational need while effectively performing the necessary nonlinear analyses and producing reliable results. However, this simplification does not possess redundancy elements and does not account for geometric effects in the structural response.

For this research study, it was proposed to modify the set of earthquakes suggested for the municipalities of Ponce, PR and San Juan, PR in Irizarry (1999) and make them compatible to the elastic design response spectrum in ASCE7-16. In addition, these modified suggested earthquakes

were scaled in accordance to the soil type to consider soil amplification effects. For this study, soil type D was proposed for both structures due to the lack of information in this respect. These probable earthquakes were used as input for the corresponding nonlinear dynamic time history analisis.

In the case of the Ponce Highway Bridge [ID: 2348], the structure behaved predominantly in the linear-elastic range. However, the dynamic responses showed spontaneous events of minor inelasticities at the nonlinear hinges. In fact, six of the seven probable earthquakes' responses showed minor nonlinearities. This was predominantly caused by the impulsive characteristic of most of the probable earthquakes but mostly due to the high PGA of all the input earthquakes, which is far higher than the design PGA in the late 1980s and early 1990s, when the highway bridge was designed. For instance, by visually inspecting the frequency spectrum of each input earthquake, only two of them have high peaks in a region near the resonant frequency of the bridge, therefore discarding the possibility of damage due to resonance effects as the main cause. Finally, a static pushover analysis was performed to the bridge computational model with the same initial nonlinear properties to compare the dynamic nonlinear results with the lateral capacity curve. All except one of the input probable earthquakes generated peak displacement responses exceeding the yield limit of the bridge. In the same way, all except one produced a base shear exceeding the determined force capacity from the analysis. These results are better illustrated in Table 7-7 and in Figure 7-26.

For PRILA Condominium, the same two nonlinear analysis procedures were performed. However, the results for the nonlinear dynamic analyses showed that the building suffered a great extent of damage that caused its collapse in five of the seven earthquakes used as input excitation and for the other two the building remained standing but with permanent deformations. This is the result of a combined effect caused by frequency spectra of all input probable earthquakes predominantly located in the region where the fundamental frequency of the building is located and strong motion durations ranging from 40 to 50 seconds of duration. In addition, the effect caused by the probable earthquakes' PGA, which is far higher than the design PGA in the 1960s, when PRILA Condominium was designed, may have adversely influenced. Furthermore, a static pushover analysis was performed to PRILA's computational model with the same initial nonlinear properties to determine the lateral force-displacement capacities of the building and make comparisons with the maximum parameters' values obtained from the dynamic nonlinear analyses,

which are shown in Table 7-11. From the static analysis, the ultimate force capacity of the building was found to be $881.264\ Kips$ and its corresponding displacement capacity is $462.79\ in$. This corresponds to a displacement ductility of $\mu_\Delta = 332.5$, which is extremely high for a high-rise shear wall building designed in the 1960s. This is better illustrated in Table 7-12 and in Figure 7-27. When comparing the capacity parameters' result from both analyses it can be observed that the forces generated on PRILA Condominium from five of the seven probable earthquakes used as input far exceeded both the force and the displacement capacities of the structure, producing a total collapse of the building. However, two of the input probable earthquakes caused considerable damage as to produce permanent deformations and not collapse, at least for the duration of the computational analysis.

It is important to note that the updated 2D model of the PRILA Condominium may not accurately represent the physical system. This model only considers the capacities of the structural elements and provides no redundancy if one of the equivalent elements corresponding to a specific story fails, as opposed to the physical structure. In addition, PRILA is a massive structure with a shear wall area to floor area ratio of 3.72% in its N-S direction. High-rise buildings with a ratio between 2% and 4% have been documented by Wood (1991) to behave with good performance under seismic events in the Viña del Mar area in Chile. Furthermore, the model does not consider the increased flexural capacity of the walls due to the coupling effect. Therefore, the 2D model of the building is more flexible that the physical structure.

In conclusion, these analysis results should serve as a basis for rehabilitation and retrofitting efforts on both structures. The sequential identification analyses, the proposed simplification of complex computational models, and the adaptation of the set of probable earthquakes recommended in previous studies for this and other municipalities of Puerto Rico are highly recommended to effectively assess the aging infrastructure needs. The adequate implementation of these analysis approaches will provide fast and reliable results that will better serve to improve our infrastructure health. For future studies it should be convenient to modify the simplified 2D model of high-rise buildings to account for other effects that may positively increase the system's capacity. In addition, the effect of the modification of input seismic excitations in the structural response should be studied to assess the building performance in these cases, such as the demand requirements from the latest building codes. the considering the foundation system and the soil-structure interaction.

REFERENCES

Aggour M. S., Yang J. C. S., Al-Sanad H.. (1982). "Application of the random decrement technique in the determination of damping of soils". Proceedings of the 7th European Conference on Earthquake Engineering. Athens, Greece, September, pp. 337–344.

Aguirre-Realpe, Diego A. (2013). "Implementation of Wavelet Based Damage Detection Methods Using Full-Scale Shaking Table Data and Nonlinear Finite element Models". M.S.C.E. Thesis. Department of Civil Engineering and Surveying. University of Puerto Rico at Mayagüez, Puerto Rico.

Algan, B. B. (1982). "Drift and damage consideration in earthquake-resistant design of reinforced concrete buildings". Ph.D. dissertation. University of Illinois. Urbana-Champaign, IL.

American Society of Civil Engineers. (2016). "ASCE Minimum Design Loads and Associated Criteria for Buildings and Other Structures".

American Society of Civil Engineers. (2017). "2017 Infrastructure Report Card: A Comprehensive Assessment of America's Infrastructure". ASCE Publications.

Ansari, F. (2007). "Practical implementation of optical fiber sensors in civil structural health monitoring". J. Intell. Mater. Syst. Struct., Vol. 18, pp. 879 – 889.

Applied Technology Council (ATC)-58. (2004). "Engineering Demand Parameters for Structural Framing Systems". Project Task Report, Phase 2, Task 2.2. Redwood City, California, USA.

Arias, A.. (1970). "A Measure of Earthquake Intensity". Seismic Design of Nuclear Power Plants, Ed. Hansen, R.. Cambridge, Massachusetts, USA. pp. 438-483.

Asmussen J. C.. (1997). "Modal Analysis Based on the Random Decrement Technique: Application to Civil Engineering Structures". PhD Dissertation. University of Aalborg. Denmark.

Bennett, K. D., and Batroney, C. B. (1997). "Interstory drift monitoring in smart buildings using laser crosshair projection". Opt. Eng., Vol. 36, pp. 1,889 – 1,892.

Bodin, P., Vidale, J., Walsh,T., Çakir, R., and Celebi, M.. (2012). "Transient and Long-Term Changes in Seismic Response of the Natural Resources Building, Olympia, Washington, due to Earthquake Saking". Journal of Earthquake Engineering, Vol. 16, pp. 607 – 622.

Cabrera, Felipe N.. (1998). "Evaluation of Seismic Performance of Plaza Inmaculada Building in San Juan, Puerto Rico". M.S.C.E. Thesis. Department of Civil Engineering and Surveying. University of Puerto Rico at Mayagüez, Puerto Rico.

Cano-Saldaña, Leonardo. (2008). "On Time-Frequency Analysis for Structural Damage Detection". PhD Dissertation. Department of Civil Engineering and Surveying, University of Puerto Rico at Mayaguez, Puerto Rico.

Cartz, Louis (1995). "Nondestructive Testing – Radiography, Ultrasonics, Liquid Penetrant, Magnetic Particle, Eddy Current". ASM International. Materials Park, Ohio, USA. ISBN: 0-87170-517-6

Casas, J. R., and Cruz, P. J. S. (2003). "Fiber optic sensors for bridge monitoring". Journal of Bridge Engineering. Vol. 8, No. 6, pp. 362 – 373.

Celebi, M.. (2002). "Current Practice and Guidelines for NSMP Instrumentation of Buildings, Including Federally-Owned/Leased Buildings". In Strong-Motion Instrumentation of Buildings, Workshop Proceedings. COSMOS, Richmond, CA.

Celebi, M., and Sanli, A. (2002). "GPS in pioneering dynamic monitoring of long-period structures". Earthquake Spectra, Vol. 18, pp. 47 – 61.

Chang, C.S. (1975). "Studies for Dynamic Characteristics of Aeroelastic Systems Utilizing Randomdec Signatures". *NASA CR* 13253.

Chen, W. M., Bennett, K. D., Feng, J., Wang, Y. P., and Huan, S. L. (1998). "Laser technique for measuring three dimensional interstory drift". Proc. SPIE. 3555, pp. 305 – 309.

Chun-Lin and Liu, A.. (2010). "A tutorial of the Wavelet Transform". February 23.

Clinton, John F.. (2004). "Modern Digital Sesimology – Instrumentation, and Small Amplitude Studies in the Engineering World". Ph.D. Dissertation. California Institute of Technology.

Cole, Henry (1973). "On-line Failure Detection and Damping Measurement of Aerospace Structures by Random Decrement Signatures". Technical Report NASA CR-2205, US National Aeronautics and Space Administration.

Consortium of Organizations for Strong Motion Observation Systems (COSMOS). (2001). "Guidelines for Installation of Advanced National Seismic System Strong-Motion Reference Stations". COSMOS, Richmond, CA. URL: http://www.cosmoseq.org/Guidelines_PDF.pdr .

Consortium of Organizations for Strong-Motion Observation Systems (COSMOS). (2009). "Strong motion record processing guidelines". URL: http://www.cosmos-eq.org/recordProcessingPapers.html.

Daubechies, I.. (1992). "Ten Lectures on Wavelets". Society for Industrial and Applied Mathematics. CBMS-NSF Regional Conference Series in Applied Mathematics, Philadelphia, PA.

Daubechies, I.. (1996). "Where do wavelets come from? – A personal point of view". Proceedings of the IEEE, Vol. 84, No. 4, pp. 510 – 513.

Daubechies, I., Lu, J. y Wu, H.T. (2011). “Synchrosqueezed wavelet transforms: An empirical mode decomposition-like tool”. Applied and Computational Harmonic Analysis, Vol. 30, pp. 243 – 261.

Doebling, S.W., Farrar, C.R., and Prime, M.B. (1998). “A Summary Review of Vibration-based Damage Identification Methods”. The Shock and Vibration Digest, Vol. 30, No. 2, pp. 91 – 105.
Dowell, R., Seible, F., and Wilson, E. (1998). “Pivot Hysteresis Model for Reinforced Concrete Members”. Structural Journal, Vol. 95, No. 5, pp. 607 – 617.

Feldman, M. (2006). “Time varying vibration decomposition and analysis based on the Hilbert transform”. Journal of Sound and Vibration. Vol. 295, pp. 518 – 530.

Gabor, D.. (1946). “Theory of communication”. Proceedings of the IEEE, Vol. 93, No. 3, pp. 429 – 457.

Gandomi, A. H., Sahab, M. G., Rahaei, A., and Safari Gorji, M.. (2008). “Development in Mode Shape-Based Structural Fault Identification Technique”. Department of Civil Engineering, Tafresh University, Tafresh, Iran. World Applied Sciences Journal. Vol. 5, No. 1, pp. 29 – 38. IDOSI Publications.

Giberson, M.F.. (1967). “The Response of Nonlinear Multi-storey Structures subjected to Earthquake Excitation”, Earthquake Engineering Research Laboratory, California Institute of Technology Pasadena, California, EERL Report

Herrera-Sánchez, Juan C. (2005). “Evaluation of Structural Damage Identification Methods Based on Dynamic Characteristics”. PhD Dissertation. Department of Civil Engineering and Surveying, University of Puerto Rico at Mayagüez, Puerto Rico.

Huang, N. E., Long, S. R., and Shen, Z.. (1996). “The Mechanism for Frequency Downshift in Nonlinear Wave Evolution”. Advances in Applied Mechanics, Vol. 32, 59–117, 117A, 117B, 117C.

Huang, N. E., Shen, Z., Long, S. R., Wu, M. C., Shih, H. H., Zheng, Q., Yen, N. C., Tung, C. C., y Liu, H. H. (1998). “The Empirical Mode Decomposition and the Hilbert Spectrum for Nonlinear and Non-stationary Time Series Analysis”, Philosophical Transactions of the Royal Society, Vol. A 454, pp. 903 – 995.

Huang, N. E., Shen, Z., and Long, S. R. (1999). “A new view of nonlinear water waves: the Hilbert spectrum”. Annual Review of Fluid Mechanics, Vol. 31, pp. 417 – 57.

Huang, M. -J. and Shakal, A. F.. (2001). “CSMIP Building Instrumentation Measurement Objectives and Models”. In Strong-Motion Instrumentation of Buildings, Workshop Proceedings. COSMOS, Emeryville, CA.

Huang, N. E. and Wu, Z.. (2008). “A Review on Hilbert-Huang Transform: Method and its Applications to Geophysical Studies”. Reviews of Geophysics, Vol. 46, RG2006, doi: 10.1029/2007RG000228.

Huerta, C.I.. (2002). “Determination of Soil Properties from Earthquake Data”. PhD Dissertation. University of Texas in Austin. Austin, Texas, USA.

Hudnut, K. W., and Behr, J. (1998). “A continuous GPS monitoring of structural deformation at Pacoima Dam, CA”. Seismol. Res. Lett., Vol. 69, pp. 299 – 308.

Hunaidi, O.. (2000). “Traffic Vibrations in Buildings”. National Research Council of Canada, No.39, June.

Ibrahim, S.R. (1977). “Random Decrement Technique for Modal Identification of Structures”. Journal of Spacecraft and Rockets, Vol. 14, No. 11, pp. 696-700.

Irizarry, J.. (1999). “Design Earthquakes and Design Spectra for Puerto Rico’s Main Cities Based on Worldwide Strong Motion Records”. Ph.D. dissertation. University of Puerto Rico Mayagüez Campus. Mayagüez, PR.

Juang, J.N.. (2000). “Applied System Identification”. Prentice Hall PTR. Upper Saddle, NJ. ISBN: 0-13-079211-X.

Juang, J.N. and Phan, M.Q.. (2001). “Identification and Control of Mechanical Systems”. Cambridge University Press. Cambridge, UK. ISBN: 0-521-78355-0.

Kijewski, T. and Kareem, A. (2003). “Wavelet Transform for System Identification in Civil Engineering”. Computed-Aided Civil and Infrastructure Engineering, Vol. 18, pp. 339 – 355.

King, F.W.. (2009a). “Hilbert Transforms”, Vol. 1, Cambridge University Press, Cambridge, UK. ISBN: 9780521887625.

King, F.W.. (2009b). “Hilbert Transforms”. Vol. 2, Cambridge University Press, Cambridge, UK. ISBN: 9780521517201.

Krawinkler, H.. (1999). "Progress and Challenges in Performance-based Earthquake Engineering". International Seminar on Seismic Engineering for Tomorrow - In Honor of Professor Hiroshi Akiyama, Tokyo, Japan.

Lee, Daniel T. L. and Yamamoto, Akio. (1994). “Wavelet Analysis: Theory and Applications”. Hewlett-Packard Journal, December, pp. 44 – 52.

Liu, Y.-W. and Smith, J. O.. (2002). “Perceptually Similar Orthogonal Sounds and Applications to Multichannel Acoustic Echo Canceling”. Proceedings of the Audio Engineering Society. 22nd International Conference on Virtual, Synthetic and Entertainment Audio in Espoo, Finland.

Martínez Cruzado, J., Irizarry, J., Portela, G.. (2001). “Espectros de Diseño para las Ciudades Principales de Puerto Rico Basado en Registros de Aceleración Mundiales”. Revista Internacional de Desastres Naturales, Accidentes e Infraestructura Civil, Vol. 1, pp. 21– 23.

Michel, C. and Gueguen, P.. (2010), “Time-Frequency Analysis of Small Frequency Variations in Civil Engineering Structures Under Weak and Strong Motions Using a Reassignment Method”. Structural Health Monitoring 9, pp. 159 – 171.

Misiti, M., Misiti, Y., Oppenheim, G., and Poggi, J. M. (2000). “Wavelet toolbox user’s guide”. The Math Works Inc., Natick, Massachusetts.

Moehle, J. and Deierlein, G. G.. (2004). “A Framework Methodology for Performance-Based Earthquake Engineering”. Proceedings of the 13th World Conference on Earthquake Engineering, Vancouver, B.C., Canada.

Montejo, L. A., Kowalsky, M. J. (2007). “CUMBIA—Set of codes for the analysis of reinforced concrete members”. CFL Technical Report, No. IS-07-01, Department of Civil Construction and Environmental Engineering, North Carolina State University, Raleigh, NC, 2007, 43 pp.

Montejo, L.A.. (2011). “Signal processing based damage detection in structures subjected to random excitations”. Structural Engineering and Mechanics, Vol. 40, No. 6, pp. 745 – 762.

Nakamura, S. (2000). “GPS measurement of wind-induced suspension bridge girder displacements”. Journal of Structural Engineering, Vol. 126, pp. 1,413 – 1,419.

National Earthquake Hazards Reduction Program (NEHRP). (2010). “Nonlinear Structural Analysis for Seismic Design: A Guide for Practicing Engineers”. NEHRP Seismic Design Technical Brief No. 4. National Institute of Standards and Technology (NIST), U.S. Department of Commerce.

Nie, K., Barco, A., and Zeng, F.-G. (2006). “Spectral and Temporal Cues in Cochlear Implant Speech Perception”. Ear Hear, Vol. 27, No. 2, pp. 208–217.

Oppenheim, Alan V., Willsky, Alan S., and Nawab, S.H.. (1996). “Signals and Systems”. 2nd Edition. Prentice Hall. Upper Saddle, NJ. ISBN: 0-13-814757-4.

Ovanesova, A. and Suárez, L. E. (2004). “Applications of Wavelet Transforms to Damage Detection in Frame Structures”. Engineering Structures, Vol. 26, No. 1, pp. 39 – 49.

Polikar, R.. (1999). “The Story of Wavelets”. Proceedings of the 3rd IMACS/IEEE CSCC’99 Multiconference. Athens, Greece. pages 5,481 – 5,486.

Potamianos, A. and Maragos, P.. (1994). “A Comparison of the Energy Operator and the Hilbert Transform Approach to Signal and Speech Demodulation”. Signal Processing, Vol. 37, No. 1, pp. 95 – 120.

Ramirez-Castro, R.I. and Montejo, L.A. (2011), "Hilbert Transform, Empirical Mode Decomposition and its Applications to Free Vibration Analysis (in Spanish)". Revista Internacional de Desastres Naturales, Accidentes e Infraestructura Civil, Vol. 11, No. 2, pp. 123 – 134.

Recio-Spinoso, A., Fan, Y.-H., and Ruggero, M.. (2011). "Basilar-Membrane Responses to Broadband Noise Modeled Using Linear Filters with Rational Transfer Functions". Biomedical Engineering, IEEE Transactions, Vol. 58, No. 5, pp. 1,456 –1,465.

Rilling, G., Flandrin, P., and Gonçalvès, P.. (2003). "On empirical mode decomposition and its algorithms", IEEE-EURASIP Workshop on Nonlinear Signal and Image Processing NSIP-03, Grado, Italia.

Rodrigues J., Brincker R.. (2005). "Application of the Random Decrement Technique in Operational Modal Analysis". Proceedings of the 1st International Operational Modal Analysis Conference. Copenhagen, Denmark, pp. 191-200.

Sanguansat. P. (Editor). (2012a). "Principal Component Analysis – Multidisciplinary Applications". InTech Publisher. ISBN: 978-953-51-0229-1.

Sanguansat. P. (Editor). (2012b). "Principal Component Analysis". InTech Publisher. ISBN: 978-953-51-0195-6.

Sanguansat. P. (Editor). (2012c). "Principal Component Analysis – Engineering Applications". InTech Publisher. ISBN: 978-953-51-0182-6.

Shakal, A. F. and Huang, M.. (2002). "Current Practice and Guidelines for CSMIP Instrumentation of Buildings". In Strong-Motion Instrumentation of Buildings, Workshop Proceedings, COSMOS, Richmond, CA.

Shakal, A. F. and Huang, M.. (2008). "Strong Motion Instrumentation of Buildings". Structure Magazine, InSights, November, pp. 60 – 61.

Shoukry, S. N., William, G. W., Downie, B., and Riad, M. Y.. (2011). "Effect of Moisture and Temperature on the Mechanical Properties of Concrete". Journal of Construction and Building Materials, Vol. 25, No. 2, pp. 688 – 696.

Skolnik, D. (2008). "Building instrumentation". Ph.D. dissertation. Dept. of Civil Engineering, University of California, Los Angeles.

Skolnik, D. and Wallace, J.. (2010). "Critical Assessment of Interstory Drift Measurements". Journal of Structural Engineering, Vol. 136, No. 12, pp. 1,574 – 1,584.

Smith, L. I.. (2002). "A Tutorial on Principal Component Analysis". University of Otago, New Zealand. URL: http://www.cs.otago.ac.nz/cosc453.

Smith, Seven W.. (2003). “Digital Signal Processing – A Practical Guide for Engineers and Scientists”. Newnes: An Imprint of Elsevier. USA. ISBN: 978-0-7506-7444-7

Sozen, M.A.. (1983). “Lateral Drift of Reinforced Concrete Structures Subjected to Strong Ground Motion”. Bulletin of New Zealand National Society for Earthquake Engineering, Vol. 16, No.2, pp. 107 – 122.

Stepp, J. Carl. (2002). “Strategies and Criteria for Selecting Buildings for ANSS Strong-Motion Instrumentation”. SIMP02 Seminar on Utilization of Strong-Motion Data, pp. 147 – 160.

Su, M. B. (1998). “TDR monitoring systems for the integrity of infrastructures”. Proc. SPIE, 3325, pp. 93 – 103.

Suárez, L. E., Montejo, L. A.. (2005). “Generation of artificial earthquakes via the wavelet transform”. International Journal of Solids and Structures, Vol. 42, pp. 5905-5919.

Takeda, T., Sozen, M., Nielsen, N. (1970). “Reinforced Concrete Response to Simulated Earthquakes”. Journal of the Structural Division, 1970, Vol. 96, Issue 12, Pg. 2557-2573

Tamura, Y., Matsui, M., Pagnini, L. C., Ishibashi R., and Yoshida A. (2002). “Measurement of wind-induced response of buildings using RTK-GPS”. Journal of Wind. Eng. Ind. Aerodyn., Vol. 90, No. 15, pp. 1,783 – 1,793.

Todorovska, M. I. and Trifunac, M. D. (2007). “Earthquake Damage Detection in The Imperial County Services Building I: The Data and Time Frequency Analysis”. Soil Dynamics and Earthquake Engineering 27, pp. 564 – 576.

Uniform Building Code (UBC). (1997). International Conference of Building Officials, Whittier, California, USA.

U.S. Geological Survey. (2018). “U.S. Seismic Design Maps”. URL: https://earthquake.usgs.gov/designmaps/us/application.php.

van Drongelen, W.. (2007). “Signal Processing for Neuroscientists: Introduction to the Analysis of Physiological Signals, Academic Press, London.

Velázquez-Carrasquillo, Luis R.. (2011). “Wavelet Based Damage Detection in Civil Structures Subjected to Earthquake Loads”. M.S.C.E. Thesis. Department of Civil Engineering and Surveying. University of Puerto Rico at Mayagüez, Puerto Rico.

Ville, J.. (1948). “Theorie et application de la notion de signal analytical”. Cables et Transmissions. Vol. 2a, No. 1, pp. 61 – 74.

Wahbeh, M. A., Caffrey, J. P., and Masri, S. F.. (2003). “A vision-based approach for the direct measurement of displacements in vibrating systems”. Smart Materials and Structures, Vol. 12, pp. 785 – 794.

Weeks, M.. (2011). “Digital Signal Processing – Using MATLAB and Wavelets”. Jones and Bartlett Publishers. ISBN: 978-0-7637-8422-5.

Wood, S. (1991). Performance of Reinforced Concrete Buildings During the 1985 Chile earthquake: Implications for the Design of Structural Walls. Earthquale Spectra 7:4,607-637.

Worden, K. (1990). “Data processing and experimental design for the restoring force surface method. Part I: Integration and differentiation of measured time data.” Mechanical Systems and. Signal Processing, Vol. 4, pp. 295 – 319.

Yan, A.-M., Kerschen, G., De Boe, P. Golinval, J.-C.. (2005a). “Structural Damage Diagnosis Under Varying Environmental Conditions – Part I: A Linear Analysis”. Journal of Mechanical Systems and Signal Processing, Vol. 19, No. 4, pp. 847 – 864.

Yan, A.-M., Kerschen, G., De Boe, P. Golinval, J.-C.. (2005b). “Structural Damage Diagnosis Under Varying Environmental Conditions – Part II: Local PCA for Non-linear Cases”. Journal of Mechanical Systems and Signal Processing, Vol. 19, No. 4, pp. 865 – 880.

Yang, J.C.S., G.Z. Qi, V. Pavlin, A.J. Durelli, and L. Esteva (1989). “In-situ determination of soil damping in the lake deposit area of Mexico City”, Soil Dynamics and Earthquake Engineering, Vol. 8, No. 1, pp. 43-52.

Zeldin BA, Spanos PD.” Random Field Representation and Synthesis Using Wavelet Bases.” ASME. J. Appl. Mech. 1996;63(4):946-952.